

## Use Authorization

In presenting this dissertation in partial fulfillment of the requirements for an advanced degree at Idaho State University, I agree that the Library shall make it freely available for inspection. I further state that permission to download and/or print my dissertation for scholarly purposes may be granted by the Dean of the Graduate School, Dean of my academic division, or by the University Librarian. It is understood that any copying or publication of this dissertation for financial gain shall not be allowed without my written permission.

Signature \_\_\_\_\_

Date \_\_\_\_\_

**Analysis of the integral experiment “Measurement of Actinide  
Neutronic Transmutation Rates with Accelerator mass  
spectroscopy (MANTRA)”**

By

Jyothier Kumar Nimmagadda

A dissertation

submitted in partial fulfillment

of the requirements for the degree of

Doctor of Philosophy in the Department of Nuclear Engineering

Idaho State University

Summer 2015

To the Graduate Faculty:

The members of the committee appointed to examine the dissertation of JYOTHIER KUMAR NIMMAGADDA find it satisfactory and recommend that it be accepted.

---

Dr. George Imel  
Major Advisor, Dept. of Nuclear Engineering and Health Physics

---

Dr. Giuseppe Palmiotti  
Committee Member, Idaho National Laboratory

---

Dr. Jay Kunze  
Committee Member, Dept. of Nuclear Engineering and Health Physics

---

Dr. Jason Harris  
Committee Member, Dept. of Nuclear Engineering and Health Physics

---

Dr. Steven Shropshire  
Graduate Faculty Representative, Dept. of Physics

## ACKNOWLEDGEMENTS

I would like to thank my advisor Dr. George Imel, for all of his guidance, support, and helpfulness given throughout my time as a graduate student at ISU. I owe him an immense debt of gratitude. I could not have imagined having a better advisor for my M.S. and Ph.D. studies.

I would like to thank my mentors Dr. Giuseppe Palmiotti and Dr. Gilles J Youinou, for all the guidance and help they provided directly relating to my dissertation work. I offer my sincere appreciation for the learning opportunities provided by both of them.

I would like to thank Dr. James W Sterbentz, for his support during the post irradiation analysis of this project.

I would like to thank Dr. David Nigg, for his help on the least squares method to unfold the neutron spectra.

I would like to thank Dr. Jay Kunze, Dr. Jason Harris and Dr. Steven Shropshire, for serving on my Ph.D. committee.

I would like to thank the folks at MFC, INL, for all their support during this project.

I would also like to thank my family for the support they provided me through my entire life and in particular, I must acknowledge my wife and best friend, Swathi, without whose love, encouragement and editing assistance, I would not have finished this dissertation.

Finally, I recognize that this research would not have been possible without the financial assistance. This work is supported by the U.S. Department of Energy, Office of Science, Office of Nuclear Physics, under DOE Idaho Operations Office and by the ATR National Scientific User Facility.

## **VITA**

I was born in Tanuku, Andhra Pradesh, India, on August 16, 1988. I graduated from high school in 2003, and went to VNR Vignana Jyothi Institute of Engineering and Technology College, Hyderabad, India to complete my undergraduate degree in Mechanical Engineering. I graduated with Bachelor of Technology in Mechanical Engineering in 2009. In the fall semester of 2009, I began attending ISU and completed Master of Science in Nuclear Science and Engineering in 2012. In the summer of 2012, I started my Doctor of Philosophy (Ph.D.) degree program in Nuclear Science and Engineering. After more than 3 years of dedication and hard work, I successfully completed my Ph.D. degree program in summer 2015.

**Dedicated To My Family**

# TABLE OF CONTENTS

	Page No.
LIST OF FIGURES.....	ix
LIST OF TABLES.....	xvi
LIST OF ABBREVIATIONS.....	xix
ABSTRACT.....	xxi
1. INTRODUCTION.....	1
1.1 The Need to Improve the Nuclear Data Files.....	2
1.2 Nuclides Transmutation Equations.....	4
1.3 Past Experiments Similar to MANTRA.....	7
1.4 Advanced Test Reactor.....	9
1.5 MANTRA Experiments.....	11
1.5.1 Boron Experiment.....	13
1.5.2 Cadmium Experiment.....	16
1.5.3 Capsules and Rodlets.....	19
1.5.4 MANTRA Sample Preparation.....	21
2. MONTE CARLO CODE (MCNP5).....	27
2.1 Simple Cylindrical Models.....	29
2.2 Reduced Models.....	32
2.3 ATR Flux Traps.....	36
3. ECCO_ERANOS.....	42
3.1 MCNP Source in ECCO.....	43
3.2 Simple Infinite Cylindrical Models.....	54

3.3 Cross-section Contributions and Sensitivity Coefficients.....	58
3.4 Uncertainty Analysis on the Experiments.....	62
4. SELF-SHIELDING EFFECTS.....	67
4.1 Infinitely Diluted Vs. Actual Masses of the Samples.....	70
4.2 Sample Wafers.....	74
5. UNFOLDING THE NEUTRON SPECTRA.....	91
5.1 <i>A priori</i> Spectrum.....	92
5.2 Response Functions.....	94
5.3 Measured Activities.....	100
5.4 MAXED Unfolding Method.....	106
5.5 Least Squares Method.....	107
5.6 Data Analysis.....	109
6. CONCLUSIONS.....	117
APPENDIX A ECCO Input File.....	119
APPENDIX B FORTRAN code to create external source file for ECCO.....	124
APPENDIX C Cross-sections Sensitivity Coefficients.....	125
APPENDIX D Capture Cross-sections Plots.....	134
APPENDIX E Activity Equation for Decay Correction.....	149
APPENDIX F Least Squares Method.....	151
APPENDIX G Unfolded Neutron Fluxes.....	153
REFERENCES .....	160

## LIST OF FIGURES

	Page No.
Figure 1.1.1 Iterative process necessary to generate accurate nuclear cross-section.....	3
Figure 1.3.1 Lethargy fluxes.....	8
Figure 1.4.1 ATR core with the red circles indicating the 'b9 and b11 irradiation locations used for MANTRA.....	10
Figure 1.5.1 ATR power history during the irradiation cycle 1 of the boron experiment..	12
Figure 1.5.2 ATR power history during the irradiation cycle 2 of the boron experiment and cycle 1 of the cadmium experiment.....	12
Figure 1.5.1.1 Cross-sectional view of the boron experiment in the ATR.....	14
Figure 1.5.1.2 Absorption cross-sections of B10 (red) and B11 (green).....	15
Figure 1.5.2.1 Detailed view of the cadmium experiment in the ATR.....	17
Figure 1.5.2.2 Absorption cross-section of Cd-113.....	18
Figure 1.5.3.1 Stack of rodlets one above the other inside the capsule.....	19
Figure 1.5.3.2 Boron experiment setup.....	19
Figure 1.5.3.3 3D (left) and 2D (right) views of the rodlet with a flux wire inside it.....	20
Figure 1.5.4.1 MANTRA target loading stand.....	21
Figure 1.5.4.2 Porcelain boat with a sample.....	21
Figure 1.5.4.3 Funnel setup used to fill the vials with samples.....	22
Figure 1.5.4.4 Vial with a sample inside.....	22
Figure 2.1.1 Simple cylindrical model of the boron experiment.....	29
Figure 2.1.2 Normalized fluxes at the sample location from both the models.....	30
Figure 2.2.1 Reduced model of the cadmium experiment.....	32

Figure 2.3.1 ATR cross-sectional diagram with flux traps.....	36
Figure 2.3.2 Flux traps with aluminum filler, pressure tube and insulation tube assembly.....	38
Figure 2.3.3 Flux traps with water in flow tube, pressure tube and insulation tube assembly.....	39
Figure 2.3.4 Discrepancies between benchmark model and FTA/FTW (B experiment).....	40
Figure 2.3.5 Discrepancies between benchmark model and FTA/FTW (Cd experiment).....	41
Figure 3.1.1 Infinite cylindrical model of the boron experiment.....	43
Figure 3.1.2 Normalized fluxes in the outer void layer of the boron experiment.....	44
Figure 3.1.3 Normalized fluxes in the water-gap before the boron filter.....	45
Figure 3.1.4 Normalized fluxes in the sleeve of the boron experiment.....	46
Figure 3.1.5 Normalized fluxes in the helium gap before the boron filter.....	46
Figure 3.1.6 Normalized fluxes in the boron filter.....	47
Figure 3.1.7 Normalized fluxes in the helium gap after the boron filter.....	48
Figure 3.1.8 Normalized fluxes in the basket of the boron experiment.....	48
Figure 3.1.9 Normalized fluxes in the water-gap after the boron filter.....	49
Figure 3.1.10 Normalized fluxes in the capsule wall of the boron experiment.....	49
Figure 3.1.11 Normalized fluxes in the air-gap of the boron experiment.....	50
Figure 3.1.12 Normalized fluxes in the rodlet of the boron experiment.....	50
Figure 3.1.13 Normalized fluxes at the sample location of the boron experiment.....	51
Figure 3.1.14 Normalized fluxes in the outer void layer of the cadmium experiment.....	52

Figure 3.1.15 Normalized fluxes at the sample location of the cadmium experiment.....	53
Figure 3.2.1 Ratios of the cross-sections from ecco and mcnp (B experiment).....	55
Figure 3.2.2 Ratios of the cross-sections from ecco and mcnp (Cd experiment).....	57
Figure 3.3.1 U238 capture cross-section contributions in the boron experiment.....	58
Figure 3.3.2 U238 capture cross-section contributions in the cadmium experiment.....	59
Figure 3.3.3 Sensitivity coefficients of Pu240 $\sigma_g$ (B experiment).....	60
Figure 3.3.4 Sensitivity coefficients of Pu240 $\sigma_g$ (Cd experiment).....	61
Figure 3.4.1 $\pm X\%$ uncertainty in the layer thickness (R).....	62
Figure 3.4.2 Discrepancies greater than $\pm 5\%$ in the cross-sections of samples in the boron experiment for the cases mentioned in Table 3.4.6.....	65
Figure 3.4.3 Discrepancies greater than $\pm 5\%$ in the cross-sections of samples in the boron experiment for the cases mentioned in Table 3.4.7.....	66
Figure 4.0.1 Neutron capture cross-section of plutonium-240.....	67
Figure 4.0.2 Illustration of neutron flux dip caused by a neutron resonance as the sample mass increases.....	68
Figure 4.0.3 Infinitely diluted sample (white, left) and actual sample (green, right) inside a rodlet.....	69
Figure 4.1.1 (n, gamma) cross-sections of Cd-113 (red), Pu-242 (green) and U-235 (blue).....	73
Figure 4.2.1 Wafer.....	73
Figure 4.2.2 A sample wafer with different heights inside a rodlet.....	74
Figure 4.2.3 Capture cross-section of Pu242_2 in Cd experiment.....	75
Figure 4.2.4 Capture cross-section of Pu242_1 in B experiment.....	76

Figure 4.2.5 Self-shielding factor as a function of height in Pu242_2 (Cd experiment)...	77
Figure 4.2.6 Self-shielding factor as a function of height in Pu242_1 (B experiment)....	77
Figure 5.0.1 Flow chart of the unfolding process.....	92
Figure 5.1.1 <i>A priori</i> spectra in both the experiments.....	93
Figure 5.2.1 Copper flux wire used in the cadmium experiment.....	95
Figure 5.2.2 Response functions of all the flux wires in the Cd experiment.....	98
Figure 5.2.3 Response functions of all the flux wires in the B experiment.....	99
Figure 5.3.1 Example of the activity profile of a flux wire from a reactor.....	100
Figure 5.3.2 Example of the activity profile of a flux wire in the boron experiment.....	102
Figure 5.6.1 Average neutron spectra (top to bottom) from MAXED and MCNP.....	110
Figure 5.6.2 Average neutron spectra (top to bottom) from LSQ and MCNP.....	110
Figure 5.6.3 Neutron spectra at position 3 from MAXED and MCNP.....	111
Figure 5.6.4 Neutron spectra at position 3 from LSQ and MCNP.....	111
Figure 5.6.5 Neutron spectra at position 10 from MAXED and MCNP.....	112
Figure 5.6.6 Neutron spectra at position 10 from LSQ and MCNP.....	112
Figure 5.6.7 Neutron spectra at position 17 from MAXED and MCNP.....	113
Figure 5.6.8 Neutron spectra at position 17 from LSQ and MCNP.....	113
Figure 5.6.9 Neutron spectra at position 23 from MAXED and MCNP .....	114
Figure 5.6.10 Neutron spectra at position 23 from LSQ and MCNP.....	114
Figure 5.6.11 Neutron spectra at all the four positions from MAXED.....	115
Figure 5.6.12 Neutron spectra at all the four positions from LSQ.....	115
Figure C.1 Sensitivity coefficients of Am241 (left) and Am243 (right) $\sigma_g$ cross-sections.....	125

Figure C.2 Sensitivity coefficients of Cm244 (left) and Cm248 (right) $\sigma_g$ cross-sections.....	125
Figure C.3 Sensitivity coefficients of Cs133 (left) and Eu153 (right) $\sigma_g$ cross-sections.....	126
Figure C.4 Sensitivity coefficients of Np237 (left) and Pu239 (right) $\sigma_g$ cross-sections.....	126
Figure C.5 Sensitivity coefficients of Pu242 (left) and Pu244 (right) $\sigma_g$ cross-sections.....	127
Figure C.6 Sensitivity coefficients of Rh103 (left) and Sm149 (right) $\sigma_g$ cross-sections.....	127
Figure C.7 Sensitivity coefficients of Th232 (left) and U233 (right) $\sigma_g$ cross-sections.....	128
Figure C.8 Sensitivity coefficients of U235 (left) and U236 (right) $\sigma_g$ cross-sections....	128
Figure C.9 Sensitivity coefficients of Am241 (left) and Am243 (right) $\sigma_g$ cross-sections.....	129
Figure C.10 Sensitivity coefficients of Cm244 (left) and Cm248 (right) $\sigma_g$ cross-sections.....	129
Figure C.11 Sensitivity coefficients of Cs133 (left) and Eu153 (right) $\sigma_g$ cross-sections.....	130
Figure C.12 Sensitivity coefficients of Nd143 (left) and Nd145 (right) $\sigma_g$ cross-sections.....	130
Figure C.13 Sensitivity coefficients of Np237 (left) and Pd105 (right) $\sigma_g$ cross-sections.....	131

Figure C.14 Sensitivity coefficients of Pu239 (left) and Pu242 (right) $\sigma_g$ cross-sections.....	131
Figure C.15 Sensitivity coefficients of Pu244 (left) and Rh103 (right) $\sigma_g$ cross-sections.....	132
Figure C.16 Sensitivity coefficients of Ru101 (left) and Sm149 (right) $\sigma_g$ cross-sections.....	132
Figure C.17 Sensitivity coefficients of Th232 (left) and U233 (right) $\sigma_g$ cross-sections.....	133
Figure C.18 Sensitivity coefficients of U235 (left) and U236 (right) $\sigma_g$ cross-sections.....	133
Figure D.1 Capture cross-sections of Am241 (top) and Am243 (bottom).....	134
Figure D.2 Capture cross-sections of Cm248 (top), Cs133 (middle) and Eu153 (bottom).....	135
Figure D.3 Capture cross-sections of Np237_1 (top), Np237_2 (middle) and Pu239 (bottom) .....	136
Figure D.4 Capture cross-sections of Pu240 (top), Pu242_2 (middle) and Pu244_1 (bottom).....	137
Figure D.5 Capture cross-sections of Pu244_1 (top), Rh103 (middle) and Sm149 (bottom).....	138
Figure D.6 Capture cross-sections of Th232 (top), U233 (middle) and U235 (bottom).....	139
Figure D.7 Capture cross-sections of U236 (top) and U238 (bottom).....	140

Figure D.8 Capture cross-sections of Am241_1 (top), Am243_1 (middle) and Cm244_1 (bottom).....	141
Figure D.9 Capture cross-sections of Cm248_1 (top), Cs133 (middle) and Eu153 (bottom).....	142
Figure D.10 Capture cross-sections of Rh103 (top), Nd145 (middle) and Pd105 (bottom).....	143
Figure D.11 Capture cross-sections of Np237_1 (top), Np237_2 (middle) and Pu239 (bottom).....	144
Figure D.12 Capture cross-sections of Pu240 (top), Pu242_1 (middle) and Pu244_1 (bottom).....	145
Figure D.13 Capture cross-sections of Nd143 (top), Ru101 (middle), Sm149 (bottom).....	146
Figure D.14 Capture cross-sections of Th232 (top), U233 (middle) & U235 (bottom).....	147
Figure D.15 Capture cross-sections of U236 (top) and U238 (bottom).....	148
Figure E.1 Example of the activity profile of a flux wire in the boron experiment.....	150

## LIST OF TABLES

	Page No.
Table 1.5.1 ATR irradiation details of the three MANTRA experiments.....	11
Table 1.5.1.1 Order of samples and flux wires in boron experiment at b9 location.....	13
Table 1.5.1.2 Composition of boron filter used in MANTRA.....	15
Table 1.5.2.1 Order of samples and flux wires in cadmium experiment at b9 location....	16
Table 1.5.2.2 Composition of cadmium filter used in MANTRA.....	18
Table 1.5.4.1 Chemical forms of the samples used in the MANTRA experiments.....	23
Table 1.5.4.2 Masses of the samples measured using analytical balance.....	23
Table 1.5.4.3 Masses of the samples measured using ICP-MS.....	25
Table 2.1.1 One group cross-sections of the samples in the boron experiment.....	30
Table 2.2.1 One group cross-sections of the samples in the boron experiment.....	33
Table 2.2.2 One group cross-sections of the samples in the cadmium experiment.....	34
Table 2.3.1 ATR flux traps with different assemblies.....	37
Table 3.2.1 Cross-sections of the infinitely diluted samples in the boron experiment.....	54
Table 3.2.2 Cross-sections of the infinitely diluted samples in the cadmium experiment...	56
Table 3.4.1 Uncertainties in the filter thickness.....	63
Table 3.4.2 Uncertainties in the water-gap thickness.....	63
Table 3.4.3 Uncertainties in the boron density.....	64
Table 3.4.4 Cases with filter and water-gap uncertainties in the cadmium experiment.....	64
Table 3.4.5 Discrepancies greater than $\pm 5\%$ in the cross-sections of the samples in the cadmium experiment for the cases mentioned in Table 3.4.4.....	64
Table 3.4.6 Cases with filter and water-gap uncertainties in the boron experiment.....	65

Table 3.4.7 Cases for cumulative effects of all the three uncertainties in boron experiment.....	66
Table 4.1.1 One group effective capture cross-sections of samples in boron experiment.....	70
Table 4.1.2 One group effective capture cross-sections of samples in cadmium experiment.....	71
Table 4.2.1 One group effective capture cross-sections of samples in boron experiment.....	78
Table 4.2.2 One group effective capture cross-sections of samples in cadmium experiment.....	79
Table 4.2.3 Self-shielding factors as a function of height in boron experiment.....	81
Table 4.2.4 Self-shielding factors as a function of height in cadmium experiment.....	82
Table 4.2.5 One group capture cross-sections of all the samples with ICP-MS masses in boron experiment.....	84
Table 4.2.6 One group capture cross-sections of all the samples with ICP-MS masses in cadmium experiment.....	86
Table 4.2.7 Self-shielding factors as a function of height in boron experiment (ICP-MS).....	88
Table 4.2.8 Self-shielding factors as a function of height in cadmium experiment (ICP-MS).....	89
Table 5.1.1 ATR core parameters for both the experiments.....	93
Table 5.2.1 Compositions of the flux wires.....	94
Table 5.2.2 Parent and product isotopes of interest.....	94

Table 5.2.3 Masses of the flux wires used in the boron experiment.....	97
Table 5.2.4 Masses of the flux wires used in the cadmium experiment.....	97
Table 5.3.1 Calculated activation rates of the flux wires in the cadmium experiment....	103
Table 5.3.2 Measured activation rates of the flux wires in the cadmium experiment.....	103
Table 5.3.3 Calculated activation rates of the flux wires in the boron experiment.....	104
Table 5.3.4 Measured r activation rates of the flux wires in the boron experiment .....	104
Table 5.3.5 C/E ratios of the activation rates in the cadmium experiment.....	105
Table 5.3.6 C/E ratios of the activation rates in the boron experiment.....	105
Table G.1 Average neutron fluxes (top to bottom) in 32 energy groups (Cd experiment).....	153
Table G.2 Neutron fluxes in 32 energy groups at position 3 (B experiment).....	154
Table G.3 Neutron fluxes in 32 energy groups at position 10 (B experiment).....	155
Table G.4 Neutron fluxes in 32 energy groups at position 17 (B experiment).....	157
Table G.5 Neutron fluxes in 32 energy groups at position 23 (B experiment).....	158

## LIST OF ABBREVIATIONS

AMS	Accelerator Mass Spectroscopy
ANL	Argonne National Laboratory
ASTM	American Society for Testing and Materials
ATLAS	Argonne Tandem Linac Accelerator System
ATR	Advanced Test Reactor
B	Boron
Bq	Becquerel
C	Carbon
Cd	Cadmium
CEA	French Atomic Energy Commission
DOE	Department Of Energy
ECCO	European Cell Code
ENDF	Evaluated Data Nuclear Files
ERANOS	European Reactor Analysis Optimized calculation System
FNR	Fast Neutrons Reactor
ICP-MS	Inductively Coupled Plasma Mass Spectrometer
INL	Idaho National Laboratory
ISU	Idaho State University
LANL	Los Alamos National Laboratory
LINAC	Linear Accelerator
LSQ	Least Squares

MANTRA	Measurement of Actinide Neutronic Transmutation Rates with Accelerator mass spectroscopy
MCNP5	A General Monte Carlo N-Particle Transport Code-Version 5
MeV	Mega-electron volts
MFC	Materials and Fuels Complex
MWth	Mega Watt Thermal
MAXED	Maximum Entropy Deconvolution code
NSUF	National Scientific User Facility
ORNL	Oak Ridge National Laboratory
RSICC	Radiation Safety Information Computational Center
SST	Stainless Steel
UMG 3.3	Unfolding with MAXED and GRAVEL-Version 3.3

## ABSTRACT

The main objective of the project Measurement of Actinide Neutronic Transmutation Rates with Accelerator mass spectroscopy (MANTRA) was to obtain accurate integral information on the capture cross-sections of most actinides and some fission products (1). Nuclear data are important to understand and quantify the processes in a nuclear reactor and the fuel cycle as a whole (2). To improve the accuracy on the nuclear data, the uncertainties should be kept as low as possible. The major portion of these uncertainties comes from the input data and the assumptions made in the simulation models. For a high profile project like MANTRA, the parametric analysis is very important to study and also to characterize the experiment in a better way. Parametric analysis was performed with different possible uncertainties in the experiments, that could affect the end results using MCNP5 (a stochastic code) and ECCO-ERANOS (a deterministic code).

Very pure samples of most actinides and some fission products were irradiated in the Advanced Test Reactor (ATR) at Idaho National Laboratory (INL). Most of the time the sample sizes cannot be made small enough. Hence, the self-shielding effects must be taken into the account when calculating the actual cross-sections. Both MCNP5 and ECCO were used to calculate the self-shielding factors. Around 500 billion histories were used in MCNP5 to improve the accuracy of these self-shielding factors.

The neutron flux wires were evenly distributed in the MANTRA experiments, so that they provide good measurements of neutron fluence from top to bottom after irradiation. Using the activities measured from these irradiated flux wires, the output neutron spectra were unfolded (reconstructed). MAXED and least squares unfolding techniques were used to calculate these output spectra. The calculations and the results of the experiments MANTRA1 (thin boron) and MANTRA3 (cadmium) are included in the current work.

# 1. INTRODUCTION

The nuclides that are fissile and fertile can be recovered from the discharged irradiated fuel through fuel reprocessing. The major part of the radioactivity in discharged fuel is from the fission products, which are the reason for delaying the fuel reprocessing for up to 50 years. Also, actinides (e.g. Am-241, half-life 432.7 years) and their decay daughters are the prominent radioactive nuclides in the advanced fuel cycle systems that are responsible for the longer radioactivity (hundreds of years) in the discharged fuel (3). So there is a need to obtain accurate integral information about the neutron cross-sections of the actinides and fission products which are of concern for the advanced nuclear fuel systems to reduce proliferation risk, minimize radioactive waste, and for a reliable nuclear energy future. Most of the nuclear engineering calculations and projects require these neutron cross-sections. On the accuracy of these cross-sections the reliability of the following specializations depends on fission reactor designs, nuclear fuel cycles, nuclear safety and safeguards, nuclear waste disposal, etc.

The main objective of the project MANTRA was to obtain important integral information on the capture cross-sections of most actinides and some fission products (4). It was a collaborative project between Idaho State University (ISU), Idaho National Laboratory, and Argonne National Laboratory (ANL). Three major facilities, the Advanced Test Reactor (ATR) at INL, the Analytical lab at the Materials and Fuels Complex (MFC) at INL, and the Argonne Tandem Linac Accelerator System (ATLAS) at ANL were part of this novel project. The actinides (e.g. Am<sup>241</sup>, Cm<sup>244/248</sup>, Th<sup>232</sup>, etc.) and some fission products (e.g. Sm<sup>149</sup>, Cs<sup>133</sup>, Rh<sup>103</sup>, etc.) were irradiated in the well characterized neutron spectra of the ATR (1). Some of these irradiated samples were transported to ANL to take

advantage of the accelerator mass spectroscopy (AMS) capabilities of ATLAS facility. This facility's spectroscopy has the detection limit in the orders of magnitude lower than that of standard mass spectroscopy ( $\sim 10^{-12}$ ). Also, this spectroscopy is more sensitive when compared to conventional chemical analysis (5). At the ATLAS facility, more transmutation products can be measured. Also more neutron cross-sections can be inferred from a single sample. This project was funded by the Department of Energy (DOE) Office of Science and the ATR National Scientific User Facility (ATR-NSUF).

### **1.1 The Need to Improve the Nuclear Data Files**

In a neutron field, neutron interactions with matter can occur from either scattering or absorption reactions. Scattering reactions will result in a change in the energy and direction of the incident neutron. Absorption reactions will result in the absorption of the incident neutron. This absorption of the incident neutron by a nucleus will result in the formation of new nuclei (fission reaction) or a new nucleus and another particle or particles (e.g. protons, alpha particles and gamma-rays). Clearly, the probability of occurrence of these reactions depends on the energy of the incident neutron and also on the properties of the nucleus with which it is interacting (6). This probability of occurrence of a neutron reaction in a nucleus is defined as its neutron cross-section. Neutron cross-sections are expressed in the units of barns (b, 1 barn =  $10^{-24}$  cm<sup>2</sup>).

Nuclear data files or libraries consist of sets of neutron cross-sections and their uncertainties for several hundreds of isotopes or nuclides. There are different formats of these data libraries. Evaluated Nuclear Data Files (ENDF) formats are widely used in the USA. The latest release of these formats was ENDF-VII.1. However, ENDF-VII.0 format was used for the calculations in the current work because the ENDF-VII.1 library was not

readily available for the software European Cell Code (ECCO). These evaluated data files serve as input to the simulation codes. Hence, these data files play an important role in the modeling of nuclear systems design, development and their performance along with the emphasis on safety analyses. They help in the design and the interpretation of experiments for cost effectiveness. They are required for the accelerator driven systems, nuclear waste transmutations and the next generation reactor designs. Inadequacies in the data of some existing cross-sections are a big concern for the nuclear criticality calculations (7).

To improve the nuclear data files, high quality experiments and calculations are required. MANTRA, a nuclear data experiment was one among those high quality integral experiments aiming to improve the nuclear data files of most of the actinides and some fission products. There were few integral experiments similar to MANTRA in the past aiming to improve the accuracy of the neutron capture cross-sections (see section 1.2). However, it is an iterative process to improve and to generate accurate neutron cross-sections. One can find MANTRA in this iterative process (Figure 1.1.1). Integral experiments in reactors play an important role in nuclear data validation and improvements.

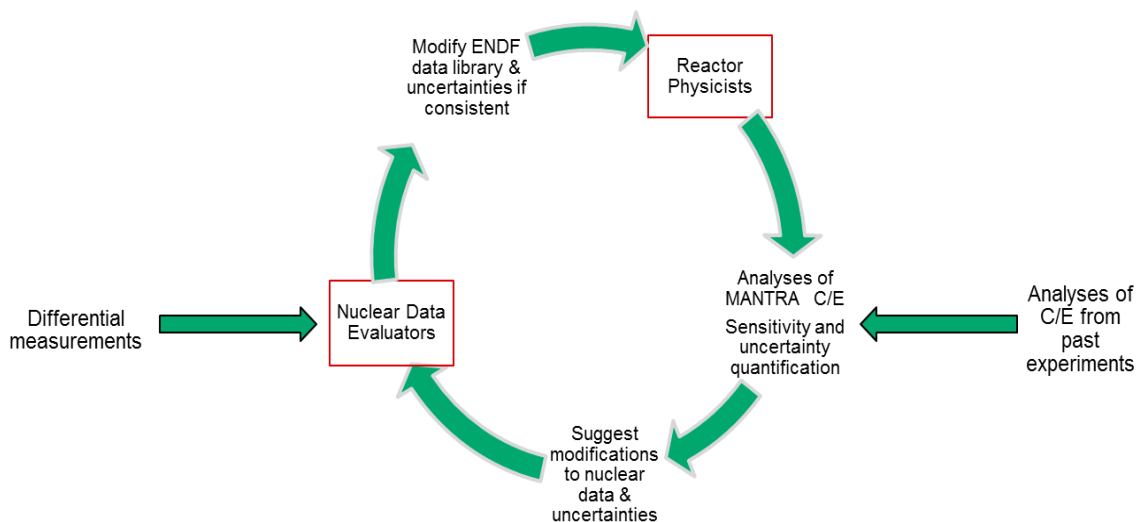


Figure 1.1.1 Iterative process necessary to generate accurate nuclear cross-sections

## 1.2 Nuclides Transmutation Equations

In a neutron field by capturing a neutron, a nuclide of mass number A and atomic number Z will produce heavier nuclides of mass number A+1, A+2, etc. and if beta decay occurs the atomic number will change into Z+1. If no decay occurs in the chain reaction, then the transmutation equations are:

$$\begin{aligned}\frac{dN_A^Z(t)}{dt} &= -N_A^Z(t) \tilde{\sigma}_{A,Z}^a(t) \phi(t) \\ \frac{dN_{A+1}^Z(t)}{dt} &= +N_A^Z(t) \bar{\sigma}_{A,Z}^c(t) \phi(t) - N_{A+1}^Z(t) \tilde{\sigma}_{A+1,Z}^a(t) \phi(t) \\ \frac{dN_{A+2}^Z(t)}{dt} &= +N_{A+1}^Z(t) \bar{\sigma}_{A+1,Z}^c(t) \phi(t) - N_{A+2}^Z(t) \tilde{\sigma}_{A+2,Z}^a(t) \phi(t)\end{aligned}$$

Where,  $N_A^Z$  = atom density of parent nuclide with mass number A and atomic number Z

$\tilde{\sigma}_{A,Z}^a$  = absorption cross-section of parent nuclide

$\bar{\sigma}_{A,Z}^c$  = effective one group capture cross-section of parent nuclide

$\phi(t) = \int \varphi(E, t) dE$ , energy-integrated time-dependent neutron flux

If decay occurs in the chain reaction, then the transmutation equations are:

$$\begin{aligned}\frac{dN_A^Z(t)}{dt} &= -N_A^Z(t) \tilde{\sigma}_{A,Z}^a(t) \phi(t) \\ \frac{dN_{A+1}^Z(t)}{dt} &= +N_A^Z(t) \bar{\sigma}_{A,Z}^c(t) \phi(t) - N_{A+1}^Z(t) \tilde{\sigma}_{A+1,Z}^a(t) \phi(t) \\ \frac{dN_{A+1}^{Z+1}(t)}{dt} &= +\lambda_{A+1,Z}^\beta N_{A+1}^Z(t) - N_{A+1}^{Z+1}(t) \tilde{\sigma}_{A+1,Z+1}^a(t) \phi(t)\end{aligned}$$

Where,  $\lambda_{A+1,Z}^\beta$  = decay constant of nuclide with mass number A+1 and atomic number Z

The general solution to the above transmutation equations by neglecting the time-dependence of the effective one group cross-section is

$$\begin{aligned}N_A^Z(T) &= N_A^Z(0) e^{-\tilde{\sigma}_A^a \bar{\phi} T} \\ N_{A+n}^{Z+m}(T) &= N_A^Z(0) \prod_{j=0}^{j=n-1} \bar{\sigma}_{A+j}^c \sum_{k=0}^{k=n} \frac{e^{-\tilde{\sigma}_{A+k}^a \bar{\phi} T}}{\prod_{t=0}^{t=n, t \neq k} (\tilde{\sigma}_{A+t}^a - \tilde{\sigma}_{A+k}^a)} \\ \bar{\phi} &= \frac{\int_0^T \phi(t) dt}{T}\end{aligned}$$

Where, T = irradiation time

m = number of beta decays in the chain reaction (m=0 if no beta decay)

n = number of capture reactions in the chain reaction

$\bar{\phi}$  = average neutron flux

$\bar{\sigma}^c = \frac{\lambda^\beta}{\bar{\phi}}$ , where beta decay occurs

The first non-zero terms of the Taylor expansions of these expressions are as follows:

$$N_A^Z(T) \sim N_A^Z(0) [1 - \tilde{\sigma}_A^a \bar{\phi} T]$$

$$N_{A+n}^{Z+m}(T) \sim \frac{1}{n!} N_A^Z(0) \left( \prod_{j=0}^{j=n-1} \bar{\sigma}_{A+j}^c \right) [\bar{\phi} T]^n$$

If no beta occurs, then the expressions for A+1 and A+2 are:

$$N_{A+1}(T) = N_A(0) \bar{\sigma}_A^c \left( \frac{e^{-\tilde{\sigma}_A^a \bar{\phi} T}}{\tilde{\sigma}_{A+1}^a - \tilde{\sigma}_A^a} + \frac{e^{-\tilde{\sigma}_{A+1}^a \bar{\phi} T}}{\tilde{\sigma}_A^a - \tilde{\sigma}_{A+1}^a} \right) \sim N_A(0) \bar{\sigma}_A^c \bar{\phi} T$$

$$N_{A+2}(T) = N_A(0) \bar{\sigma}_A^c \bar{\sigma}_{A+1}^c \left( \frac{e^{-\tilde{\sigma}_A^a \bar{\phi} T}}{(\tilde{\sigma}_{A+1}^a - \tilde{\sigma}_A^a)(\tilde{\sigma}_{A+2}^a - \tilde{\sigma}_A^a)} + \frac{e^{-\tilde{\sigma}_{A+1}^a \bar{\phi} T}}{(\tilde{\sigma}_A^a - \tilde{\sigma}_{A+1}^a)(\tilde{\sigma}_{A+2}^a - \tilde{\sigma}_{A+1}^a)} \right. \\ \left. + \frac{e^{-\tilde{\sigma}_{A+2}^a \bar{\phi} T}}{(\tilde{\sigma}_A^a - \tilde{\sigma}_{A+2}^a)(\tilde{\sigma}_{A+1}^a - \tilde{\sigma}_{A+2}^a)} \right) \sim \frac{1}{2} N_A(0) \bar{\sigma}_A^c \bar{\sigma}_{A+1}^c [\bar{\phi} T]^2$$

By using these expressions, the neutron capture cross-sections of pure samples can be inferred. The atom density of a nuclide with mass number A+1 after an irradiation time T can be expressed as:

$$N_{A+1}(T) \sim \frac{1}{2} N_{A-1}(0) \bar{\sigma}_{A-1}^c \bar{\sigma}_A^c [\bar{\phi} T]^2 + N_A(0) \bar{\sigma}_A^c [\bar{\phi} T] + N_{A+1}(0) \{1 - \tilde{\sigma}_{A+1}^a [\bar{\phi} T]\}$$

Since the samples are pure,  $N_{A-1}(0) \ll N_A(0)$ .

$$N_{A+1}(T) \sim N_A(0) \bar{\sigma}_A^c [\bar{\phi} T] + N_{A+1}(0) \{1 - \tilde{\sigma}_{A+1}^a [\bar{\phi} T]\}$$

The atom densities by the end of irradiation time T and the time-integrated neutron flux can be measured (the subscript M stands for measured) from the experiment. Using these

measured quantities the neutron capture cross-section of a nuclide with mass number A can be inferred.

$$\bar{\sigma}_A^c \sim \frac{\left[ \frac{N_{A+1}(T)}{N_A(0)} \right]_M - \left[ \frac{N_{A+1}(0)}{N_A(0)} \right]_M \{1 - \tilde{\sigma}_{A+1}^a [\bar{\Phi}T]_M\}}{[\bar{\Phi}T]_M}$$

But, at time T the measurement provides  $\left[ \frac{N_{A+1}(T)}{N_A(T)} \right]_M \equiv [R_{A+1}(T)]_M$

Where,  $[R_{A+1}(T)]_M$  = ratio of atom densities of nuclides A+1 and A at time T

$$\begin{aligned} \bar{\sigma}_A^c &\sim \frac{\left[ \frac{N_{A+1}(T)}{N_A(T)} \right]_M \{1 - \tilde{\sigma}_A^a [\bar{\Phi}T]_M\} - \left[ \frac{N_{A+1}(0)}{N_A(0)} \right]_M \{1 - \tilde{\sigma}_{A+1}^a [\bar{\Phi}T]_M\}}{[\bar{\Phi}T]_M} \\ &\equiv \frac{[R_{A+1}(T)]_M \{1 - \tilde{\sigma}_A^a [\bar{\Phi}T]_M\} - [R_{A+1}(0)]_M \{1 - \tilde{\sigma}_{A+1}^a [\bar{\Phi}T]_M\}}{[\bar{\Phi}T]_M} \end{aligned}$$

Also,  $\tilde{\sigma}_A^a = \bar{\sigma}_A^c + \bar{\sigma}_A^f + \frac{\lambda_A}{\bar{\Phi}}$  (capture + fission + decay)

$$\bar{\sigma}_A^c \sim \frac{[R_{A+1}(T)]_M \{1 - \tilde{\sigma}_A^f [\bar{\Phi}T]_M - \lambda_A [T]_M\} - [R_{A+1}(0)]_M \{1 - \tilde{\sigma}_{A+1}^a [\bar{\Phi}T]_M\}}{[\bar{\Phi}T]_M (1 + [R_{A+1}(T)]_M)}$$

If the terms  $\{1-\dots\}$  and  $\{1+\dots\}$  are approximated by 1, the expression simplifies as:

$$\bar{\sigma}_A^c \sim \frac{[R_{A+1}(T)]_M - [R_{A+1}(0)]_M}{[\bar{\Phi}T]_M}$$

Since, the initial A+1 and A+2 nuclide atom densities are negligible when compared to A nuclide at time T=0, the capture cross-section of A+1 nuclide is expressed as:

$$\bar{\sigma}_{A+1}^c \sim 2 \frac{[R_{A+2}(T)]_M - [R_{A+2}(0)]_M}{([R_{A+1}(T)]_M + [R_{A+1}(0)]_M) [\bar{\Phi}T]_M} \sim 2 \frac{[R_{A+2}(T)]_M}{[R_{A+1}(T)]_M [\bar{\Phi}T]_M}$$

Similarly, if all the initial atom densities are negligible in comparison to those at time T, the A+n capture cross-section is simply equal to:

$$\bar{\sigma}_{A+n}^c \sim (n + 1) \frac{[R_{A+n+1}(T)]_M}{[R_{A+n}(T)]_M [\bar{\Phi}T]_M}$$

### **1.3 Past Experiments Similar to MANTRA**

Actinides produced in fission reactors are the major contributors to the decay heat and longer radioactivity of spent nuclear fuel. So the accuracy of the capture cross-sections of most of the actinides is very important. To improve the precision of these cross-sections there is a need for the transmutation of the actinides in a reactor. The irradiation experiments are very powerful for evaluating cross-section data and validating transmutation rates for the actinides (8).

As mentioned earlier, there were few irradiation experiments similar to MANTRA. PROFIL and TRAPU irradiation experiments were among them (9). Both these experiments were performed at the CEA (French Atomic Energy Commission) French fast reactor PHENIX. The results from these integral experiments had been successfully used to validate and adjust the nuclear data of minor actinides (10). In fact, the success of these irradiation experiments was the initial motivation for MANTRA. MANTRA is the first reactor physics integral experiment performed in the USA in more than 20 years (8).

To improve the cross-section data and to effectively predict the transmutation rate, it is necessary to irradiate samples in a variety of neutron spectra (8). The data from the PROFIL and TRAPU irradiation experiments are relevant to fast energy spectrum reactors. Therefore, it would be useful to add experiments that provide information in the thermal and epi-thermal energy regions. The cadmium (Cd) filter was used to cover the epi-thermal energy region and the boron (B) filter was used to cover the fast energy region.

The neutron spectra from PROFIL1 and MANTRA experiments were plotted (Figure 1.3.1). This neutron spectra comparison showed how different the MANTRA experiments were from the past experiments.

### PROFIL1 Vs. MANTRA

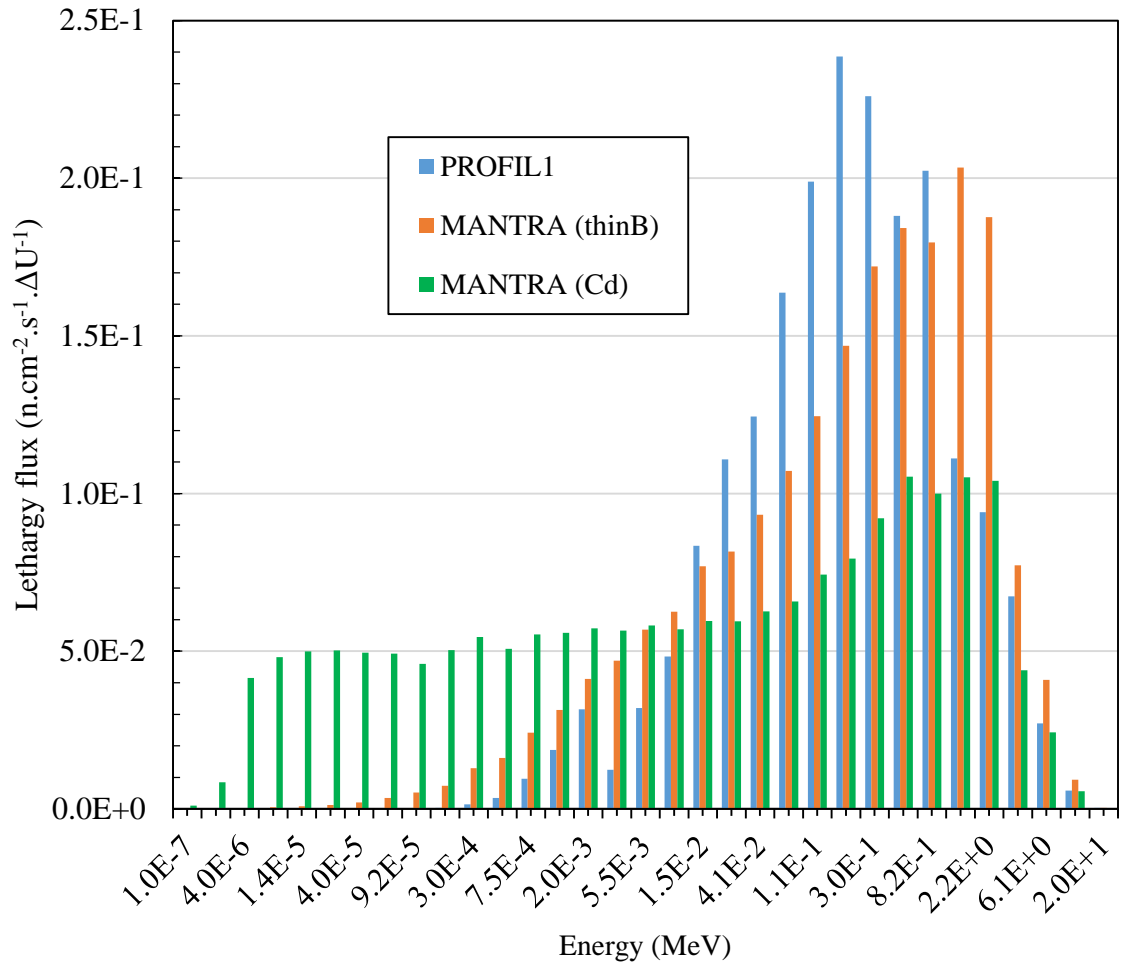


Figure 1.3.1 Lethargy fluxes

The current research work is focused on the post irradiation analysis of this project. The post irradiation analysis includes performing parametric analysis on the effective cross-sections using both MCNP5 (Monte Carlo N-Particle) and ECCO, calculating the self-shielding effects, and finally unfolding the neutron spectra using Maximum Entropy Deconvolution (MAXED) and Least Squares (LSQ) methods.

#### **1.4 Advanced Test Reactor**

ATR is a National Scientific User Facility (NSUF), located at the ATR Complex on the INL site. Advanced nuclear fuels and materials which will be used in larger scale and prototype reactors are investigated in this premier facility (11). Unlike commercial reactors, ATR is a low temperature and low pressure test reactor designed to generate high energy concentrated neutrons and deliver them with precision to the desired locations in the reactor (12). Because of this advantage the materials can be exposed to high neutron fluence depending on the number of irradiation cycles (each cycle would be around 55 days) and locations within the reactor. ATR has a unique serpentine core configuration that offers a large number of test locations. For MANTRA, the locations b9 and b11 were used for the irradiation process. The maximum thermal power rating of ATR is 250 MWth but typically operates at much lower power levels.

Inserted in the ATR neutron field, the isotopic composition of a sample will change as the neutron induced reactions as well as the natural alpha and beta decays occur. Hence, by irradiating a sample made up of initially only one isotope, you can potentially end up with many different ones in different amounts. MANTRA consists of three irradiation experiments (MANTRA 1, MANTRA 2 and MANTRA 3). In MANTRA 1 and 2, thin and thick boron (with 70% enriched boron-10 (B10)) filters were used respectively to obtain fast neutron spectra. In MANTRA 3, cadmium filter was used to attenuate the thermal part of the neutron spectrum. Two irradiation cycles for both MANTRA 1 and 2, and one irradiation cycle for MANTRA 3 were used in the ATR.

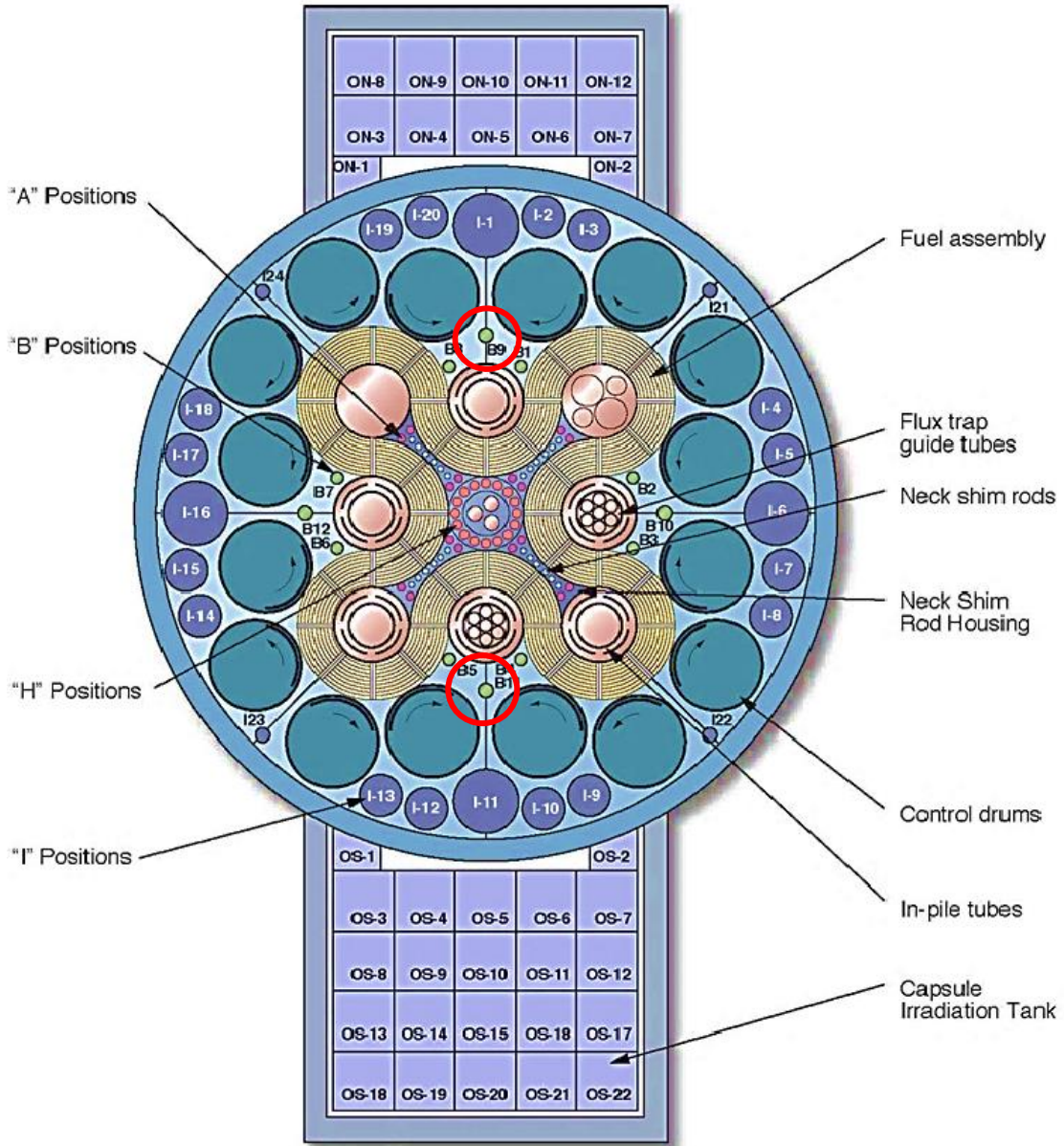


Figure 1.4.1 ATR core with the red circles indicating the b9 and b11 irradiation locations used for MANTRA (12)

The location b9 was used to irradiate the samples in MANTRA 1 and 2. The location b11 was used to irradiate the samples in MANTRA 3. These two irradiation locations were mirror images to each other (Figure 1.4.1), but the neutron fields at both these locations were different from each other in terms of levels.

## 1.5 MANTRA Experiments

The irradiation details of all three MANTRA experiments with the scrams in the ATR were included in the table below.

Table 1.5.1 ATR irradiation details of the three MANTRA experiments

<b>Filters</b>	<b>ATR irradiation details</b>
Thin Boron (b9 location) (MANTRA 1)	<b>Cycle 1:</b> Mar 1, 2012 (5:30 am) – Mar 22, 2012 (7:00 am, scram), Mar 25, 2012 (8:00 am) – Mar 27, 2012 (1:30 pm, scram), Apr 6, 2012 (11:00 pm) – May 5, 2012 (9:30 am) <b>Cycle 2:</b> Nov 27, 2012 (10:30 pm) – Jan 18, 2013 (10:00 am)
Cadmium (b11 location) (MANTRA 3)	<b>Cycle 1:</b> Nov 27, 2012 (10:30 pm) – Jan 18, 2013 (10:00 am)
Thick Boron (b9 location) (MANTRA 2)	<b>Cycle 1:</b> Aug 23, 2013 (1:30 pm) – Oct 16, 2013 (9:00 am) <b>Cycle 2:</b> Nov 8, 2013 (11:00 pm) – Nov 13, 2013 (1:30 am, scram), Nov 28, 2013 (9:30 pm) – Jan 17, 2014 (3:00 pm)

In the present work, the focus will be only on the two experiments MANTRA 1 (thin B) and MANTRA 3 (Cd). Thus, the calculations and the results discussed will be between the boron and cadmium experiments. The irradiation cycle 2 of the boron experiment was same as the irradiation cycle 1 of the cadmium experiment. There were two scrams during the boron experiment. The time gap between cycle 1 and the cycle 2 of this experiment was more than six months. Also, the activities of the neutron flux wires were counted after almost 13 months. So most of the activity measured from these flux wires should be coming from the cycle 2. To normalize the neutron fluxes it is always important to have the power history of the reactor during the irradiation (Figure 1.5.1 and Figure 1.5.2).

Boron experiment (cycle 1)

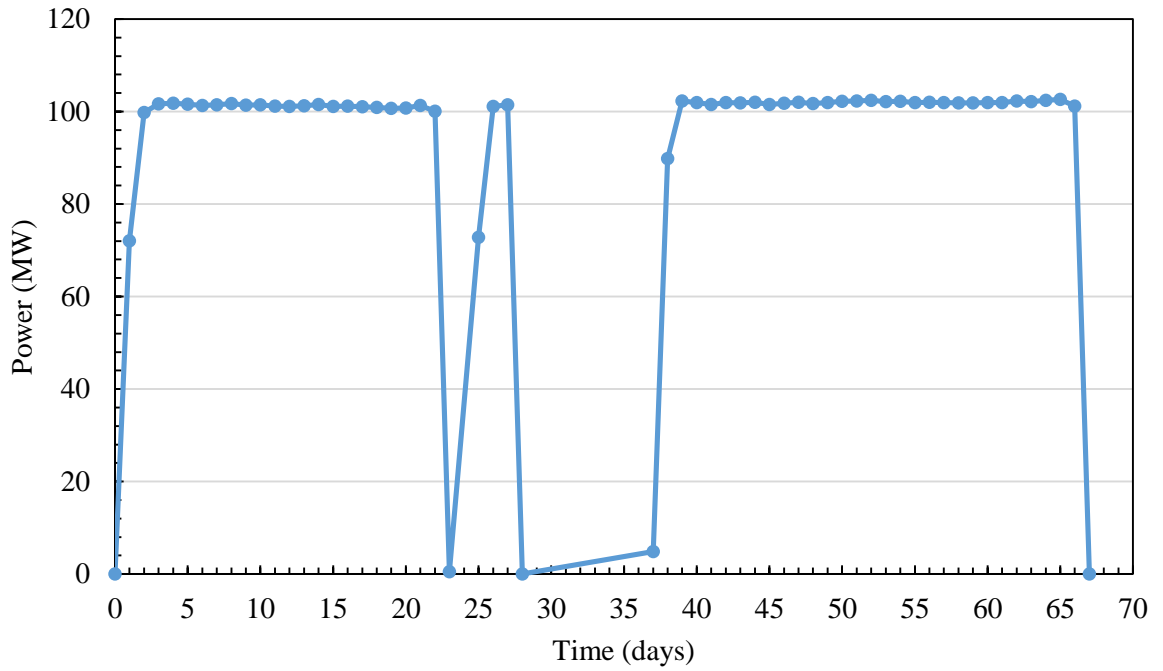


Figure 1.5.1 ATR power history during the irradiation cycle 1 of the boron experiment

Boron experiment (cycle2) and Cadmium experiment (cycle1)

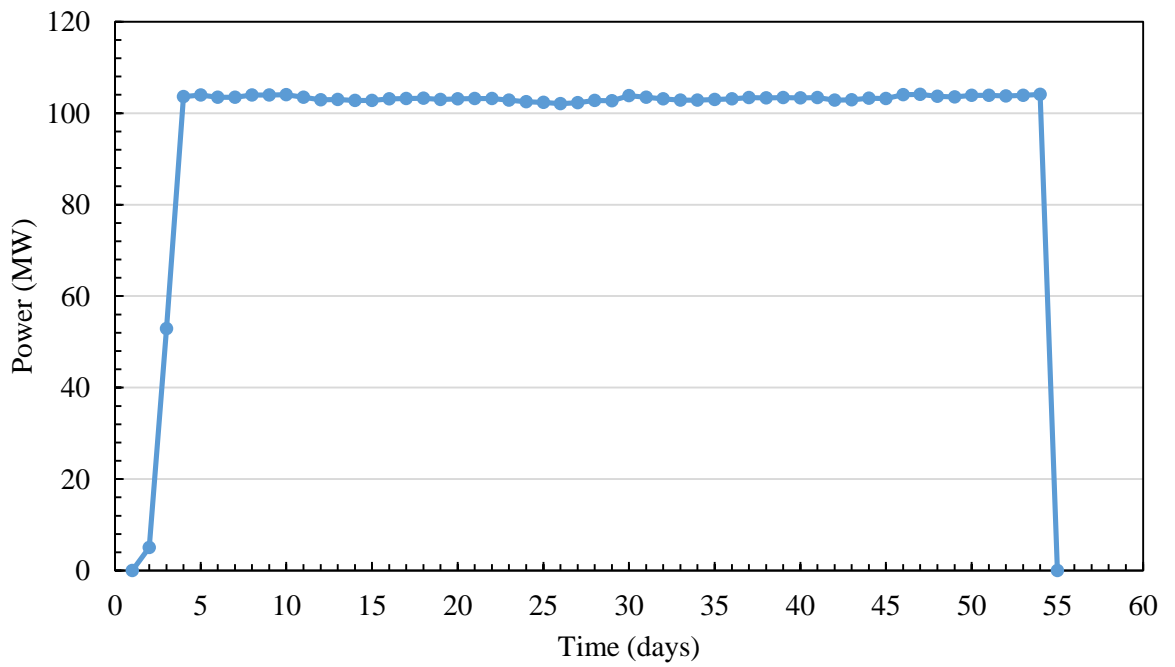


Figure 1.5.2 ATR power history during the irradiation cycle 2 of the boron experiment and cycle 1 of the cadmium experiment

### 1.5.1 Boron Experiment

The flux wires were evenly distributed so that they would provide good measurements of neutron fluence from top to bottom. The order of the samples with the flux wires inside the 25 rodlets (top to bottom) was shown in the Table 1.5.1.1. Some of the samples were repeated more than once in both the experiments.

Table 1.5.1.1 Order of samples and flux wires in boron experiment at b9 location

<b>Samples</b>	<b>Order</b>
Sm149	1
Np237	2
<u>Flux wires</u>	<u>3</u>
Am243	4
U233	5
U235	6
Cm248	7
Pu242	8
Pu244	9
<u>Flux wires</u>	<u>10</u>
Pu240	11
Th232	12
Am241	13
Np237	14
Pu244	15
Cm248	16
<u>Flux wires</u>	<u>17</u>
U238	18
Am243	19
Pu239	20
U236	21
Pu242	22
<u>Flux wires</u>	<u>23</u>
Am241	24
Eu153-Cs133-Rh103	25

Different layers of the materials and their dimensions (inches) in the boron experiment can be seen in the figure below.

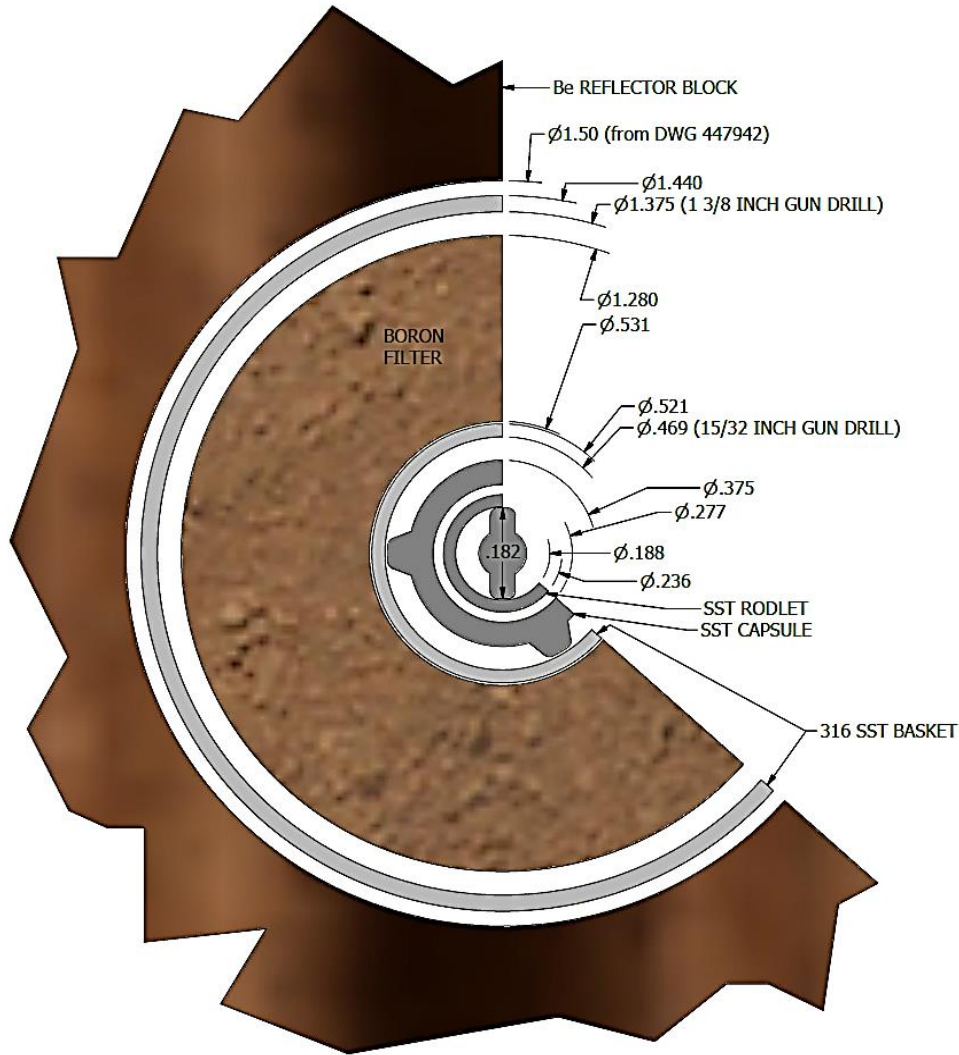


Figure 1.5.1.1 Cross-sectional view of the boron experiment in the ATR

The most widely used neutron filter other than cadmium is boron because of its higher neutron absorption cross-section at 150-300 eV. This cross-section could be even higher depending on the percentage of B10 present in the boron (13) (14). For MANTRA, both the thin and thick boron filters were used because the effective neutron energy of the filter can be varied by changing its thickness. Boron can effectively remove both the thermal and

epi-thermal neutrons, making the neutron spectrum hard. It is important to note that the boron filters have the tendency to shift the responses of some of the well-known dosimeters into an energy region where the cross-section is not as well known. One can take this into account by using the cross-sections uncertainty in the unfolding process (15). Both MAXED and least squares methods use these uncertainties in the unfolding process. B10 has larger absorption cross-section than boron-11 (B11).

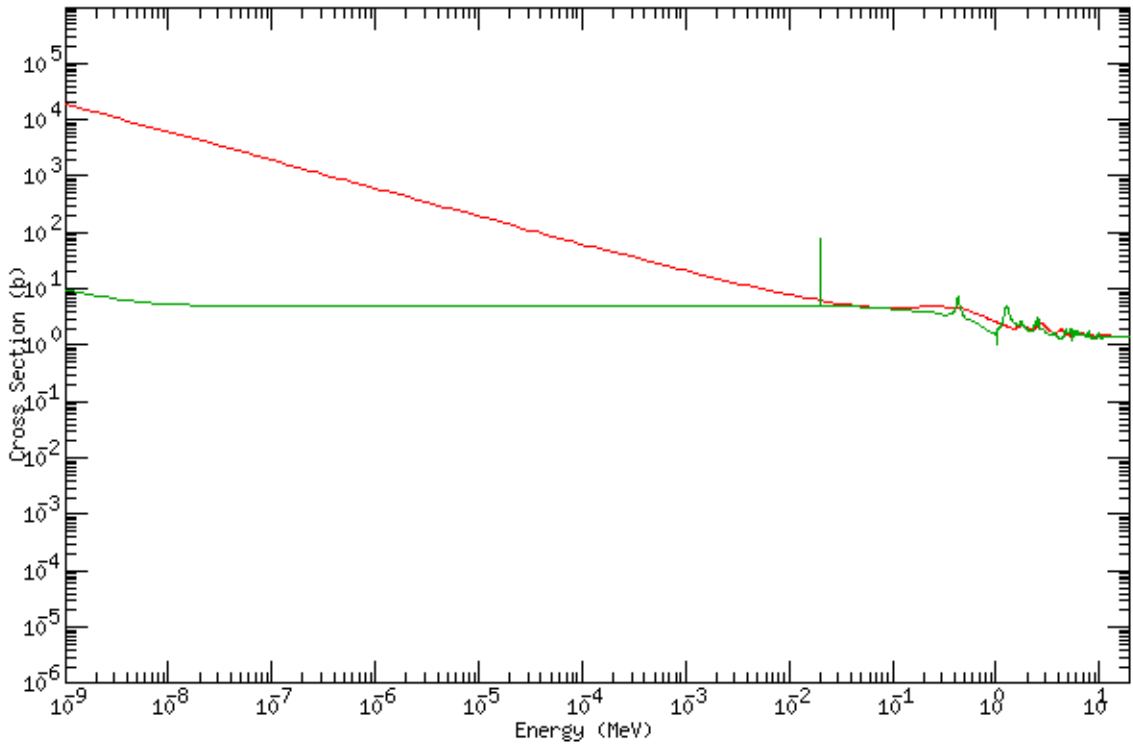


Figure 1.5.1.2 Absorption cross-sections of B10 (red) and B11 (green)

The thickness of the boron filter (thin) used in the experiment was 5 mm. This filter was in the form of boron carbide (B4C) with 70% enriched B10 in the boron.

Table 1.5.1.2 Composition of boron filter used in MANTRA

Isotopes	C	B11	B10	Total
atoms.b <sup>-1</sup> .cm <sup>-1</sup>	2.730E-02	3.269E-02	7.647E-02	1.365E-01

### 1.5.2 Cadmium Experiment

In cadmium experiment, there were 28 rodlets with flux wires at four different positions from top to bottom (Table 1.5.2.1).

Table 1.5.2.1 Order of samples and flux wires in cadmium experiment at b9 location

<b>Samples</b>	<b>Order</b>
Nd145-Pd105	1
Sm149-Ru101-Nd143	2
Np237	3
<u>Flux wires</u>	<u>4</u>
Am243	5
U233	6
U235	7
Cm248	8
Pu242	9
Pu244	10
<u>Flux wires</u>	<u>11</u>
Cm244	12
Th232	13
Pu240	14
Am241	15
Np237	16
Pu244	17
Cm248	18
<u>Flux wires</u>	<u>19</u>
U238	20
Am243	21
Cm244	22
Pu239	23
U236	24
Pu242	25
<u>Flux wires</u>	<u>26</u>
Am241	27
Eu153-Cs133-Rh103	28

A detailed view of the cadmium experiment with the dimensions (inches) was shown below. Different colors in the Figure 1.5.2.1 specify different materials in the cadmium experiment.

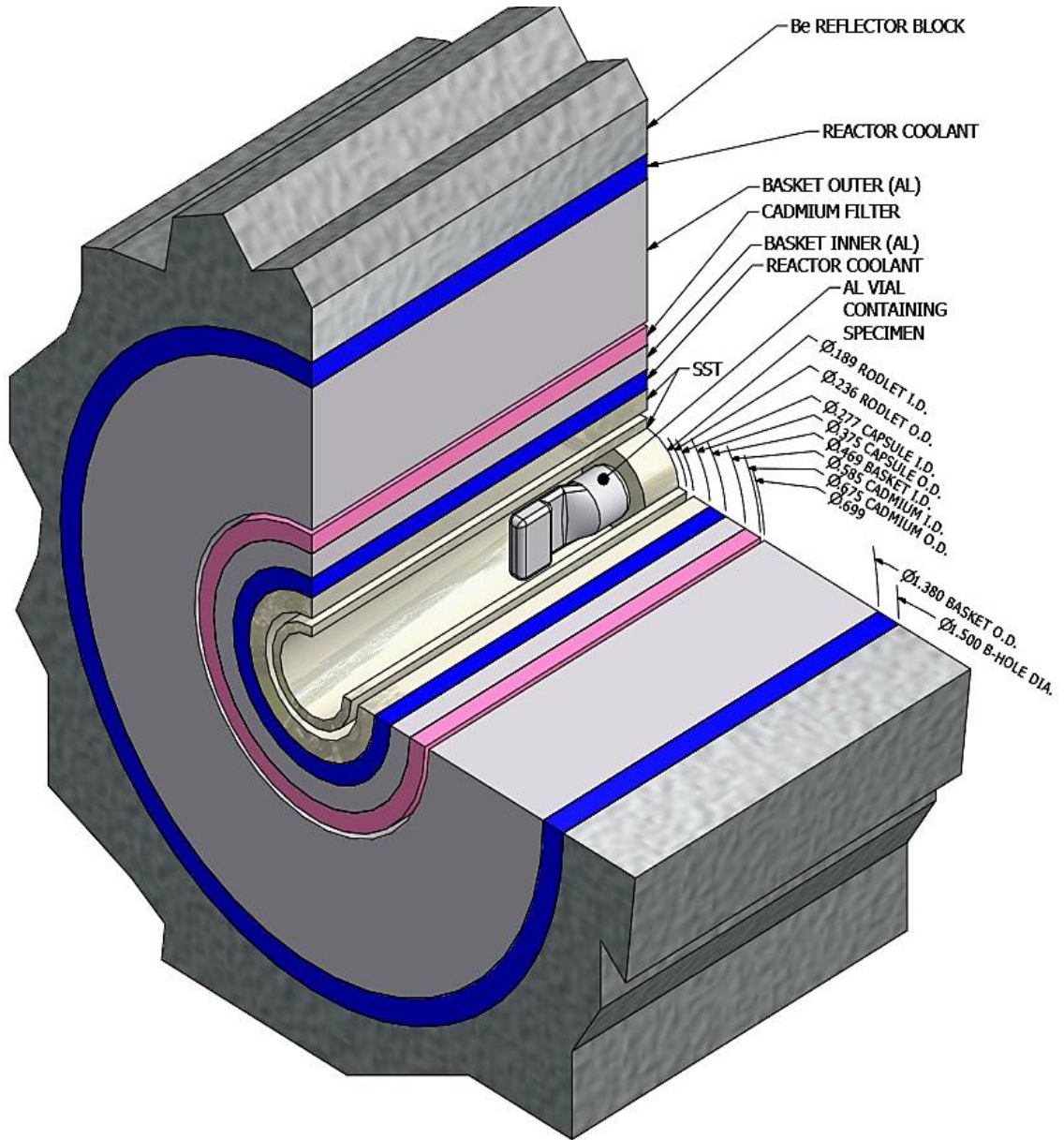


Figure 1.5.2.1 Detailed view of the cadmium experiment in the ATR

The cadmium cut-off is about 0.5 eV. This means cadmium absorbs the incident neutrons with energies less than 0.5 eV. Hence, it can effectively absorb all the thermal neutrons passing through it. The thickness of the cadmium filter used in the experiment was 1 mm.

Of all the isotopes of Cd, Cd-113 has the largest absorption cross-section (Figure 1.5.2.2).

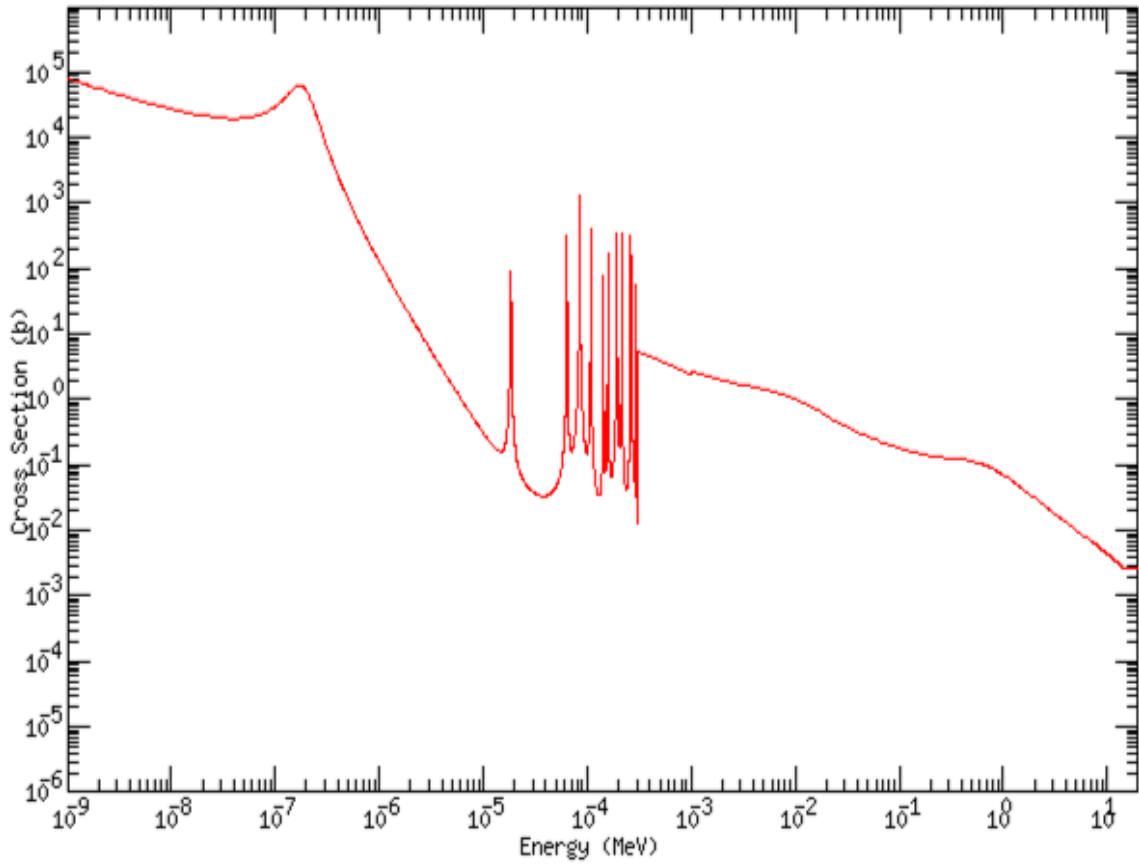


Figure 1.5.2.2 Absorption cross-section of Cd-113

Table 1.5.2.2 Composition of cadmium filter used in MANTRA

Isotopes	atoms.b <sup>-1</sup> .cm <sup>-1</sup>
Cd106	5.649E-04
Cd108	4.074E-04
Cd110	5.737E-03
Cd111	5.904E-03
Cd112	1.114E-02
Cd113	5.574E-03
Cd114	1.347E-02
Cd116	3.510E-03
Total	4.631E-02

### 1.5.3 Capsule and Rodlets

The capsule was a long tube made of 316L Stainless Steel (SST) material which was enclosed within the filter. It consisted of vertical series of rodlets with each rodlet having different neutron flux wire monitors or samples within them. The capsule was around 36 inches long with the stack of the rodlets inside (Figure 1.5.3.1).

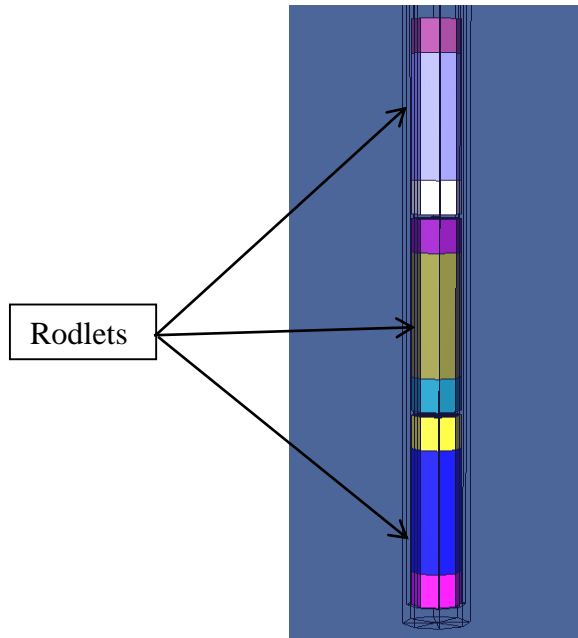


Figure 1.5.3.1 Stack of rodlets one above the other inside the capsule



Figure 1.5.3.2 Boron experiment setup

The inner part of the capsule was the stack of rodlets made with the same material (316L SST) as the capsule. The rodlet consists of a tube and end caps with a vial inside them. Each rodlet was one inch long with 0.189 inches inner diameter and 0.236 inches outer diameter. The rodlets with the flux wires had no vials in them (Figure 1.5.3.3).

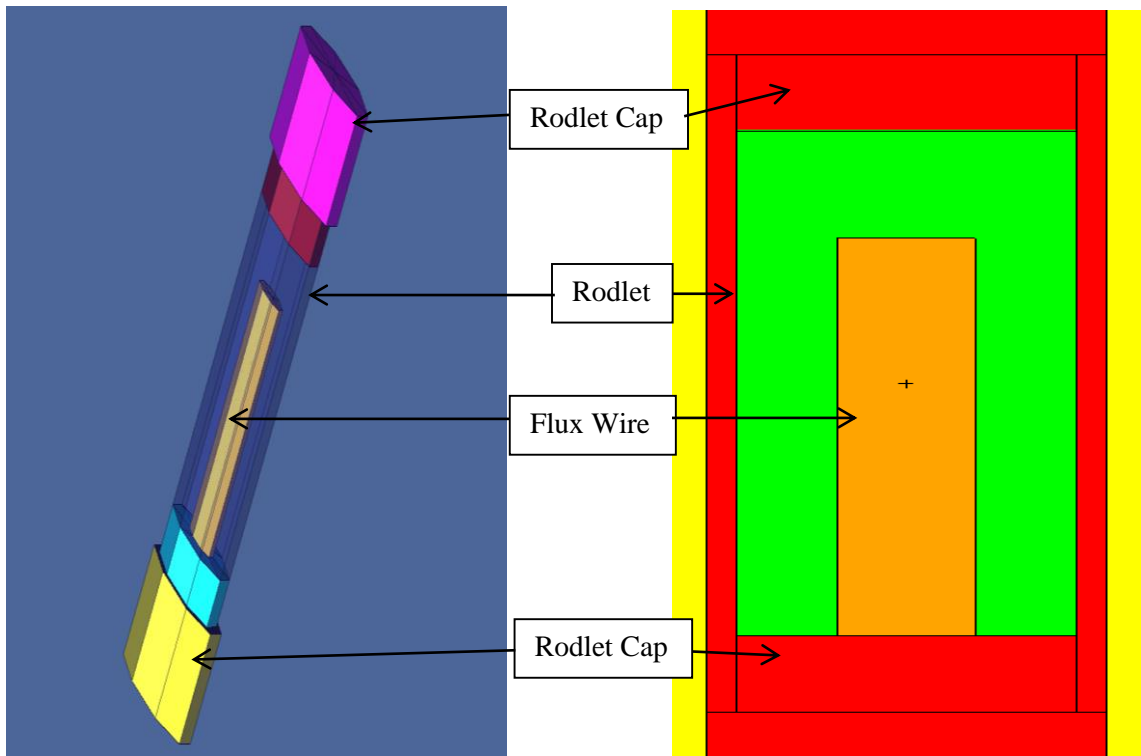


Figure 1.5.3.3 3D (left) and 2D (right) views of the rodlet with a flux wire inside it  
Oxide and nitrate forms of the samples were used in both the experiments. The samples were prepared at the Materials and Fuels Complex, INL. These samples were heated overnight in quartz or porcelain boats. The dried samples in powder form were then loaded into the vials. The inner diameter of the vial was 0.098 inches and the outer diameter was 0.114 inches.

### 1.5.4 MANTRA Sample Preparation

A MANTRA target loading stand was used at MFC to load the samples into vials (Figure 1.5.4.1).

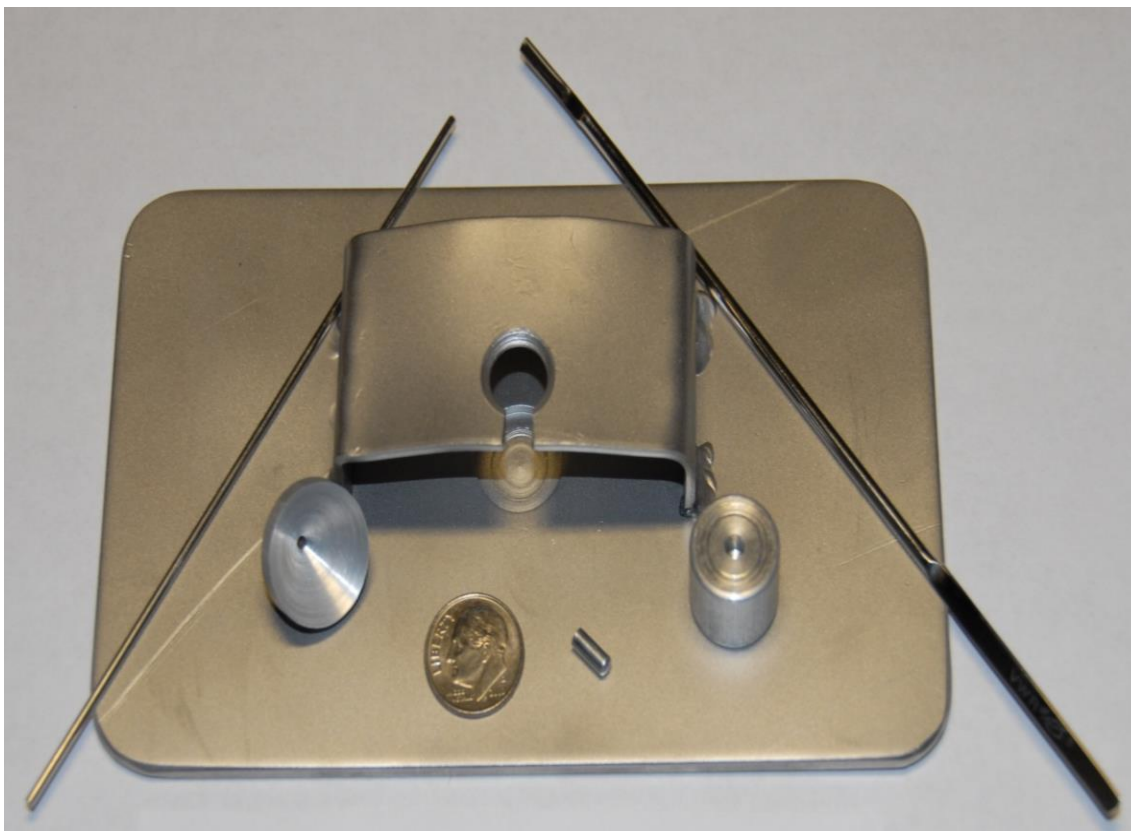


Figure 1.5.4.1 MANTRA target loading stand

Thorium oxide in the porcelain boat before heating can be seen here.



Figure 1.5.4.2 Porcelain boat with a sample

After heating, the sample was loaded into a vial using the funnel setup (Figure 1.5.4.3).



Figure 1.5.4.3 Funnel setup used to fill the vials with samples

The open end of the vial was then pinched after the sample was loaded (Figure 1.5.4.4).

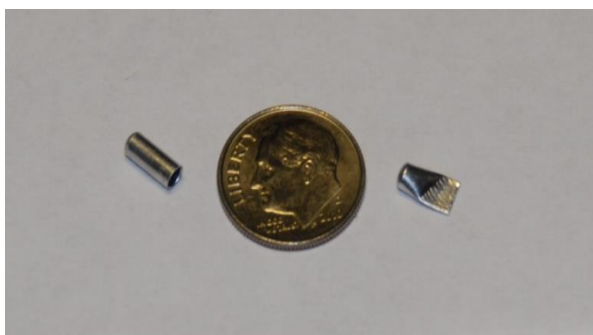


Figure 1.5.4.4 Vial with a sample inside

From Figure 1.5.4.4, one can notice how small the vial was and the sample inside it was even smaller. The exact geometry of the sample inside the vial was not known, since the sample was in the powder form.

Table 1.5.4.1 Chemical forms of the samples used in the MANTRA experiments

<b>MANTRA samples</b>	<b>Chemical forms</b>
Eu-153, Cs-133, Rh-103	Eu(NO <sub>3</sub> ) <sub>3</sub> , CsNO <sub>3</sub> , Rh(NO <sub>3</sub> ) <sub>3</sub>
Nd-145, Pd-105	Nd <sub>2</sub> O <sub>3</sub> , PdO
Ru-101, Nd-143	Ru <sub>2</sub> O <sub>3</sub> , Nd <sub>2</sub> O <sub>3</sub>
Sm-149	Sm <sub>2</sub> O <sub>3</sub> / Sm(NO <sub>3</sub> ) <sub>3</sub>
Th-232	ThO <sub>2</sub>
U-233, U-235, U-236, U-238	U <sub>3</sub> O <sub>8</sub>
Np-237	NpO <sub>2</sub> / Np(NO <sub>3</sub> ) <sub>4</sub>
Pu-239, Pu-240, Pu-242	Pu(NO <sub>3</sub> ) <sub>4</sub>
Am-241, Am-243	Am(NO <sub>3</sub> ) <sub>3</sub>
Pu-244	PuO <sub>2</sub> / Pu(NO <sub>3</sub> ) <sub>4</sub>
Cm-244, Cm-248	Cm(NO <sub>3</sub> ) <sub>3</sub>

The densities of the oxide samples were 3 to 4 times higher than the densities of nitrate samples. The masses of the samples were measured by using an analytical balance before loading into the vial. The given uncertainty on all these masses was  $\pm 30\%$  (2-sigma). This  $\pm 30\%$  uncertainty included all the uncertainties from the sample preparation process.

Table 1.5.4.2 Masses of the samples measured using analytical balance

<b>Boron experiment</b>		<b>Cadmium experiment</b>	
Samples	mg	Samples	mg
Am-241-1	1.50	Am-241-1	1.50
Am-241-2	1.50	Am-241-2	1.50
Am-243-1	3.00	Am-243-1	3.00
Am-243-2	3.00	Am-243-2	3.00

Table 1.5.4.2 cont.

<b>Boron experiment</b>		<b>Cadmium experiment</b>	
Samples	mg	Samples	mg
Cm-248-1	3.00	Cm-244-1	0.50
Cm-248-2	3.00	Cm-244-2	0.50
Cs133	0.42	Cm-248-1	3.00
Eu153	0.21	Cm-248-2	3.00
Np-237-1	1.70	Cs133	0.32
Np-237-2	1.20	Eu153	0.16
Pu-239	2.00	Nd-143	0.10
Pu-240	0.20	Nd-145	0.46
Pu-242-1	1.40	Np-237-1	0.70
Pu-242-2	1.10	Np-237-2	0.50
Pu-244-1	2.10	Pd-105	0.46
Pu-244-2	1.90	Pu-239	2.00
Rh103	0.32	Pu-240	0.20
Sm149	0.40	Pu-242-1	1.70
Th-232	1.80	Pu-242-2	2.00
U-233	1.50	Pu-244-1	0.50
U-235	1.60	Pu-244-2	0.50
U-236	1.40	Rh103	0.32
U-238	1.50	Ru101	0.10
		Sm149	0.05
		Th-232	1.70
		U-233	1.90
		U-235	1.50
		U-236	1.50
		U-238	1.80

The masses of the samples after irradiation were also measured using Inductively Coupled Plasma Mass Spectrometer (ICP-MS). The given uncertainty on these masses was  $\pm 5\%$  (2-sigma). Since these masses were measured after the irradiation, they have to be corrected for burn-up.

Table 1.5.4.3 Masses of the samples measured using ICP-MS

<b>Boron experiment</b>		<b>Cadmium experiment</b>	
Samples	mg	Samples	mg
Am-241-1	0.018	Am-241-1	0.062
Am-241-2	0.707	Am-241-2	0.647
Am-243-1	1.140	Am-243-1	0.563
Am-243-2	2.690	Am-243-2	2.520
Cm-248-1	2.600	Cm-244-1	0.242
Cm-248-2	2.230	Cm-244-2	0.230
Cs133	0.426	Cm-248-1	2.140
Eu153	0.196	Cm-248-2	2.650
Np-237-1	2.060	Cs133	0.161
Np-237-2	1.200	Eu153	0.159
Pu-239	2.410	Nd-143	0.118
Pu-240	0.178	Nd-145	0.514
Pu-242-1	1.430	Np-237-1	0.834
Pu-242-2	1.700	Np-237-2	0.481
Pu-244-1	1.390	Pd-105	0.336
Pu-244-2	1.300	Pu-239	3.140

Table 1.5.4.3 cont.

<b>Boron experiment</b>		<b>Cadmium experiment</b>	
Samples	mg	Samples	mg
Rh103	0.351	Pu-240	0.138
Sm149	0.558	Pu-242-1	1.630
Th-232	1.440	Pu-242-2	1.670
U-233	0.978	Pu-244-1	0.471
U-235	0.016	Pu-244-2	0.436
U-236	0.010	Rh103	0.146
U-238	1.580	Ru101	0.006
		Sm149	0.027
		Th-232	0.010
		U-233	1.160
		U-235	1.230
		U-236	0.990
		U-238	1.490

There were anomalies in the measured masses between analytical balance (pre-irradiated masses) and ICP-MS (post-irradiated masses). For most of the parametric analysis, the pre-irradiated masses measured using the analytical balance were used. However, for the final calculations the burn-up corrected post-irradiated masses measured using ICP-MS will be used.

## 2. MONTE CARLO CODE (MCNP5)

MCNP5 is a general purpose Monte Carlo N-Particle software code recognized internationally that can be used to analyze the transport of individual or coupled particles (neutron/electron/photon) by using Monte Carlo method. MCNP5 can effectively consider the factors like self-shielding, resonance absorption and neutron scattering in its calculations. In case of complex problems that are difficult to be modeled with the deterministic methods, one can use the Monte Carlo method to simulate the statistical process (16). One of the advantages of MCNP is that it has large cross-section libraries for many isotopes (17). Tally cards are the important data entries that specify MCNP what to calculate in order to reach the problem goals. ENDF7.0 cross-section library was used in the current work.

To obtain good end results, it is always necessary to understand and predict the experiment. This can be done with the help of the simulation codes like MCNP5, ECCO\_ERANOS, etc. For a high profile project like MANTRA, the parametric analysis is very important to study and also to characterize the experiments in a better way. The parametric analysis was performed on the experiments with different possible uncertainties that could affect the end results using MCNP5 and ECCO\_ERANOS. This analysis was done step by step starting with a simple cylindrical model and progressing to a more complex model. To obtain good statistical convergence, billions of starting particles were used in the analysis. MCNP5 was also used to calculate the response functions of the neutron flux wires and the *a priori* spectra required for the unfolding process. The ATR full core benchmark model was adopted for both the cadmium and boron experiments.

The effective one group cross-sections ( $\bar{\sigma}^r$ ) of the samples for different reactions were calculated using F4 and Fm4 tally cards. The F4 tally card can be used to calculate the flux averaged over a volume ( $n.cm^{-2}$ ).

$$F4 = \int_0^{\infty} \phi(E) dE \quad [2.0.1]$$

The Fm4 tally card can then be used to calculate the energy-integrated neutron cross-section ( $b. n.cm^{-2}$ ).

$$Fm4 = \int_0^{\infty} \sigma^r(E)\phi(E) dE \quad [2.0.2]$$

Finally, the effective one group cross-section ( $b$ ) can be calculated by taking the simple ratio:

$$\bar{\sigma}^r = \frac{Fm4}{F4} = \frac{\int_0^{\infty} \sigma^r(E)\phi(E) dE \left(\frac{b*n}{cm^2}\right)}{\int_0^{\infty} \phi(E) dE \left(\frac{n}{cm^2}\right)} \quad [2.0.3]$$

The absolute error (abs) of the one cross-section can be calculated by using the equation below.

$$\pm \Delta\alpha_{\sigma} = \frac{Fm4}{F4} \sqrt{(\Delta\alpha_{Fm4}/Fm4)^2 + (\Delta\alpha_{F4}/F4)^2} \quad [2.0.4]$$

Where,  $\Delta\alpha$  = absolute error and  $\Delta\alpha_{F4}/F4$  = relative error in F4

The parametric analysis was started with the complete ATR full core model. Clearly from Figure 1.5.4.4, the size of the samples was very small when compared to the entire full core model. In this situation, it always takes very long time to do the analysis with the full core model especially when using billions of particles. So the fixed source calculations were performed on both the experiments. At first, a simple cylindrical model of the boron experiment was used and then the reduced models of both the experiments were used.

## 2.1 Simple Cylindrical Model

A simple cylindrical model of the boron experiment was used in MCNP to calculate the one group cross-sections. The fixed source calculations were performed using the surface source files (SSW) generated from the ATR full core models of both the experiments. To calculate the cross-sections with no self-shielding effects, the samples were infinitely diluted by fixing their atom densities to  $10^{-10}$  (atoms.b<sup>-1</sup>.cm<sup>-1</sup>).

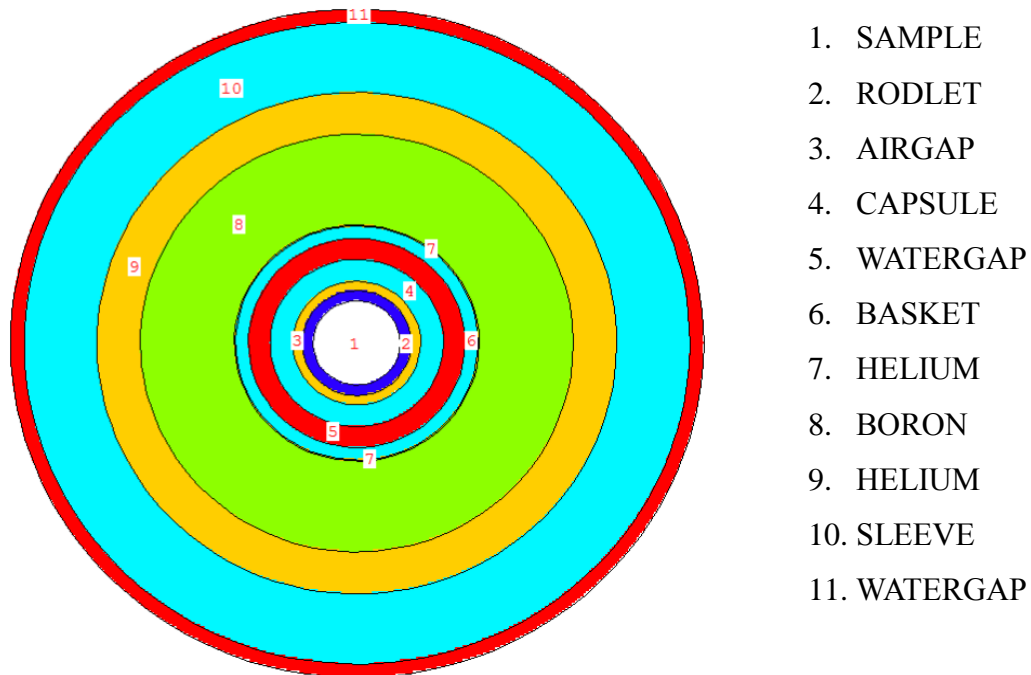


Figure 2.1.1 Simple cylindrical model of the boron experiment

The SSW files were generated outside the experiment locations (b9 and b11). For example (Figure 2.1.1), the SSW file for the boron experiment was generated outside region 11 by adding a very thin layer of void gap. The one group cross-sections of the infinitely diluted samples calculated using the simple cylindrical model can be seen in the Table 2.1.1. These cross-sections were in good agreement with the ones calculated using the full core benchmark model. The normalized fluxes between these two models at the sample location were plotted for comparison (Figure 2.1.1).

Sample location (B experiment)

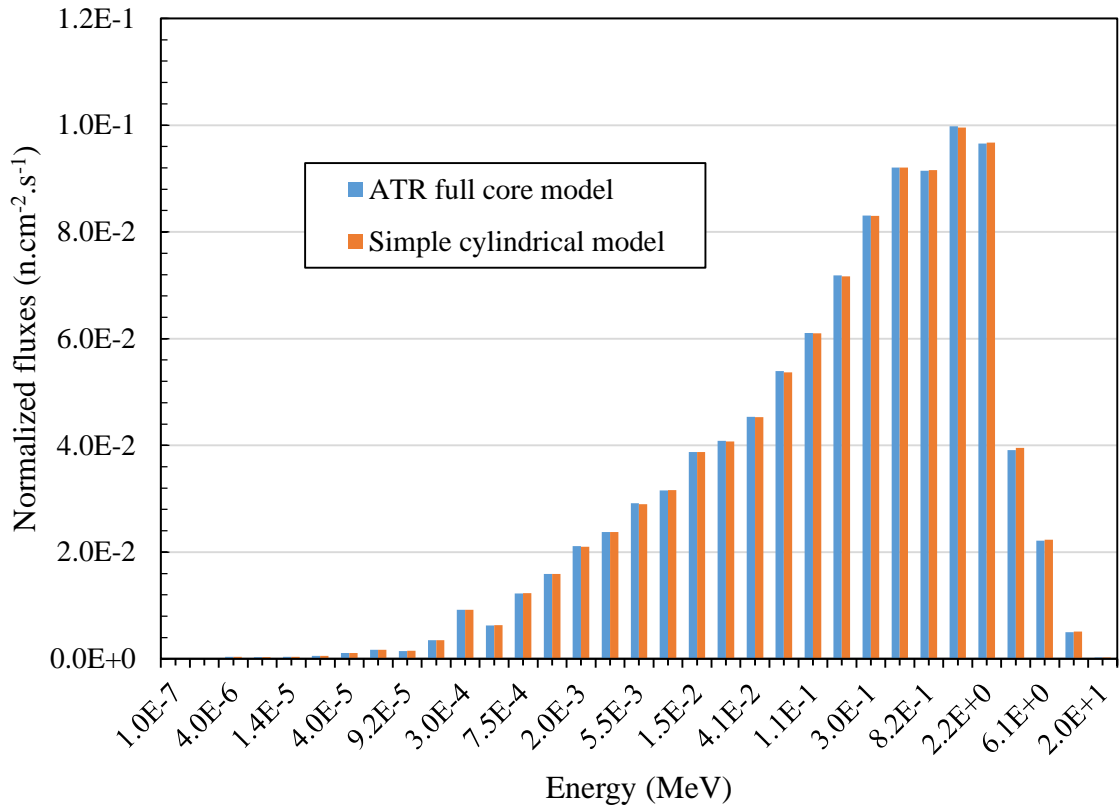


Figure 2.1.2 Normalized fluxes at the sample location from both the models

In Table 2.1.1, the one group cross-sections of the samples and their percentage relative errors in both the models were included.

Table 2.1.1 One group cross-sections of the samples in the boron experiment

	ATR full core model		Simple cylindrical model	
	$\sigma$	relative error	$\sigma$	relative error
Samples	barns	%	barns	%
Am241 $\sigma_f$	0.49309	0.030	0.49362	0.125
Am241 $\sigma_g$	2.94110	0.030	2.94933	0.108
Am243 $\sigma_f$	0.37170	0.030	0.37209	0.134
Am243 $\sigma_g$	2.63440	0.050	2.64635	0.180

Where,  $\sigma_g$  = capture cross-section;  $\sigma_f$  = fission cross-section

Table 2.1.1 cont.

	ATR full core model		Simple cylindrical model	
	$\sigma$	relative error	$\sigma$	relative error
Samples	barns	%	barns	%
Cm244 $\sigma_f$	0.66671	0.020	0.66721	0.117
Cm244 $\sigma_g$	1.44900	0.130	1.44709	0.464
Cm248 $\sigma_f$	0.53425	0.030	0.53509	0.125
Cm248 $\sigma_g$	0.69360	0.130	0.70025	0.514
Np237 $\sigma_f$	0.53495	0.020	0.53533	0.117
Np237 $\sigma_g$	2.63640	0.020	2.64349	0.100
Pu239 $\sigma_f$	2.62730	0.020	2.63408	0.100
Pu239 $\sigma_g$	1.11090	0.040	1.11529	0.143
Pu240 $\sigma_f$	0.57564	0.020	0.57597	0.117
Pu240 $\sigma_g$	2.28460	0.300	2.30397	1.102
Pu242 $\sigma_f$	0.43800	0.020	0.43824	0.125
Pu242 $\sigma_g$	1.03390	0.210	1.01860	0.752
Pu244 $\sigma_f$	0.38149	0.030	0.38171	0.125
Pu244 $\sigma_g$	0.67555	0.070	0.67703	0.257
Th232 $\sigma_f$	0.01893	0.040	0.01899	0.180
Th232 $\sigma_g$	0.73162	0.070	0.73073	0.218
U233 $\sigma_f$	3.64550	0.010	3.65086	0.078
U233 $\sigma_g$	0.47901	0.020	0.47979	0.092
U235 $\sigma_f$	2.61380	0.010	2.61795	0.078
U235 $\sigma_g$	0.90257	0.020	0.90406	0.092
U236 $\sigma_f$	0.19481	0.030	0.19507	0.134
U236 $\sigma_g$	0.87650	0.100	0.87923	0.395
U238 $\sigma_f$	0.08211	0.040	0.08232	0.171
U238 $\sigma_g$	0.83231	0.110	0.83328	0.385

## 2.2 Reduced models

Unlike the simple cylindrical model, the reduced model consisted of the stack of rodlets from top to bottom. The cross-sections calculated from this reduced model were compared against the full core model cross-sections. The cross-sections from both the models were in good agreement with each other (Tables 2.2.1-2.2.2).

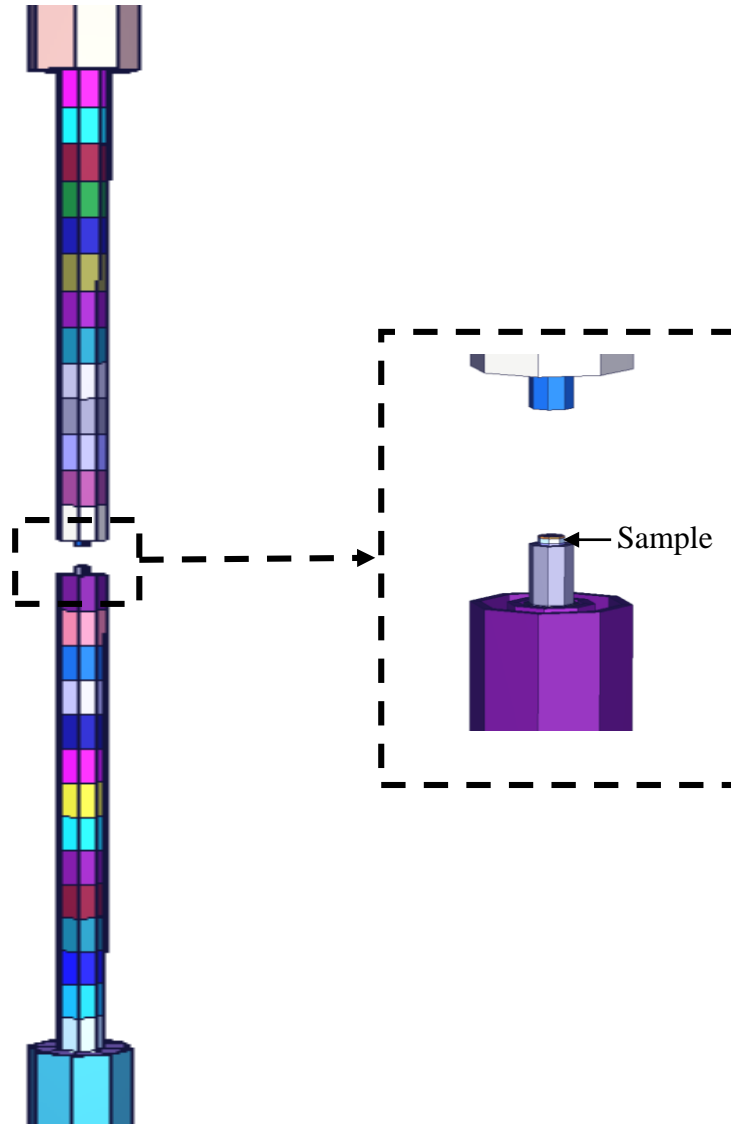


Figure 2.2.1 Reduced model of the cadmium experiment

In tables of this section, 2<sup>nd</sup> & 4<sup>th</sup> columns = one group cross-sections

3<sup>rd</sup> & 5<sup>th</sup> columns = percentage relative errors  $\left(\frac{\Delta\alpha_X}{X}\right)*100$

6<sup>th</sup> column = % discrepancies. The discrepancies were calculated with respect to ATR full core model.

$$\left(\frac{\sigma_R - \sigma_A}{\sigma_A}\right) * 100$$

Where,  $\sigma_R$  = cross-sections from reduced model;  $\sigma_A$  = cross-sections from full core model.

Table 2.2.1 One group cross-sections of the samples in the boron experiment

Samples	ATR full core model		Reduced model		%discrepancy
	$\sigma$ (barns)	% relative error	$\sigma$ (barns)	% relative error	
Am241 $\sigma_f$	0.49309	0.030	0.49253	0.175	-0.113
Am241 $\sigma_g$	2.94110	0.030	2.94032	0.099	-0.027
Am243 $\sigma_f$	0.37170	0.030	0.37116	0.184	-0.146
Am243 $\sigma_g$	2.63440	0.050	2.63339	0.099	-0.038
Cm244 $\sigma_f$	0.66671	0.020	0.66642	0.148	-0.043
Cm244 $\sigma_g$	1.44900	0.130	1.44350	0.148	-0.380
Cm248 $\sigma_f$	0.53425	0.030	0.53377	0.166	-0.090
Cm248 $\sigma_g$	0.69360	0.130	0.69345	0.212	-0.021
Np237 $\sigma_f$	0.53495	0.020	0.53478	0.157	-0.031
Np237 $\sigma_g$	2.63640	0.020	2.63479	0.099	-0.061
Pu239 $\sigma_f$	2.62730	0.020	2.62637	0.099	-0.035
Pu239 $\sigma_g$	1.11090	0.040	1.11053	0.122	-0.034
Pu240 $\sigma_f$	0.57564	0.020	0.57539	0.157	-0.043
Pu240 $\sigma_g$	2.28460	0.300	2.27666	0.221	-0.347
Pu242 $\sigma_f$	0.43800	0.020	0.43773	0.166	-0.061
Pu242 $\sigma_g$	1.03390	0.210	1.03194	0.184	-0.189
Pu244 $\sigma_f$	0.38149	0.030	0.38119	0.175	-0.078
Pu244 $\sigma_g$	0.67555	0.070	0.67515	0.166	-0.059

Table 2.2.1 cont.

Samples	ATR full core model		Reduced model		%discrepancy
	$\sigma$ (barns)	% relative error	$\sigma$ (barns)	% relative error	
Th232 $\sigma_f$	0.01893	0.040	0.01889	0.260	-0.196
Th232 $\sigma_g$	0.73162	0.070	0.73177	0.175	0.020
U233 $\sigma_f$	3.64550	0.010	3.64315	0.092	-0.064
U233 $\sigma_g$	0.47901	0.020	0.47854	0.099	-0.099
U235 $\sigma_f$	2.61380	0.010	2.61363	0.092	-0.006
U235 $\sigma_g$	0.90257	0.020	0.90188	0.099	-0.076
U236 $\sigma_f$	0.19481	0.030	0.19445	0.184	-0.184
U236 $\sigma_g$	0.87650	0.100	0.87566	0.166	-0.096
U238 $\sigma_f$	0.08211	0.040	0.08195	0.240	-0.189
U238 $\sigma_g$	0.83231	0.110	0.83148	0.184	-0.100

Table 2.2.2 One group cross-sections of the samples in the cadmium experiment

Samples	ATR full core model		Reduced model		%discrepancy
	$\sigma$ (barns)	% relative error	$\sigma$ (barns)	% relative error	
Am241 $\sigma_f$	0.71483	0.040	0.71452	0.130	-0.044
Am241 $\sigma_g$	72.08400	0.060	71.97215	0.139	-0.155
Am243 $\sigma_f$	0.30282	0.030	0.30276	0.121	-0.019
Am243 $\sigma_g$	86.16800	0.100	85.58490	0.275	-0.677
Cm244 $\sigma_f$	0.64849	0.070	0.64851	0.187	0.002
Cm244 $\sigma_g$	33.30300	0.240	33.12949	0.622	-0.521
Cm248 $\sigma_f$	0.71956	0.130	0.71352	0.344	-0.839
Cm248 $\sigma_g$	12.46100	0.200	12.37411	0.512	-0.697
Np237 $\sigma_f$	0.31958	0.030	0.32011	0.130	0.165

Table 2.2.2 cont.

Samples	ATR full core model		Reduced model		%discrepancy
	$\sigma$ (barns)	% relative error	$\sigma$ (barns)	% relative error	
Np237 $\sigma_g$	35.98000	0.050	35.88570	0.139	-0.262
Pu239 $\sigma_f$	31.02400	0.070	31.07297	0.094	0.158
Pu239 $\sigma_g$	18.85900	0.070	18.86624	0.112	0.038
Pu240 $\sigma_f$	0.42241	0.040	0.42204	0.130	-0.089
Pu240 $\sigma_g$	377.41000	0.150	373.69984	0.393	-0.983
Pu242 $\sigma_f$	0.24761	0.030	0.24779	0.139	0.074
Pu242 $\sigma_g$	61.77600	0.220	61.35519	0.572	-0.681
Pu244 $\sigma_f$	0.20925	0.030	0.20944	0.139	0.089
Pu244 $\sigma_g$	5.32410	0.180	5.28299	0.453	-0.772
Th232 $\sigma_f$	0.01055	0.040	0.01059	0.216	0.398
Th232 $\sigma_g$	4.36930	0.180	4.34520	0.453	-0.552
U233 $\sigma_f$	40.89000	0.030	40.85620	0.103	-0.083
U233 $\sigma_g$	7.16280	0.040	7.14080	0.139	-0.307
U235 $\sigma_f$	17.17500	0.040	17.24273	0.094	0.394
U235 $\sigma_g$	7.74070	0.040	7.74686	0.130	0.080
U236 $\sigma_f$	0.32135	0.150	0.32224	0.393	0.276
U236 $\sigma_g$	16.79900	0.230	16.87803	0.602	0.470
U238 $\sigma_f$	0.04580	0.040	0.04597	0.206	0.382
U238 $\sigma_g$	13.91100	0.190	13.92372	0.493	0.091

The above tables confirmed that the reduced model generates the same cross-sections as the full core model.

### 2.3 ATR Flux Traps

ATR has an unusual core shaped like a four-leaf clover (Figure 2.3.1). In the center of each leaf, between each adjacent pair of leaves, and in the center of the core are located test facilities called flux traps. Because the flux traps are close to reactor fuel, the neutron current coming into the test regions includes a large contingent of high-energy fission neutrons. However, the region in and immediately around each flux trap contains cooling water that moderates the neutrons (18).

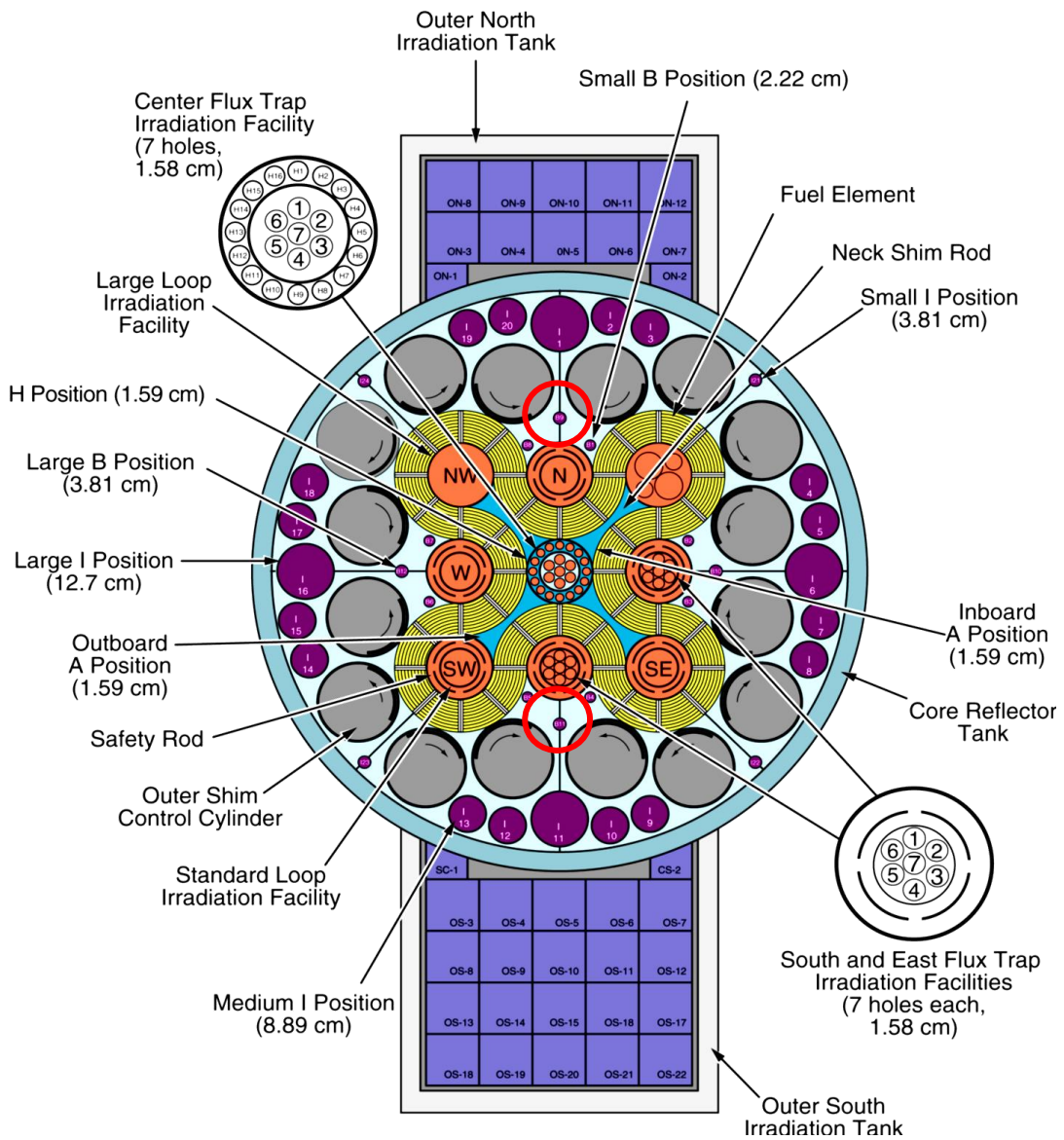


Figure 2.3.1 ATR cross-sectional diagram with flux traps (19)

ATR is used all year around for various research experiments. Because of the presence of high neutron flux levels, the test facilities in these flux traps are extensively used for research experiments like advanced fuel cycle experiments, naval reactor experiments, etc. Some of the flux traps may be modified according to the goals of these research experiments. Therefore, presence of these experiments could affect the MANTRA experiments. The flux traps in the actual benchmark model contain different assemblies (Table 2.3.1).

Table 2.3.1 ATR flux traps with different assemblies

<b>Flux Traps</b>	<b>Assembly</b>
North (N)	Water in Flow Tube + Pressure Tube + Insulation Tube (FTW)
South (S)	Six Co targets in seven target array
East (E)	Six Co targets in seven target array
West (W)	Water in Flow Tube + Pressure Tube + Insulation Tube
North East (NE)	Nine Co targets in 23 target array
South East (SE)	Water in Flow Tube + Pressure Tube + Insulation Tube
North West (NW)	Aluminum Filler + Pressure Tube + Insulation Tube (FTA)
South West (SW)	Water in Flow Tube + Pressure Tube + Insulation Tube

As mentioned earlier, the irradiation locations used in the project MANTRA were b9 and b11. The location b9 is close to the north flux trap and the location b11 is close to the south flux trap (Figure 2.3.1). Therefore, these flux traps could affect the MANTRA experiments. It is difficult to get the exact configuration of the nearby flux traps during the irradiation process. The work in this section was done during the irradiation process of the boron

experiment. So, all the flux traps were modified with different assemblies to study their effects on MANTRA. Two cases were mainly used to study the effects of these flux traps.

**Case 'FTA': Flux Traps with Aluminum filler and pressure tube assembly**

All the flux traps were replaced with an aluminum filler, a pressure tube and an insulation tube assembly (Figure 2.3.2). This case was used to study the influence of aluminum fillers on the samples. In the benchmark model, four flux traps contain water in their flow tubes. When these flow tubes are replaced with aluminum fillers, the amount of the moderator is reduced, increasing the fast neutron flux near the flux traps. In the benchmark model, this FTA assembly was only present in the North West flux trap close to b9.

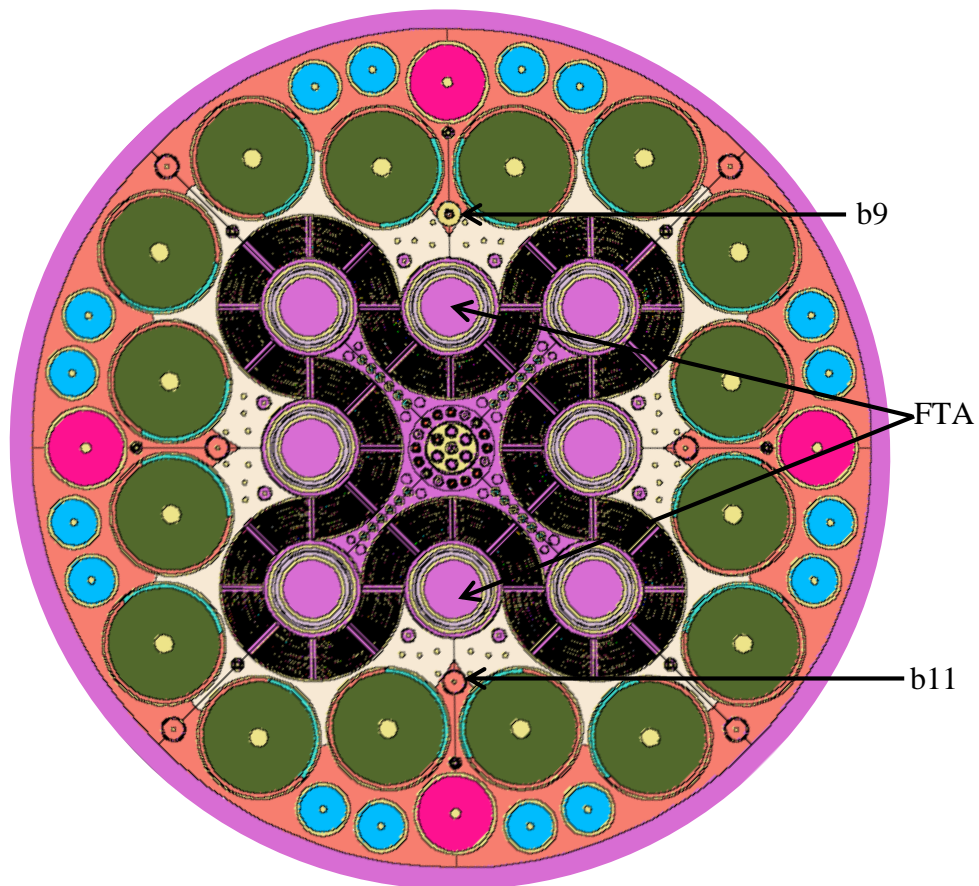


Figure 2.3.2 Flux traps with aluminum filler, pressure tube and insulation tube assembly

**Case ‘FTW’:** Flux Traps with Water and pressure tube assembly

In this case the flux traps were replaced with water in a flow tube, a pressure tube and an insulation tube assembly (Figure 2.3.3). This case was intended to study how the water in the flux traps effects the samples.

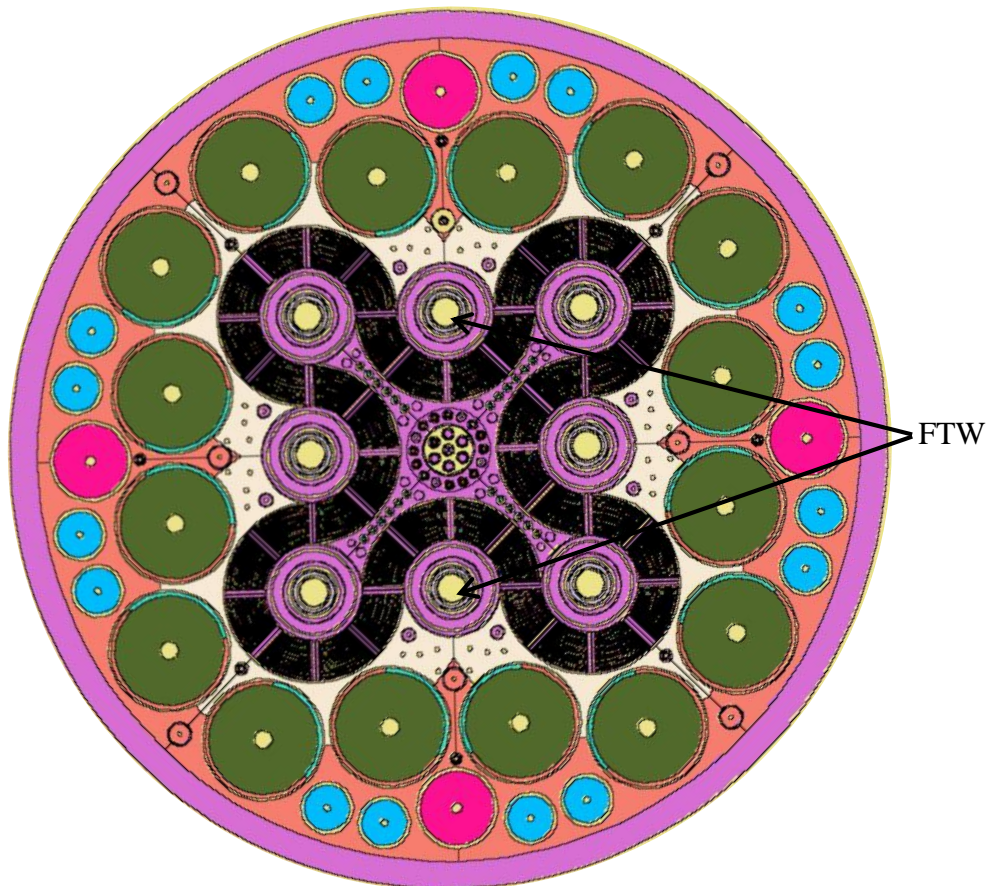


Figure 2.3.3 Flux traps with water in flow tube, pressure tube and insulation tube assembly

The FTW assembly was present in north, west, south east and south west flux traps of the benchmark model. These flux traps were close to both b9 and b11 irradiation locations. By replacing all the flux traps with this assembly, the amount of moderation was increased, thus thermalizing the spectrum near them.

The discrepancies in the cross-sections of the samples in both the cases FTA and FTW were calculated with reference to the cross-sections from the benchmark model. The mass

of each sample used in this analysis was 1 mg. In Figure 2.3.4 and Figure 2.3.5, the solid lines represent the  $\pm 5\%$  discrepancies.

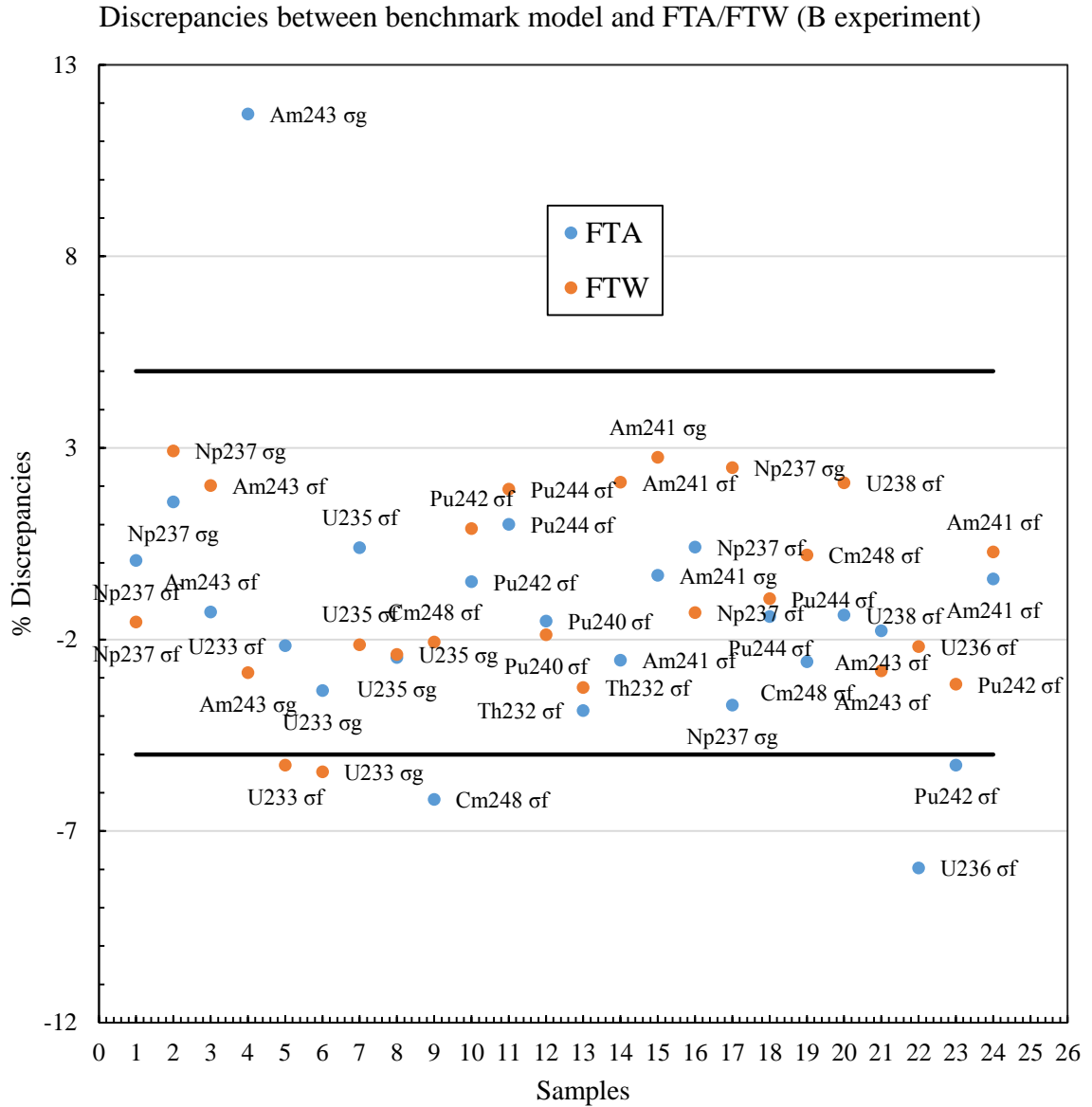


Figure 2.3.4 Discrepancies between benchmark model and FTA/FTW (B experiment)

From Figure 2.3.4, most of the samples in the boron experiment were not affected by the assemblies FTA and FTW. The samples Am243 and U236 had discrepancies of around 12% and 8% respectively. This might be because of the decrease in the amount of moderation near b9.

Discrepancies between benchmark model and FTA/FTW (Cd experiment)

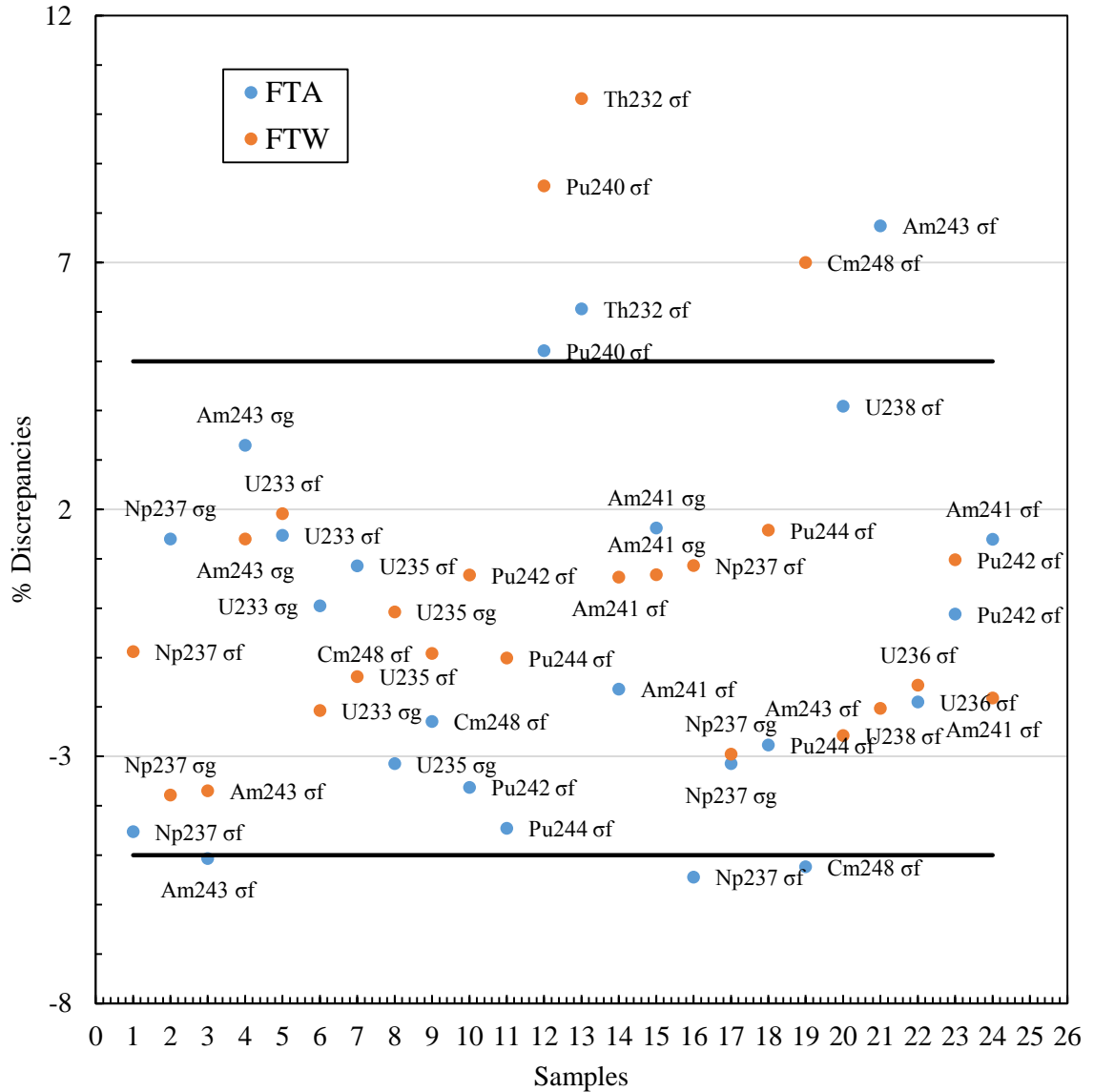


Figure 2.3.5 Discrepancies between benchmark model and FTA/FTW (Cd experiment)

From Figure 2.3.5, most of the samples in the cadmium experiment were also not affected by the assemblies FTA and FTW. The increase in moderation near b11 might have caused the samples Th232, Pu240 and Cm248 to have discrepancies greater than 5%. However, the calculations done by James W Sterbentz (INL) during post irradiation analysis confirmed that the experiments in the flux traps had no significant effects on MANTRA experiments.

### 3. ECCO\_ERANOS

The European Reactor Analysis Optimized Calculation System (ERANOS) has been developed to provide a basis for reliable neutronic analysis. This is a deterministic code system which consists of neutron and gamma codes. ECCO is a cell/lattice code that is part of the ERANOS package. This code was used to calculate the effective one group cross-sections. ECCO prepares self-shielded cross-sections and matrices by combining a slowing-down treatment in many groups (1,968 groups) with the subgroup method (20). This code uses collision probabilities to calculate fluxes and effective cross-sections. Using these probability tables, ECCO can calculate the self-shielded cross-sections. These cross-sections can be condensed and homogenized.

Two calculation routes can be used in ECCO. The first route is the design route which is faster since some simplifying hypotheses are made. In this route, the elastic scattering is treated with fine group structure, and the sub-group parameters are treated at the broad group level. The second route is the reference route which is more accurate than the first one. In this route, both the elastic scattering and the sub-group parameters are treated with the fine group structure for the resonance self-shielding treatment. Intermediate structures are possible, in particular to collapse data for shielding purposes (21). Fine (1,968 groups), intermediate (172 groups) and broad (33 groups), are the three energy group structures used in this code. ECCOLIB is a cross-section library used by ECCO which can be generated by implementing processing codes and interface tools on the ENDF data files. The ECCOLIB generated from ENDF7.0 was used in the calculations. ECCO can produce multi-group cross-sections in the output. The broad energy group structure was chosen for the cross-sections. The infinitely diluted and the actual masses (pre-irradiated masses) of the samples were used to calculate the cross-sections. A sample input file for ECCO can be seen in the Appendix A.

### 3.1 MCNP Source in ECCO

External source calculations were performed in ECCO for both the MANTRA experiments analyzed. The net neutron currents from MCNP5 were used in ECCO as external sources. A small FORTRAN code was used to generate these source files (see Appendix B). Using these source files, the one group cross-sections can be calculated in ECCO that are comparable to MCNP. So, one can verify the results from a stochastic code with a deterministic code or vice-versa. A simple one-dimensional infinite cylindrical model was used.

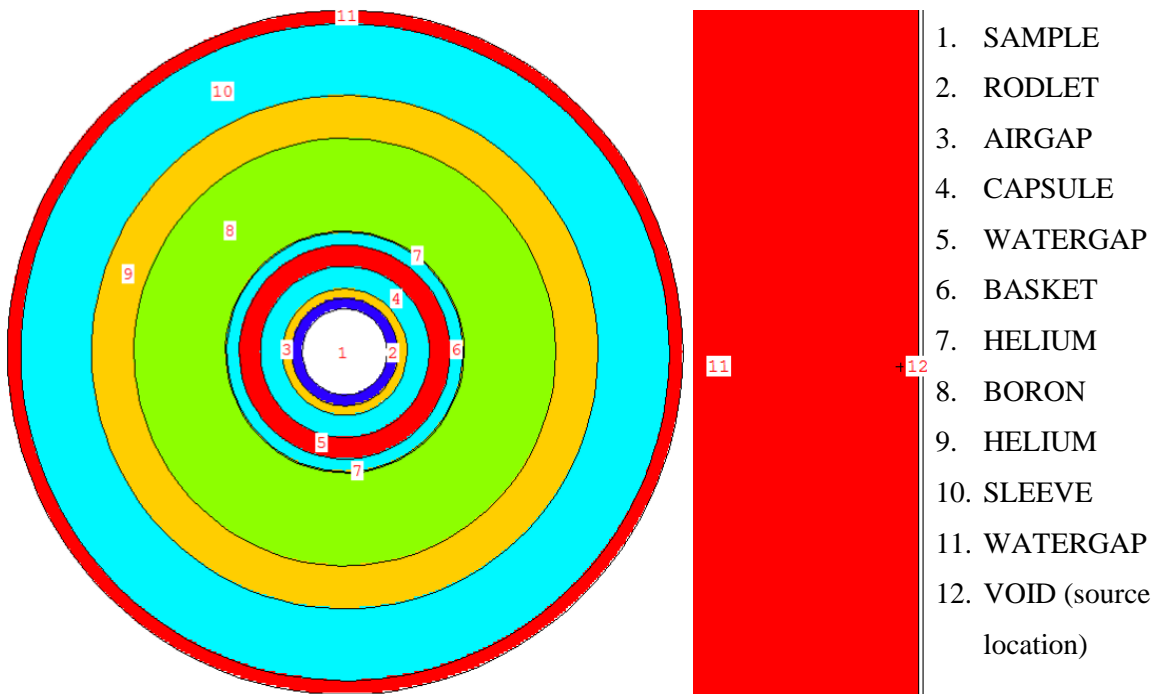


Figure 3.1.1 Infinite cylindrical model of the boron experiment

The external sources were used outside both the experiments in a very thin void layer (e.g. layer 12 in Figure 3.1.1), similar to the fixed source calculations in MCNP. It is important to verify if the external source from MCNP was successfully implemented in ECCO. To verify the same, the propagation of neutrons in different layers of the boron experiment was compared between MCNP and ECCO.

The normalized fluxes in each layer of the boron experiment from MCNP5 and ECCO were plotted. For MCNP, the normalized fluxes from the simple cylindrical model (see section 2.1) of the boron experiment were used. The propagation of neutrons starting from the source location to the sample location can be seen in the figures below.

### 12. Void layer (source location in ECCO)

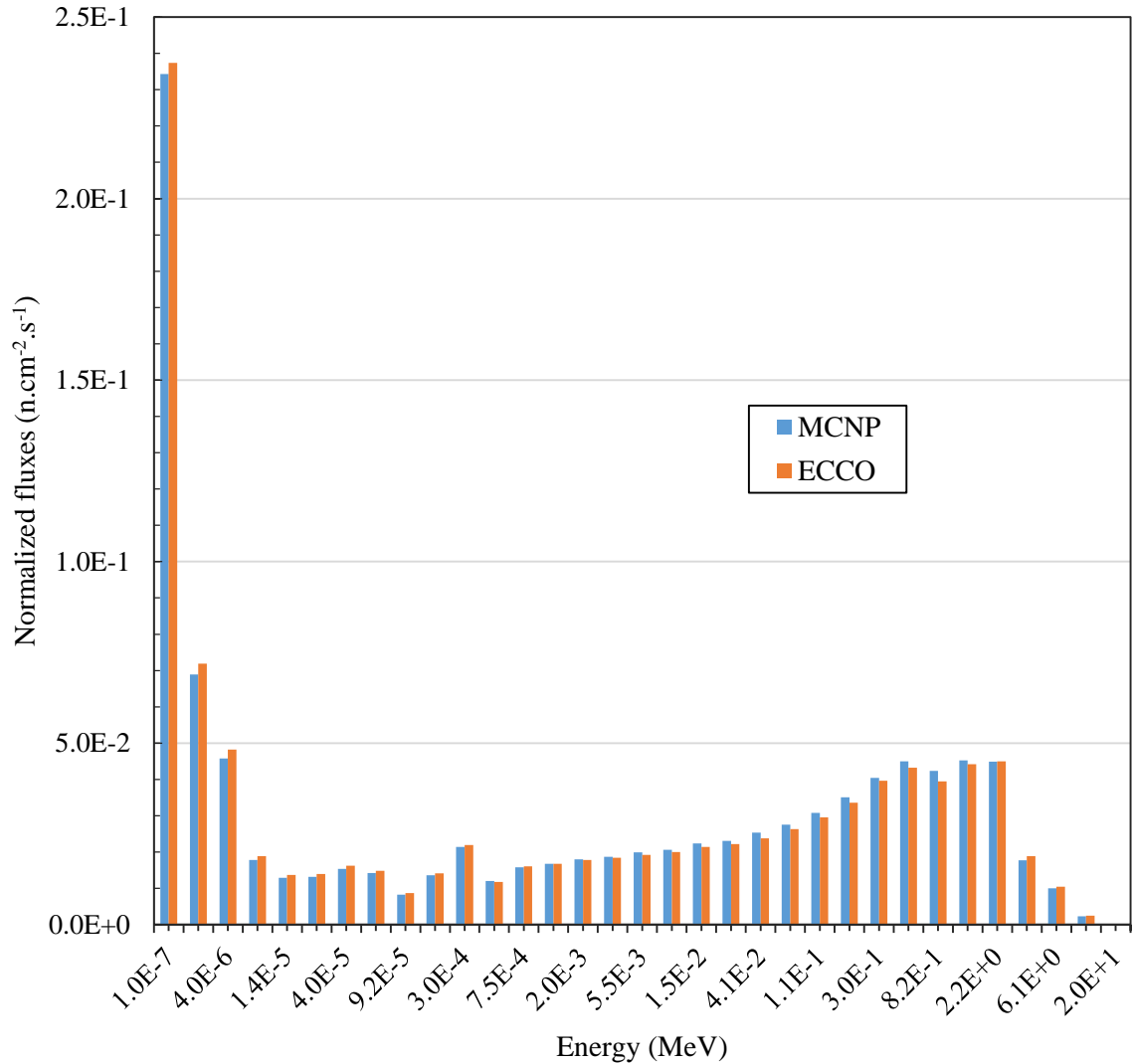


Figure 3.1.2 Normalized fluxes in the outer void layer of the boron experiment

## 11. Water-gap

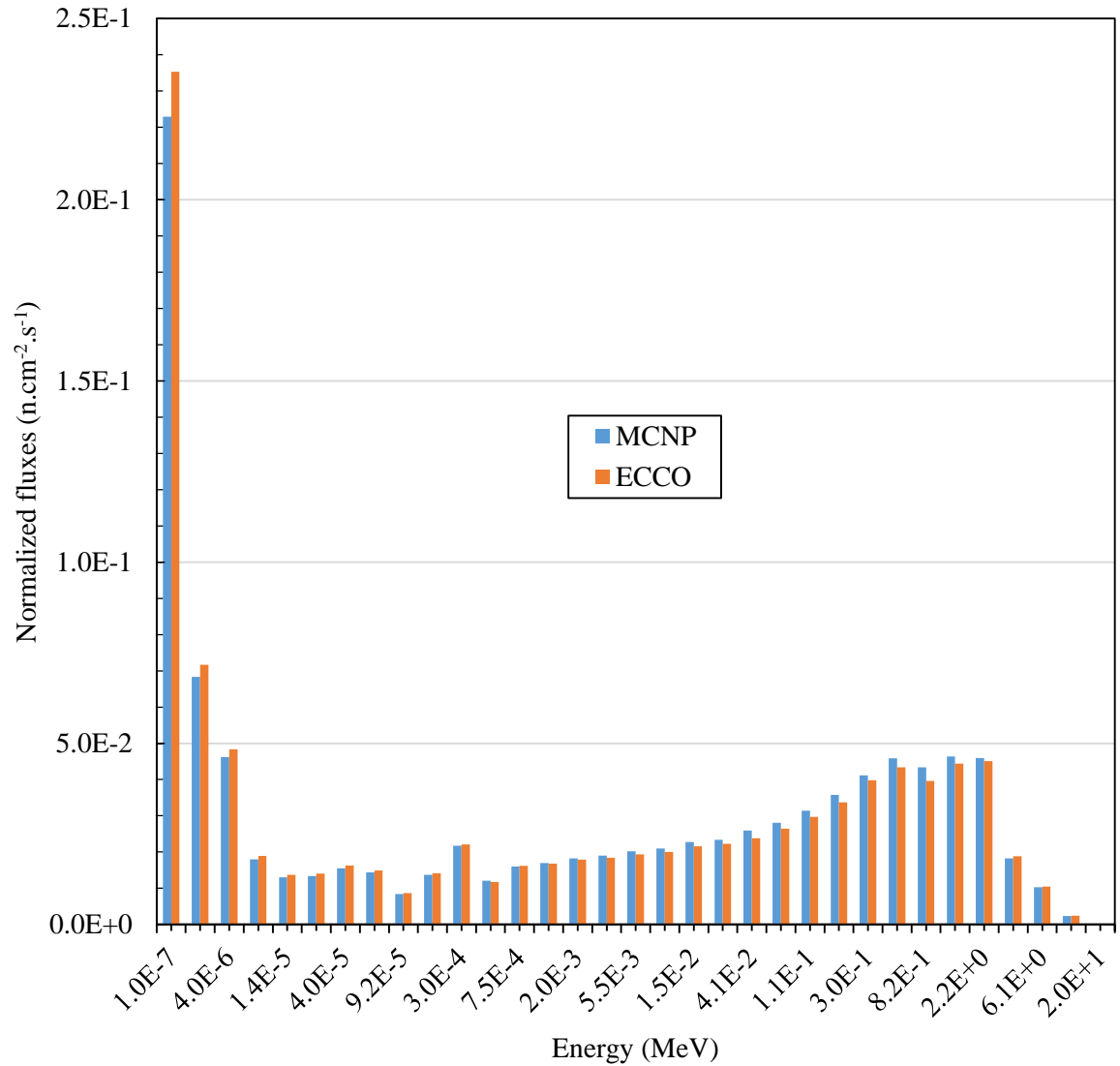


Figure 3.1.3 Normalized fluxes in the water-gap before the boron filter

This water gap was the outmost layer where the propagation of neutrons starts. In the lower energy groups, the fluxes from ECCO were dominating the MCNP fluxes. In the mid-higher energy groups, the fluxes from MCNP were dominating the fluxes from ECCO.

### 10. Sleeve

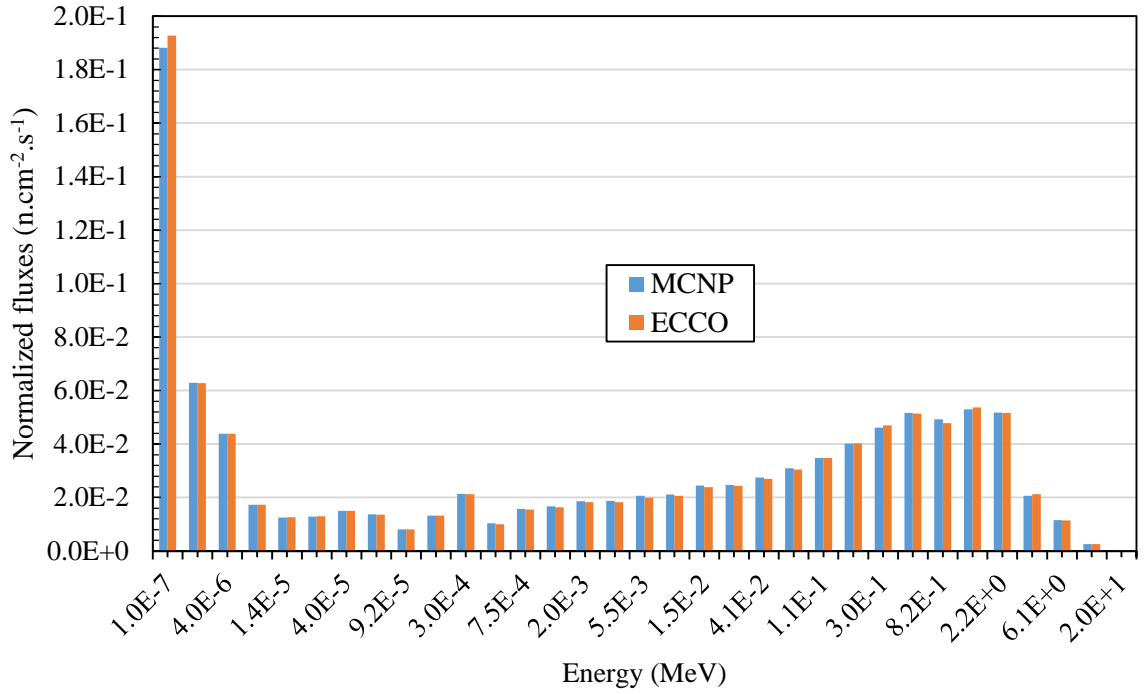


Figure 3.1.4 Normalized fluxes in the sleeve of the boron experiment

### 9. Helium (He) before filter

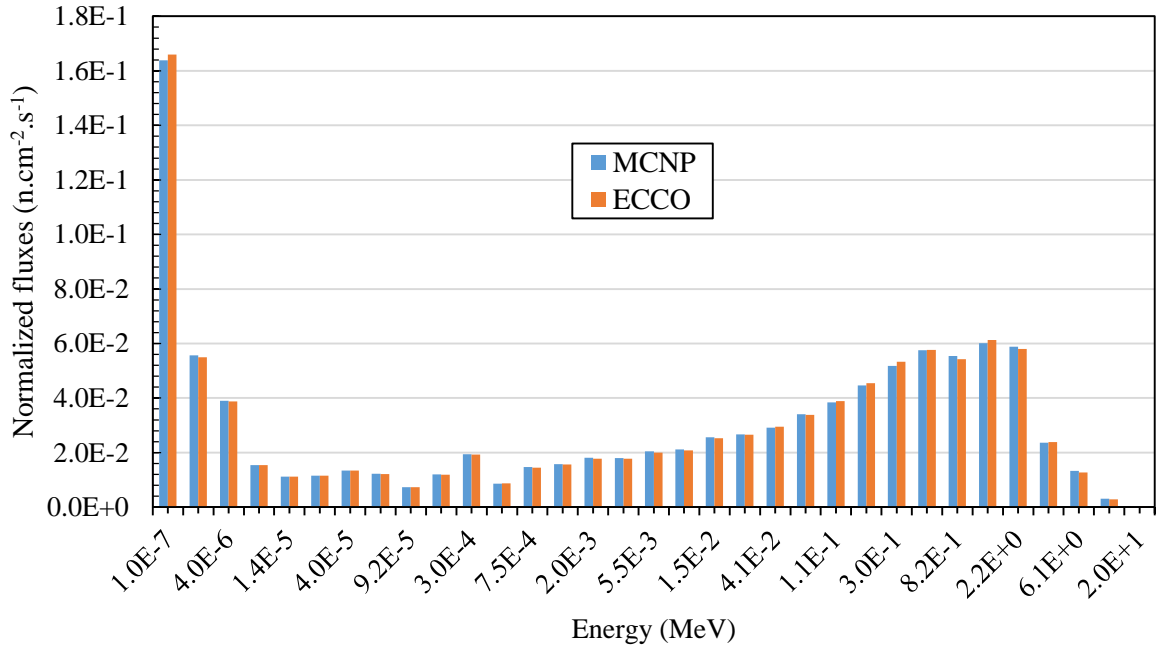


Figure 3.1.5 Normalized fluxes in the helium gap before the boron filter

## 8. Boron filter

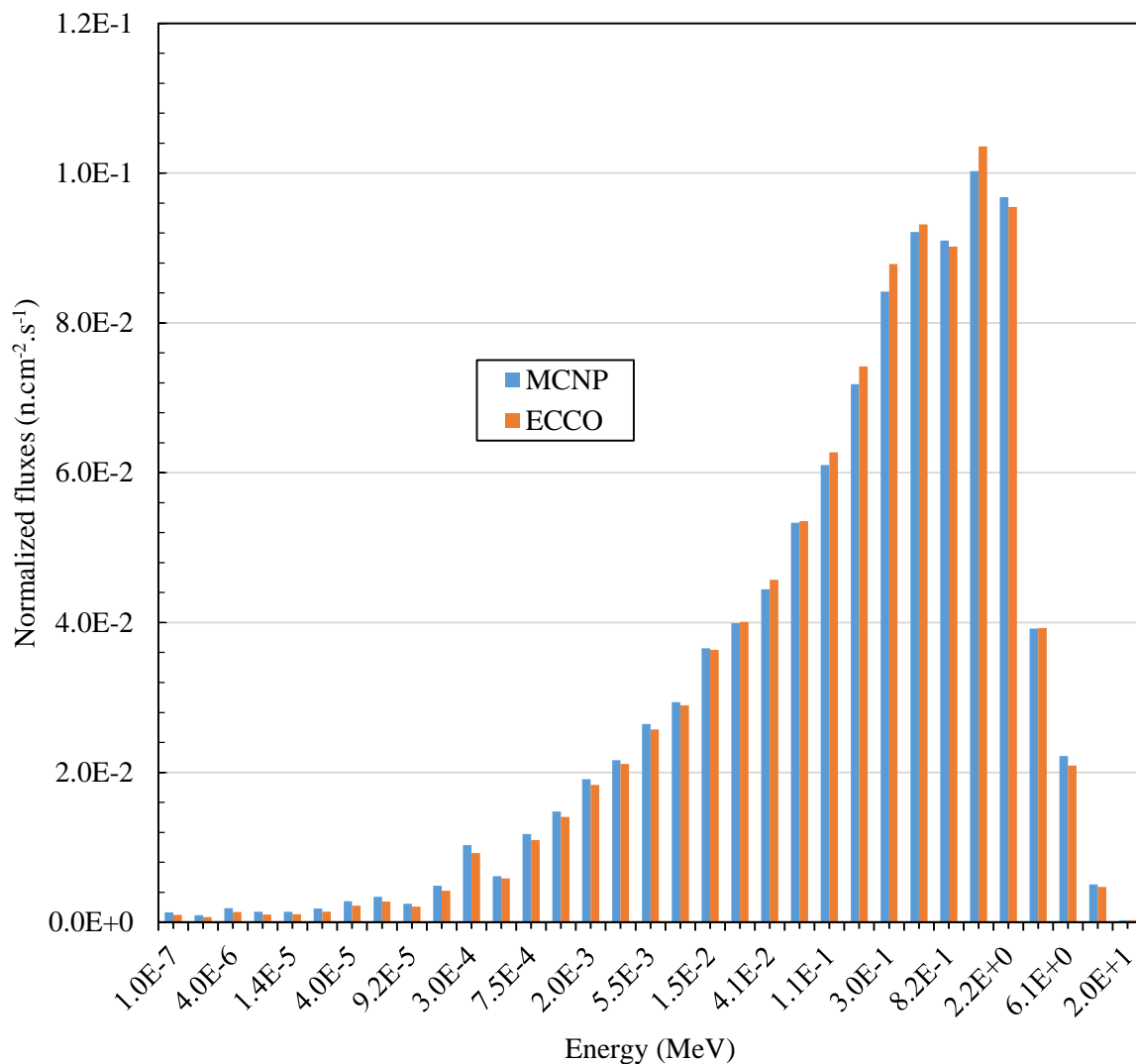


Figure 3.1.6 Normalized fluxes in the boron filter

In the lower energy groups (Figure 3.1.6), the neutron fluxes from MCNP were higher than the ones from ECCO but still very close to each other. In some of the mid-higher energy groups, the fluxes from ECCO were dominating the fluxes from MCNP. Also from Figure 3.1.5 and Figure 3.1.6, one can observe the removal of thermal and epi-thermal neutrons by the boron filter.

### 7. He after filter

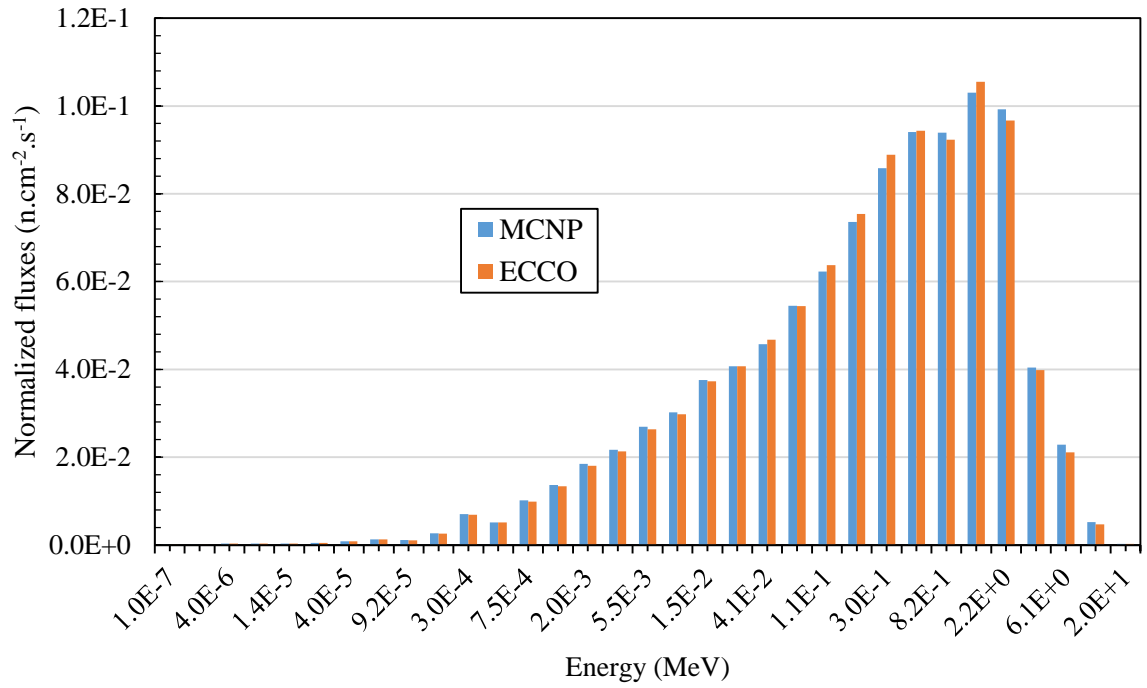


Figure 3.1.7 Normalized fluxes in the helium gap after the boron filter

### 6. Basket

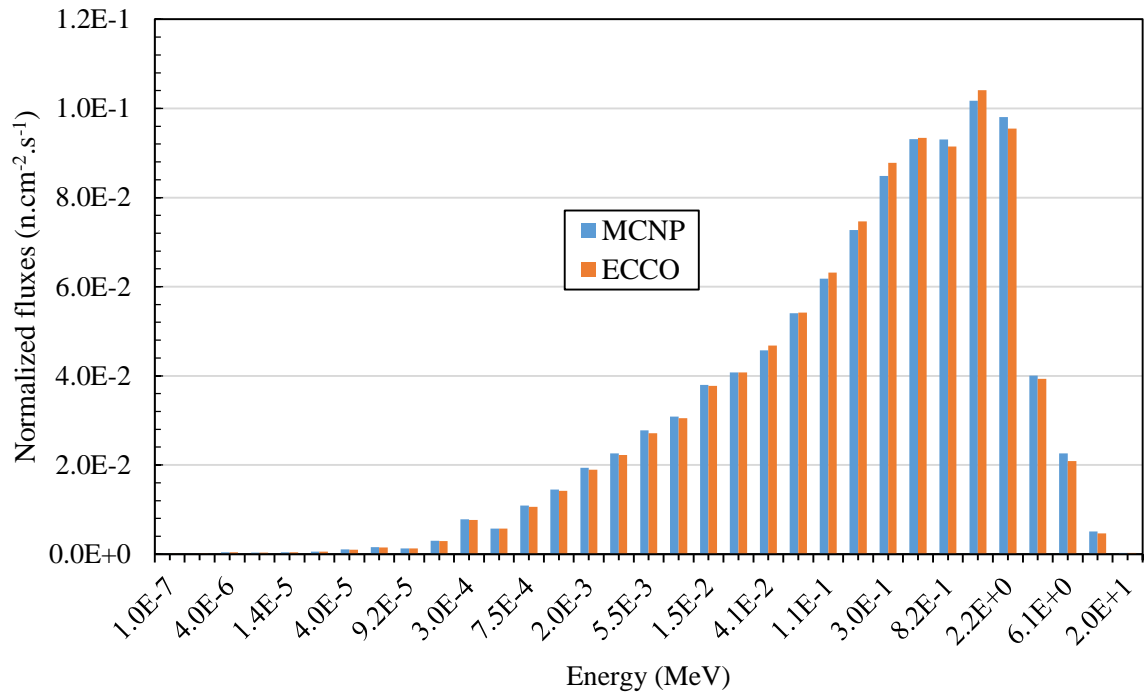


Figure 3.1.8 Normalized fluxes in the basket of the boron experiment

### 5. Water-gap

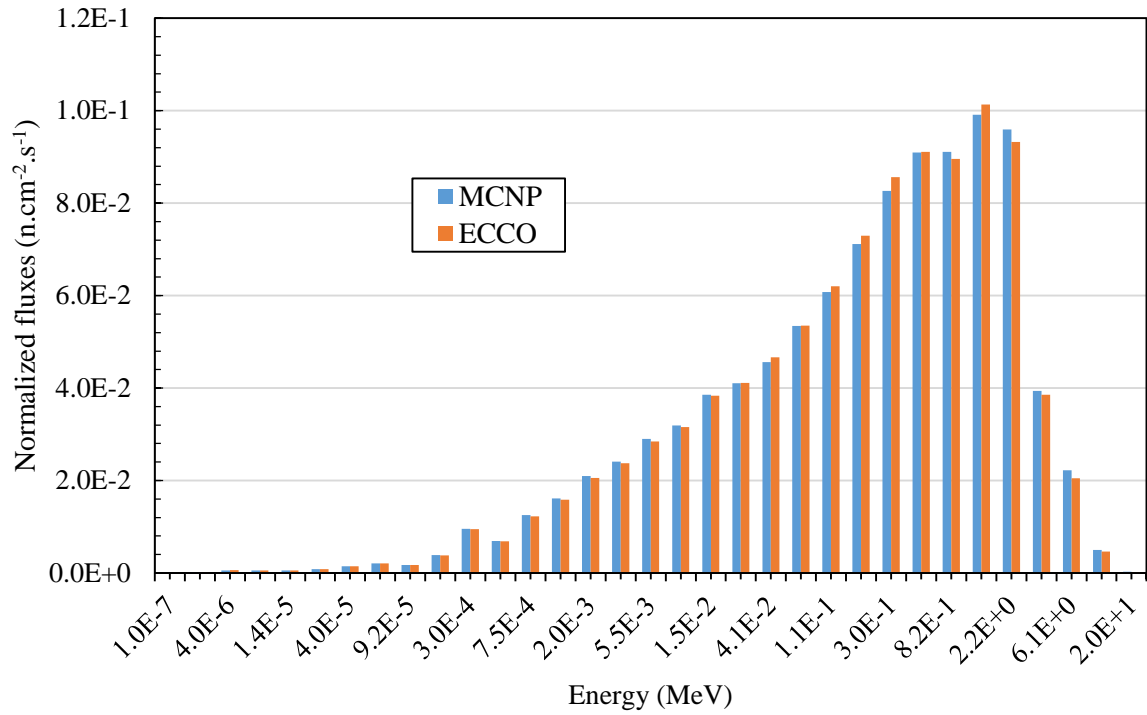


Figure 3.1.9 Normalized fluxes in the water-gap after the boron filter

### 4. Capsule

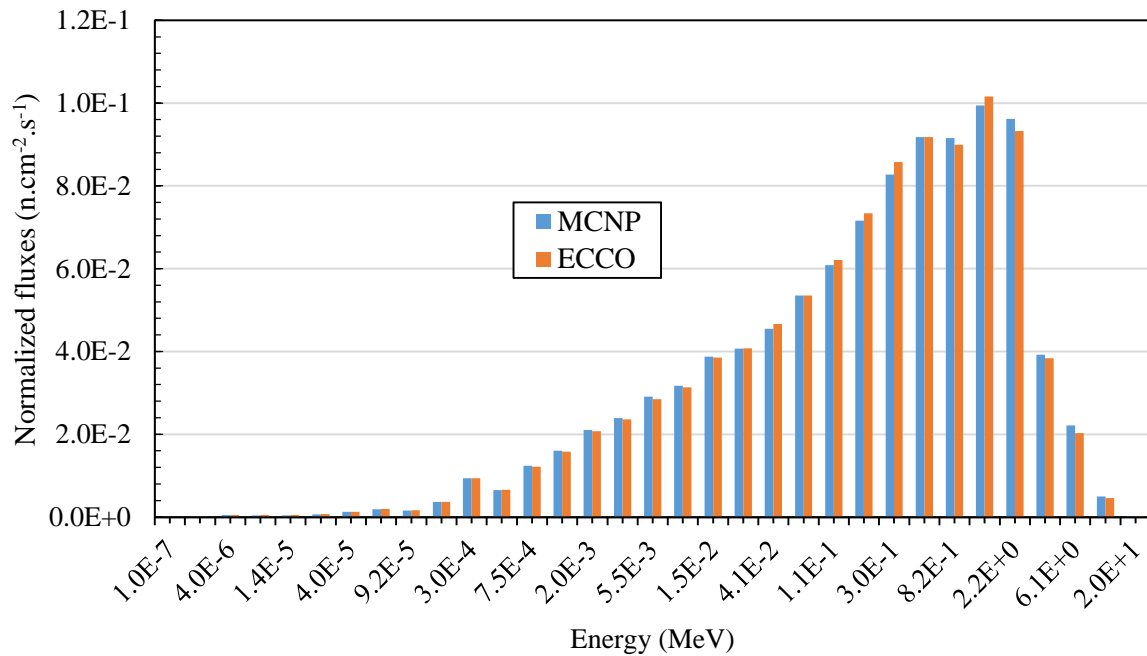


Figure 3.1.10 Normalized fluxes in the capsule wall of the boron experiment

### 3. Air-gap

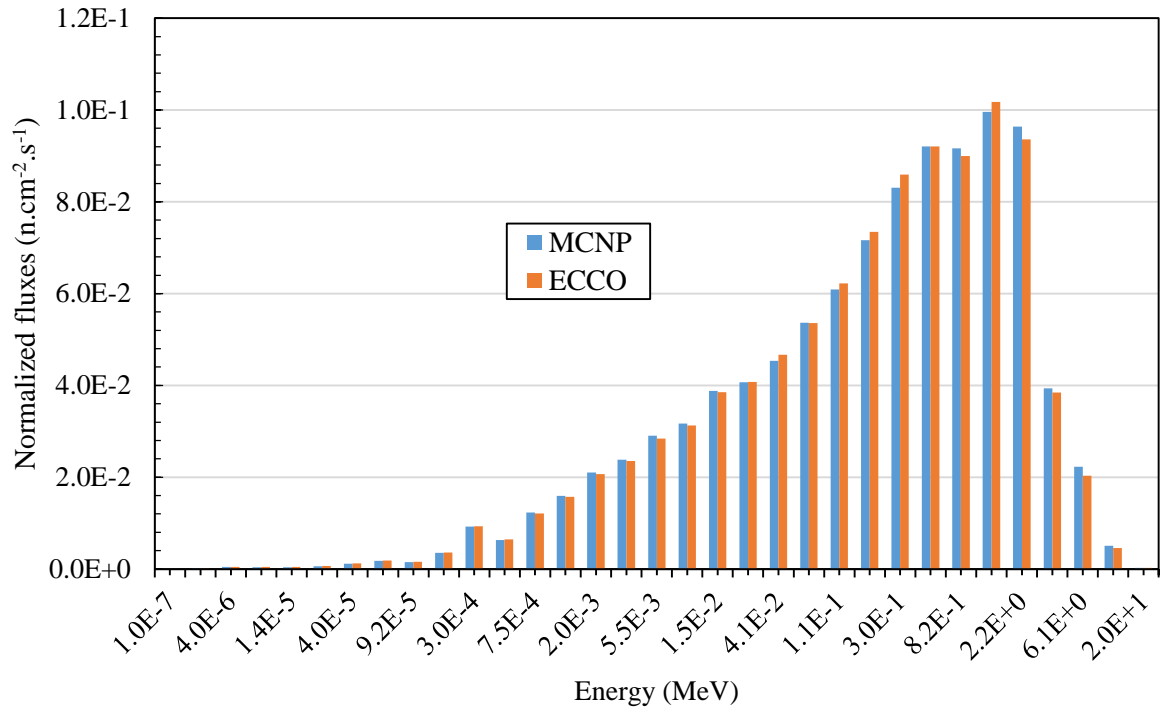


Figure 3.1.11 Normalized fluxes in the air-gap of the boron experiment

### 2. Rodlet

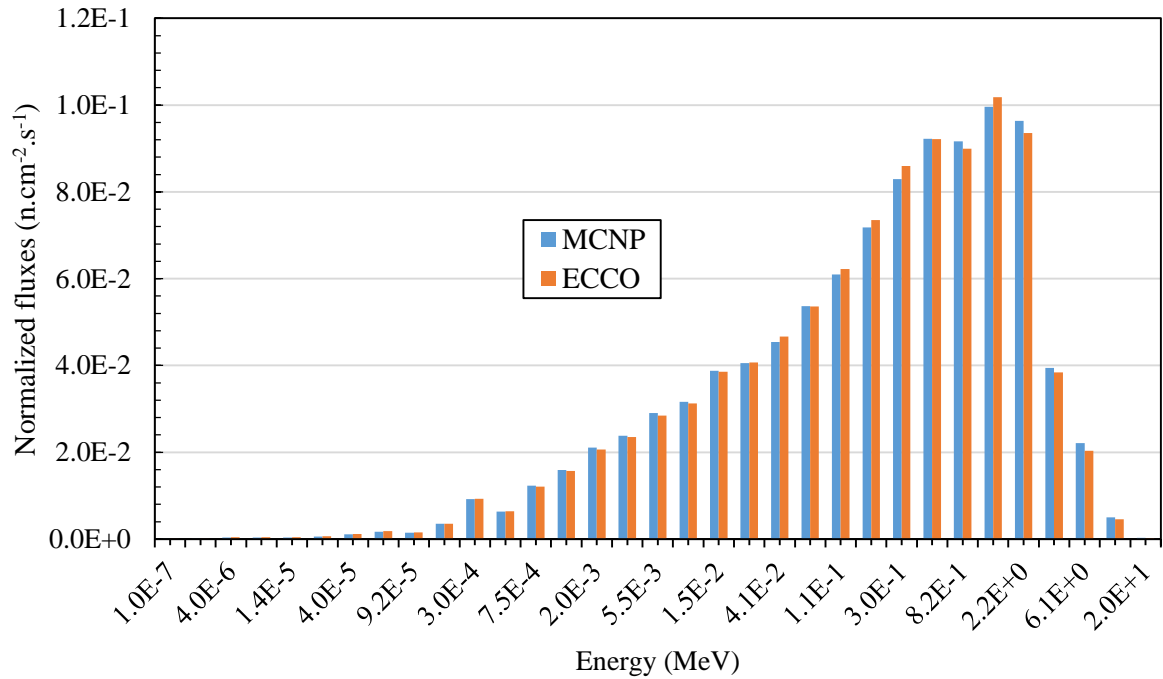


Figure 3.1.12 Normalized fluxes in the rodlet of the boron experiment

## 1. Sample location

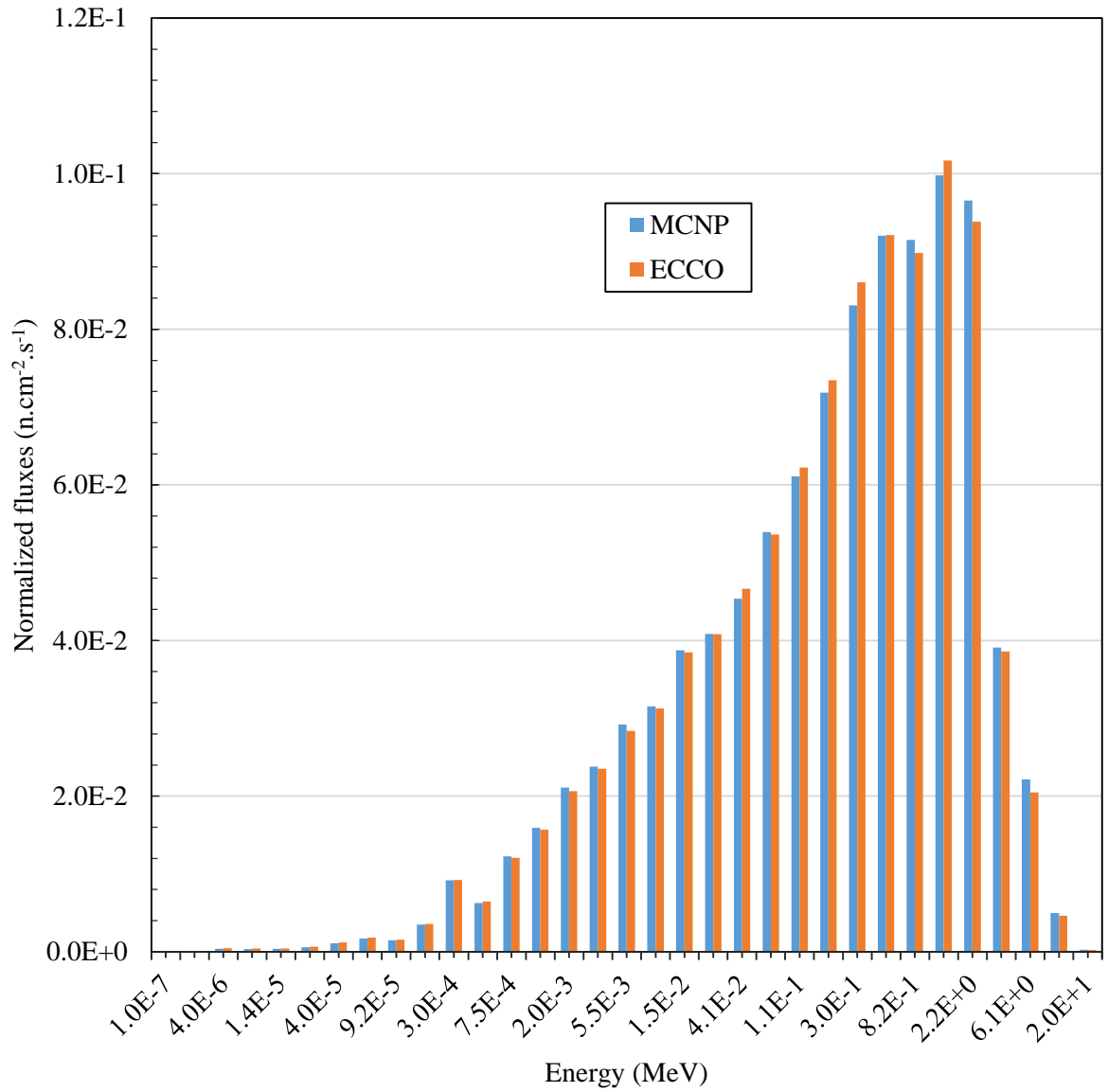


Figure 3.1.13 Normalized fluxes at the sample location of the boron experiment

The fluxes from MCNP5 and ECCO in most of the energy groups were close to each other. The propagation of neutrons from all the layers confirmed that the infinite cylindrical model of the boron experiment in ECCO generates the cross-sections very close to that of the ones from MCNP5.

The propagation of neutrons was also studied for the cadmium experiment. The layers in the cadmium experiment were different from the boron experiment (see section 1.4.2).

Propagation of neutrons only in the source and the sample locations were included here.

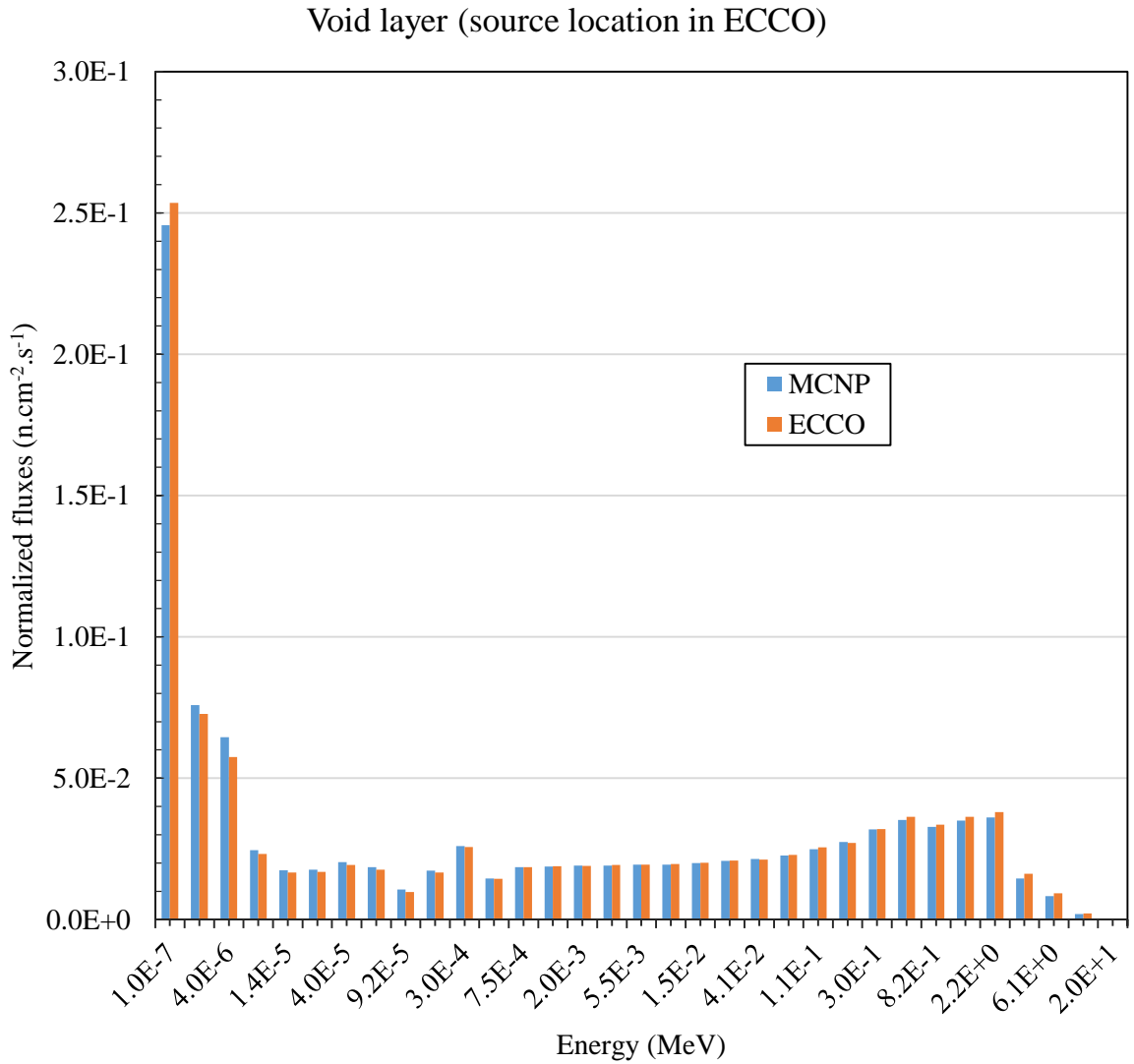


Figure 3.1.14 Normalized fluxes in the outer void layer of the cadmium experiment

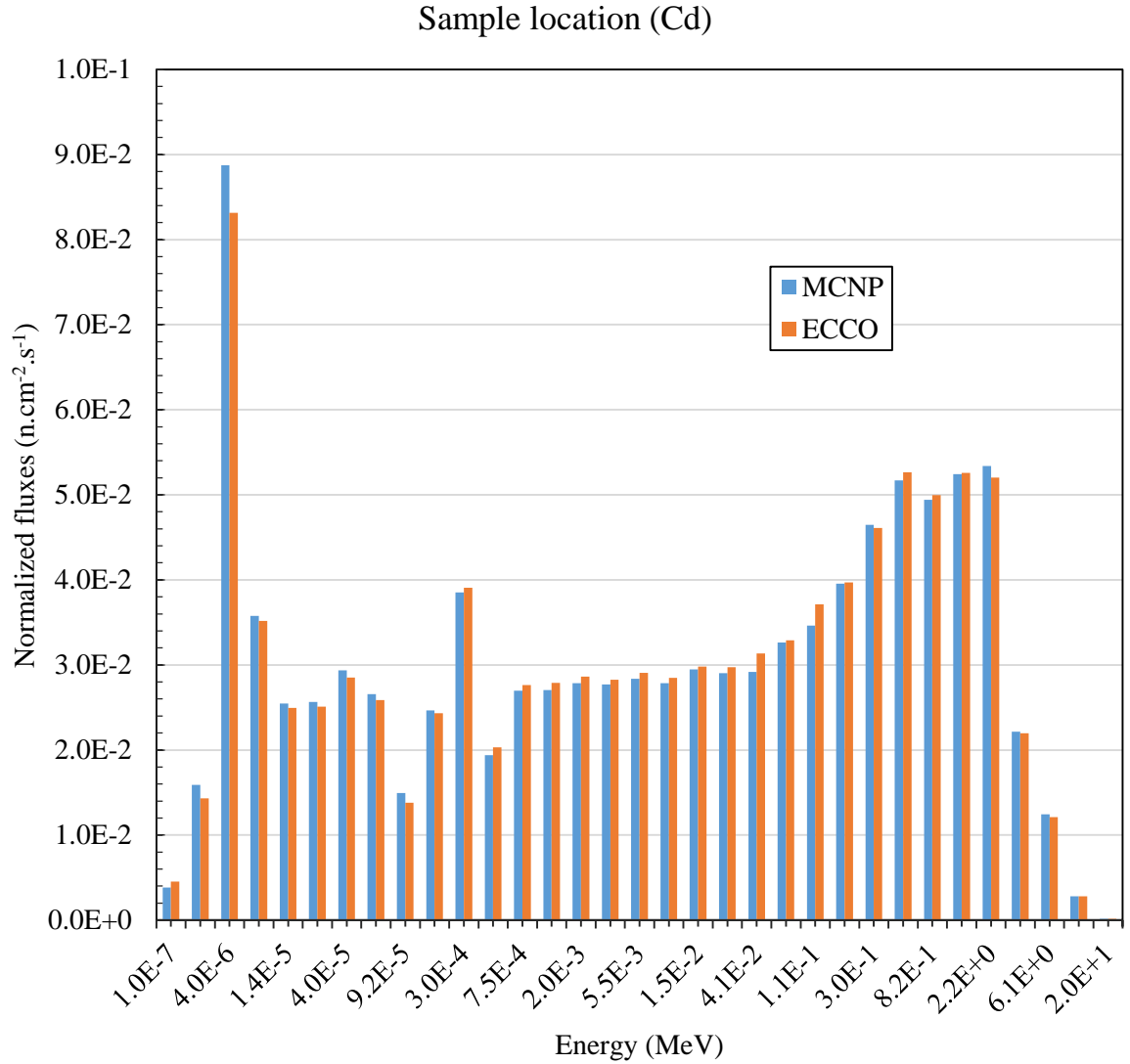


Figure 3.1.15 Normalized fluxes at the sample location of the cadmium experiment

Clearly from Figure 3.1.15, the normalized fluxes from both MCNP5 and ECCO in most of the energy groups were close to each other. At the energy group 4 eV, it was interesting to note that the flux from MCNP5 was 6% higher than the flux from ECCO. Overall, the propagation of neutrons in this experiment also confirmed that the infinite cylindrical model of the cadmium experiment in ECCO generates the effectively equivalent cross-sections as MCNP5.

### 3.2 Simple Infinite Cylindrical Models

As mentioned earlier, a simple infinite cylindrical model with reflector boundary conditions was used in ECCO. All the layers with the exact radial thicknesses were used in this model. In the first step, the external source had 172 energy groups which were expanded to a very fine energy structure of 1968 groups in the second step. Later this fine energy structure was collapsed to a 33 broad energy group structure. The cross-sections of the samples were produced in this 33 energy group structure in the output. From this output the one group cross-sections were then calculated.

Table 3.2.1 Cross-sections of the infinitely diluted samples in the boron experiment

<b>Samples</b>	<b><math>\sigma</math> (barns)</b>	<b>Samples</b>	<b><math>\sigma</math> (barns)</b>
Am241 $\sigma_f$	0.48462	Pu239 $\sigma_f$	2.67710
Am241 $\sigma_g$	3.01373	Pu239 $\sigma_g$	1.14344
Am243 $\sigma_f$	0.36496	Pu240 $\sigma_f$	0.56670
Am243 $\sigma_g$	2.71186	Pu240 $\sigma_g$	2.50647
Cm244 $\sigma_f$	0.65629	Pu242 $\sigma_f$	0.43104
Cm244 $\sigma_g$	1.47903	Pu242 $\sigma_g$	1.09857
Cm248 $\sigma_f$	0.52679	Pu244 $\sigma_f$	0.37502
Cm248 $\sigma_g$	0.71440	Pu244 $\sigma_g$	0.68249
Cs133 $\sigma_g$	1.06960	Rh103 $\sigma_g$	1.00298
Eu153 $\sigma_g$	4.98807	Sm149 $\sigma_g$	9.50685
Np237 $\sigma_f$	0.52575	Th232 $\sigma_f$	0.01812
Np237 $\sigma_g$	2.67728	Th232 $\sigma_g$	0.74094

Table 3.2.1 cont.

Samples	$\sigma$ (barns)	Samples	$\sigma$ (barns)
U233 $\sigma_f$	3.69778	U236 $\sigma_f$	0.19086
U233 $\sigma_g$	0.48828	U236 $\sigma_g$	0.89918
U235 $\sigma_f$	2.63675	U238 $\sigma_f$	0.07881
U235 $\sigma_g$	0.91659	U238 $\sigma_g$	0.86218

ECCO/MCNP (B experiment)

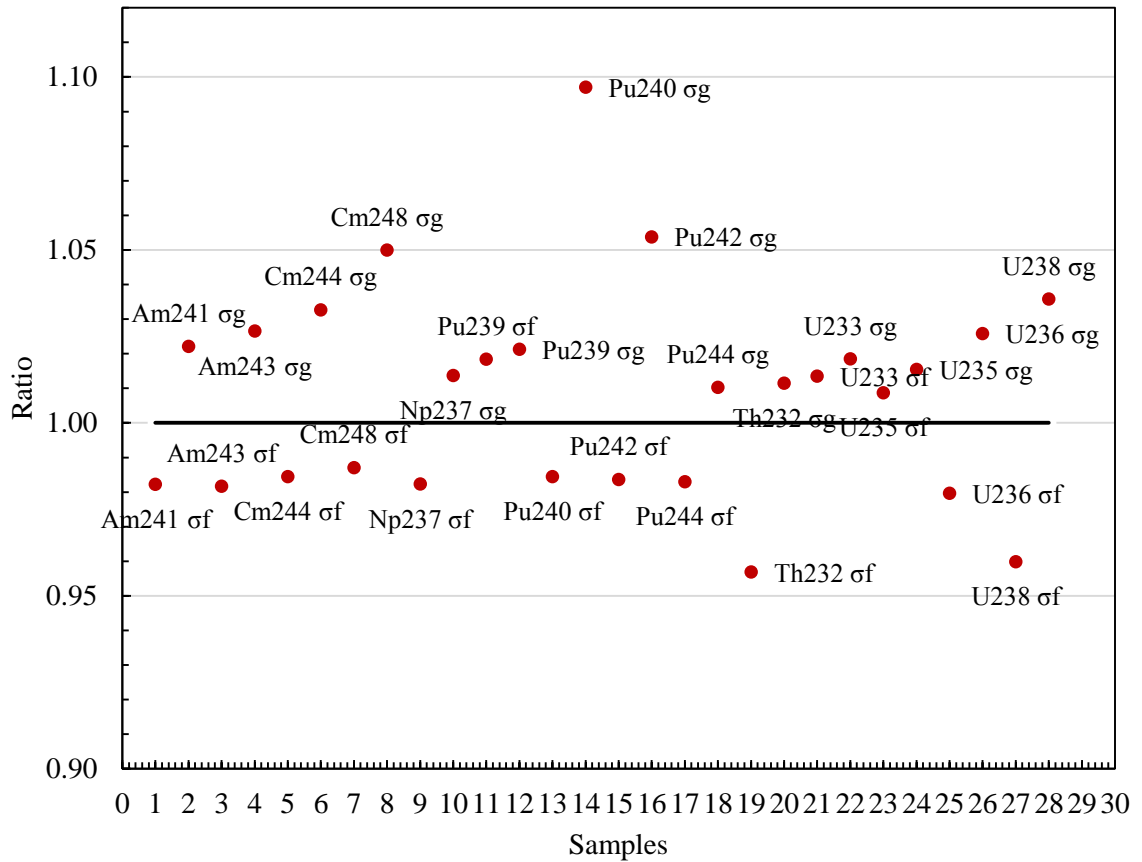


Figure 3.2.1 Ratios of the cross-sections from ECCO and MCNP (B experiment)

From Figure 3.2.1, the discrepancies in Pu-240, Pu-242 and Cm-248 (n, gamma) cross-sections between ECCO and MCNP were 9.7%, 5.4% and 5% respectively. Both Th-232

and U-238 (n, fission) cross-sections had around 4% discrepancies. All the other cross-sections were within 4% of the MCNP.

The one group cross-sections of the samples with the infinitely diluted samples in the cadmium experiment can be seen in the table below.

Table 3.2.2 Cross-sections of the infinitely diluted samples in cadmium experiment

<b>Samples</b>	<b><math>\sigma</math> (barns)</b>	<b>Samples</b>	<b><math>\sigma</math> (barns)</b>
Am241 $\sigma_f$	0.68843	Pu244 $\sigma_f$	0.20648
Am241 $\sigma_g$	68.07481	Pu244 $\sigma_g$	5.34952
Am243 $\sigma_f$	0.29600	Sm149 $\sigma_g$	613.22813
Am243 $\sigma_g$	81.67636	Th232 $\sigma_f$	0.01032
Cm244 $\sigma_f$	0.63191	Th232 $\sigma_g$	4.35876
Cm244 $\sigma_g$	32.68453	U233 $\sigma_f$	39.72993
Cm248 $\sigma_f$	0.69441	U233 $\sigma_g$	6.93378
Cm248 $\sigma_g$	12.01457	U235 $\sigma_f$	17.13378
Np237 $\sigma_f$	0.32035	U235 $\sigma_g$	7.67098
Np237 $\sigma_g$	34.03624	U236 $\sigma_f$	0.32121
Pu239 $\sigma_f$	30.06326	U236 $\sigma_g$	16.60613
Pu239 $\sigma_g$	18.13692	U238 $\sigma_f$	0.04484
Pu240 $\sigma_f$	0.42677	U238 $\sigma_g$	13.70696
Pu240 $\sigma_g$	347.51249	Eu153 $\sigma_g$	70.79852
Pu242 $\sigma_f$	0.24500	Cs133 $\sigma_g$	20.61308
Pu242 $\sigma_g$	59.21927	Rh103 $\sigma_g$	44.86485

Table 3.2.2 cont.

Samples	$\sigma$ (barns)	Samples	$\sigma$ (barns)
Ru101 $\sigma_g$	5.75793	Nd145 $\sigma_g$	12.21522
Nd143 $\sigma_g$	8.22449	Pd105 $\sigma_g$	5.00094

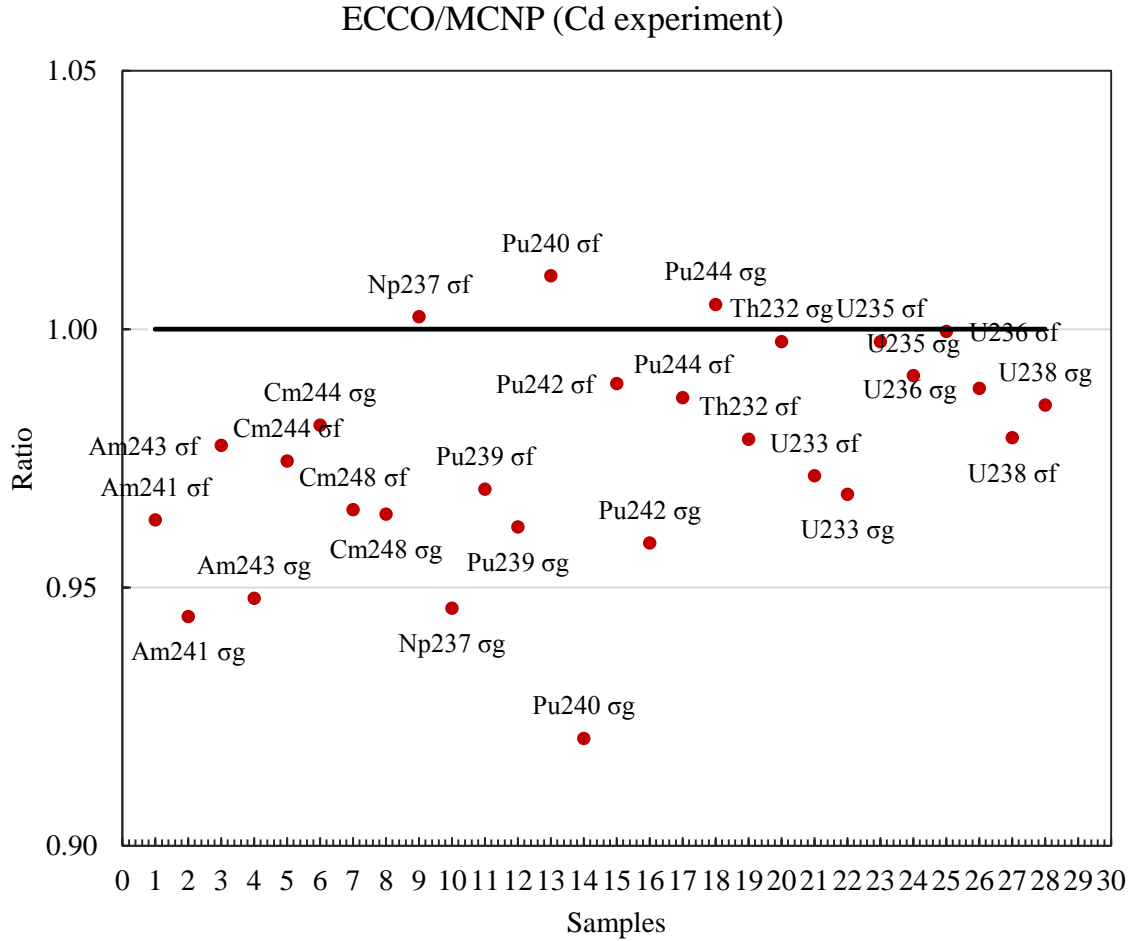


Figure 3.2.2 Ratios of the cross-sections from ECCO and MCNP (Cd experiment)

From Figure 3.2.2, the discrepancies in Am-241, Am-243, Np-237 and Pu-240 (n, gamma) cross-sections between ECCO and MCNP were 5.6%, 5.2%, 5.4% and 7.9% respectively. Pu-242 (n, gamma) had a discrepancy of 4.1%. All the other cross-sections were within 4% discrepancy.

### 3.3 Cross-section Contributions and Sensitivity Coefficients

The cross-section contributions of all the samples in the boron and cadmium experiments were calculated. These contributions were used to understand which energy groups were contributing to the overall one group cross-section. The cross-section contributions can be calculated with the equation below.

$$C_i = \frac{\sigma_i \phi_i}{\sum \phi_i} \quad [3.3.1]$$

Where,  $C_i$  = group contribution ( $i = 33$  energy groups)

$\sigma_i$  = group cross-section

$\phi_i$  = group flux

$\sum \phi_i$  = total flux

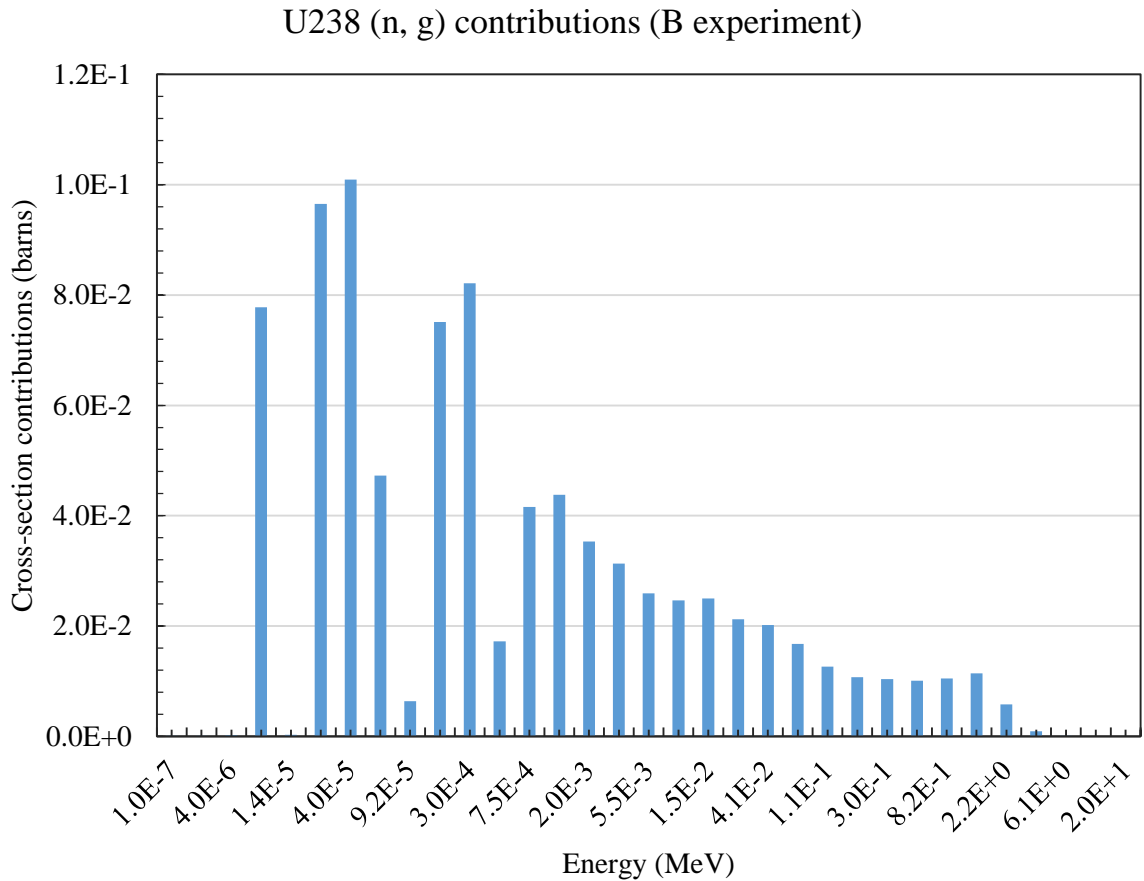


Figure 3.3.1 U238 capture cross-section contributions in the boron experiment

From Figure 3.3.1, the cross-sections from most of the energy groups were contributing to the overall one group cross-section.

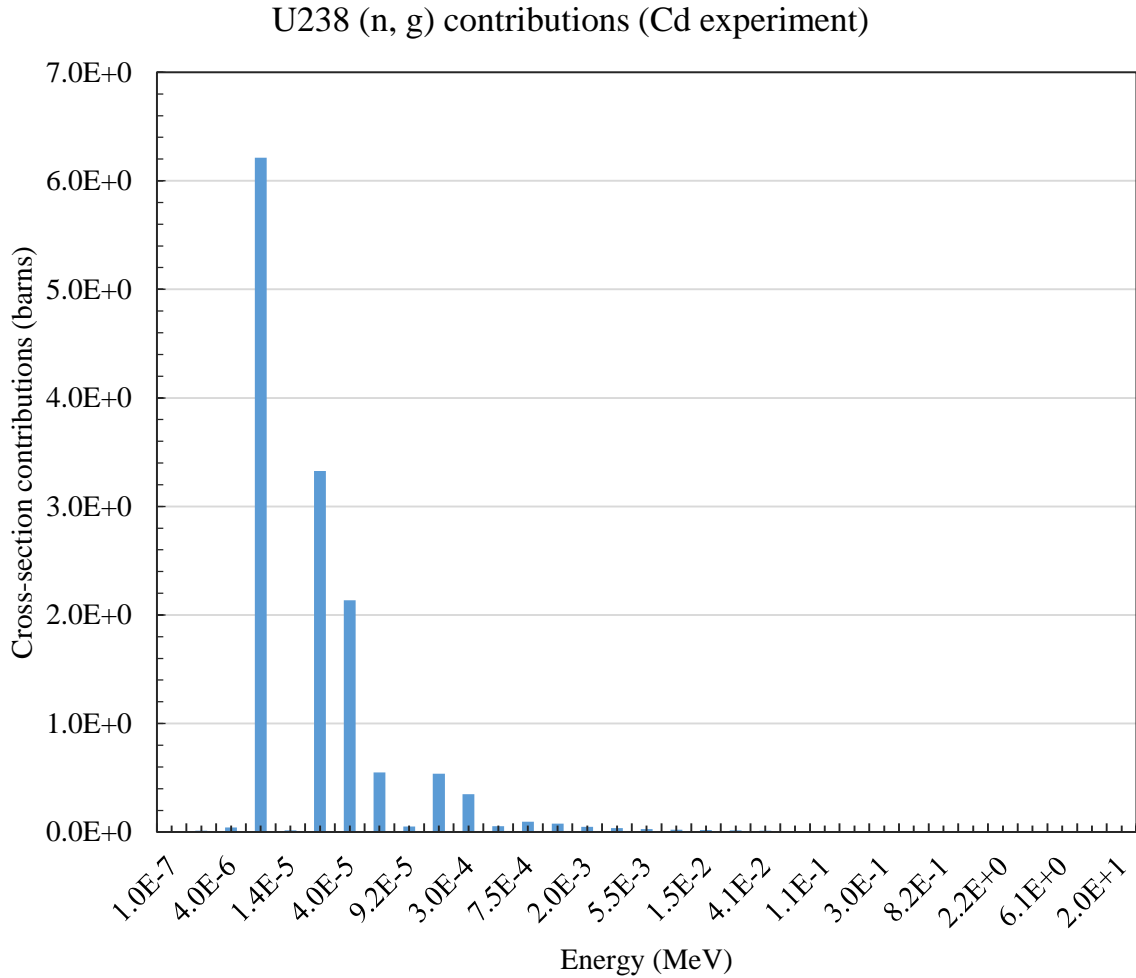


Figure 3.3.2 U238 capture cross-section contributions in the cadmium experiment

From Figure 3.3.2, the cross-sections from only three energy groups were contributing to the most of the one group cross-section. The sensitivity coefficients can be calculated using these cross-section contributions. The cross-section contributions were divided by the corresponding one group cross-section to obtain the first approximation of the sensitivity coefficients. The assumption was that the one group cross-section has sensitivity equal to one. So the sum of all the sensitivity coefficients of a cross-section will be equal to one.

The sensitivity coefficients of the capture cross-sections of all the samples in both the experiments were calculated and plotted. The sensitivity coefficients can be calculated using the equation below.

$$\sigma = \frac{\sum \sigma_i \phi_i}{\sum \phi_i} \quad [3.3.2]$$

$$S_i = \frac{C_i}{\sigma} \quad [3.3.3]$$

Where,  $\sigma$  = one group cross-section

$S_i$  = sensitivity coefficient in the energy group

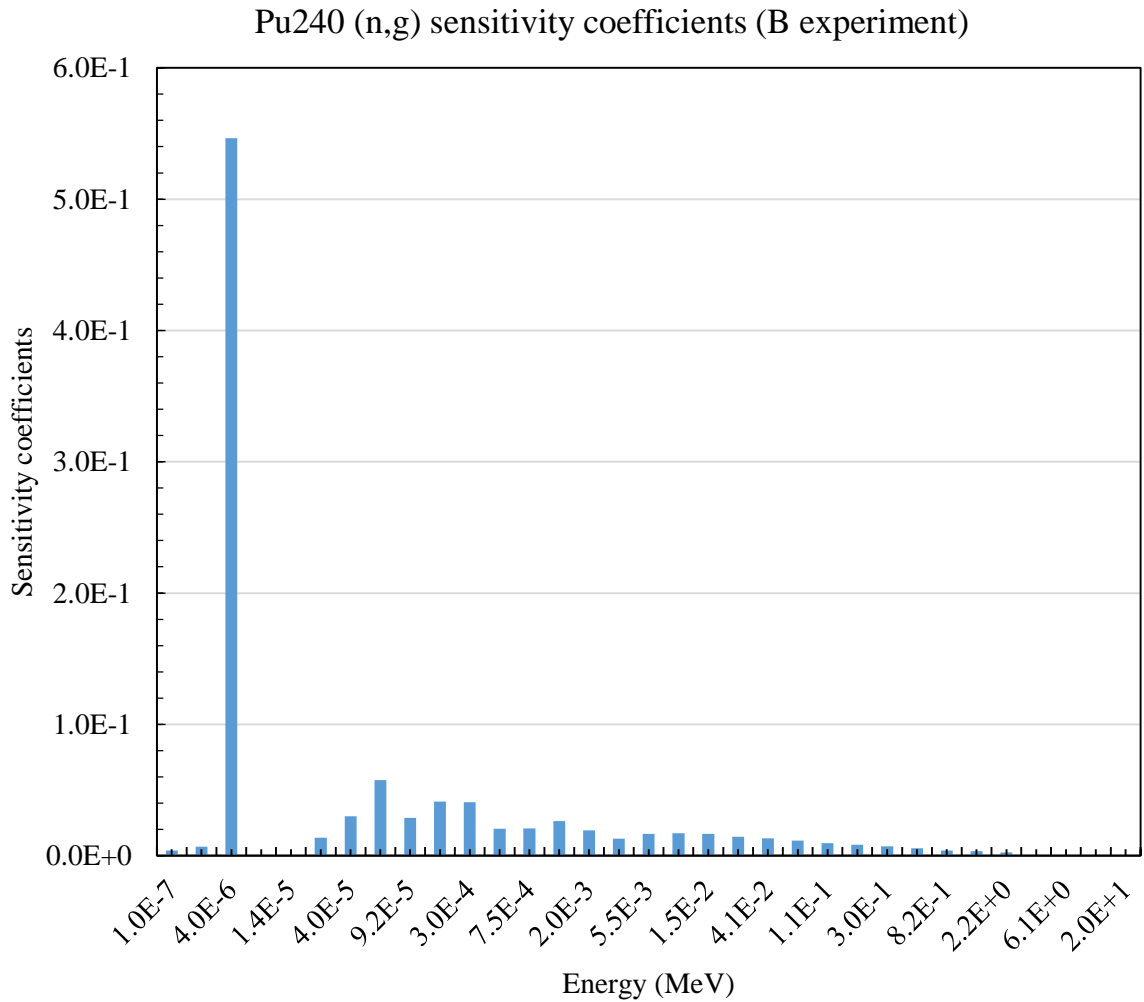


Figure 3.3.3 Sensitivity coefficients of Pu240  $\sigma_g$  (B experiment)

From Figure 3.3.3, almost 55% of the one group cross-section was coming from the energy group 4 eV. Hence, the one group capture cross-section of pu240 was sensitive to this energy group in the boron experiment.

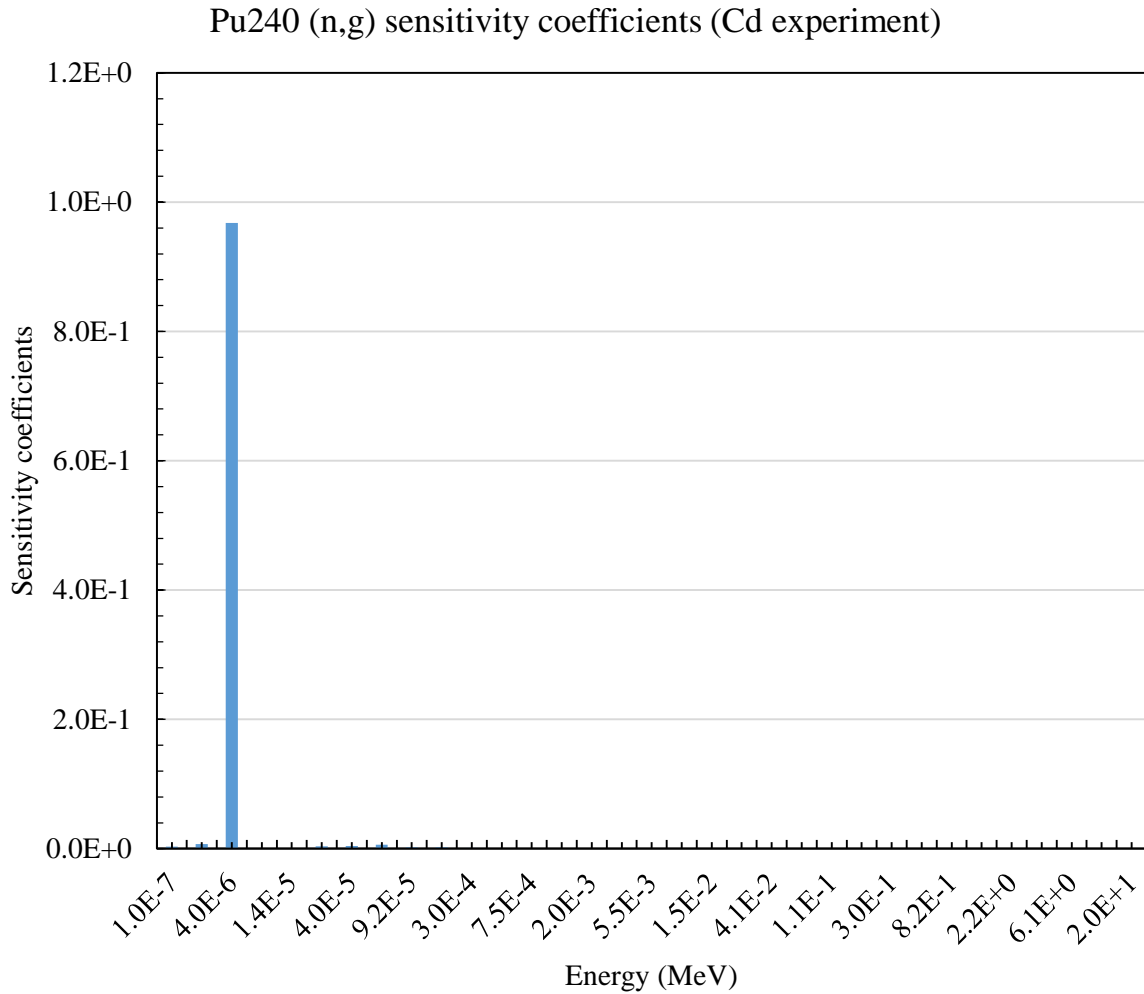


Figure 3.3.4 Sensitivity coefficients of Pu240  $\sigma_g$  (Cd experiment)

From Figure 3.3.4, more than 95% of the one group cross-section was coming from the energy group 4 eV. So the cross-section was very sensitive to this energy group in the cadmium experiment. These sensitivity coefficients were very helpful to understand how sensitive the samples were to the energy groups. The plots of the sensitivity coefficients of all the samples in both the experiments can be seen in the Appendix C.

### 3.4 Uncertainty Analysis on the Experiments

The uncertainties in the experiment setup could affect the end results. To study these effects, some layers of the boron and cadmium experiments were modified. The uncertainties in the thicknesses of the layers like the filter and the water gap after the filter were used in this analysis. Apart from this, increasing or decreasing the amount of B10 in the boron filter could also affect the end results in the boron experiment. The infinite cylindrical models of both the experiments with infinitely diluted samples were used in this study.

The layer thickness (R) was modified in steps of X% up and down (Figure 3.4.1). The one group cross-sections were calculated for all these  $\pm X\%$  uncertainties. The discrepancies in these cross-sections with respect to the ones from the actual model were then calculated. The final  $\pm X\%$  was chosen where the discrepancies in the cross-sections of all the samples were just under  $\pm 5\%$ .

$$\% \text{discrepancy} = \left( \frac{\sigma(R \pm X\%) - \sigma(R)}{\sigma(R)} \right) * 100 \quad [3.4.1]$$

Where,  $\sigma(R \pm X\%)$  = one group cross-section with additional  $\pm X\%$  uncertainty in the layer thickness

$\sigma(R)$  = actual one group cross-section

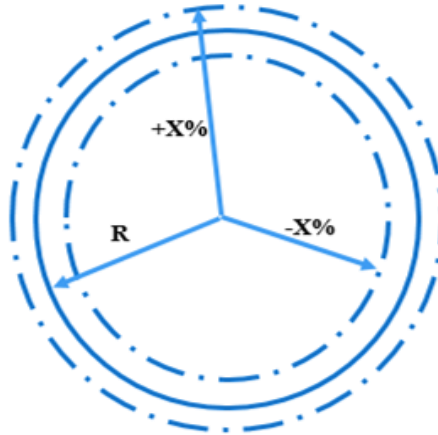


Figure 3.4.1  $\pm X\%$  uncertainty in the layer thickness (R)

The  $\pm X\%$  uncertainty in the filter thickness where the discrepancies in the cross-sections of all the samples were under  $\pm 5\%$  can be seen in the table below.

Table 3.4.1 Uncertainties in the filter thickness

	<b>Boron experiment</b>	<b>Cadmium experiment</b>
Filter thickness (cm)	0.51689	0.11430
%Uncertainty	$\pm 4\%$ ( $\pm 0.02067$ )	$+8\%, -6\%$ ( $+ 9.144E-3, - 6.858E-3$ )

From Table 3.4.1, the discrepancies in the cross-sections of all the samples would be under  $\pm 5\%$  as long as the uncertainty on the thickness of the boron filter was under  $\pm 4\%$ . This was also true for the cadmium experiment as long as the uncertainty on the thickness of the cadmium filter was under  $+8\%$  and  $-6\%$ . The one group cross-sections were more sensitive to the uncertainty on the boron thickness when compared to the cadmium thickness.

The  $\pm X\%$  uncertainty in the thickness of the water-gap after the filter (e.g. layer 5 in the boron experiment, see Figure 3.1.1) can be seen in the table below.

Table 3.4.2 Uncertainties in the water-gap thickness

	<b>Boron experiment</b>	<b>Cadmium experiment</b>
Water-gap thickness (cm)	0.11938	0.15875
%Uncertainty	$\pm 3.5\%$ ( $\pm 4.1783E-3$ )	$\pm 4.5\%$ ( $\pm 7.1437E-3$ )

The neutron absorption cross-section of the boron filter depends on the amount of B10 present in it. Therefore, the amount of B10 in the boron was modified to find the  $\pm X\%$  uncertainty where the discrepancies in the cross-sections of all the samples were under  $\pm 5\%$ .

Table 3.4.3 Uncertainties in the boron density

	<b>B10</b>	<b>B11</b>
Boron density (a/b-cm)	7.65E-02	3.27E-02
%Uncertainty	±3% (± 2.2950E-3)	∓3% (∓ 9.8100E-4)

From Table 3.4.3, as long as the uncertainty on the amount of B10 in the boron filter was under ±3%, the discrepancies in the cross-sections of all the samples would be under ±5%. To study the cumulative effects of all these uncertainties, different cases from both the experiments were used.

Table 3.4.4 Cases with filter and water-gap uncertainties in the cadmium experiment

<b>Cases</b>	<b>Filter thickness</b>	<b>Water-gap thickness</b>
1	+8%	+4.5%
2	-6%	-4.5%
3	+8%	-4.5%
4	-6%	+4.5%

All the samples except for the ones mentioned in the table below had discrepancies in the cross-sections under ±5%.

Table 3.4.5 Discrepancies greater than ±5% in the cross-sections of the samples in the cadmium experiment for the cases mentioned in Table 3.4.4

<b>Samples</b>	<b>Case 3</b>	<b>Case 4</b>
Pu239 $\sigma_f$	-7.22%	6.88%
Pu239 $\sigma_g$	-7.08%	6.74%
Sm149 $\sigma_g$	-9.07%	8.92%

Table 3.4.6 Cases with filter and water-gap uncertainties in the boron experiment

Cases	Filter thickness	Water-gap thickness
1	+4%	+3.5%
2	-4%	-3.5%
3	+4%	-3.5%
4	-4%	+3.5%

The samples with discrepancies in the cross-sections greater than  $\pm 5\%$  (solid lines in Figure 3.4.2) for the cases mentioned in Table 3.4.6 were plotted.

Discrepancies with filter and water-gap uncertainties

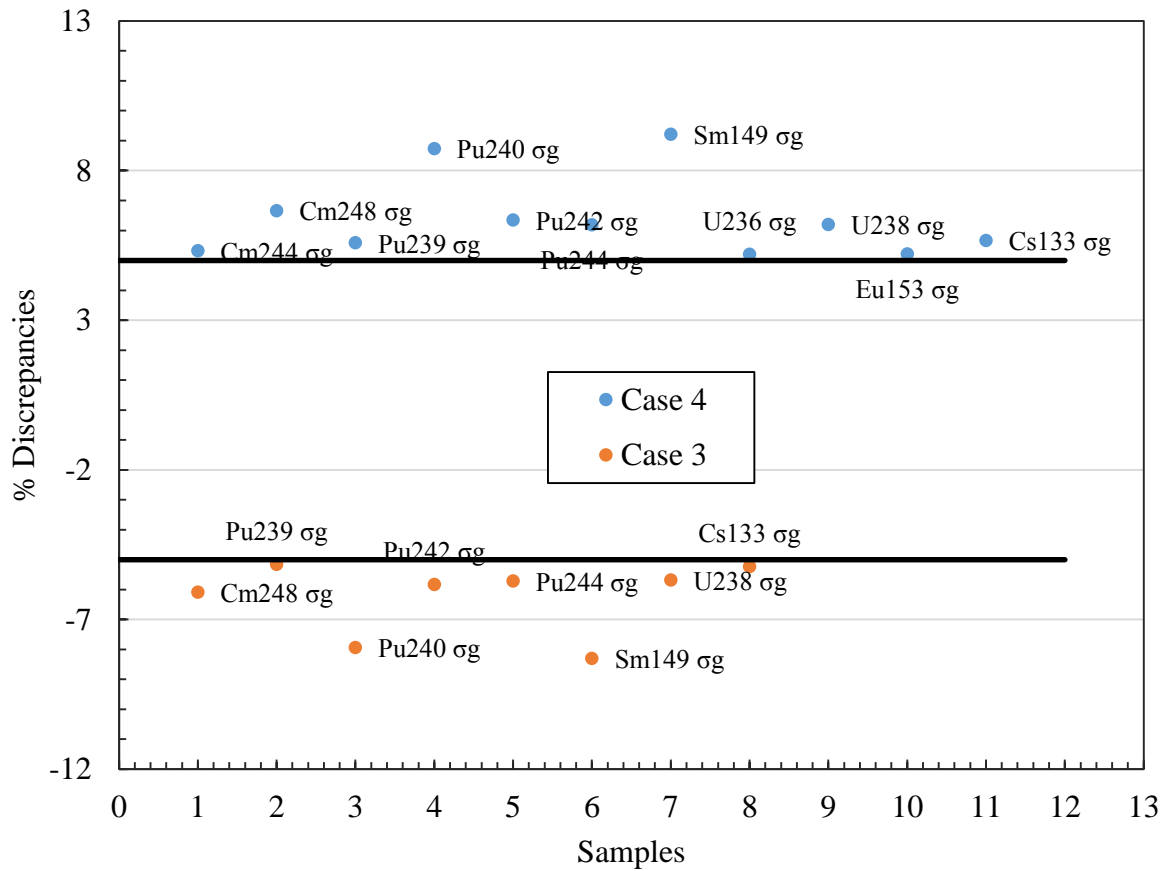


Figure 3.4.2 Discrepancies greater than  $\pm 5\%$  in the cross-sections of samples in the boron experiment for the cases mentioned in Table 3.4.6

Two extreme cases were chosen in the boron experiment to study the cumulative effects of the uncertainties in filter thickness, water-gap thickness and boron density.

Table 3.4.7 Cases for cumulative effects of all the three uncertainties in boron experiment

Cases	Filter thickness	Water thickness	Boron density (B10)
1	4%	3.5%	3%
2	-4%	-3.5%	-3%

Discrepancies with filter, water-gap and B10 uncertainties

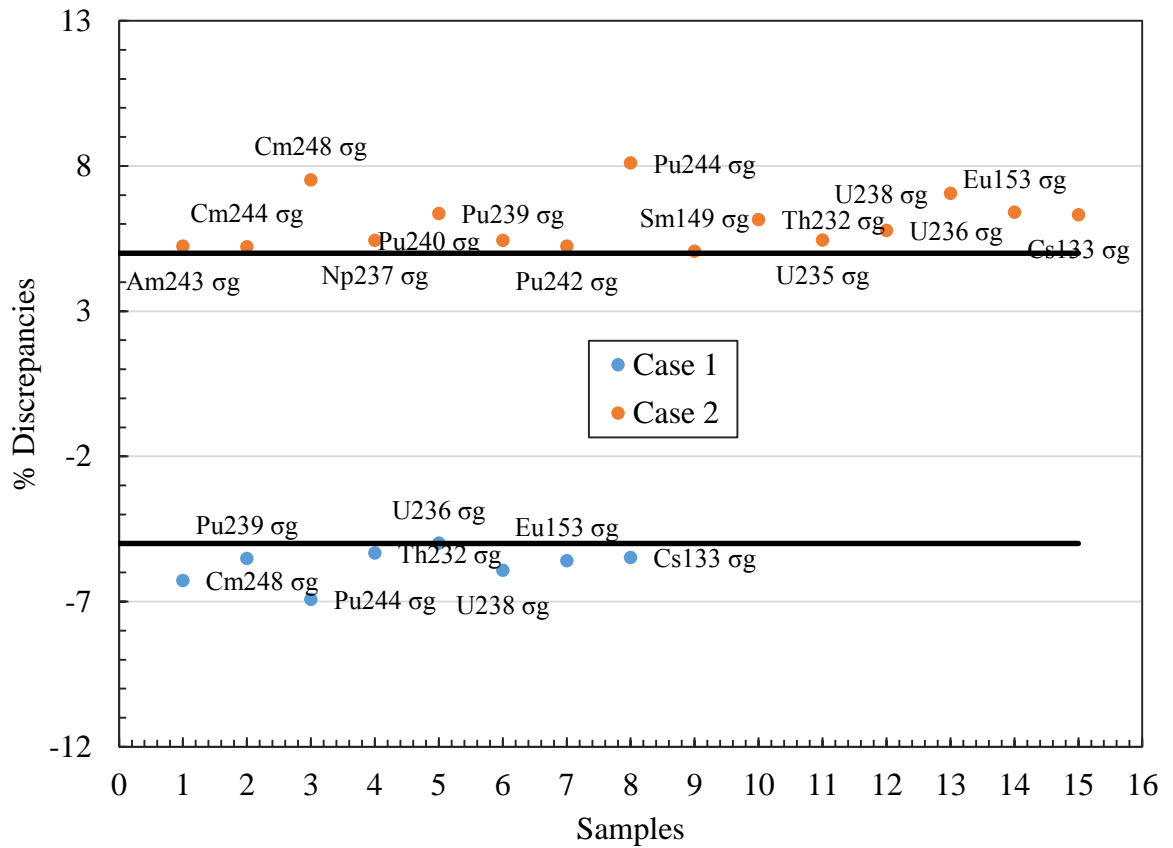


Figure 3.4.3 Discrepancies greater than  $\pm 5\%$  in the cross-sections of samples in the boron experiment for the cases mentioned in Table 3.4.7

In conclusion, the capture cross-sections of most samples were sensitive to the uncertainties in the boron experiment when compared to the uncertainties in the cadmium experiment.

## 4. SELF-SHIELDING EFFECTS

Strong resonances in the cross-sections of nuclides can deplete the neutron spectrum due to strong absorption or scattering. This depletion in the neutron spectrum occurs if there is enough sample material. Therefore, there will be dips in the neutron flux at the resonance energies reducing the neutron reaction rate (22). This is called the neutron energy self-shielding effect. Most of the actinides have these strong resonances in their cross-sections. An example of the plutonium-240 capture cross-section with resonances can be seen below.

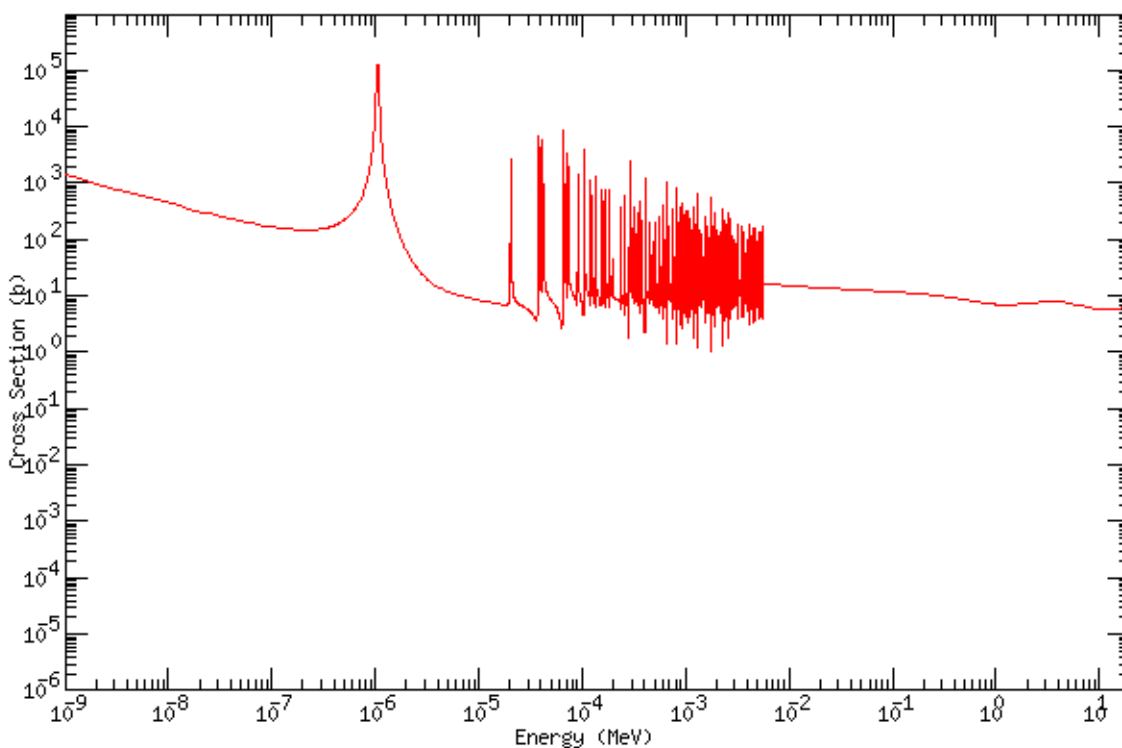


Figure 4.0.1 Neutron capture cross-section of plutonium-240

The self-shielding effects can be significant in case of the cadmium experiment because of the presence of the neutron fluxes at epi-thermal energies. For this reason, these self-shielding effects have to be taken into account for calculating the actual reaction rates of

the samples. From Figure 4.0.2, one can notice the increase in the depth of the neutron flux dip as the mass of the sample increases.

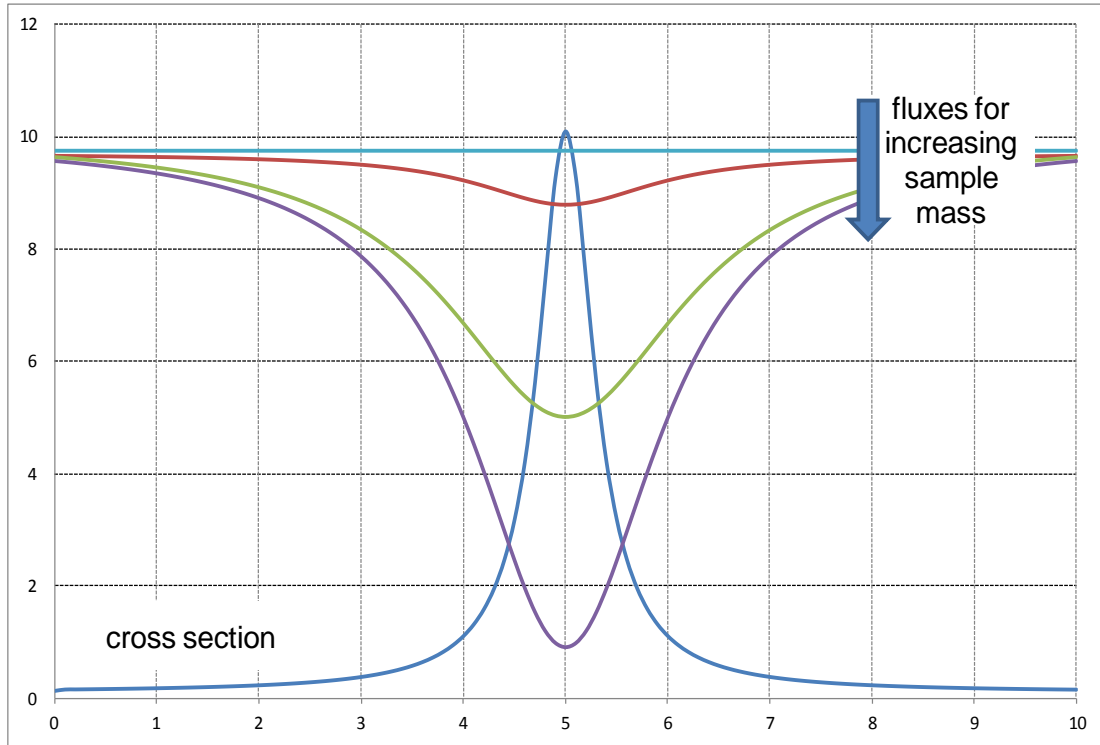


Figure 4.0.2 Illustration of neutron flux dip caused by a neutron resonance as the sample mass increases

In general, the self-shielding effects depend on the mass and the geometry of a sample. The self-shielding factor (SS) can be calculated by taking the ratio between the one group effective cross-sections in the actual sample and in the same infinitely diluted sample (23).

$$\bar{\sigma} = \frac{\int \sigma(E)\phi(E)}{\int \phi(E)} \quad [4.0.1]$$

$$\bar{\sigma}_0 = \frac{\int \sigma(E)\phi_0(E)}{\int \phi_0(E)} \quad [4.0.2]$$

$$SS = \frac{\bar{\sigma}}{\bar{\sigma}_0} \quad [4.0.3]$$

Where,  $\sigma(E)$  = microscopic cross-section of the sample (barns)

$\phi(E)$  = perturbed neutron flux within the actual sample ( $\text{n.cm}^{-2}.\text{s}^{-1}$ )

$\phi_0(E)$  = unperturbed neutron flux within the same infinitely diluted sample

$\bar{\sigma}$  = one group cross-section of the actual sample

$\bar{\sigma}_0$  = one group cross-section of the same infinitely diluted sample

Initially, the one group cross-section of an actual sample was calculated by smearing the sample inside the rodlet (green color in Figure 4.0.3). The one group cross-section of an infinitely diluted sample was calculated by taking an atom density of  $10^{-10}$ ( $\text{atoms.b}^{-1}.\text{cm}^{-1}$ ) and smearing it inside the rodlet (white color in Figure 4.0.3). In this case, there was hardly any sample material inside the rodlet to perturb or to cause any dips in the neutron flux. Thus, there were no self-shielding effects on the one group cross-sections calculated from these infinitely diluted samples. The self-shielding factors were calculated for all the samples in both the experiments except for all the flux wires.

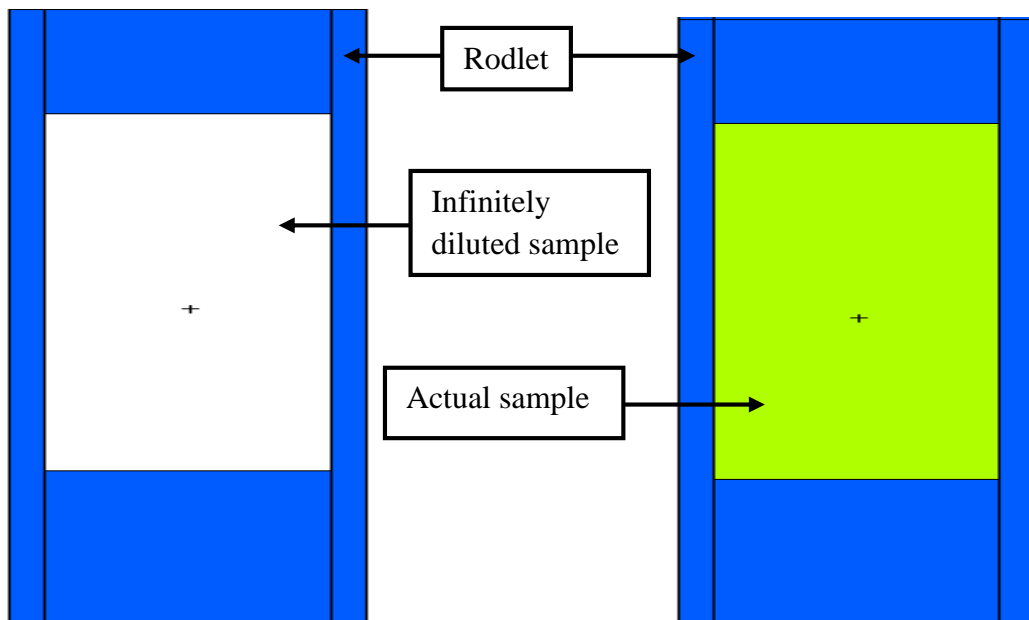


Figure 4.0.3 Infinitely diluted sample (white, left) and actual sample (green, right) inside a rodlet

#### 4.1 Infinitely Diluted vs. Actual Masses of the Samples

At first ECCO was used to study the self-shielding effects. The infinite cylindrical models of both the experiments were used to calculate the one group capture cross-sections of all the samples. In the last column, the self-shielding factors were included. Here, the actual masses were the masses measured before irradiation using the analytical balance.

Table 4.1.1 One group effective capture cross-sections of samples in boron experiment

Samples	Actual samples		Infinitely diluted samples	Discrepancies	SS
	Mass (mg)	$\bar{\sigma}$	$\bar{\sigma}_0$	%	ratio
Am241-1	1.50	2.99952	3.00622	-0.22	1.00
Am243-1	3.00	2.66924	2.70457	-1.31	0.99
Cm248-1	3.00	0.70018	0.72826	-3.86	0.96
Cs133	0.42	1.06875	1.06960	-0.08	1.00
Eu153	0.21	4.98685	4.98807	-0.02	1.00
Np237-1	1.70	2.66937	2.67260	-0.12	1.00
Np237-2	1.20	2.66990	2.67260	-0.10	1.00
Pu239	2.00	1.12955	1.13453	-0.44	1.00
Pu240	0.20	2.41240	2.50647	-3.75	0.96
Pu242-1	1.40	1.02844	1.08955	-5.61	0.94
Pu242-2	1.10	1.03987	1.08955	-4.56	0.95
Pu244-1	2.10	0.68200	0.68249	-0.07	1.00
Pu244-2	1.90	0.68204	0.68249	-0.07	1.00
Rh103	0.32	1.00046	1.00298	-0.25	1.00

Table 4.1.1 cont.

Samples	Actual samples		Infinitely diluted samples	Discrepancies	SS
	Mass (mg)	$\bar{\sigma}$	$\bar{\sigma}_0$	%	ratio
Sm149	0.40	8.67193	9.50685	-8.78	0.91
Th232	1.80	0.73567	0.74005	-0.59	0.99
U233	1.50	0.48758	0.48787	-0.06	1.00
U235	1.60	0.91601	0.91659	-0.06	1.00
U236	1.40	0.88693	0.89918	-1.36	0.99
U238	1.50	0.84710	0.86218	-1.75	0.98

From Table 4.1.1, the self-shielding was found to be most important for the two samples plutonium-242 and samarium-149 in the boron experiment.

Table 4.1.2 One group effective capture cross-sections of samples in cadmium experiment

Samples	Actual samples		Infinitely diluted samples	Discrepancies	SS
	Mass (mg)	$\bar{\sigma}$	$\bar{\sigma}_0$	%	ratio
Am241-1	1.50	67.23852	68.07481	-1.23	0.99
Am243-1	3.00	75.06878	81.67636	-8.09	0.92
Cm244-1	0.50	31.54164	32.68453	-3.50	0.97
Cm248-1	3.00	11.30183	12.01457	-5.93	0.94
Cs133	0.32	20.52610	20.61308	-0.42	1.00
Eu153	0.16	70.70391	70.79852	-0.13	1.00
Nd143	0.10	8.22465	8.22449	0.00	1.00

Table 4.1.2 cont.

Samples	Actual samples		Infinitely diluted samples	Discrepancies	SS
	Mass (mg)	$\bar{\sigma}$	$\bar{\sigma}_0$	%	ratio
Nd145	0.46	12.19416	12.21522	-0.17	1.00
Np237-1	0.70	33.94901	34.03624	-0.26	1.00
Np237-2	0.50	33.97360	34.03624	-0.18	1.00
Pd105	0.46	4.99987	5.00094	-0.02	1.00
Pu239	2.00	17.80447	18.13692	-1.83	0.98
Pu240	0.20	327.14036	347.51249	-5.86	0.94
Pu242-1	1.70	50.49910	59.21927	-14.73	0.85
Pu242-2	2.00	49.28341	59.21927	-16.78	0.83
Pu244-1	0.50	5.34807	5.34952	-0.03	1.00
Rh103	0.32	44.45120	44.86485	-0.92	0.99
Ru101	0.10	5.75742	5.75793	-0.01	1.00
Sm149	0.05	598.29676	613.22813	-2.43	0.98
Th232	1.70	4.30595	4.35876	-1.21	0.99
U233	1.90	6.89936	6.93378	-0.50	1.00
U235	1.50	7.65482	7.67098	-0.21	1.00
U236	1.50	15.80100	16.60613	-4.85	0.95
U238	1.80	13.18787	13.70696	-3.79	0.96

From Table 4.1.2, the samples Am-243, Cm-248, Pu-240 and Pu-242 exhibited the largest self-shielding effects in the cadmium experiment. Cadmium is used to suppress the thermal responses of the samples. As a result, the primary response of any sample inside the

cadmium filter is in the region of a resonance (15). Strong resonances deplete the neutron spectrum at the resonance energy due to absorption and scattering, therefore causing dip in the neutron spectrum (Figure 4.0.2) (22). This is the reason why the self-shielding effects are significant in the cadmium experiment. However, the resonance structure varies for each sample. Thus, the self-shielding also varies for each sample. As an illustration, the (n, gamma) cross-sections with resonances of Cd-113 (filter, red), Pu-242 (largest self-shielding, see Table 4.1.2, green) and U-235 (no self-shielding, see Table 4.1.2, blue) were included.

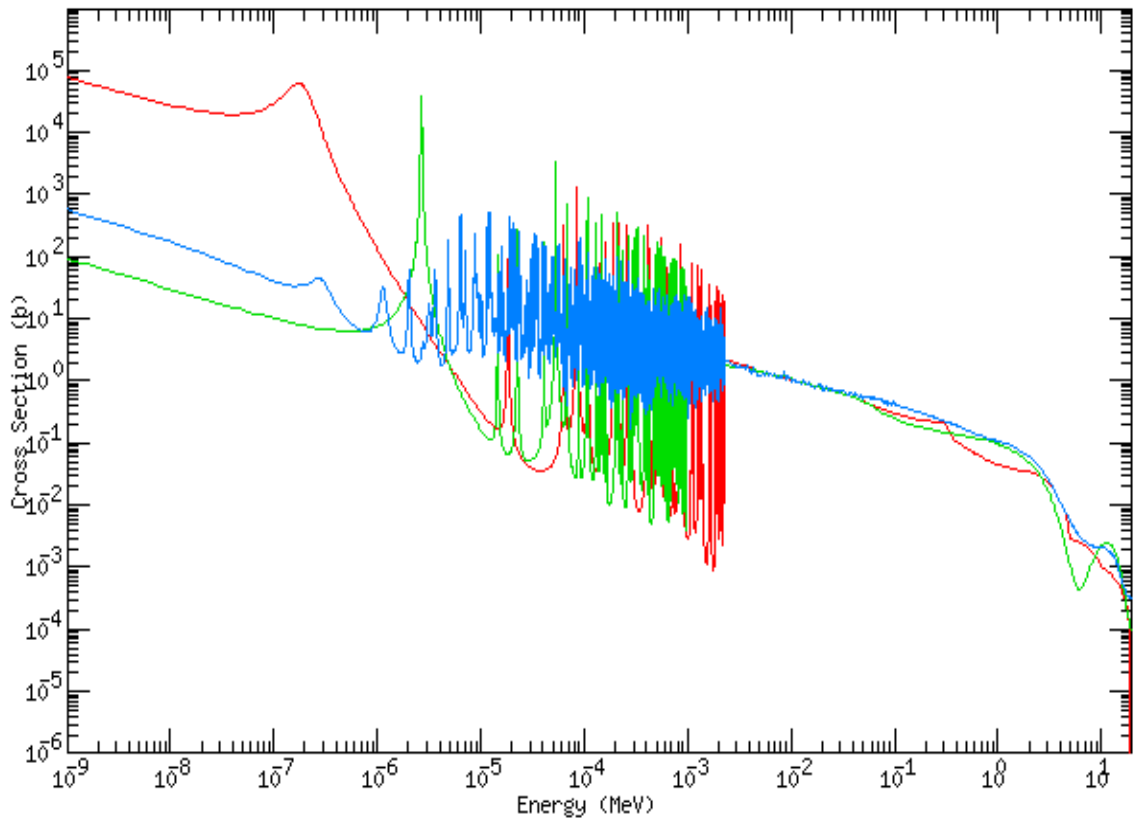


Figure 4.1.1 (n, gamma) cross-sections of Cd-113 (red), Pu-242 (green) and U-235 (blue)  
 From Figure 4.1.1, after the 0.5 eV cadmium cut-off, one can observe the strong resonances in the capture cross-section of Pu-242. Whereas, the resonances in the capture cross-section of U-235 are relatively low.

## 4.2 Sample Wafers

The self-shielding effects also depend on the geometry of the samples. These effects should be taken into account, whenever the sample size cannot be made small enough (22). The exact geometry of the sample inside the vial was not known, since the sample was in the powder form. A rough estimation of 1 to 2 mm on the heights of the samples was given. However, it was important to do parametric analysis on these heights to find the actual heights and the self-shielding effects of the samples. Considering the height, the shape of the sample was more like a wafer. The radius of the vial was taken as the radius of the samples. Therefore, the self-shielding as a function of the height of a sample was calculated. The sample wafers were designed inside the rodlets.

In Figure 4.2.1,  $H$  = height of the wafer  
 $R$  = radius of the wafer (1.25 mm)

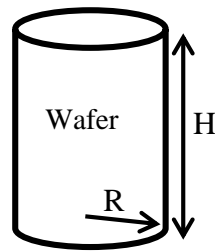


Figure 4.2.1 Wafer

A sample wafer with different heights inside a rodlet can be seen in the figure below.

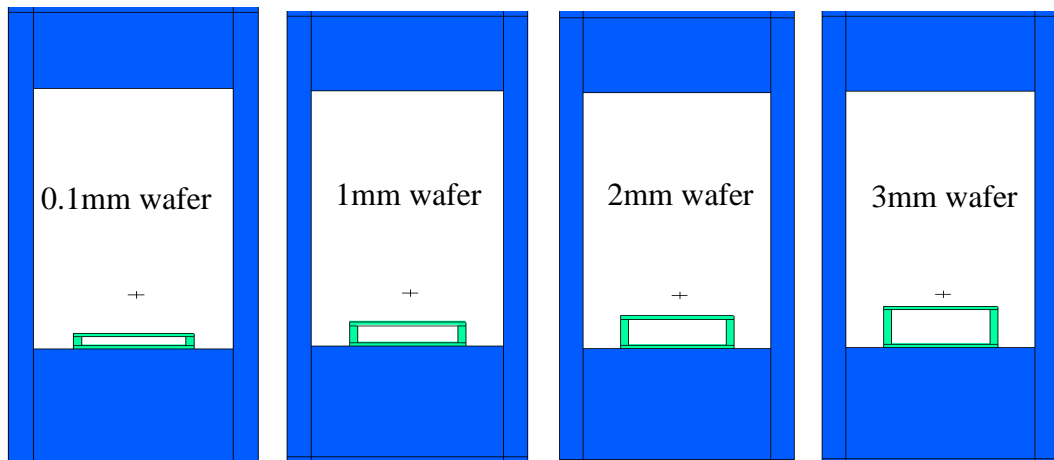


Figure 4.2.2 A sample wafer with different heights inside a rodlet

The wafer heights used in the parametric analysis were 0.1 mm, 0.5 mm, 1 mm, 2 mm and 3 mm. The densities of the oxide samples were 3 to 4 times higher than the densities of the nitrate samples. To accommodate these oxide samples the smallest height 0.1 mm was used. MCNP5 was used to calculate the one group capture cross-sections of all the sample wafers. The number of atoms of all these samples was kept constant. That is the masses of all the samples were kept constant in all the wafers. Only their densities were changed according to their wafer heights.

As mentioned earlier, the given uncertainty on the actual masses (pre-irradiated masses) of all the samples measured before irradiation was  $\pm 30\%$ . The capture cross-sections of all the samples with pre-irradiated masses at different wafer heights were plotted.

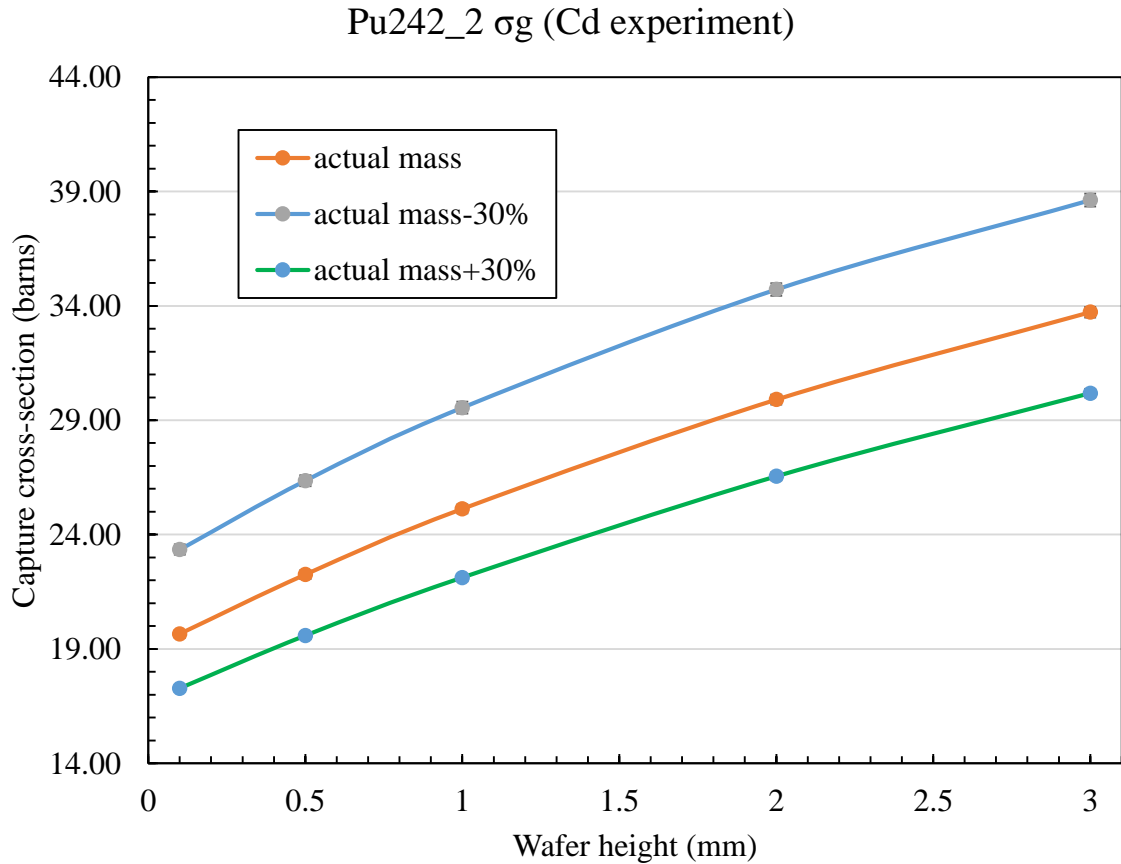


Figure 4.2.3 Capture cross-section of Pu242\_2 in Cd experiment

In Figure 4.2.3, the cross-section plots with +30% and -30% were the uncertainties on the actual mass of the sample. There was almost 72% discrepancy in the capture cross-section of Pu-242 wafers between the heights 0.1 mm and 3 mm in the cadmium experiment.

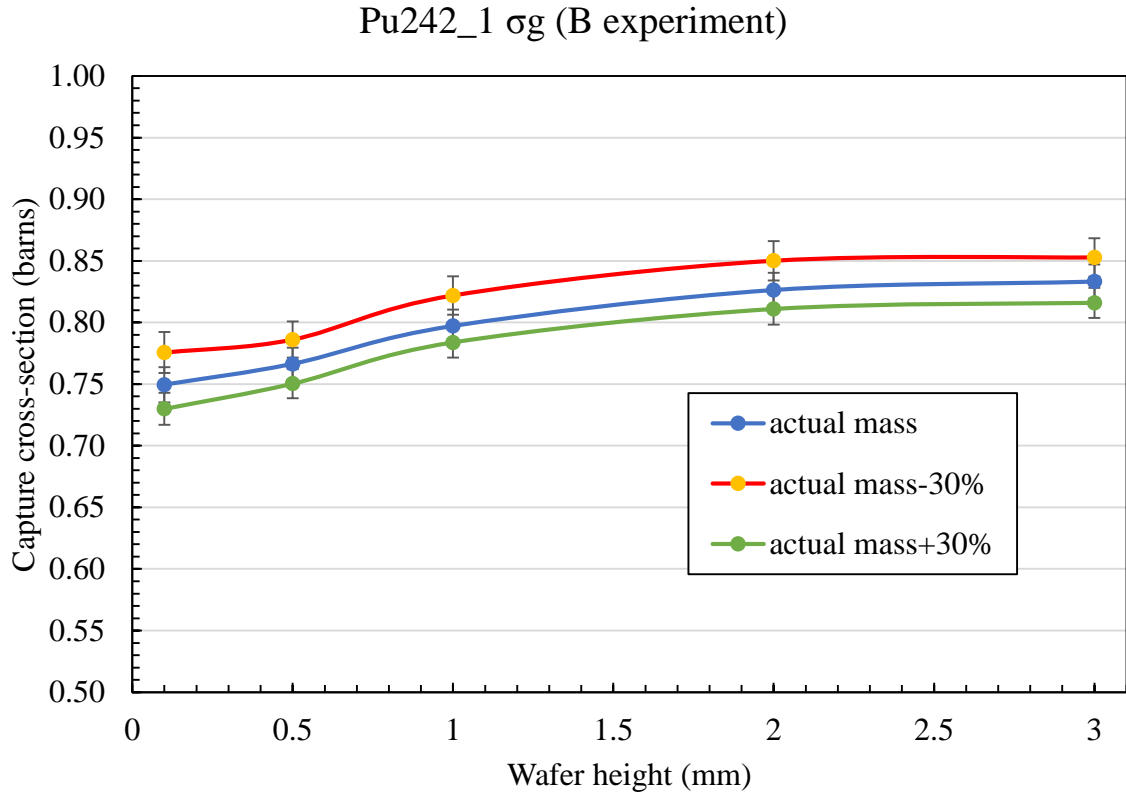


Figure 4.2.4 Capture cross-section of Pu242\_1 in B experiment

There was 11% discrepancy in the capture cross-section of Pu-242 wafers between the heights 0.1 mm and 3 mm in the boron experiment. These cross-section plots of all the samples for both the experiments were included in the Appendix D. When these cross-sections were divided by the infinitely diluted cross-sections, one can obtain the self-shielding factors as a function of height of the sample. If the self-shielding factors are close to one, then the self-shielding effects are negligible. Example plots of the self-shielding factors as a function of sample height can be seen in the Figure 4.2.5 and Figure 4.2.6.

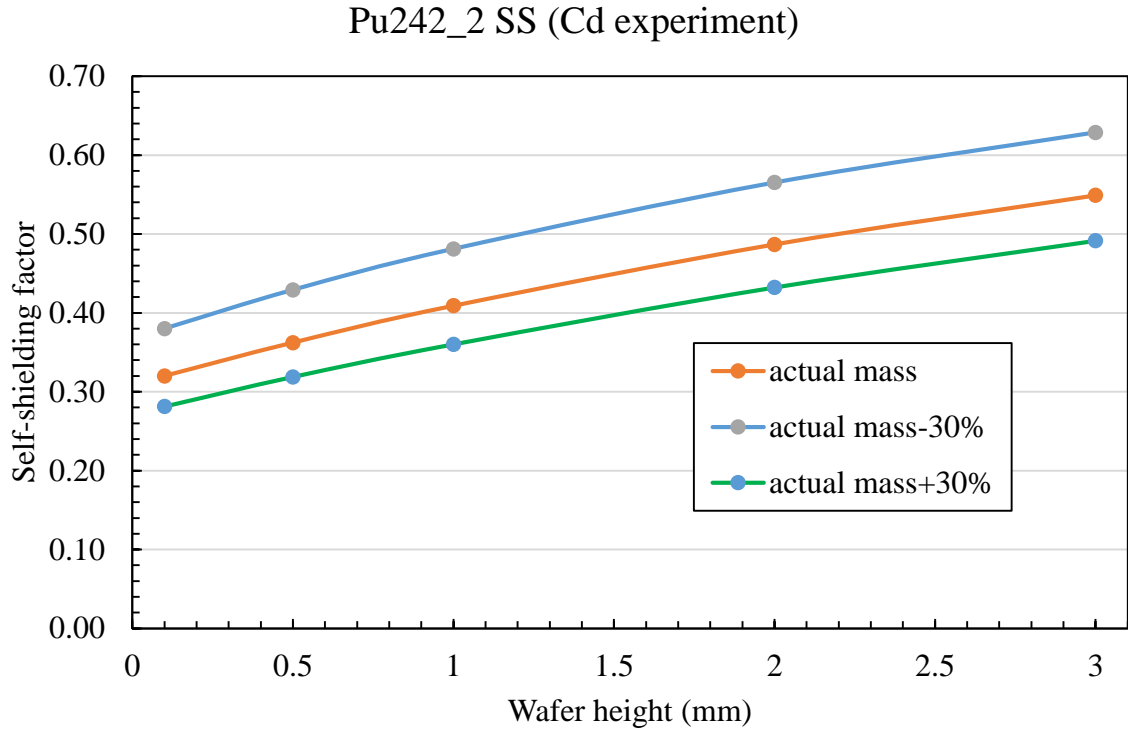


Figure 4.2.5 Self-shielding factor as a function of height in Pu242\_2 (Cd experiment)

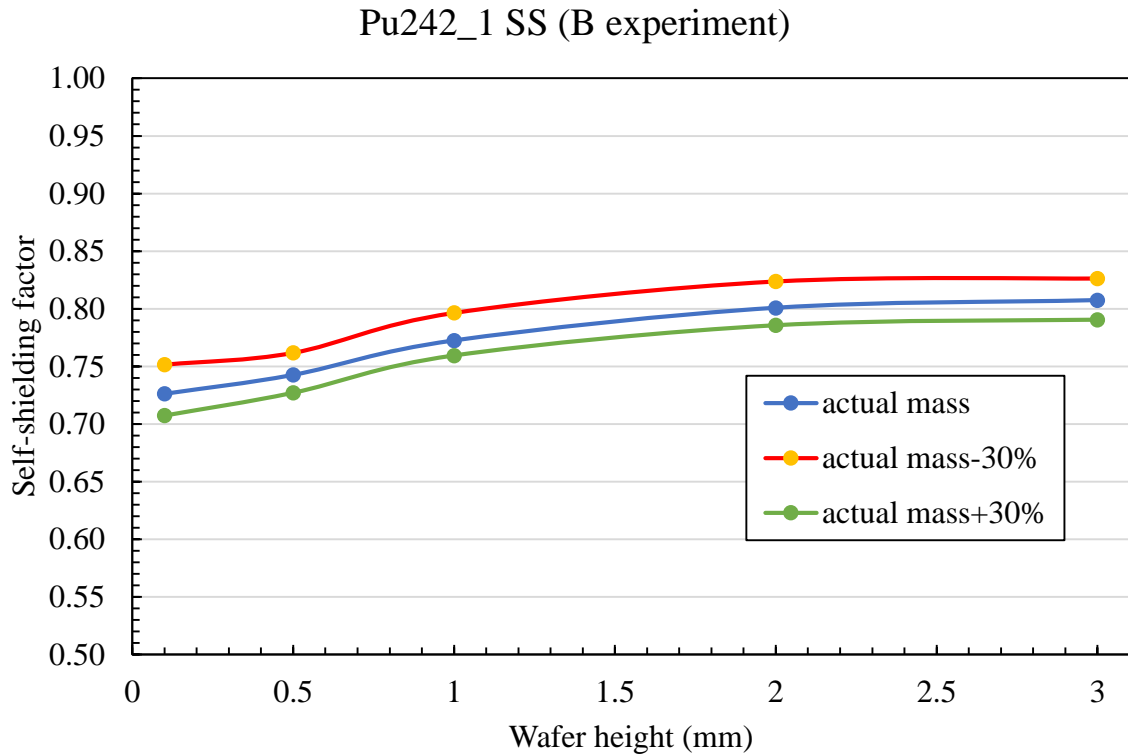


Figure 4.2.6 Self-shielding factor as a function of height in Pu242\_1 (B experiment)

The one group capture cross-sections with absolute errors (abs err) of all the samples with actual masses at different wafer heights can be seen in the tables below.

Table 4.2.1 One group effective capture cross-sections of samples in boron experiment

Wafer height	0.1mm	0.5mm	1mm	2mm	3mm
<b>Samples</b>	<b>Capture cross-sections (barns)</b>				
Am241-1	2.89506	2.90854	2.92460	2.93318	2.92755
abs err	0.02372	0.01857	0.01640	0.01365	0.01195
Am243-1	2.41690	2.45667	2.48878	2.51420	2.52438
abs err	0.01938	0.01628	0.01504	0.01312	0.01206
Cm248-1	0.50856	0.53799	0.57748	0.59968	0.62036
abs err	0.01118	0.01152	0.01238	0.01172	0.01106
Cs133	0.99242	0.97278	0.98964	1.01622	1.01720
abs err	0.02246	0.01768	0.01554	0.01363	0.01172
Eu153	4.85890	4.85585	4.87866	4.88543	4.86894
abs err	0.04022	0.03043	0.02648	0.02168	0.01884
Np237-1	2.59398	2.61853	2.62218	2.63069	2.62450
abs err	0.02007	0.01602	0.01353	0.01096	0.00952
Np237-2	2.60470	2.62579	2.62840	2.63372	2.62699
abs err	0.02037	0.01607	0.01364	0.01098	0.00961
Pu239	1.07980	1.08059	1.09167	1.09955	1.10095
abs err	0.01527	0.01163	0.00965	0.00820	0.00700
Pu240	1.55947	1.64686	1.68873	1.82795	1.89561
abs err	0.06181	0.06309	0.06430	0.06653	0.06626
Pu242-1	0.74944	0.76638	0.79718	0.82640	0.83326
abs err	0.01436	0.01308	0.01322	0.01380	0.01377
Pu242-2	0.76674	0.77789	0.81547	0.84069	0.84482
abs err	0.01577	0.01393	0.01508	0.01504	0.01485
Pu244-1	0.58536	0.61264	0.62837	0.64378	0.64631
abs err	0.01449	0.01304	0.01189	0.00949	0.00823

Table 4.2.1 cont.

Wafer height	0.1mm	0.5mm	1mm	2mm	3mm
<b>Samples</b>	<b>Capture cross-sections (barns)</b>				
Pu244-2	0.59065	0.61928	0.63277	0.64699	0.64822
abs err	0.01419	0.01331	0.01186	0.00956	0.00817
Rh103	1.00473	0.97458	0.96881	0.95571	0.94847
abs err	0.02532	0.01707	0.01391	0.01073	0.00918
Sm149	5.80839	6.07032	6.31498	6.62531	6.92207
abs err	0.07966	0.07852	0.07996	0.08059	0.08457
Th232	0.68658	0.69141	0.69971	0.70511	0.71177
abs err	0.01495	0.01245	0.01087	0.00889	0.00770
U233	0.47091	0.47424	0.47599	0.47599	0.47610
abs err	0.00337	0.00271	0.00228	0.00183	0.00159
U235	0.90296	0.90047	0.90432	0.90869	0.90845
abs err	0.00758	0.00570	0.00472	0.00387	0.00338
U236	0.79799	0.80328	0.81516	0.83172	0.85033
abs err	0.01897	0.01538	0.01317	0.01229	0.01185
U238	0.68988	0.71671	0.72437	0.75180	0.76024
abs err	0.01414	0.01377	0.01297	0.01221	0.01123

Table 4.2.2 One group effective capture cross-sections of samples in cadmium experiment

Wafer height	0.1mm	0.5mm	1mm	2mm	3mm
<b>Samples</b>	<b>Capture cross-sections (barns)</b>				
Am241-1	60.63642	63.51823	65.37134	67.18952	68.28474
abs err	0.22825	0.21568	0.20138	0.17274	0.15406
Am243-1	48.67088	52.48509	56.20329	61.70424	65.68022
abs err	0.19254	0.19356	0.20061	0.20089	0.19976
Cm244-1	21.87104	23.56722	25.19384	27.49566	28.57575
abs err	0.28098	0.28814	0.28775	0.27820	0.26043

Table 4.2.2 cont.

<b>Wafer height</b>	<b>0.1mm</b>	<b>0.5mm</b>	<b>1mm</b>	<b>2mm</b>	<b>3mm</b>
<b>Samples</b>	<b>Capture cross-sections (barns)</b>				
Cm248-1	6.74725	7.50325	8.25115	9.28457	9.85662
abs err	0.07123	0.07452	0.07695	0.07634	0.07311
Cs133	18.39146	19.16868	19.62847	20.13572	20.26704
abs err	0.17589	0.16556	0.14981	0.12943	0.11395
Eu153	69.78822	70.77625	71.34259	71.83509	72.01676
abs err	0.30300	0.25411	0.21978	0.17771	0.15546
Rh103	42.28123	43.95803	45.00038	45.78590	46.29381
abs err	0.24960	0.23127	0.20494	0.17614	0.15451
Nd145	11.09895	11.46555	11.70409	11.96897	12.07536
abs err	0.09623	0.08876	0.08001	0.06860	0.06068
Pd105	4.96575	5.03528	5.07760	5.10420	5.11218
abs err	0.03421	0.02749	0.02413	0.01964	0.01757
Np237-1	34.46448	34.98150	35.23780	35.50569	35.62845
abs err	0.14630	0.12219	0.10855	0.08784	0.07691
Np237-2	34.86301	35.23704	35.42750	35.63951	35.72673
abs err	0.15474	0.12651	0.10914	0.08817	0.07712
Pu239	15.11937	15.94918	16.47941	17.10697	17.45835
abs err	0.06711	0.06350	0.06044	0.05402	0.04966
Pu240	213.68111	236.16964	259.48287	285.13942	302.51751
abs err	1.68321	1.75784	1.79962	1.74774	1.67071
Pu242-1	21.28458	24.09891	27.09535	32.09295	35.98409
abs err	0.19299	0.20815	0.22299	0.24147	0.25253
Pu242-2	19.65746	22.25222	25.12359	29.90294	33.72689
abs err	0.17238	0.18555	0.19925	0.21605	0.22996
Pu244	5.08049	5.17471	5.21990	5.28459	5.30778
abs err	0.06932	0.05965	0.05285	0.04398	0.03884

Table 4.2.2 cont.

<b>Wafer height</b>	<b>0.1mm</b>	<b>0.5mm</b>	<b>1mm</b>	<b>2mm</b>	<b>3mm</b>
<b>Samples</b>	<b>Capture cross-sections (barns)</b>				
Nd143	7.75928	7.91947	8.00814	8.08879	8.14543
abs err	0.04428	0.03542	0.03094	0.02634	0.02317
Ru101	5.70951	5.66762	5.67058	5.66674	5.67042
abs err	0.06028	0.04500	0.03820	0.03135	0.02737
Sm149	449.28223	476.92818	498.49359	521.91000	535.08942
abs err	2.96186	2.93417	2.86276	2.57646	2.36955
Th232	3.68529	3.83559	3.95707	4.12438	4.17642
abs err	0.04294	0.04077	0.03769	0.03350	0.02973
U233	6.62752	6.82405	6.89722	6.98229	7.02571
abs err	0.02243	0.01987	0.01724	0.01458	0.01245
U235	7.42606	7.52631	7.59377	7.66246	7.68607
abs err	0.02654	0.02192	0.01971	0.01600	0.01436
U236	10.06652	11.15158	12.03254	13.21001	13.94013
abs err	0.11930	0.12522	0.12782	0.12443	0.11870
U238	9.08010	9.95744	10.70973	11.40868	11.92969
abs err	0.09677	0.10089	0.09988	0.09266	0.08610

The self-shielding factors for all the samples with actual masses as a function of wafer height can be seen in the tables below.

Table 4.2.3 Self-shielding factors as a function of height in boron experiment

<b>Wafer height</b>	<b>0.1mm</b>	<b>0.5mm</b>	<b>1mm</b>	<b>2mm</b>	<b>3mm</b>
<b>Samples</b>	<b>Self-shielding factors (SS)</b>				
Am241-1	0.98	0.99	0.99	1.00	1.00
Am243-1	0.92	0.93	0.95	0.95	0.96
Cm248-1	0.73	0.78	0.83	0.86	0.89
Cs133	0.95	0.93	0.95	0.97	0.97

Table 4.2.3 cont.

<b>Wafer height</b>	<b>0.1mm</b>	<b>0.5mm</b>	<b>1mm</b>	<b>2mm</b>	<b>3mm</b>
<b>Samples</b>	<b>Self-shielding factors (SS)</b>				
Eu153	1.00	1.00	1.00	1.00	1.00
Np237-1	0.98	0.99	1.00	1.00	1.00
Np237-2	0.99	1.00	1.00	1.00	1.00
Pu239	0.97	0.97	0.98	0.99	0.99
Pu240	0.68	0.72	0.74	0.80	0.83
Pu242-1	0.73	0.74	0.77	0.80	0.81
Pu242-2	0.74	0.75	0.79	0.81	0.82
Pu244-1	0.87	0.91	0.93	0.95	0.96
Pu244-2	0.87	0.92	0.94	0.96	0.96
Rh103	1.02	0.99	0.99	0.97	0.97
Sm149	0.68	0.71	0.74	0.77	0.81
Th232	0.94	0.94	0.96	0.96	0.97
U233	0.98	0.99	0.99	0.99	0.99
U235	1.00	1.00	1.00	1.01	1.01
U236	0.91	0.92	0.93	0.95	0.97
U238	0.83	0.86	0.87	0.90	0.91

Table 4.2.4 Self-shielding factors as a function of height in cadmium experiment

<b>Wafer height</b>	<b>0.1mm</b>	<b>0.5mm</b>	<b>1mm</b>	<b>2mm</b>	<b>3mm</b>
<b>Samples</b>	<b>Self-shielding factors (SS)</b>				
Am241-1	0.84	0.88	0.90	0.93	0.94
Am243-1	0.57	0.61	0.66	0.72	0.77
Cm244-1	0.66	0.71	0.76	0.83	0.87
Cm248-1	0.55	0.61	0.67	0.75	0.80
Cs133	0.88	0.92	0.94	0.97	0.97
Eu153	0.97	0.98	0.99	0.99	1.00
Rh103	0.88	0.92	0.94	0.96	0.97

Table 4.2.4 cont.

<b>Wafer height</b>	<b>0.1mm</b>	<b>0.5mm</b>	<b>1mm</b>	<b>2mm</b>	<b>3mm</b>
<b>Samples</b>	<b>Self-shielding factors (SS)</b>				
Nd145	0.89	0.92	0.94	0.96	0.97
Pd105	0.97	0.98	0.99	0.99	1.00
Np237-1	0.95	0.97	0.98	0.98	0.99
Np237-2	0.96	0.98	0.98	0.99	0.99
Pu239	0.79	0.84	0.87	0.90	0.92
Pu240	0.57	0.63	0.69	0.76	0.81
Pu242-1	0.35	0.39	0.44	0.52	0.59
Pu242-2	0.32	0.36	0.41	0.49	0.55
Pu244	0.96	0.98	0.98	1.00	1.00
Nd143	0.93	0.95	0.96	0.97	0.98
Ru101	1.00	1.00	1.00	1.00	1.00
Sm149	0.75	0.80	0.84	0.88	0.90
Th232	0.85	0.88	0.91	0.95	0.96
U233	0.93	0.96	0.97	0.98	0.98
U235	0.96	0.97	0.98	0.99	1.00
U236	0.60	0.67	0.72	0.79	0.83
U238	0.66	0.72	0.77	0.82	0.86

The self-shielding factors calculated by using MCNP5 were simply the ratios of the reaction rates. Special care is required for the statistics on these reaction rates. Around 500 billion histories were used in MCNP5 to obtain good statistics (22). The masses of the samples after irradiation were also measured using ICP-MS. The given uncertainty on these masses ( $\pm 5\%$ ) was much lower compared to the uncertainty on the actual masses (pre-irradiated masses). So the capture cross-sections and the self-shielding factors for all the samples with these masses were also calculated.

Table 4.2.5 One group capture cross-sections of all the samples with ICP-MS masses in boron experiment

Wafer height	0.1mm	0.5mm	1mm	2mm	3mm
Samples	Capture cross-sections (barns)				
Am241-1	2.99771	2.96366	2.96883	2.96335	2.94825
abs err	0.03226	0.02129	0.01822	0.01462	0.01259
Am241-2	2.93826	2.93718	2.94938	2.94877	2.93914
abs err	0.02678	0.02001	0.01736	0.01418	0.01227
Am243-1	2.50752	2.53062	2.55664	2.57046	2.56772
abs err	0.02337	0.01977	0.01855	0.01625	0.01454
Am243-2	2.42768	2.46916	2.49962	2.52240	2.53103
abs err	0.01975	0.01667	0.01542	0.01357	0.01242
Cm248-1	0.52219	0.54747	0.58580	0.60799	0.63117
abs err	0.01198	0.01220	0.01289	0.01218	0.01149
Cm248-2	0.53537	0.56089	0.59949	0.62021	0.63888
abs err	0.01277	0.01291	0.01371	0.01273	0.01179
Cs133	0.99814	0.97925	0.99212	1.01926	1.02072
abs err	0.02246	0.01810	0.01542	0.01371	0.01180
Eu153	4.86186	4.85663	4.88167	4.88667	4.86982
abs err	0.04039	0.03044	0.02649	0.02169	0.01884
Np237-1	2.58950	2.61600	2.61923	2.62909	2.62390
abs err	0.01989	0.01585	0.01343	0.01096	0.00952
Np237-2	2.60678	2.62513	2.62958	2.63537	2.62748
abs err	0.02061	0.01614	0.01364	0.01098	0.00961
Pu239	1.06884	1.07544	1.08722	1.09436	1.09778
abs err	0.01466	0.01147	0.00962	0.00801	0.00695
Pu240	1.59653	1.70215	1.72807	1.87366	1.95058
abs err	0.06717	0.07082	0.06911	0.07002	0.07114

Table 4.2.5 cont.

<b>Wafer height</b>	<b>0.1mm</b>	<b>0.5mm</b>	<b>1mm</b>	<b>2mm</b>	<b>3mm</b>
<b>Samples</b>	<b>Capture cross-sections (barns)</b>				
Pu242-1	0.75294	0.77024	0.79681	0.82373	0.82873
abs err	0.01437	0.01306	0.01316	0.01350	0.01314
Pu242-2	0.73902	0.75792	0.78700	0.81354	0.81758
abs err	0.01330	0.01215	0.01239	0.01276	0.01231
Pu244-1	0.61215	0.63712	0.64779	0.65995	0.65602
abs err	0.01611	0.01400	0.01255	0.00989	0.00834
Pu244-2	0.61252	0.63820	0.64876	0.66149	0.65715
abs err	0.01570	0.01431	0.01245	0.00989	0.00835
Rh103	0.99865	0.97414	0.96818	0.95526	0.94749
abs err	0.02433	0.01710	0.01393	0.01072	0.00914
Sm149	5.54578	5.81222	6.05283	6.33679	6.60277
abs err	0.06893	0.06767	0.06810	0.06763	0.07079
Th232	0.69585	0.69635	0.70717	0.71031	0.71460
abs err	0.01568	0.01290	0.01150	0.00916	0.00778
U233	0.47250	0.47554	0.47804	0.47675	0.47653
abs err	0.00345	0.00273	0.00231	0.00183	0.00159
U235	0.91178	0.90581	0.90818	0.91118	0.91024
abs err	0.00790	0.00581	0.00479	0.00388	0.00341
U236	0.90044	0.87412	0.87443	0.87373	0.88511
abs err	0.02862	0.02114	0.01899	0.01530	0.01438
U238	0.68552	0.71521	0.72364	0.75005	0.75902
abs err	0.01384	0.01362	0.01293	0.01211	0.01121

Table 4.2.6 One group capture cross-sections of all the samples with ICP-MS masses in cadmium experiment

Wafer height	0.1mm	0.5mm	1mm	2mm	3mm
<b>Samples</b>	<b>Capture cross-sections (barns)</b>				
Am241-1	70.57630	71.06655	71.21408	71.25035	71.43962
abs err	0.35443	0.28293	0.24024	0.19707	0.17514
Am241-2	65.51668	67.55719	68.58683	69.47453	70.06163
abs err	0.27812	0.24914	0.21797	0.18538	0.16491
Am243-1	69.83600	73.37765	76.12977	79.03543	80.86727
abs err	0.41227	0.40056	0.38436	0.34314	0.31796
Am243-2	50.77521	54.73822	58.49933	63.95006	67.77260
abs err	0.21064	0.21256	0.21454	0.22079	0.21281
Cm244-1	25.35768	26.95223	28.20105	29.96090	30.59391
abs err	0.37127	0.36987	0.35307	0.32408	0.29104
Cm244-2	25.54543	27.16834	28.37006	30.08755	30.70020
abs err	0.37912	0.37826	0.35801	0.32545	0.29206
Cm248-1	7.56558	8.37895	9.09917	10.03190	10.49472
abs err	0.08439	0.08823	0.08849	0.08548	0.07993
Cm248-2	7.05640	7.83171	8.57166	12.15119	10.11122
abs err	0.07590	0.08013	0.08080	0.11445	0.07600
Cs133	19.40781	19.95074	20.25445	20.62810	20.59519
abs err	0.20490	0.18026	0.15862	0.13465	0.11784
Eu153	69.81637	70.77943	71.35069	72.00595	72.04653
abs err	0.30312	0.25412	0.21980	0.18513	0.15553
Nd143	8.09048	8.18109	8.21168	8.23575	8.26245
abs err	0.04617	0.03659	0.03173	0.02600	0.02350
Nd145	10.97193	11.35890	11.61560	11.90465	12.02314
abs err	0.09295	0.08680	0.07940	0.06823	0.06042

Table 4.2.6 cont.

<b>Wafer height</b>	<b>0.1mm</b>	<b>0.5mm</b>	<b>1mm</b>	<b>2mm</b>	<b>3mm</b>
<b>Samples</b>	<b>Capture cross-sections (barns)</b>				
Np237-1	34.20536	34.80657	35.10097	35.41897	35.55915
abs err	0.14520	0.12157	0.10472	0.08762	0.07676
Np237-2	34.88381	35.25221	35.43430	35.64632	35.73232
abs err	0.15483	0.12656	0.10916	0.09165	0.07714
Pd105	4.99701	5.05358	5.09201	5.11415	5.11977
abs err	0.03491	0.02809	0.02420	0.02018	0.01759
Pu239	13.93974	14.87952	15.56574	16.39672	16.87865
abs err	0.05783	0.05633	0.05403	0.05016	0.04635
Pu240	241.92386	264.32309	286.44179	307.99088	321.96803
abs err	2.04951	2.09883	2.10062	1.97978	1.84226
Pu242-1	21.69370	24.56514	27.62010	32.66212	36.57334
abs err	0.19885	0.21462	0.23006	0.24900	0.25667
Pu242-2	21.44144	24.27292	27.32240	32.34601	36.26388
abs err	0.19654	0.20965	0.22486	0.24337	0.25449
Pu244-1	5.10258	5.18927	5.22869	5.29066	5.31291
abs err	0.07013	0.06034	0.05294	0.04455	0.03888
Pu244-2	5.12464	5.20540	5.24052	5.29960	5.31921
abs err	0.07146	0.06053	0.05306	0.04463	0.03892
Rh103	45.06113	46.01154	46.59429	46.87727	47.11435
abs err	0.29262	0.25117	0.22141	0.18034	0.16191
Ru101	5.78803	5.70363	5.69627	5.68538	5.68413
abs err	0.06514	0.04586	0.03894	0.03146	0.02743
Sm149	492.41214	515.58298	530.86584	546.28498	554.65605
abs err	3.58651	3.42775	3.15408	2.75102	2.51131
Th232	4.35693	4.33851	4.34690	4.39870	4.38916
abs err	0.07031	0.05304	0.04574	0.03748	0.03255

Table 4.2.6 cont.

<b>Wafer height</b>	<b>0.1mm</b>	<b>0.5mm</b>	<b>1mm</b>	<b>2mm</b>	<b>3mm</b>
<b>Samples</b>	<b>Capture cross-sections (barns)</b>				
U233	6.81064	6.94806	6.98836	7.04499	7.07451
abs err	0.02434	0.02023	0.01747	0.01471	0.01322
U235	7.46608	7.55314	7.61146	7.67641	7.69738
abs err	0.02739	0.02272	0.01976	0.01603	0.01438
U236	11.32745	12.43561	13.25127	14.21467	14.78507
abs err	0.14553	0.15204	0.15003	0.14098	0.13032
U238	9.57166	10.46209	11.15974	11.74379	12.21434
abs err	0.10581	0.10913	0.10630	0.09656	0.08937

The self-shielding factors for all the samples (with ICP-MS masses) as a function of wafer height can be seen in the tables below.

Table 4.2.7 Self-shielding factors as a function of height in boron experiment (ICP-MS)

<b>Wafer height</b>	<b>0.1mm</b>	<b>0.5mm</b>	<b>1mm</b>	<b>2mm</b>	<b>3mm</b>
<b>Samples</b>	<b>Self-shielding factors (SS)</b>				
Am241-1	1.02	1.01	1.01	1.01	1.00
Am241-2	1.00	1.00	1.00	1.00	1.00
Am243-1	0.95	0.96	0.97	0.98	0.98
Am243-2	0.92	0.94	0.95	0.96	0.96
Cm248-1	0.75	0.79	0.84	0.88	0.91
Cm248-2	0.77	0.81	0.86	0.89	0.92
Cs133	0.96	0.94	0.95	0.98	0.98
Eu153	1.00	1.00	1.00	1.00	1.00
Np237-1	0.98	0.99	0.99	1.00	1.00
Np237-2	0.99	1.00	1.00	1.00	1.00
Pu239	0.96	0.97	0.98	0.99	0.99
Pu240	0.70	0.75	0.76	0.82	0.86

Table 4.2.7 cont.

<b>Wafer height</b>	<b>0.1mm</b>	<b>0.5mm</b>	<b>1mm</b>	<b>2mm</b>	<b>3mm</b>
<b>Samples</b>	<b>Self-shielding factors (SS)</b>				
Pu242-1	0.73	0.75	0.77	0.80	0.80
Pu242-2	0.72	0.73	0.76	0.79	0.79
Pu244-1	0.91	0.94	0.96	0.98	0.97
Pu244-2	0.91	0.95	0.96	0.98	0.97
Rh103	1.02	0.99	0.99	0.97	0.96
Sm149	0.65	0.68	0.70	0.74	0.77
Th232	0.95	0.95	0.97	0.97	0.98
U233	0.99	0.99	1.00	1.00	1.00
U235	1.01	1.00	1.01	1.01	1.01
U236	1.03	1.00	1.00	1.00	1.01
U238	0.82	0.86	0.87	0.90	0.91

Table 4.2.8 Self-shielding factors as a function of height in cadmium experiment (ICP-MS)

<b>Wafer height</b>	<b>0.1mm</b>	<b>0.5mm</b>	<b>1mm</b>	<b>2mm</b>	<b>3mm</b>
<b>Samples</b>	<b>Self-shielding factors (SS)</b>				
Am241-1	0.97	0.98	0.98	0.98	0.98
Am241-2	0.90	0.93	0.95	0.96	0.97
Am243-1	0.82	0.86	0.89	0.92	0.94
Am243-2	0.59	0.64	0.68	0.75	0.79
Cm244-1	0.77	0.82	0.86	0.91	0.93
Cm244-2	0.77	0.82	0.86	0.91	0.93
Cm248-1	0.61	0.68	0.73	0.81	0.85
Cm248-2	0.57	0.63	0.69	0.98	0.82
Cs133	0.93	0.96	0.97	0.99	0.99
Eu153	0.97	0.98	0.99	1.00	1.00
Nd143	0.97	0.98	0.98	0.99	0.99

Table 4.2.8 cont.

Wafer height	0.1mm	0.5mm	1mm	2mm	3mm
<b>Samples</b>	<b>Self-shielding factors (SS)</b>				
Nd145	0.88	0.91	0.93	0.96	0.97
Np237-1	0.95	0.96	0.97	0.98	0.98
Np237-2	0.97	0.98	0.98	0.99	0.99
Pd105	0.97	0.99	0.99	1.00	1.00
Pu239	0.73	0.78	0.82	0.86	0.89
Pu240	0.64	0.70	0.76	0.82	0.86
Pu242-1	0.35	0.40	0.45	0.53	0.60
Pu242-2	0.35	0.40	0.44	0.53	0.59
Pu244-1	0.96	0.98	0.99	1.00	1.00
Pu244-2	0.97	0.98	0.99	1.00	1.00
Rh103	0.94	0.96	0.97	0.98	0.99
Ru101	1.02	1.00	1.00	1.00	1.00
Sm149	0.83	0.87	0.89	0.92	0.93
Th232	1.00	1.00	1.00	1.01	1.01
U233	0.95	0.97	0.98	0.99	0.99
U235	0.97	0.98	0.99	0.99	1.00
U236	0.68	0.74	0.79	0.85	0.88
U238	0.69	0.76	0.81	0.85	0.88

From Tables 4.2.3, 4.2.4, 4.2.7 and 4.2.8, the self-shielding effects were significant in some of the samples mostly in the cadmium experiment. In the boron experiment, the samples Cm-248, Pu-240, Pu-242, Sm-149 and U-238 displayed self-shielding effects. In the cadmium experiment, the samples Am-243, Cm-244, Cm-248, Pu-239, Pu-240, Pu-242, Sm-149, Nd-145, U-236 and U-238 displayed significant self-shielding effects. These self-shielding factors can be used to correct the final calculated (C) over experiment (E) reaction rate ratios (C/E).

## 5. UNFOLDING THE NEUTRON SPECTRA

The neutron spectrum can be unfolded using the data obtained from the irradiated neutron flux wires. The neutron flux wires when placed in a neutron field can be activated by the neutrons with different energies. The neutron cross-section of an element is simply defined as the interaction probability between the incident neutron and the element itself. These cross-sections of the flux wires are sensitive to the energies of the incident neutrons (e.g. thermal, epi-thermal and fast neutrons). Hence, by activating different flux wires with different sensitivities to the incident neutrons in the presence of same neutron field, one can unfold (reconstruct) the neutron spectrum using the measured activities. These measured activities are proportional to the neutron fluxes present in the neutron field in which they are activated. In general, the level of spectral detail that can be reliably obtained corresponds to the number of different materials, and different interactions in the same materials, that are available (24).

Enclosing the flux wires inside the cut-off materials (filters) like cadmium and boron, one can get rid of the thermal and the epi-thermal neutrons. The boron filters were used to obtain the spectra that were closer to that of a fast neutron reactor (FNR).

Two unfolding techniques, MAXED and least squares methods were used to calculate the solution spectra. In any unfolding process, the input data consists of an *a priori* spectrum, measured activities and response functions (Figure 5.0.1). Making use of these input data, the above mentioned techniques can unfold the neutron spectrum. However, unfolding codes are not black-boxes. Proper care should be taken for the input data before starting the unfolding process.

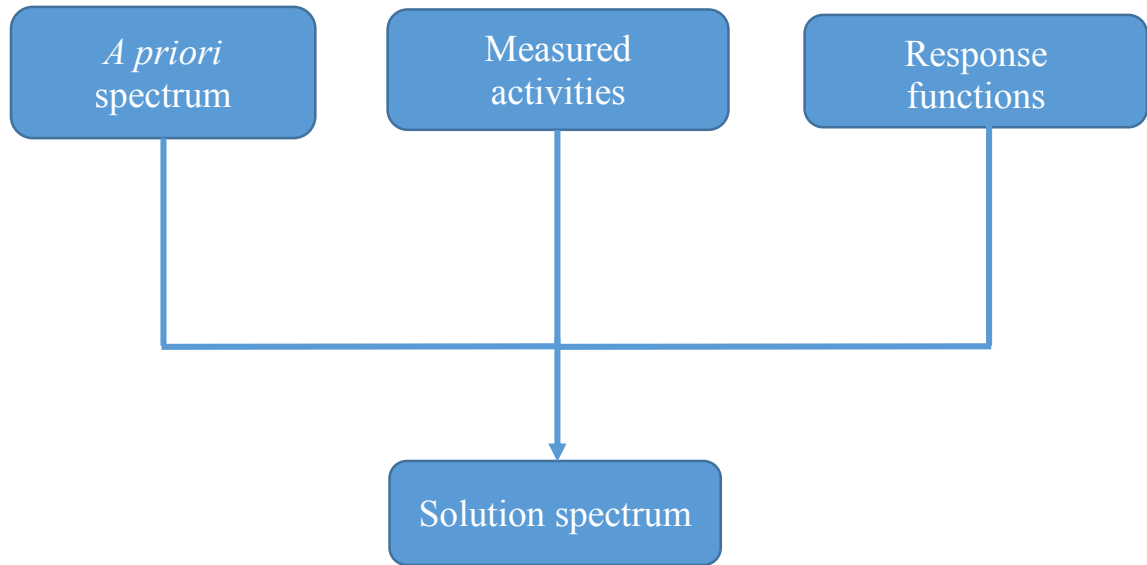


Figure 5.0.1 Flow chart of the unfolding process

### 5.1 *A priori* Spectrum

An *a priori* spectrum, also known as default spectrum, is the best estimate of the experiment which can be calculated using simulation software like MCNP5. This spectrum was normalized to the actual reactor power since MCNP5 always calculates the spectrum per one fission source neutron. The normalization factor was calculated using the equation below (25).

$$F \left[ \frac{\text{neutrons}}{\text{sec}} \right] = \frac{P[\text{MW}] \bar{\nu} \left[ \frac{\text{neutrons}}{\text{fission}} \right]}{1.6022 \times 10^{-19} \left[ \frac{\text{MJ}}{\text{MeV}} \right] Q_T \left[ \frac{\text{MeV}}{\text{fission}} \right] k_{\text{eff}}} \frac{1}{k_{\text{eff}}} \quad [5.1.1]$$

Where, F = number of neutrons produced per second from fission

P = average reactor power

$\bar{\nu}$  = average number of neutrons produced per fission

$Q_T$  = average energy released per fission

$k_{\text{eff}}$  = effective neutron multiplication factor

*A priori* spectra were calculated in 32 equal logarithmic energy bins from  $10^{-7}$  MeV to 19 MeV.

Table 5.1.1 ATR core parameters for both the experiments

Parameters	Boron experiment	Cadmium experiment
P [MW]	102.448	103.273
$\bar{\nu}$ $\left[ \frac{\text{neutrons}}{\text{fission}} \right]$	2.439	2.439
$Q_T$ $\left[ \frac{\text{MeV}}{\text{fission}} \right]$	201.400	201.400
$k_{\text{eff}}$	0.986	1.000
F $\left[ \frac{\text{neutrons}}{\text{sec}} \right]$	7.850E+18	7.806E+18

The values of the parameters  $\bar{\nu}$  and  $Q_T$  are for the ATR core. For the reactor power, the average value during the irradiation cycles was taken. The normalized *a priori* spectrum calculated in the boron experiment was accounted for all the scrams and the long wait time between the irradiation cycles.

*A priori* spectra

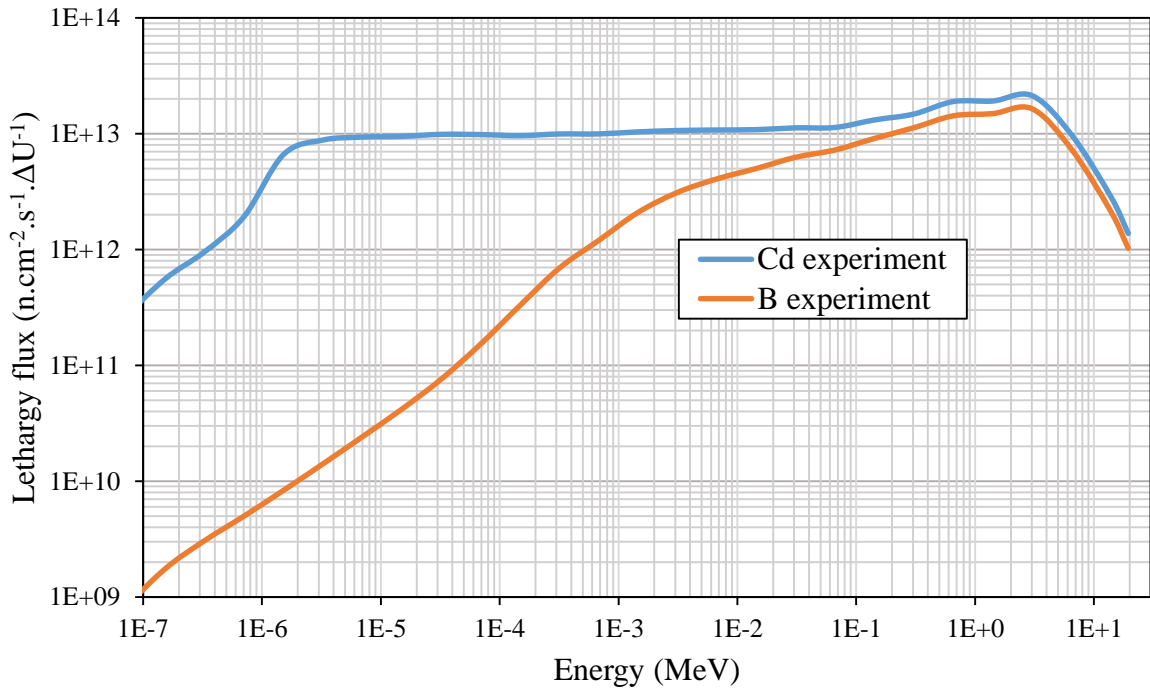


Figure 5.1.1 *A priori* spectra in both the experiments

## 5.2 Response Functions

The response functions of the flux wires are very essential for the unfolding process. The general mathematical formulations used to calculate these response functions are described here. The volume averaged reaction rates (R) for any flux wire in the presence of a neutron field can be calculated using the Equation 5.2.1.

$$R = \int_0^{\infty} \sigma_w(E) \Psi_w(E) dE \quad [5.2.1]$$

Where,  $\sigma_w(E)$  = microscopic cross-section of the flux wire (barns)

$\Psi_w(E)$  = volume averaged scalar neutron flux within the flux wire ( $n.cm^{-2}.s^{-1}$ )

Rearranging the Equation 5.2.1, one can calculate the self-shielding effects if any at the region of interest. The presence of the flux wire, a cut-off material and any other supporting structure materials in the region of interest can cause these self-shielding effects.

$$R = \int_0^{\infty} \sigma_w(E) \left( \frac{\Psi_w(E)}{\Psi(E)} \right) \Psi(E) dE = \int_0^{\infty} \sigma_w(E) F_w(E) \Psi(E) dE \quad [5.2.2]$$

Where,  $\Psi(E)$  = unperturbed neutron flux in the absence of flux wire, cut-off material and other supporting materials at the region of interest ( $n.cm^{-2}.s^{-1}$ )

$F_w(E)$  = self-shielding function

The response functions or the activation constants (A) for any flux wire can then be calculated using the equation below.

$$A = \frac{\int_0^{\infty} \sigma_w(E) F_w(E) \Psi(E) dE}{\int_0^{\infty} \Psi(E) dE} \quad [5.2.3]$$

In general, most of the perturbation in the neutron flux is caused by the cut-off (filter) material at the region of interest. For all the MANTRA experiments, the region of interest was inside the cut-off materials (cadmium and boron). So, the self-shielding function was

equal to one. The final equation for calculating the response functions of the flux wires is below.

$$A = \frac{\int_0^{\infty} \sigma_w(E) \Psi_w(E) dE}{\int_0^{\infty} \Psi_w(E) dE} \quad [5.2.4]$$

These response functions can be calculated using a continuous energy Monte Carlo code like MCNP5. The response functions were calculated using 32 equal logarithmic energy bins from  $10^{-7}$  MeV to 19 MeV. The denominator of the Equation 5.2.4 which is the volume averaged flux within a flux wire can be calculated using an “F4” tally card in MCNP5. The numerator of the Equation 5.2.4 which is the volume averaged reaction rate of a flux wire can be calculated using an “Fm4” tally multiplier card in MCNP5. By taking the ratio of these two tally cards, the response functions of all the flux wires in the 32 energy bins were calculated.

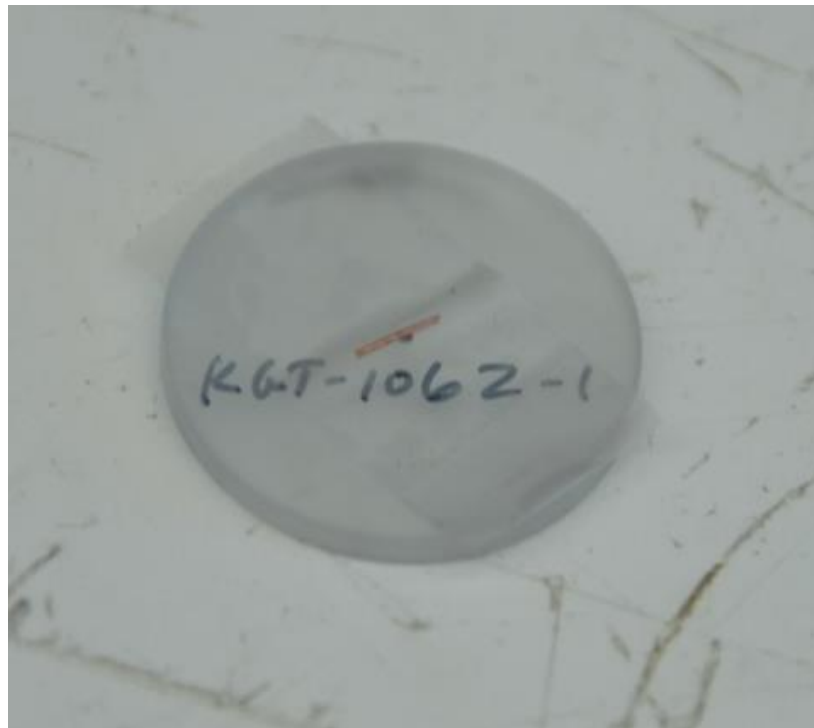


Figure 5.2.1 Copper flux wire used in the cadmium experiment

The flux wires and their compositions used in both the experiments were included in the table below. As mentioned earlier, all these flux wires were repeated evenly at four different positions from top to bottom.

Table 5.2.1 Compositions of the flux wires

<b>Composition</b>		<b>density</b>
<b>Flux wires</b>	<b>%</b>	<b>g.cm<sup>-3</sup></b>
<b>Co-Al alloy</b>	Co59 (0.098), Al27 (99.902)	2.70
<b>Copper</b>	Cu63 (69.17), Cu65 (30.83)	8.92
<b>Iron</b>	Fe54 (5.845), Fe56 (91.754), Fe57 (2.119), Fe58 (.282)	7.87
<b>Nickel</b>	Ni58 (68.07), Ni60 (26.22), Ni61 (1.13), Ni62 (3.63), Ni64 (0.92)	8.91
<b>Titanium</b>	Ti46 (8.25), Ti47 (7.44), Ti48 (73.72), Ti49 (5.41), Ti50 (5.18)	4.51
<b>U-Al alloy</b>	U (~10), Al (~90) {U235 in U~90}	2.94

The parent and the product isotopes of interest along with their half-lives can be seen here.

Table 5.2.2 Parent and product isotopes of interest

<b>Parent</b>	<b>reaction</b>	<b>Product</b>	<b>half-life</b>
Co-59 (26)	(n, g)	Co-60	5.271 y (27)
Cu-63 (28)	(n, $\alpha$ )	Co-60	5.271 y
Fe-54 (29)	(n, p)	Mn-54	312.1 d
Fe-58	(n, g)	Fe-59	45 d
Ni-58 (30)	(n, p)	Co-58	71 d
Ni-60	(n, p)	Co-60	5.271 y
Ti-46 (31)	(n, p)	Sc-46	84 d
U-235	(n, f)	Cs137	30.07 y

Here, y = years; d = days

Table 5.2.3 Masses of the flux wires used in the boron experiment

	<b>Mass (g) (B experiment)</b>			
<b>Flux wire positions</b>	<b>3</b>	<b>10</b>	<b>17</b>	<b>23</b>
Co-Al alloy	0.01284	0.01206	0.01292	0.01146
Copper	0.01318	0.01262	0.01214	0.01179
Iron	0.01086	0.01168	0.01175	0.01069
Nickel	0.01849	0.01847	0.01804	0.01618
Titanium	0.00666	0.00666	0.00701	0.00614
U-Al alloy	0.01426	0.01523	0.01530	0.01502

Table 5.2.4 Masses of the flux wires used in the cadmium experiment

	<b>Mass (g) (Cd experiment)</b>			
<b>Flux wire positions</b>	<b>4</b>	<b>11</b>	<b>19</b>	<b>26</b>
Co-Al alloy	0.01235	0.01208	0.01242	0.01374
Copper	0.01209	0.01163	0.01228	0.01228
Iron	0.01172	0.00853	0.00985	0.00962
Nickel	0.01882	0.01776	0.01789	0.01732
Titanium	0.00592	0.00582	0.00605	0.00641
U-Al alloy	0.01461	0.01508	0.01468	0.01515

The radius of the alloy form of the flux wires (cobalt-aluminum and uranium-aluminum) was 0.0508 cm. The radius of all the other flux wires was 0.0254 cm. Care must be taken as the response functions depend strongly on the geometry and the composition of a flux

wire (32). The calculated response functions of the all flux wires in the cadmium experiment in the 32 energy groups were plotted (Figure 5.2.2).

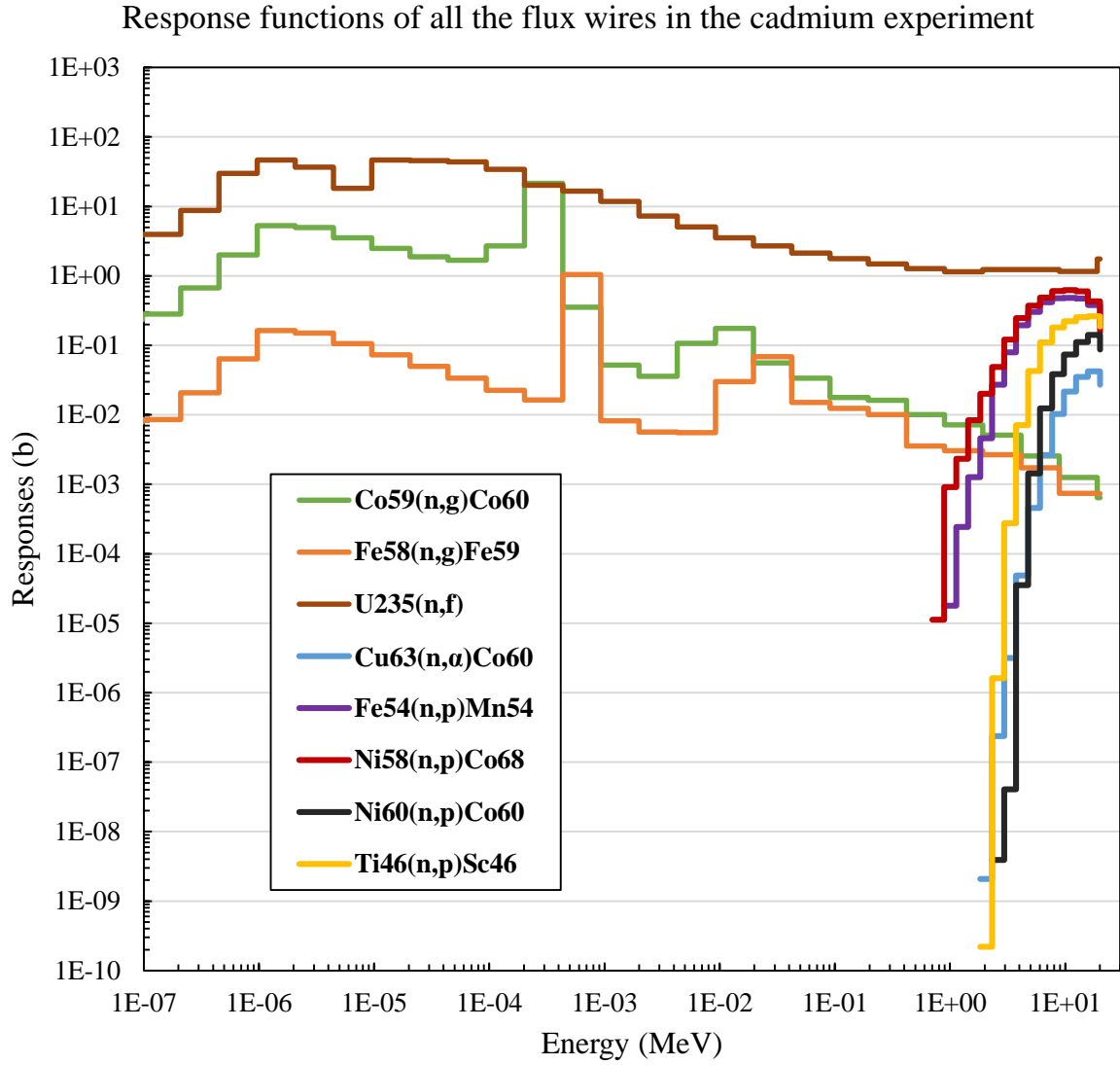


Figure 5.2.2 Response functions of all the flux wires in the Cd experiment

The calculated response functions of the all flux wires in the boron experiment in the 32 energy groups were plotted (Figure 5.2.3).

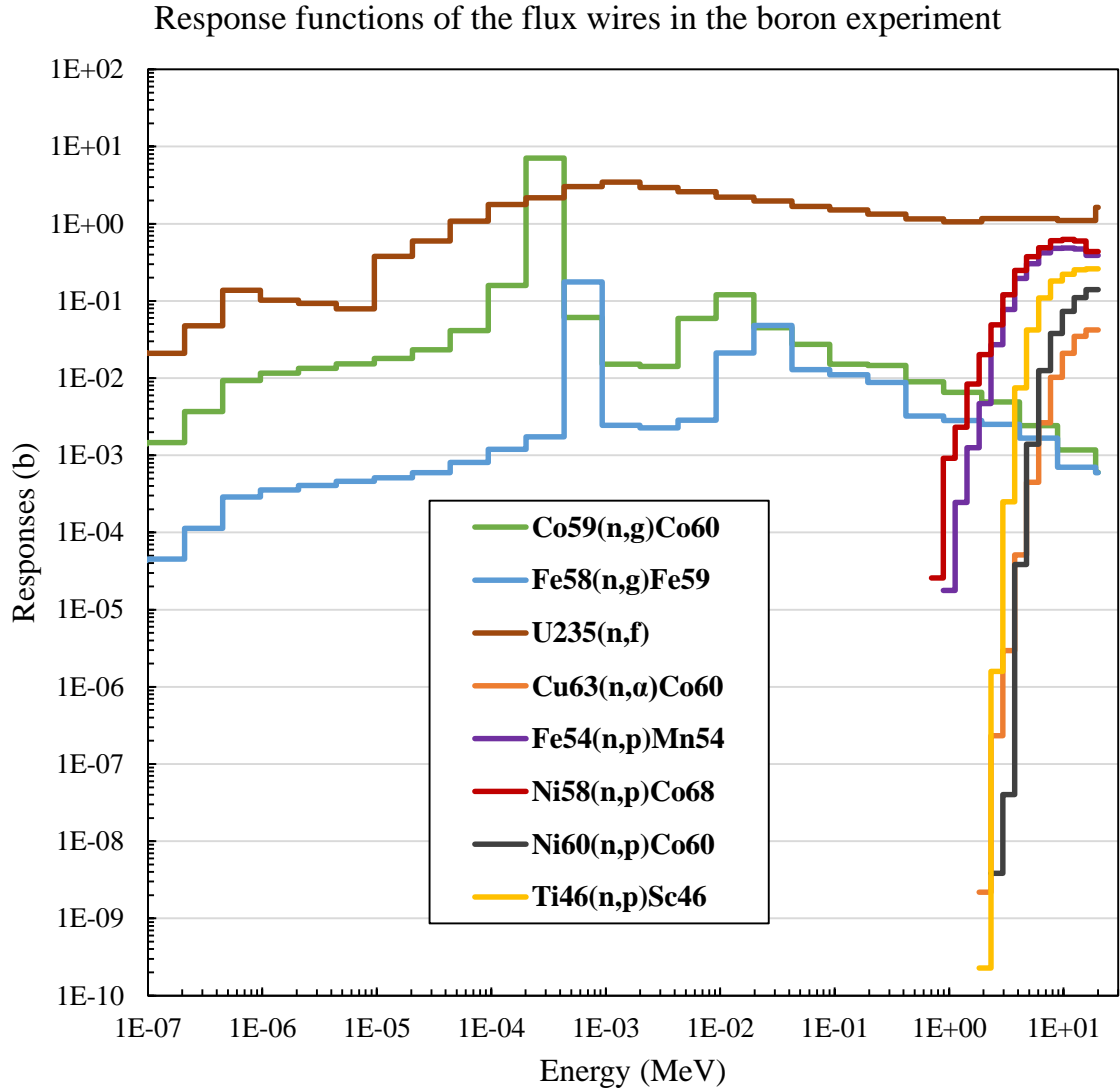


Figure 5.2.3 Response functions of all the flux wires in the B experiment

### 5.3 Measured Activities

The saturation activity or the activation rate was calculated using the activities measured from the irradiated flux wires. The activity profile of a dosimeter or a flux wire from the reactor can be seen in the figure below.

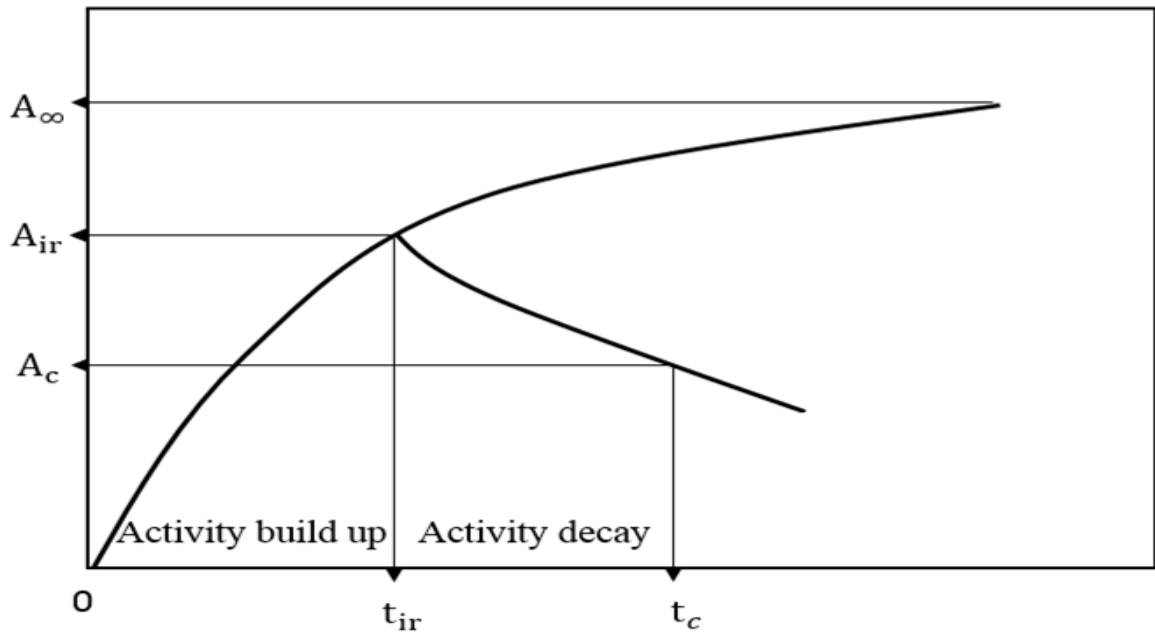


Figure 5.3.1 Example of the activity profile of a flux wire from a reactor

The activity of a flux wire at the end of irradiation can be calculated using the equation

$$(33) \quad A_{ir} = A_c e^{\lambda t_w} \quad [5.3.1]$$

Where,  $A_{ir}$  = activity at the end of irradiation (Bq)

$A_c$  = activity at the time of counting (Bq)

$A_\infty$  = saturation activity or activation rate (Bq)

$\lambda$  = decay constant of the product nuclide ( $s^{-1}$ )

$t_w$  = wait time ( $t_c - t_{ir}$ ) (s)

$t_c$  = time when the flux wires were counted (s)

$t_{ir}$  = irradiation time (s)

The saturation activity or the activation rate can then be calculated

$$A_{\infty} = \frac{A_{ir}}{1 - e^{-\lambda t_{ir}}} \quad [5.3.2]$$

The activation rates calculated from MCNP5 are per atom. So the activation rate per atom from the measured activities can be calculated using the equation below (34).

$$R_m = \frac{A_{\infty} M}{m N_a} \quad [5.3.3]$$

Where,  $R_m$  = measured activation rate per atom (measured responses) (Bq/atom)

$M$  = atomic weight of the nuclide of interest (g.mol<sup>-1</sup>)

$m$  = mass of the nuclide of interest (g)

$N_a$  = Avogadro's number (atoms.mol<sup>-1</sup>)

The above described equations are true in case of cadmium experiment, where there were no scrams during the irradiation cycle. On the other hand, the boron experiment had two scrams and more than six months wait time between irradiation cycle 1 and 2 (Table 1.4.1). So to calculate the activation rates per atom, the measured activities at the end of irradiation must be decay corrected.

In case of decay with production, the rate of change of the number of daughter nuclides (35) is given by

$$\frac{dN_d(t)}{dt} = \text{rate of production} - \text{rate of decay} \quad [5.3.4]$$

$$\frac{dN_d(t)}{dt} = \phi \sigma N_p(t) - \lambda N_d(t) \quad [5.3.5]$$

Where,  $N_p$  = number of parent nuclides

$N_d$  = number of daughter nuclides

$\phi \sigma$  = activation rate (Bq)

By applying Equation 5.3.5 to the boron experiment, the activation rates were decay corrected. The activity of a flux wire during this experiment from the reactor can be seen in the Figure 5.3.2. The shape would be different for different daughter nuclides depending on their decay constant.

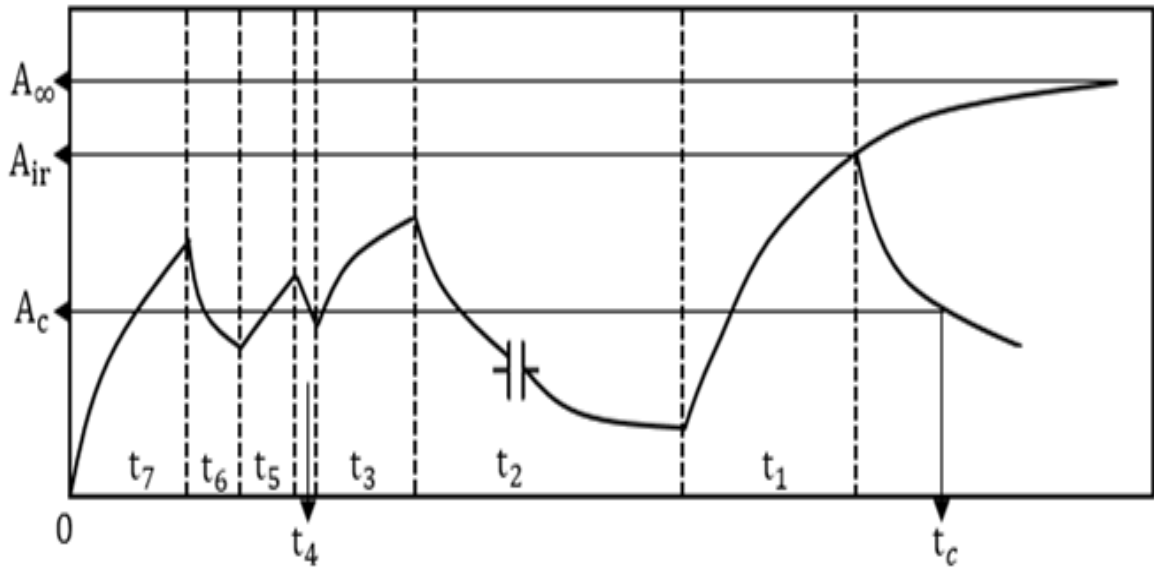


Figure 5.3.2 Example of the activity profile of a flux wire in the boron experiment

The final equation used to calculate the activation rate per atom ( $R_m$ ) for a flux wire in the case of the boron experiment is below.

$$\frac{A_{ir}/N_p}{(1 - e^{-\lambda t_1}) + (1 - e^{-\lambda t_3})e^{-\lambda(t_1+t_2)} + (1 - e^{-\lambda t_5})e^{-\lambda(t_1+t_2+t_3+t_4)} + (1 - e^{-\lambda t_7})e^{-\lambda(t_1+t_2+t_3+t_4+t_5+t_6)}} \quad [5.3.6]$$

Where,  $t_1, t_3, t_5, t_7$  = irradiation times (s)

$t_2$  = wait time between irradiation cycle 1 and cycle2 (s)

$t_4, t_6$  = decay time during scrams (s)

The complete derivation of the Equation 5.3.6 was included in the appendix E.

The activation rates per atom ( $R_c$ ) calculated using MCNP5 for the cadmium experiment were included in the table below.

Table 5.3.1 Calculated activation rates of the flux wires in the cadmium experiment

<b>Calculated (MCNP5)</b>	<b>Activation rates (Bq/atom)</b>			
<b>Flux wire positions</b>	<b>4</b>	<b>11</b>	<b>19</b>	<b>26</b>
Co59(n, g)Co60	6.62809E+14	8.24602E+14	8.43757E+14	7.21471E+14
Cu63(n, $\alpha$ )Co60	9.96163E+09	1.23832E+10	1.26491E+10	1.08301E+10
Fe54(n, p)Mn54	1.47441E+12	1.83729E+12	1.87410E+12	1.60502E+12
Fe58(n, g)Fe59	1.33367E+13	1.64236E+13	1.68662E+13	1.44377E+13
Ni58(n, p)Co58	2.02952E+12	2.52315E+12	2.57734E+12	2.20864E+12
Ni60(n, p)Co60	3.73917E+10	4.63739E+10	4.73892E+10	4.05903E+10
Ti46(n, p)Sc46	2.43874E+11	3.03493E+11	3.10427E+11	2.65723E+11
U235(n, f)Cs137	1.82151E+14	2.26715E+14	2.31597E+14	1.98310E+14

The measured activation rates per atom ( $R_m$ ) for the cadmium experiment were included here.

Table 5.3.2 Measured activation rates of the flux wires in the cadmium experiment

<b>Measured (experiment)</b>	<b>Activation rates (Bq/atom)</b>			
<b>Flux wire positions</b>	<b>4</b>	<b>11</b>	<b>19</b>	<b>26</b>
Co59(n, g)Co60	7.28461E+14	8.95408E+14	9.08856E+14	7.67582E+14
Cu63(n, $\alpha$ )Co60	1.17114E+10	1.41893E+10	1.41455E+10	1.18591E+10
Fe54(n, p)Mn54	1.53683E+12	1.92281E+12	1.85103E+12	1.57973E+12
Fe58(n, g)Fe59	1.34758E+13	1.69124E+13	1.62036E+13	1.38620E+13
Ni58(n, p)Co58	2.14038E+12	2.61421E+12	2.57863E+12	2.19685E+12
Ni60(n, p)Co60	4.80916E+10	5.90599E+10	6.01194E+10	5.07344E+10
Ti46(n, p)Sc46	2.29885E+11	2.78053E+11	2.76780E+11	2.31784E+11
U235(n, f)Cs137	1.96286E+14	2.40264E+14	2.46758E+14	2.07581E+14

The activation rates per atom ( $R_c$ ) calculated using MCNP5 for the boron experiment were included in the table below.

Table 5.3.3 Calculated activation rates of the flux wires in the boron experiment

Calculated (MCNP5) Flux wire positions	Activation rates (Bq/atom)			
	3	10	17	23
Co59(n, g)Co60	3.62353E+13	4.08337E+13	4.09321E+13	3.71218E+13
Cu63(n, $\alpha$ )Co60	8.00014E+09	9.04975E+09	9.10147E+09	8.28470E+09
Fe54(n, p)Mn54	1.17565E+12	1.32661E+12	1.32931E+12	1.20348E+12
Fe58(n, g)Fe59	1.63414E+12	1.84744E+12	1.85434E+12	1.67391E+12
Ni58(n, p)Co58	1.61779E+12	1.82335E+12	1.82619E+12	1.65310E+12
Ni60(n, p)Co60	2.96681E+10	3.34488E+10	3.36231E+10	3.05239E+10
Ti46(n, p)Sc46	1.97853E+11	2.22991E+11	2.22566E+11	2.03036E+11
U235(n, f)Cs137	1.24443E+13	1.40326E+13	1.40594E+13	1.27442E+13

The measured activation rates per atom ( $R_m$ ) for the boron experiment can be seen in the table below.

Table 5.3.4 Measured r activation rates of the flux wires in the boron experiment

Measured (experiment) Flux wire positions	Activation rates (Bq/atom)			
	3	10	17	23
Co59(n, g)Co60	2.87586E+13	6.30358E+13	3.98891E+13	2.92583E+13
Cu63(n, $\alpha$ )Co60	7.52011E+09	8.06879E+09	8.04461E+09	7.46201E+09
Fe54(n, p)Mn54	8.23760E+11	9.13891E+11	9.23999E+11	8.40206E+11
Fe58(n, g)Fe59	7.54226E+11	1.82184E+12	1.32720E+12	7.36949E+11
Ni58(n, p)Co58	9.48238E+11	1.07275E+12	1.05707E+12	9.87140E+11
Ni60(n, p)Co60	3.05937E+10	3.42477E+10	3.39988E+10	3.19463E+10
Ti46(n, p)Sc46	9.78809E+10	1.08288E+11	1.08106E+11	1.00475E+11
U235(n, f)Cs137	1.03926E+13	2.73681E+13	1.93445E+13	1.10971E+13

The ratios of the calculated over experiment activation rates per atom ( $R_c/R_m$ ) for all the flux wires were calculated.

Table 5.3.5 C/E ratios of the activation rates in the cadmium experiment

<b>Cd experiment</b>	<b>Calculated/Experiment (C/E)</b>			
	<b>4</b>	<b>11</b>	<b>19</b>	<b>26</b>
Co59(n, g)Co60	0.91	0.92	0.93	0.94
Cu63(n, $\alpha$ )Co60	0.85	0.87	0.89	0.91
Fe54(n, p)Mn54	0.96	0.96	1.01	1.02
Fe58(n, g)Fe59	0.99	0.97	1.04	1.04
Ni58(n, p)Co58	0.95	0.97	1.00	1.01
Ni60(n, p)Co60	0.78	0.79	0.79	0.80
Ti46(n, p)Sc46	1.06	1.09	1.12	1.15
U235(n, f)Cs137	0.93	0.94	0.94	0.96

From Table 5.3.5, the C/E ratios of each flux wire were close to each other in all the four positions. So the measured and the calculated activation rates of all the flux wires from the four positions were used together in the unfolding process.

Table 5.3.6 C/E ratios of the activation rates in the boron experiment

<b>B experiment</b>	<b>Calculated/Experiment (C/E)</b>			
	<b>3</b>	<b>10</b>	<b>17</b>	<b>23</b>
Co59(n, g)Co60	1.26	0.65	1.03	1.27
Cu63(n, $\alpha$ )Co60	1.06	1.12	1.13	1.11
Fe54(n, p)Mn54	1.43	1.45	1.44	1.43
Fe58(n, g)Fe59	2.17	1.01	1.40	2.27
Ni58(n, p)Co58	1.71	1.70	1.73	1.67
Ni60(n, p)Co60	0.97	0.98	0.99	0.96
Ti46(n, p)Sc46	2.02	2.06	2.06	2.02
U235(n, f)Cs137	1.20	0.51	0.73	1.15

Clearly from Table 5.3.6, the C/E ratios of the reactions Co59(n, g)Co60, Fe58(n, g)Fe59 and U235(n, f)Cs137 were different in all the four positions. Also, the C/E ratios of most of the threshold reactions were far from one. The possible reasons for these strange ratios could be: the leaks since the boron filters were stacked one above the other and the compositions of the boron filters were different from top to bottom.

## 5.4 MAXED Unfolding Method

The unfolding package UMG 3.3 (Unfolding with MAXED and GRAVEL) consists of two different unfolding techniques. In the current work, only MAXED unfolding program of the package was used to calculate the solution spectra. The MAXED program uses the maximum entropy principle where the maximum relative entropy is used to unfold the neutron spectrum. This method is based on the Bayesian statistics and provides a consistent probabilistic theory to obtain unbiased results (36). The term “entropy” here refers to the information-theory entropy and is synonymous with the uncertainty rather than the thermodynamic view (37). The following equations are used in this code.

$$M_k + d_k = \sum_i R_{ki} S_i \quad [5.4.1]$$

$$O = -\sum_i \left\{ S_i \ln \left( \frac{S_i}{S_i^D} \right) + S_i^D - S_i \right\} \quad [5.4.2]$$

Where,  $M_k$  = measured activation rates

$d_k$  = difference between measured and calculated activation rates

$R_{ki}$  = response functions

$S_i^D$  = default spectrum (best estimate)

$S_i$  = solution spectrum or output spectrum

$O$  = maximum entropy of the distribution

$k$  = number of flux wires

$i$  = number of desired energy groups

This unfolding technique selects the maximum entropy of the distribution according to the Equation 5.4.2 (38) (39). In other words, of all the spectra that fits the data, the one that is closest to the default spectrum is chosen. Implementing this principle helps to write the output spectrum in a closed form (i.e. with finite number of well-known functions or parameters). This allows the use of general methods for both sensitivity analysis and uncertainty propagation throughout the unfolding process (40).

## 5.5 Least Squares Method

Least squares method can be applied to unfold the neutron spectrum (41). The Equation 5.5.1 can be utilized to solve for the solution spectrum.

$$\begin{bmatrix} a_{11} & a_{12} & a_{13} & \cdots & a_{1NG} \\ a_{21} & a_{22} & a_{23} & \cdots & a_{2NG} \\ a_{31} & a_{32} & a_{33} & \cdots & a_{3NG} \\ \vdots & \vdots & \vdots & & \vdots \\ \vdots & \vdots & \vdots & & \vdots \\ a_{NF1} & a_{NF2} & a_{NF3} & & a_{NFNG} \end{bmatrix} \cdot \begin{bmatrix} \phi_1 \\ \phi_2 \\ \phi_3 \\ \vdots \\ \phi_{NG} \end{bmatrix} = \begin{bmatrix} R_1 \\ R_2 \\ R_3 \\ \vdots \\ R_{NF} \end{bmatrix} \quad [5.5.1]$$

The above equation can simply be expressed as

$$A\Phi = R \quad [5.5.2]$$

Where, A = response matrix

R = reaction rates

$\Phi$  = flux matrix (solution spectrum)

NF = number of flux wires

NG = number of energy groups

In the Equation 5.5.1, the number of independent flux wire responses (NF) is equal to the number of desired energy groups (NG) which is a fully determined case. This may not be the case every time. If NF is greater than the NG then the scenario is over determined case. There is more information available than needed in this case. The other possible scenario is when NF is less than the NG. This is the under determined case where the number of equations are less than the number of unknowns; therefore, additional information in the form of an *a priori* spectrum is needed. The under determined case is the most common scenario. In the present work, the focus is on the under determined case since the number of flux wires are less than the number of desired energy groups. The Equation 5.5.3 represents the under determined case with the *a priori* spectrum making it over determined

case. The complete methodology for the application of the least squares to the under determined case can be found, for example in (42) and (43).

$$\begin{bmatrix} a_{11} & a_{12} & a_{13} & \cdots & \cdots & a_{1,NG} \\ a_{21} & a_{22} & a_{23} & \cdots & \cdots & a_{2,NG} \\ \vdots & \vdots & \vdots & & & \vdots \\ a_{NF,1} & a_{NF,2} & a_{NF,3} & \cdots & \cdots & a_{NF,NG} \\ 1 & 0 & 0 & \cdots & \cdots & 0 \\ 0 & 1 & 0 & \cdots & \cdots & 0 \\ 0 & 0 & 1 & \cdots & \cdots & 0 \\ \vdots & \vdots & \vdots & & & \vdots \\ \vdots & \vdots & \vdots & & & \vdots \\ 0 & 0 & 0 & \cdots & \cdots & 1 \end{bmatrix} \cdot \begin{bmatrix} \varphi_1 \\ \varphi_2 \\ \varphi_3 \\ \vdots \\ \vdots \\ \varphi_{NG} \end{bmatrix} = \begin{bmatrix} R_1 \\ R_2 \\ \vdots \\ R_{NF} \\ \varphi_{01} \\ \varphi_{02} \\ \varphi_{03} \\ \vdots \\ \vdots \\ \varphi_{0NG} \end{bmatrix} = [A][\Phi] = [C] \quad [5.5.3]$$

Where,  $\varphi_{01} \dots \varphi_{0NG} = a \text{ priori}$  spectrum

[C]= augmented matrix

To properly weight measured responses and *a priori* fluxes, it is very important to include a covariance matrix. The final equations used to calculate the solution spectrum and its covariance matrix can be seen below.

$$\Phi = \Phi_0 + \text{Cov}(\Phi_0) A_0^T [\text{Cov}(R) + A_0 \text{Cov}(\Phi_0) A_0^T]^{-1} [R - A_0 \Phi_0] \quad [5.5.4]$$

$$\text{Cov}(\Phi) = \text{Cov}(\Phi_0) - \text{Cov}(\Phi_0) A_0^T [\text{Cov}(R) + A_0 \text{Cov}(\Phi_0) A_0^T]^{-1} A_0 \text{Cov}(\Phi_0) \quad [5.5.5]$$

Where,  $\Phi$  = solution spectrum matrix

$\Phi_0 = a \text{ priori}$  spectrum matrix

$A_0$  = response matrix

R = reaction rate matrix

T = matrix transpose

Cov = covariance matrix

More detailed explanation of the Equation 5.5.4 and the Equation 5.5.5 is described in Appendix F.

## 5.6 Data Analysis

Only the counting uncertainties of the measured activities were given. So an additional 5% uncertainty was added in quadrature to the counting uncertainties. The sources for this assumed 5% uncertainty could be detector calibration uncertainty, background count correction uncertainty, sample mass uncertainty, etc. The random uncertainty of the *a priori* spectrum was set to 20% in the least squares method. This gives more room for this method to calculate less biased solution spectrum. Also, *a priori* normalization uncertainty of 10% was assumed. So the combined uncertainty of 22.4% of the *a priori* spectrum was used in the least squares method (44).

As discussed earlier, the measured and the calculated activation rates of all the flux wires from the four positions were used together in the unfolding process for the cadmium experiment. So an average *a priori* spectrum from top to bottom was used to calculate the average solution spectrum of this experiment. But for the boron experiment, the neutron spectrum was unfolded at each position. The four positions of all the flux wires in this experiment were 3, 10, 17 and 23 (see Table 1.4.1.1). A total of 32 equal logarithmic energy bins from  $10^{-7}$  MeV to 19 MeV were used in the unfolding process. All the unfolded neutron spectra were compared with the *a priori* (MCNP5) spectra.

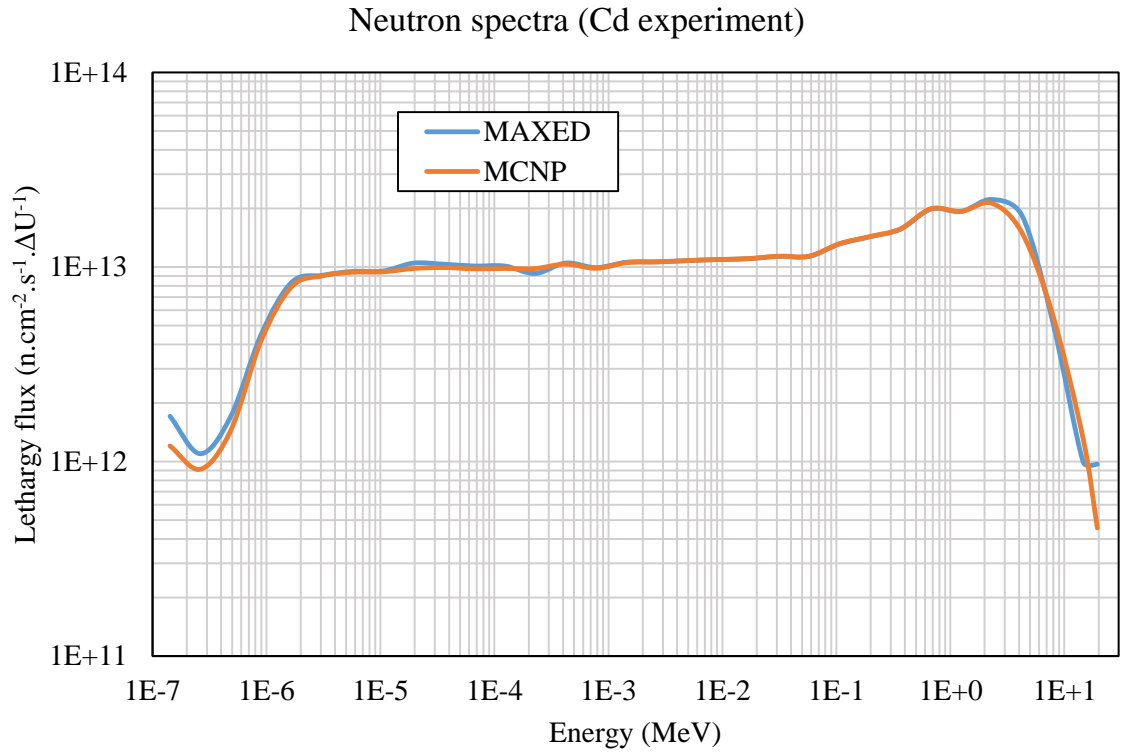


Figure 5.6.1 Average neutron spectra (top to bottom) from MAXED and MCNP

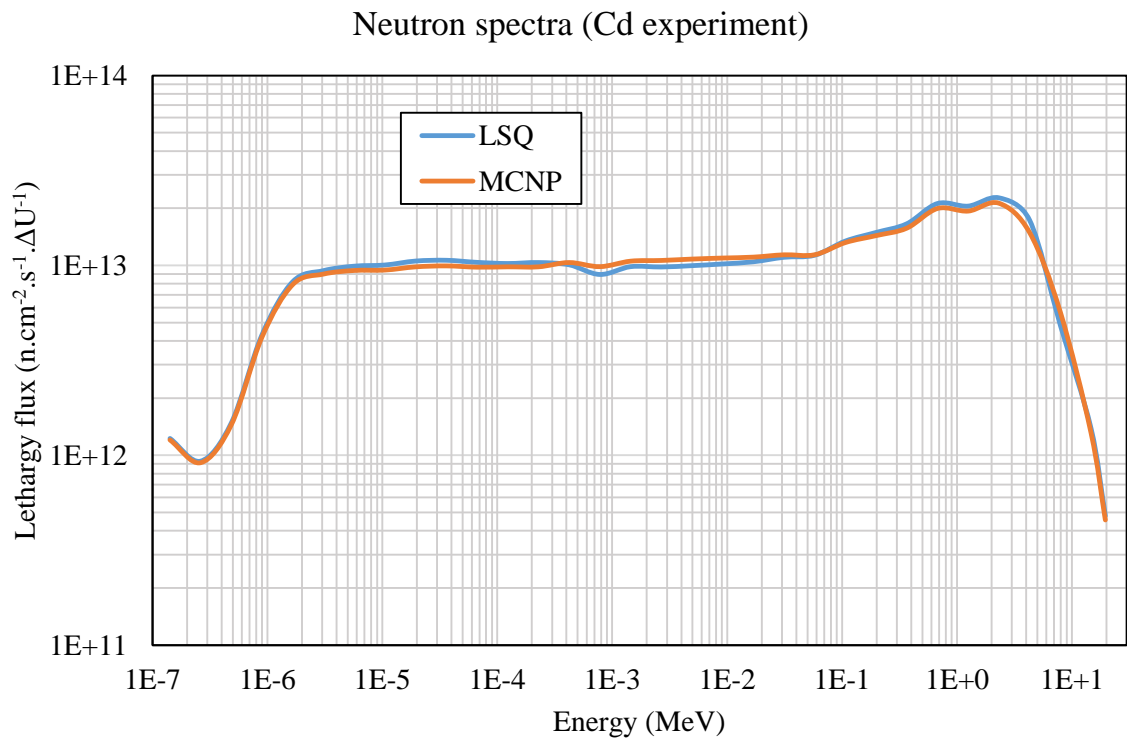


Figure 5.6.2 Average neutron spectra (top to bottom) from LSQ and MCNP

Neutron spectra at position 3 (B experiment)

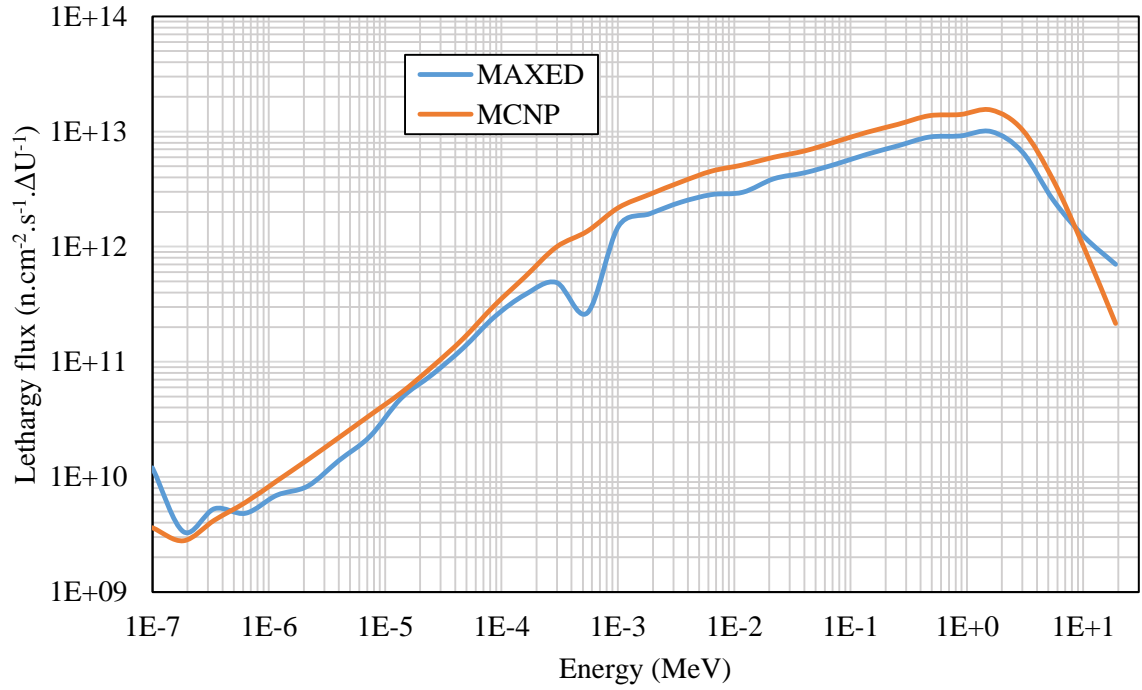


Figure 5.6.3 Neutron spectra at position 3 from MAXED and MCNP

Neutron spectra at position 3 (B experiment)

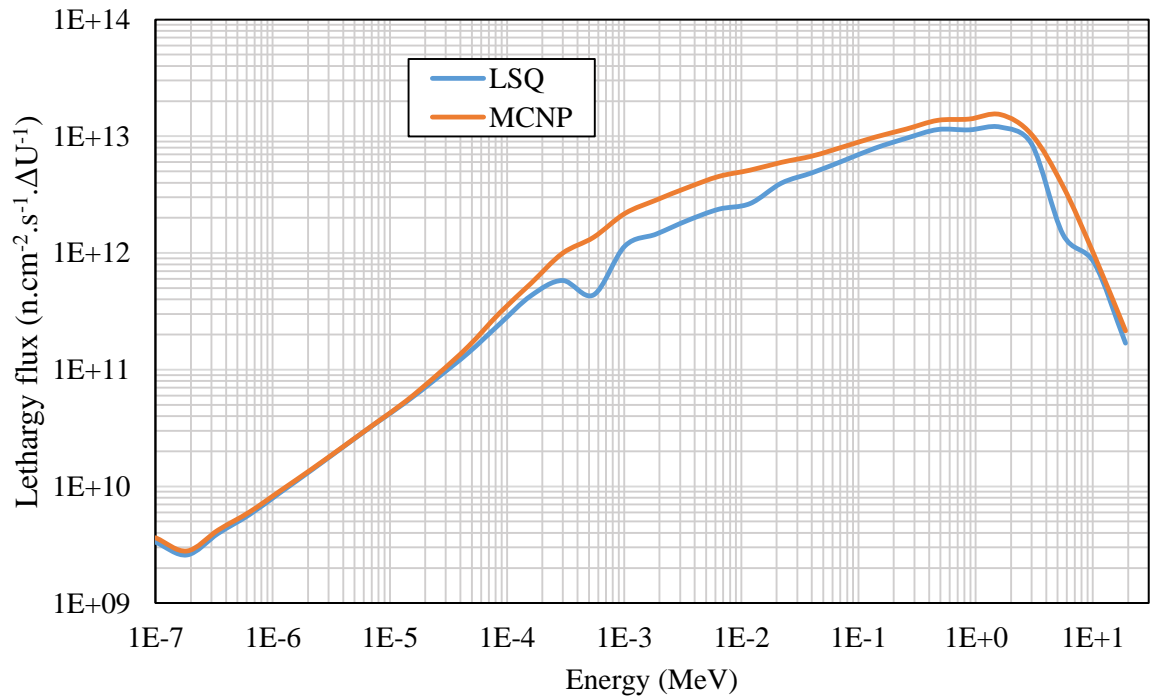


Figure 5.6.4 Neutron spectra at position 3 from LSQ and MCNP

Neutron spectra at position 10 (B experiment)

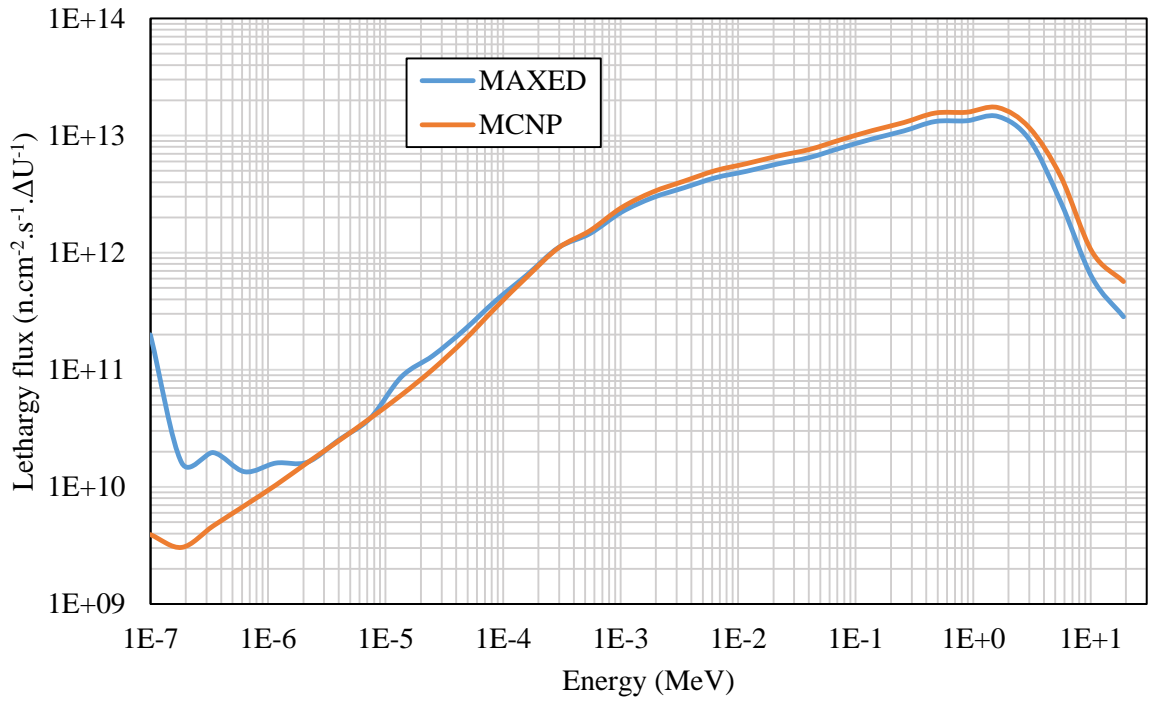


Figure 5.6.5 Neutron spectra at position 10 from MAXED and MCNP

Neutron spectra at position 10 (B experiment)

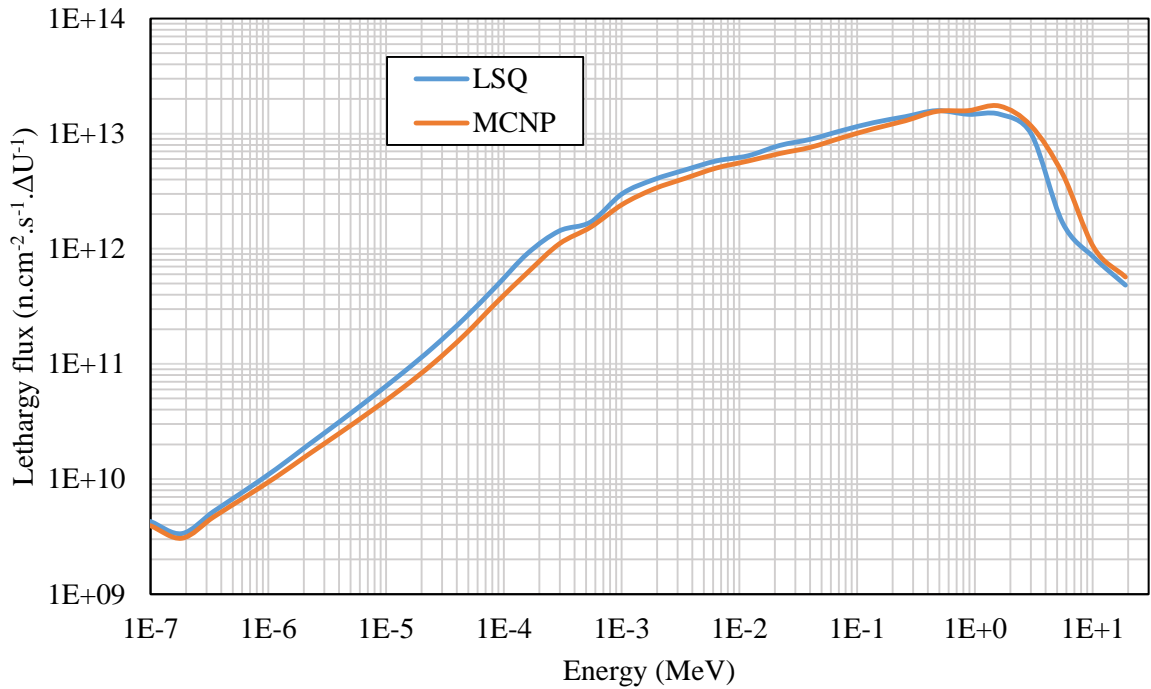


Figure 5.6.6 Neutron spectra at position 10 from LSQ and MCNP

Neutron spectra at position 17 (B experiment)

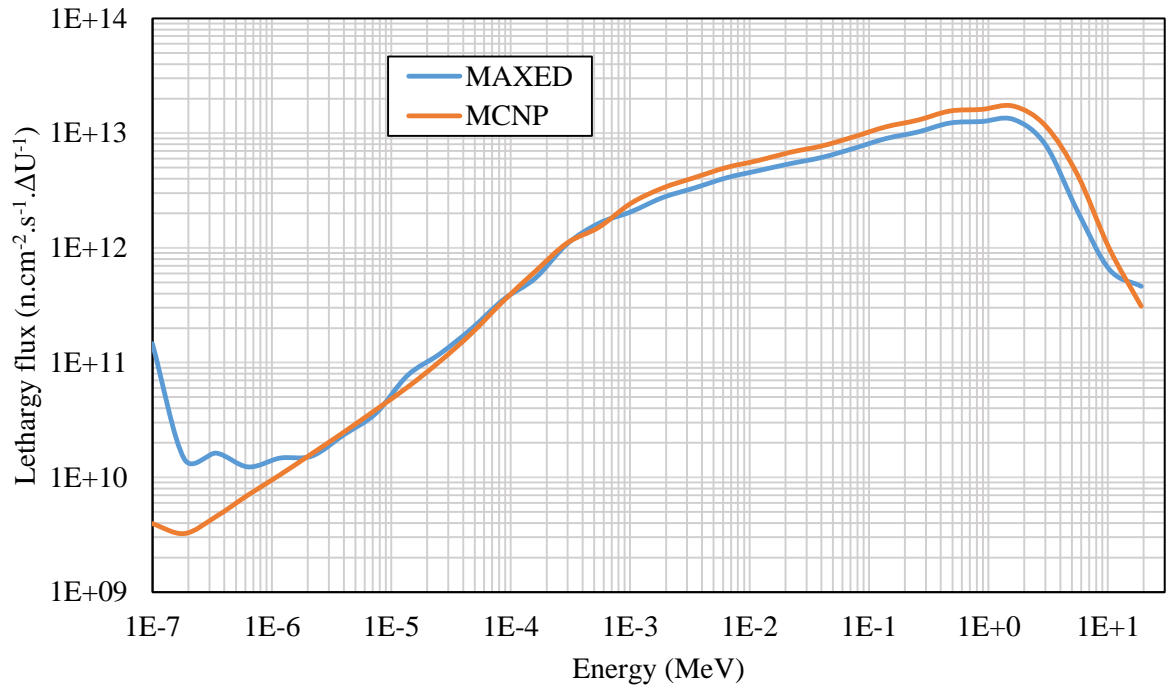


Figure 5.6.7 Neutron spectra at position 17 from MAXED and MCNP

Neutron spectra at position 17 (B experiment)

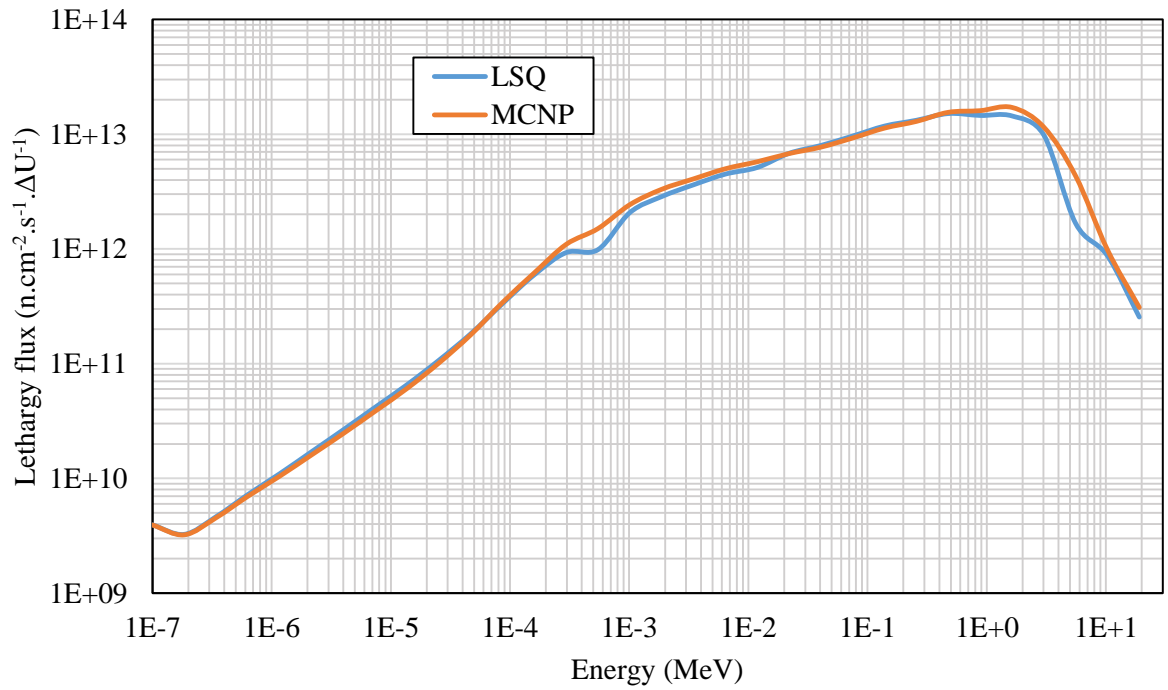


Figure 5.6.8 Neutron spectra at position 17 from LSQ and MCNP

Neutron spectra at position 23 (B experiment)

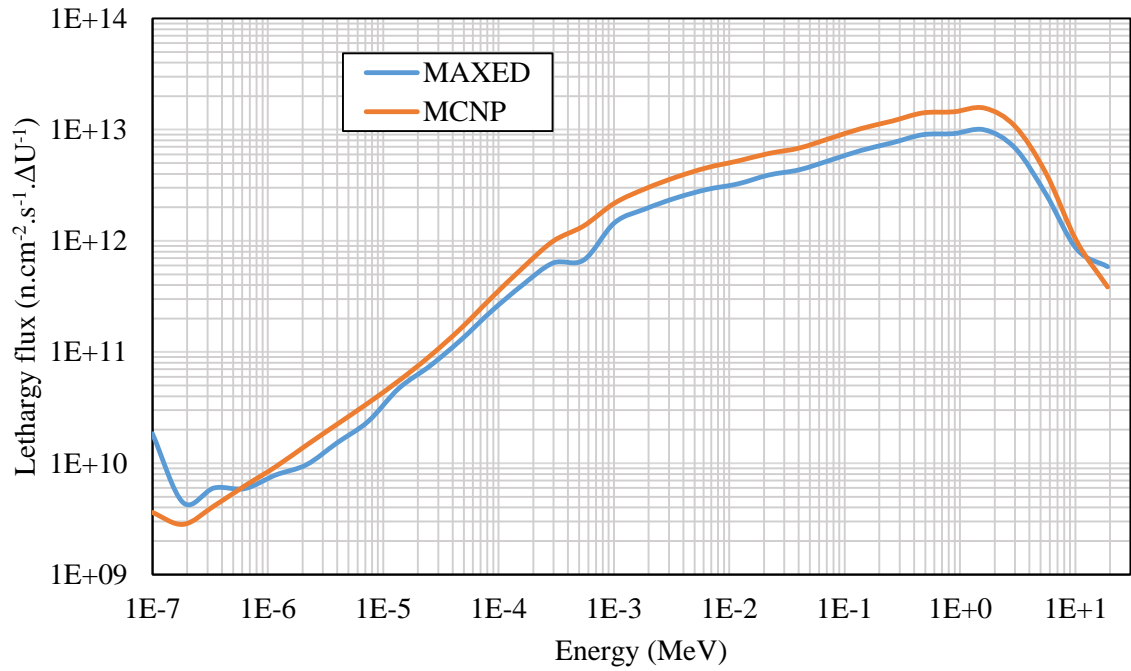


Figure 5.6.9 Neutron spectra at position 23 from MAXED and MCNP

Neutron spectra at position 23 (B experiment)

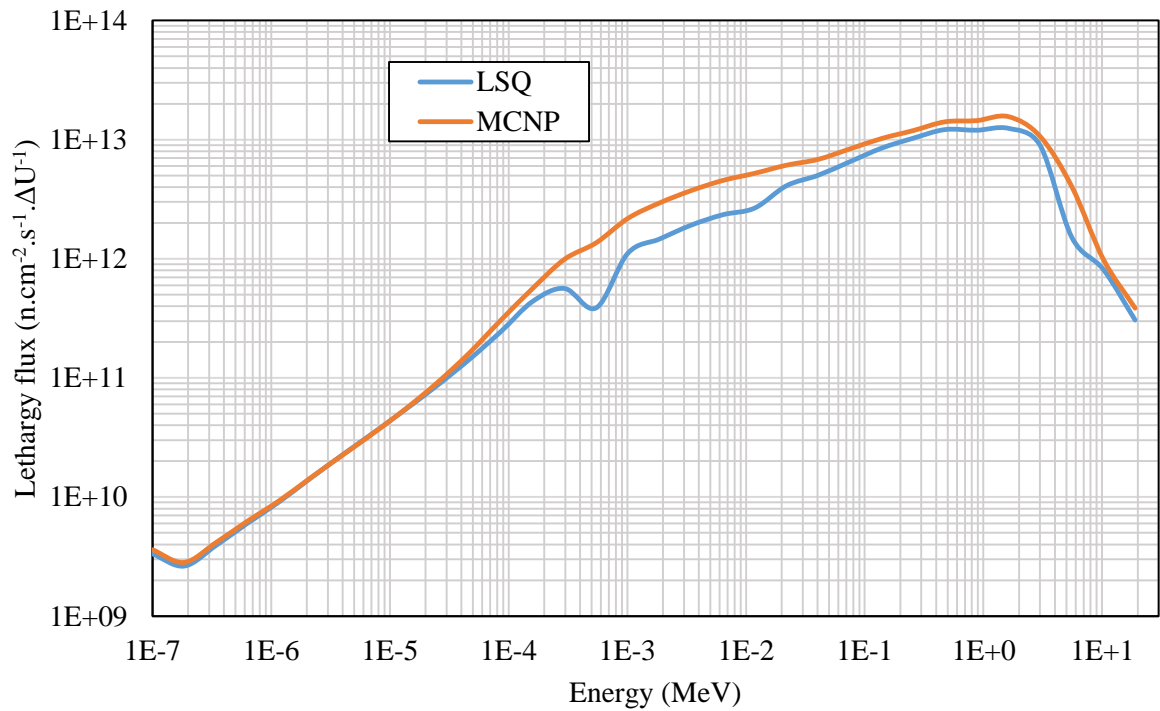


Figure 5.6.10 Neutron spectra at position 23 from LSQ and MCNP

Neutron spectra (top to bottom) from MAXED (B experiment)

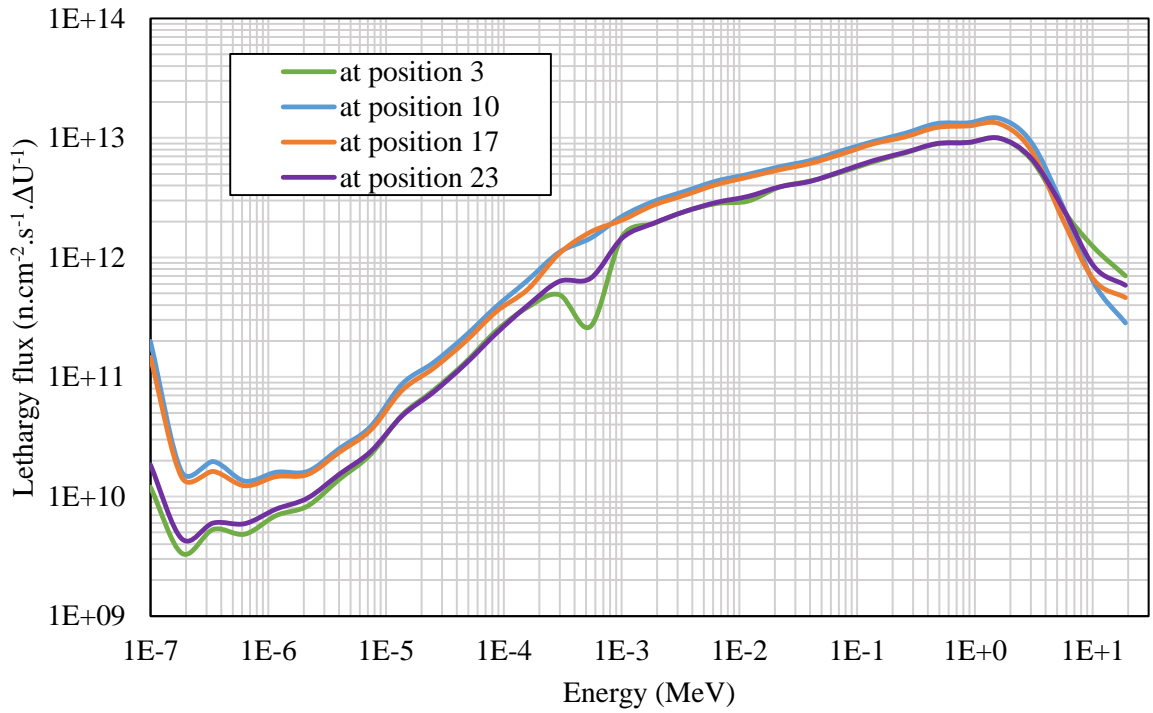


Figure 5.6.11 Neutron spectra at all the four positions from MAXED

Neutron spectra (top to bottom) from LSQ (B experiment)

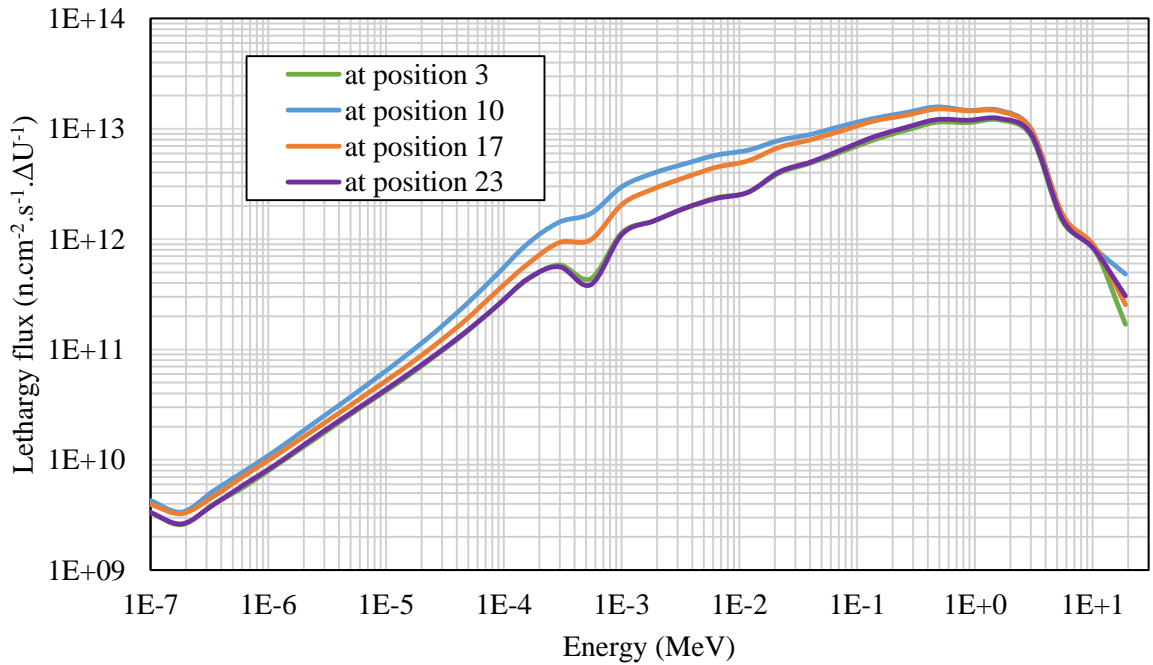


Figure 5.6.12 Neutron spectra at all the four positions from LSQ

From Figure 5.6.1 and Figure 5.6.2, the average solution spectra calculated using MAXED and LSQ were in good agreement with the average *a priori* spectrum of the cadmium experiment. From Figure 5.6.11, the solution neutron spectra from MAXED at all the four positions suggest that there was a leak especially near the center of the boron experiment. This was because of the increase in the thermal peak of the solution spectra at positions 10 and 17 which were close to the center of the experiment. However from Figure 5.6.12, the solution spectra from LSQ did not confirm the leak in this experiment. Clearly from both the Figure 5.6.11 and Figure 5.6.12, the solution spectra at positions 3 and 23 were close to each other. Also, the solution spectra at positions 10 and 17 were close to each other. However, the discrepancies in the solution spectra relative to the *a priori* spectra can be noted from Figures 5.6.3-5.6.10.

The main possible reason for this could be the leaks since the boron filters were stacked one above the other. During the six months wait time between the irradiation cycles, the boron experiment was removed from the ATR and stored in the fuel storage pool. Since there were thin layers of helium before and after the boron filters, multiple transportations of the boron experiment might have caused misalignment in some of the boron filters. Inconsistency in the amount of B10 present in the boron filters from top to bottom might have also caused the discrepancies between the solution and the *a priori* spectra. Post irradiation examination analysis of this experiment could throw some light on the possible causes for the strange C/E ratios and the differences between the solution spectra and the *a priori* spectra. The flux wires with short half-lives might be effected because of the longer wait times between the irradiation cycles and before counting their activities. Also the actual total propagated uncertainties on the measured activities were not known. Tables with the group fluxes of solution and *a priori* spectra were included in the Appendix G.

## 6. CONCLUSIONS

An intense parametric analysis was performed on both the boron and cadmium experiments using MCNP5 and ECCO codes. From section 3, different possible uncertainties in the experiments that could affect the end results were studied. The cross-sections of some samples were sensitive to the uncertainties in the boron experiment setup. Therefore, the post irradiation examination analysis of this experiment could throw some light on the possible causes for the strange C/E ratios and the differences between the solution spectra and the *a priori* spectra. The source files from MCNP5 were successfully implemented in ECCO for the external source calculations.

From section 4, the self-shielding effects were significant in the cadmium experiment because of the presence of the neutron fluxes at epi-thermal energies. The samples with strong resonances at these epi-thermal energies exhibited the largest self-shielding effects. More accurate self-shielding factors were calculated by using MCNP5. The statistics on the MCNP5 results were improved significantly by implementing fixed source calculations and using 500 billion starting particles. It was also important to note that the magnitude of the self-shielding factors for some of the samples depend on their size and shape (45). These self-shielding factors will be used to calculate the final reaction rate ratios (C/E).

MCNP5 was used to calculate the response functions and the *a priori* spectra for the boron and cadmium experiments. From section 5, MAXED and LSQ unfolding techniques were successfully implemented for both the experiments analyzed. The solution spectra in the cadmium experiment were in good agreement with the *a priori* spectrum. In the boron experiment, the solution spectra calculated using MAXED at the two center locations suggest that there was a leak. But the LSQ method did not confirm the same. The solution

spectra calculated at all the positions in this experiment exhibited discrepancies when compared with the *a priori* spectra. The actual total propagated uncertainties on the measured activities of the flux wires were not known. This could be one of the possible reasons for not yielding very good solution spectra. However, one can use the unfolded neutron spectra to calculate the final C/E ratios in the boron experiment.

## APPENDIX A

Example of an input file for ECCO used to calculate the cross-sections can be seen below.

```
= 'TYPE DE TRACE' 2 ;
= 'FICHIER ECHO' 6 ;
PROCEDURE ->IS10ECVA
;
TIME ;
->BBL172G 'ENDF_70.172' ;
->BBL1968G 'ENDF_70.1968' ;
->BBLREF 'ENDF_70.REFM' ;
!!! abundances
->SI28 0.9223 ;
->SI29 0.04670 ;
->SI30 0.03100 ;

->MO92 0.1484003;
->MO94 0.0925003;
->MO95 0.1592001;
->MO96 0.1667994;
->MO97 0.0955003;
->MO98 0.2412999;
->MO100 0.0962998;

->FE54 (5.845/100.) ;
->FE56 (91.754/100.) ;
->FE57 (2.119/100.) ;
->FE58 (0.282/100.) ;

->CR50 (4.345/100.) ;
->CR52 (83.789/100.) ;
->CR53 (9.501/100.) ;
->CR54 (2.365/100.) ;

->NI58 (68.0769/100.) ;
->NI60 (26.2231/100.) ;
->NI61 (1.1399/100.) ;
->NI62 (3.6345/100.) ;
->NI64 (0.9256/100.) ;

->TI46 (8.25/100) ;
->TI47 (7.44/100) ;
->TI48 (73.72/100) ;
->TI49 (5.41/100) ;
->TI50 (5.18/100) ;

!=====
! DONNEES CONSTANTES
!=====
->DPA_SECTION
```

1059.3 399.5 171.16 45.87 12.45 5.44E-2 ;

!=====  
!           CREATION MILIEU  
!=====

!ARCHIVE INITIALISER 2000 4096 ;  
MEDIUM\_CREATION ->EDL\_MILIEU  
REFERENCE\_UNIT (BBLREF)  
INITIAL\_TEMPERATURE 20.

!=====  
!       DEFINITION DES MATERIAU  
!=====

SIMPLE\_MATERIAL 'SAMPLE' ABSORBER  
WEIGHT\_PERCENTAGE 7.735E-3  
ELEMENT CIP 100.0  
'AM241' 100.0  
EXPANSION 20. 0. 1327. 0.

SIMPLE\_MATERIAL 'SS316L' STRUCTURE  
NUMBER\_OF\_ATOMS  
ISOTOPE  
  'FE54' 3.32016e-03 'FE56' 5.20726e-02  
  'FE57' 1.20320e-03 'FE58' 1.58914e-04  
  'CR50' 6.87752e-04 'CR52' 1.32475e-02  
  'CR53' 1.50199e-03 'CR54' 3.73125e-04  
  'NI58' 6.73132e-03 'NI60' 2.59247e-03  
  'NI61' 1.12716e-04 'NI62' 3.58911e-04  
  'NI64' 9.19525e-05  
  'MO92' 1.86998e-04 'MO94' 1.16559e-04  
  'MO95' 2.00607e-04 'MO96' 2.10184e-04  
  'MO97' 1.20339e-04 'MO98' 3.04061e-04  
  'MO100' 1.21347e-04  
  'S32' 4.52418e-05  
  'N14' 3.45244e-04  
  'P31' 7.02558e-05 'SI28' (1.29135e-03\*SI28)  
  'SI29' (1.29135e-03\*SI29) 'SI30' (1.29135e-03\*SI30)  
  'CO' 1.20783e-04  
  'MN55' 1.76044e-03  
EXPANSION 20. 0. 1327. 0.

SIMPLE\_MATERIAL 'SS316' STRUCTURE  
NUMBER\_OF\_ATOMS  
ISOTOPE  
  'FE54' 3.31763e-03 'FE56' 5.20329e-02  
  'FE57' 1.20229e-03 'FE58' 1.20229e-04  
  'CR50' 6.87752e-04 'CR52' 1.32475e-02  
  'CR53' 1.50199e-03 'CR54' 3.73125e-04  
  'NI58' 6.73132e-03 'NI60' 2.59247e-03  
  'NI61' 1.12716e-04 'NI62' 3.58911e-04  
  'NI64' 9.19525e-05  
  'MO92' 1.86998e-04 'MO94' 1.16559e-04  
  'MO95' 2.00607e-04 'MO96' 2.10184e-04

'MO97' 1.20339e-04 'MO98' 3.04061e-04  
'MO100' 1.21347e-04  
'S32' 4.52418e-05  
'N14' 3.45244e-04  
'P31' 7.02558e-05 'SI28' (1.29135e-03\*SI28)  
'SI29' (1.29135e-03\*SI29) 'SI30' (1.29135e-03\*SI30)  
'C0' 3.22088e-04  
'MN55' 1.76044e-03  
EXPANSION 20. 0. 1327. 0.

SIMPLE\_MATERIAL 'B4C\_THIN' ABSORBER  
NUMBER\_OF\_ATOMS  
ISOTOPE  
'C0' 2.730295E-02  
'B10' 7.647252E-02  
'B11' 3.268709E-02  
EXPANSION 20. 0. 1327. 0.

SIMPLE\_MATERIAL 'ALUMINUM' STRUCTURE  
NUMBER\_OF\_ATOMS  
ISOTOPE  
'AL27' 6.00620e-02  
'FE54' 4.27394e-06 'FE56' 6.70315e-05  
'FE57' 1.54885e-06 'FE58' 2.04565e-07  
'SI28' 1.33982e-04 'SI29' 6.78409e-06  
'SI30' 4.50336e-06 'MN55' 7.42649e-06  
'ZN0' 6.69848E-5  
'CU63' 2.22053e-05 'CU65' 9.89721e-06  
EXPANSION 20. 0. 1327. 0.

SIMPLE\_MATERIAL 'HELIUM' COOLANT  
NUMBER\_OF\_ATOMS  
ISOTOPE  
'HE4' 2.60000E-05  
EXPANSION 20. 0. 1327. 0.

SIMPLE\_MATERIAL 'VOID' COOLANT  
NUMBER\_OF\_ATOMS  
ISOTOPE  
'HE4' 1.00000E-10  
EXPANSION 20. 0. 1327. 0.

SIMPLE\_MATERIAL 'WATER' COOLANT  
NUMBER\_OF\_ATOMS  
ISOTOPE  
'O16' 3.34253E-2 'H1' 6.68506E-2  
EXPANSION 20. 0. 1327. 0.

MEDIUM 'SAMPLE'  
'SAMPLE' 100.  
MEDIUM 'SS316L'

'SS316L' 100.  
MEDIUM 'SS316'  
'SS316' 100.  
MEDIUM 'WATER'  
'WATER' 100.  
MEDIUM 'HE'  
'HELIUM' 100.  
MEDIUM 'B4C'  
'B4C\_THIN' 100.  
MEDIUM 'VOID'  
'VOID' 100.

CELL 'MANTRA'  
EDITION

COMPOSITION\_ORDER 'SAMPLE' 'SS316L' 'HE' 'SS316' 'WATER' 'HE' 'B4C'  
'VOID'

GEOMETRY DATA

!!! Boron experiment

CYL 19

0.24003	REGION 1	'SAMPLE'	COMP 1	293.16
0.29972	REGION 2	'RODLET'	COMP 2	293.16
0.35179	REGION 3	'AIRGAP'	COMP 3	293.16
0.47625	REGION 4	'CAPSULE'	COMP 4	293.16
0.59563	REGION 5	'WATERGAP'	COMP 5	293.16
0.66675	REGION 6	'BASKET'	COMP 4	293.16
0.67310	REGION 7	'HELIUM'	COMP 6	293.16
0.77310	REGION 8	'B4C'	COMP 7	293.16
0.87310	REGION 9	'B4C'	COMP 7	293.16
0.97310	REGION 10	'B4C'	COMP 7	293.16
1.07310	REGION 11	'B4C'	COMP 7	293.16
1.18999	REGION 12	'B4C'	COMP 7	293.16
1.42875	REGION 13	'HELIUM'	COMP 6	293.16
1.52880	REGION 14	'SLEEVE'	COMP 4	293.16
1.62880	REGION 15	'SLEEVE'	COMP 4	293.16
1.72880	REGION 16	'SLEEVE'	COMP 4	293.16
1.82880	REGION 17	'SLEEVE'	COMP 4	293.16
1.90499	REGION 18	'WATERGAP'	COMP 5	293.16
1.90500	REGION 19	'VOID'	COMP 8	293.16

REFLECT

END OF GEOMETRY DATA

;

ECCO

MEDIUM (EDL\_MILIEU)

REFERENCE\_UNIT (BBLREF)

CELL 'MANTRA'

EDITION MAXI

'SAMPLE'

STEPS 3

STEP

GEOMETRY ORIGINAL

ELEMENTS ALL

GROUP STRUCTURE OTHER 172  
INPUT LIBRARY (BBL172G)  
FLUX SOLUTION CP P1 CONSISTENT ORDER 1  
PROFILE TRANSPORT CROSS  
LEAKAGE DBBABS CELL BENOIST FLUXWT MEAN  
BUCKLING 0.00  
SUBCRITICAL SOURCE 54  
SELF SHIELDING DBBSH  
STEP  
GEOMETRY ORIGINAL  
GROUP STRUCTURE FINE  
INPUT LIBRARY (BBL1968G)  
FIND\_ELEMENTS\_IN\_LIST  
'U234' 'U235' 'U236' 'U238' 'AL27'  
'FE54' 'FE56' 'FE57' 'FE58' 'CR50'  
'CR52' 'CR53' 'CR54' 'SI28' 'SI29'  
'SI30' 'MN55' 'PU240' 'N14' 'MN55'  
'NI58' 'NI60' 'NI61' 'NI62' 'NI64'  
'MO92' 'MO94' 'MO95' 'MO96' 'MO97'  
'MO98' 'MO100' 'HE4' 'O16' 'H1'  
'AM241'  
FLUX SOLUTION CP P1 CONSISTENT ORDER 1  
BUCKLING 0.00  
SUBCRITICAL FROM PREVIOUS STEP  
PROFILE TRANSPORT CROSS  
LEAKAGE DBBABS CELL BENOIST FLUXWT MEAN  
SELF SHIELDING DBBSH  
CONDENSE 33  
1 82 142 202 262 322 382 442 502 564 624  
686 746 808 868 928 988 1048 1108 1168 1228 1288  
1336 1422 1480 1516 1579 1648 1708 1768 1837 1919 1952  
STEP  
GEOMETRY ORIGINAL  
GROUP STRUCTURE OTHER 33  
FLUX SOLUTION CP P1 CONSISTENT ORDER 1  
SUBCRITICAL FROM PREVIOUS STEP  
PROFILE TRANSPORT CROSS  
LEAKAGE DBBABS CELL BENOIST FLUXWT MEAN  
SELF SHIELDING DBBSH  
BFROM 2  
OUTPUT LIBRARY 'MANTRA\_33'  
PRINT DATA FLUXES  
CROSS SECTIONS MICROSCOPIC VECTORS  
ENDSTEPS  
;  
TIME ;  
SUPPRIMER\_FICHER 'MANTRA\_33' ;  
FINPROC ;  
IS10ECVA ;  
FIN ;

## APPENDIX B

The simple FORTRAN code used to create an external source file for ECCO.

```
PROGRAM Write_Source
!!!! Write source for ECCO on logical unit 54
  Implicit Double Precision (A-H,O-Z)
  INTEGER, parameter :: Nin = 5, Nout = 6
  Double Precision, Dimension(:), pointer :: MCNP_Source
  Double Precision, Dimension(:,,:), pointer :: ECCO_Source
!!!!
  read(nin,*) Number_Groups, Number_Regions, Number_Source_Region
  write(nout,*) Number_Groups, Number_Regions, Number_Source_Region
!!!! Number_Groups = Number of energy groups
!!!! Number_Regions = Number of Regions in ECCO geometry
!!!! Number_Source_Region = number of ECCO region where source has to be located
!!!! Allocate memory for arrays
  allocate (MCNP_Source (Number_Groups), &
           ECCO_Source (Number_Regions,Number_Groups))
  ECCO_Source=0.
  Do i=1, Number_Groups
    read (5,*,end=100) MCNP_Source(i)
    write(nout, *) i, MCNP_Source(i)
  enddo
  100 continue
  ECCO_Source(Number_Source_Region,1:Number_Groups)= MCNP_Source
  LU=54
  A=0.
  open(LU,FILE='FILE54',STATUS='NEW',FORM='FORMATTED')
  do j=1,Number_Groups
    write(LU,*)(ECCO_Source(i,j),i=1,Number_Regions)
  enddo
  do j=1,Number_Groups
    write(LU,*)(A,i=1,Number_Regions)
  enddo
  do j=1,Number_Groups
    write(nout,*)(ECCO_Source(i,j),i=1,Number_Regions)
  enddo
end
```

## APPENDIX C

The plots of the sensitivity coefficients of all the samples in the boron experiments can be seen below.

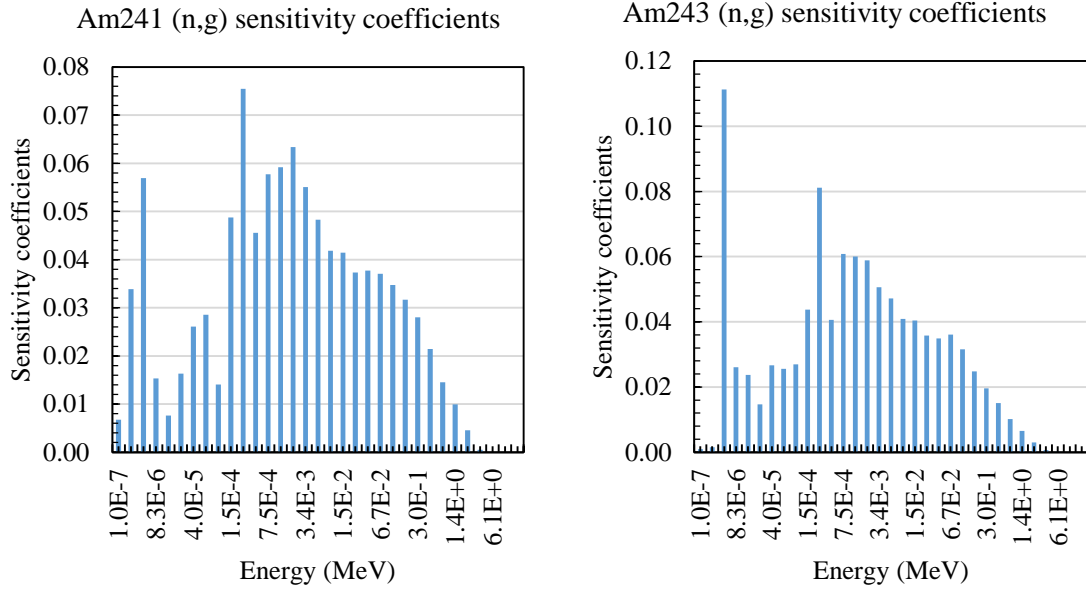


Figure C.1 Sensitivity coefficients of Am241 (left) and Am243 (right)  $\sigma_g$  cross-sections

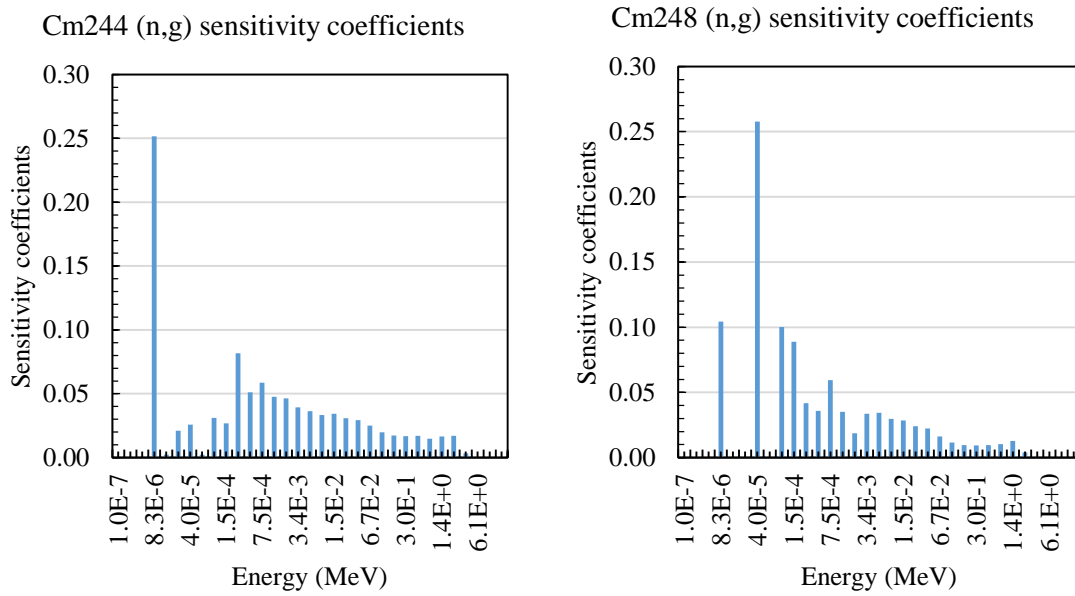


Figure C.2 Sensitivity coefficients of Cm244 (left) and Cm248 (right)  $\sigma_g$  cross-sections

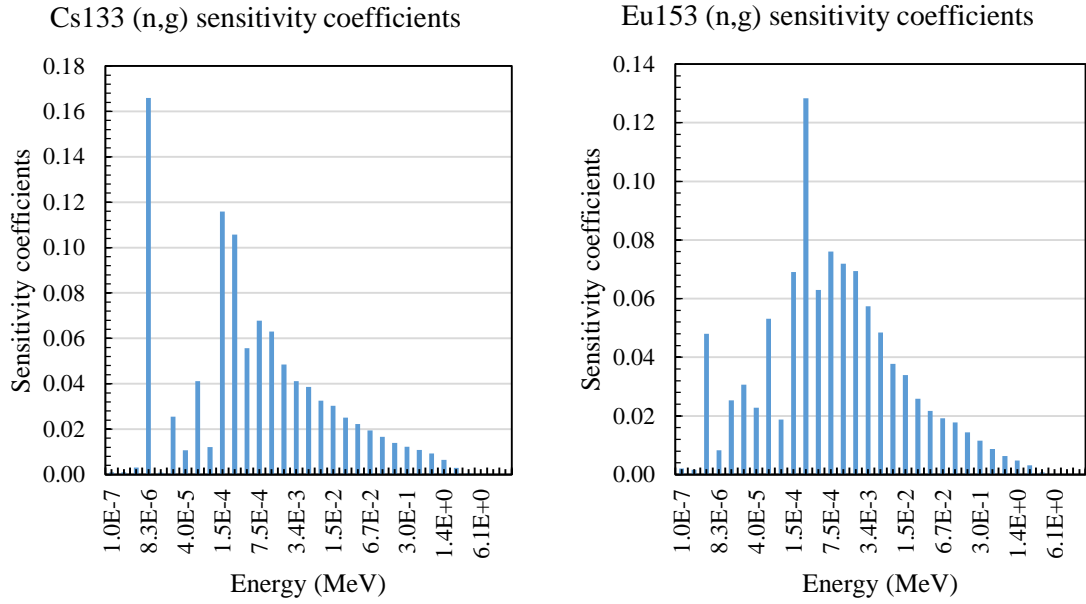


Figure C.3 Sensitivity coefficients of Cs133 (left) and Eu153 (right)  $\sigma_g$  cross-sections

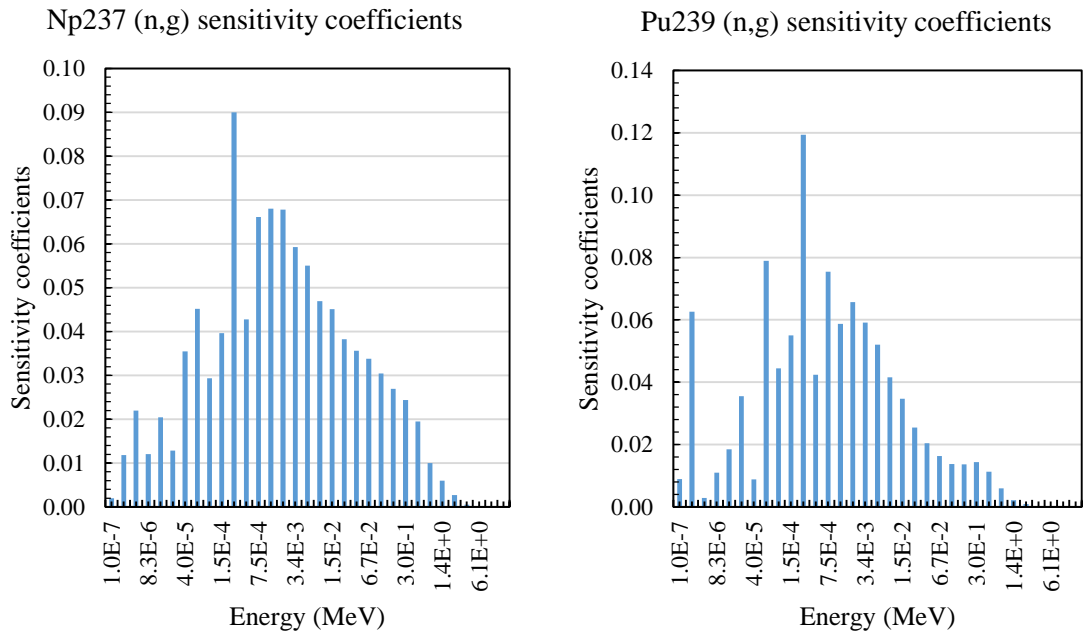


Figure C.4 Sensitivity coefficients of Np237 (left) and Pu239 (right)  $\sigma_g$  cross-sections

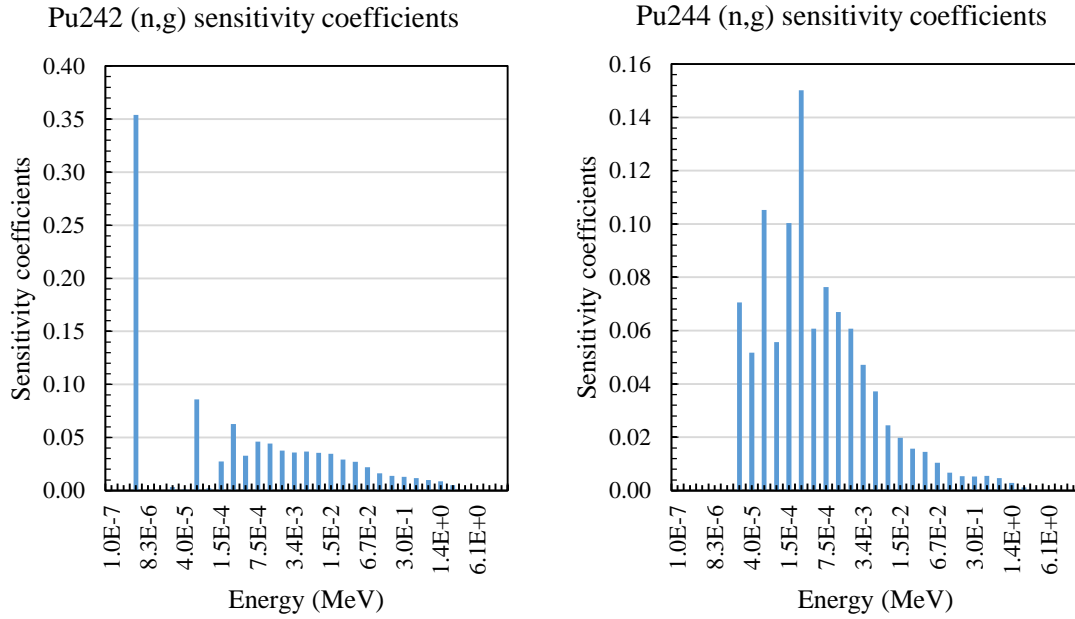


Figure C.5 Sensitivity coefficients of Pu242 (left) and Pu244 (right)  $\sigma_g$  cross-sections

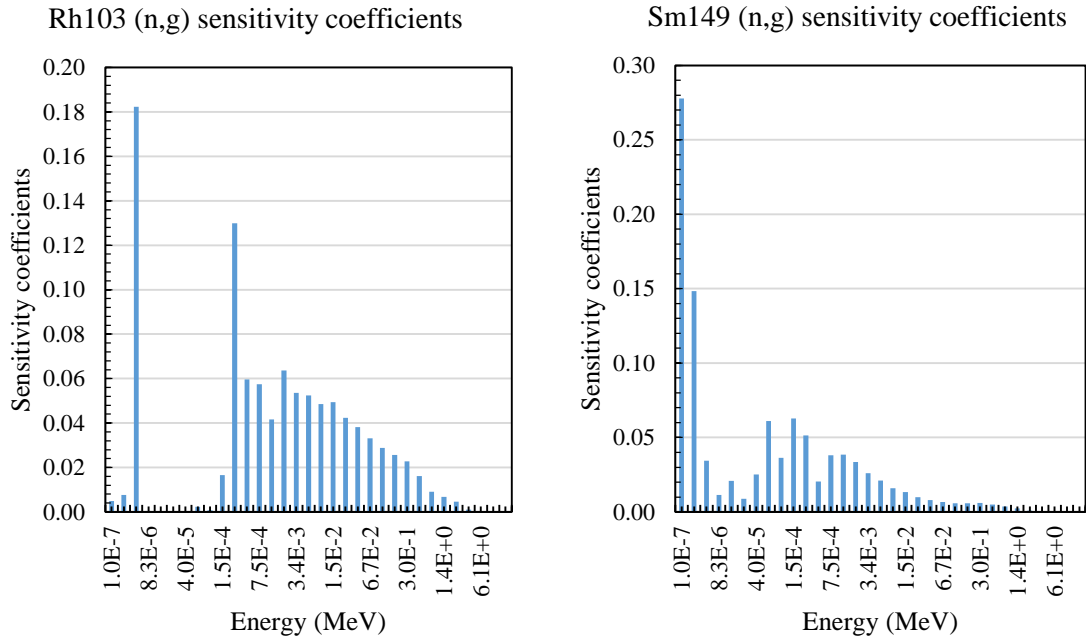


Figure C.6 Sensitivity coefficients of Rh103 (left) and Sm149 (right)  $\sigma_g$  cross-sections

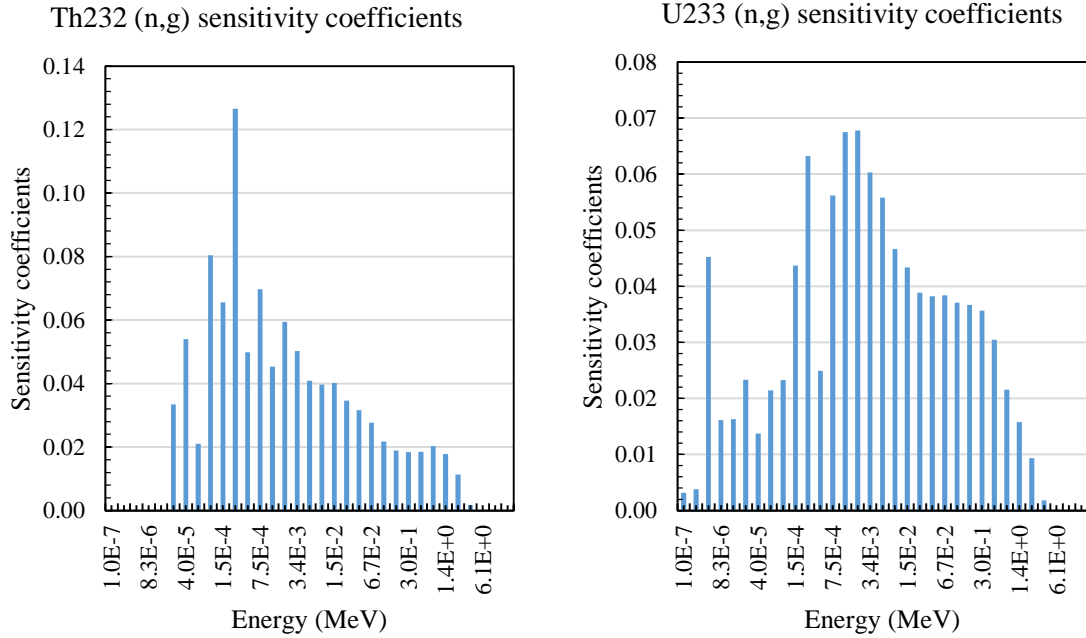


Figure C.7 Sensitivity coefficients of Th232 (left) and U233 (right)  $\sigma_g$  cross-sections

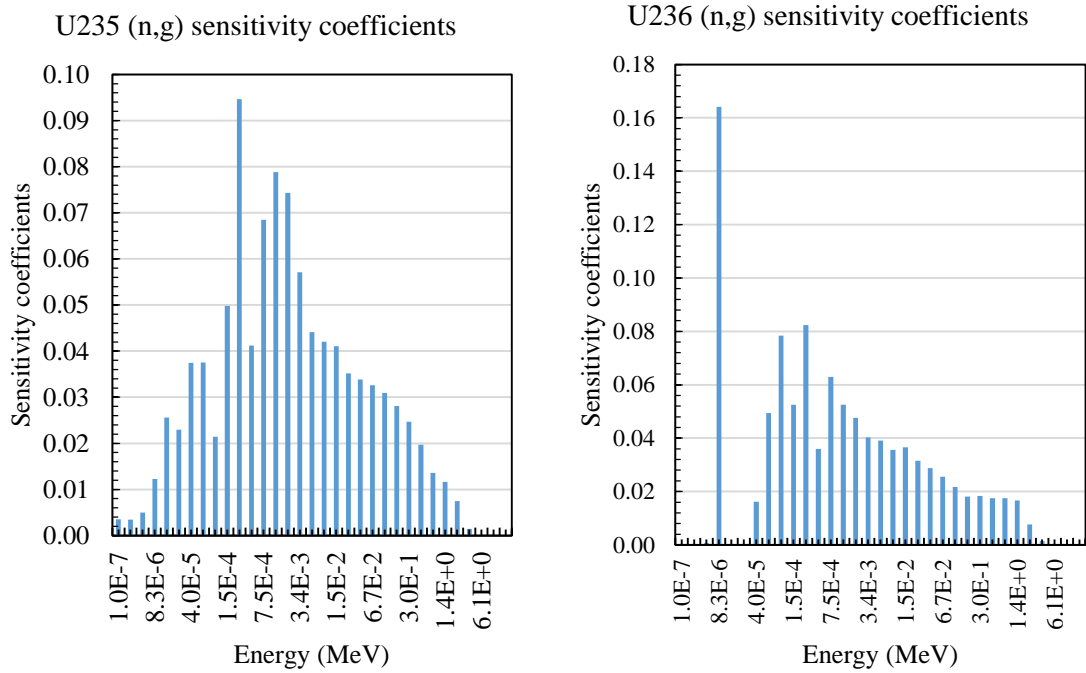


Figure C.8 Sensitivity coefficients of U235 (left) and U236 (right)  $\sigma_g$  cross-sections

The plots of the sensitivity coefficients of all the samples in the cadmium experiments can be seen below.

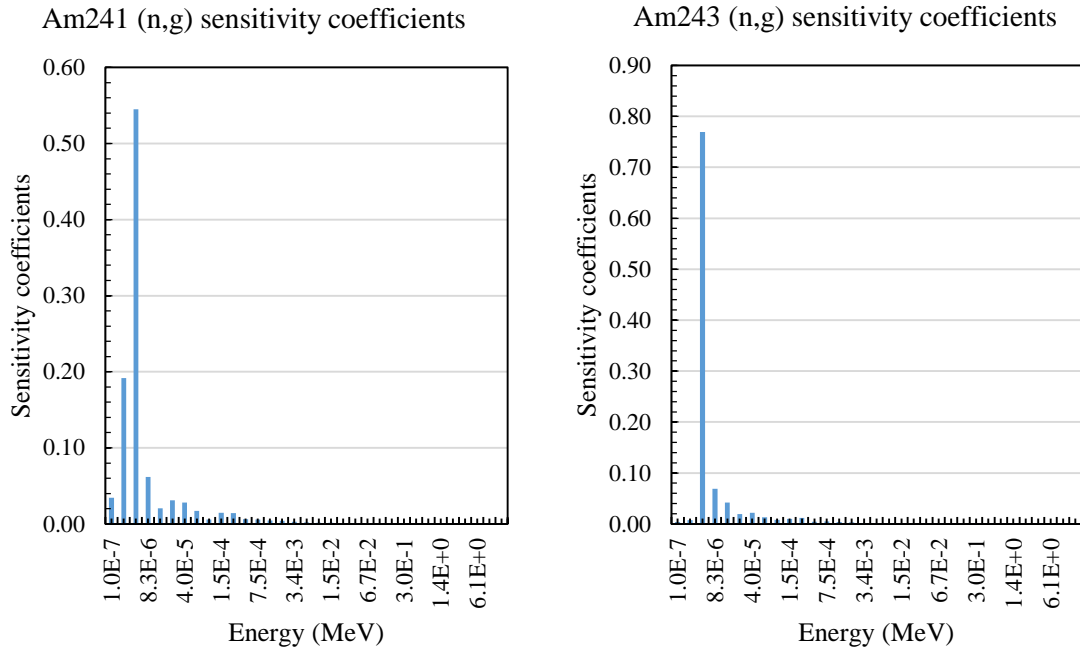


Figure C.9 Sensitivity coefficients of Am241 (left) and Am243 (right)  $\sigma_g$  cross-sections

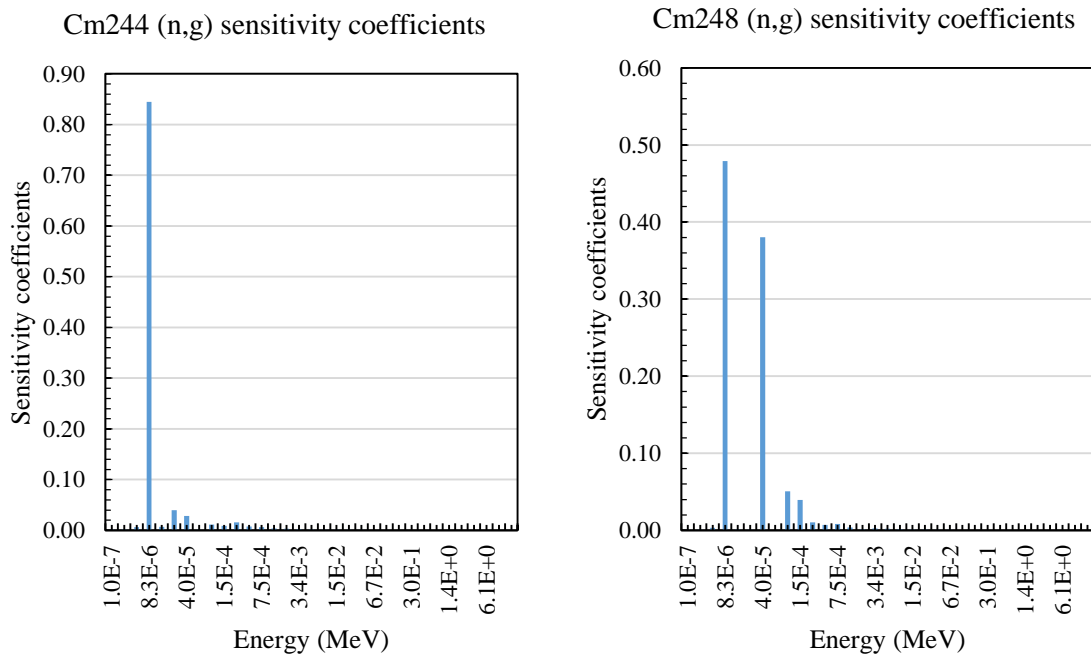


Figure C.10 Sensitivity coefficients of Cm244 (left) and Cm248 (right)  $\sigma_g$  cross-sections

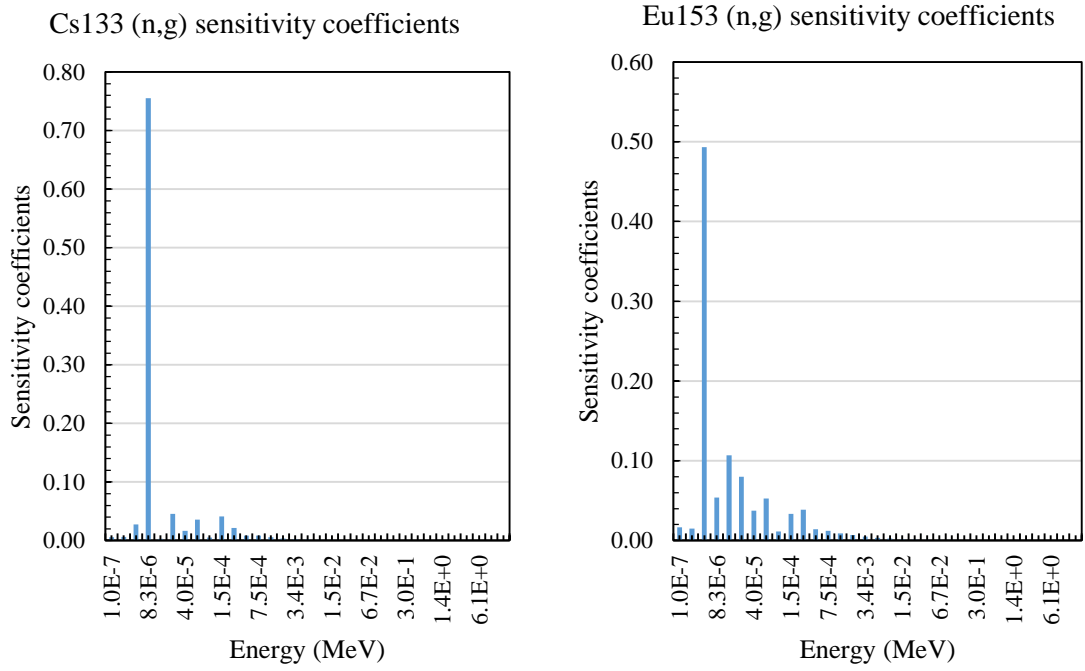


Figure C.11 Sensitivity coefficients of Cs133 (left) and Eu153 (right)  $\sigma_g$  cross-sections

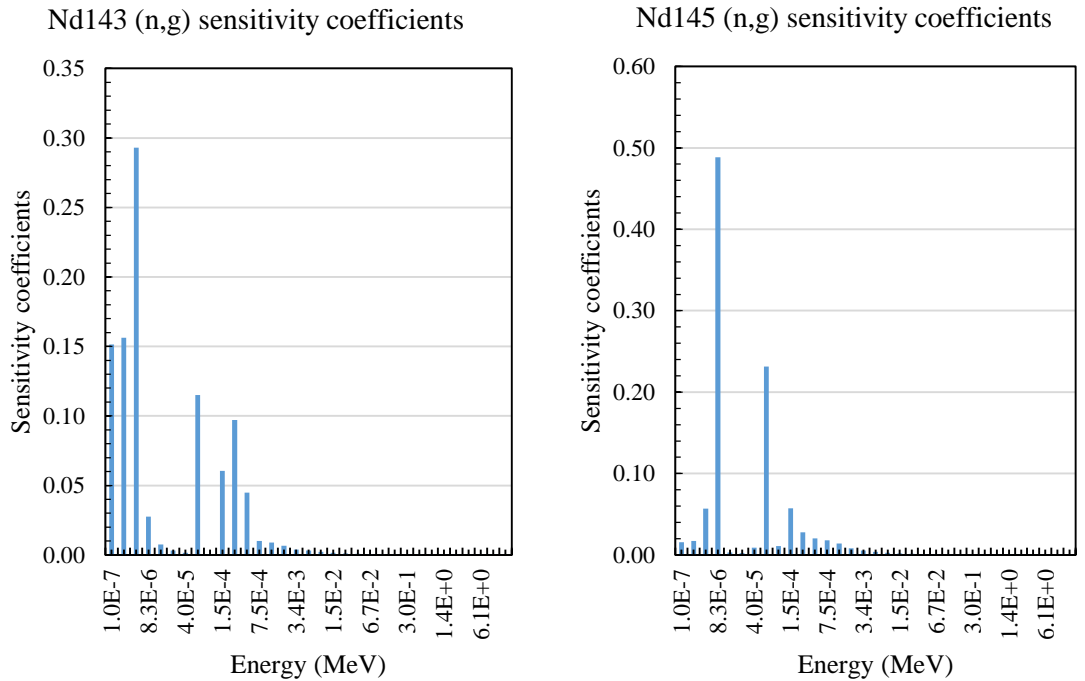


Figure C.12 Sensitivity coefficients of Nd143 (left) and Nd145 (right)  $\sigma_g$  cross-sections

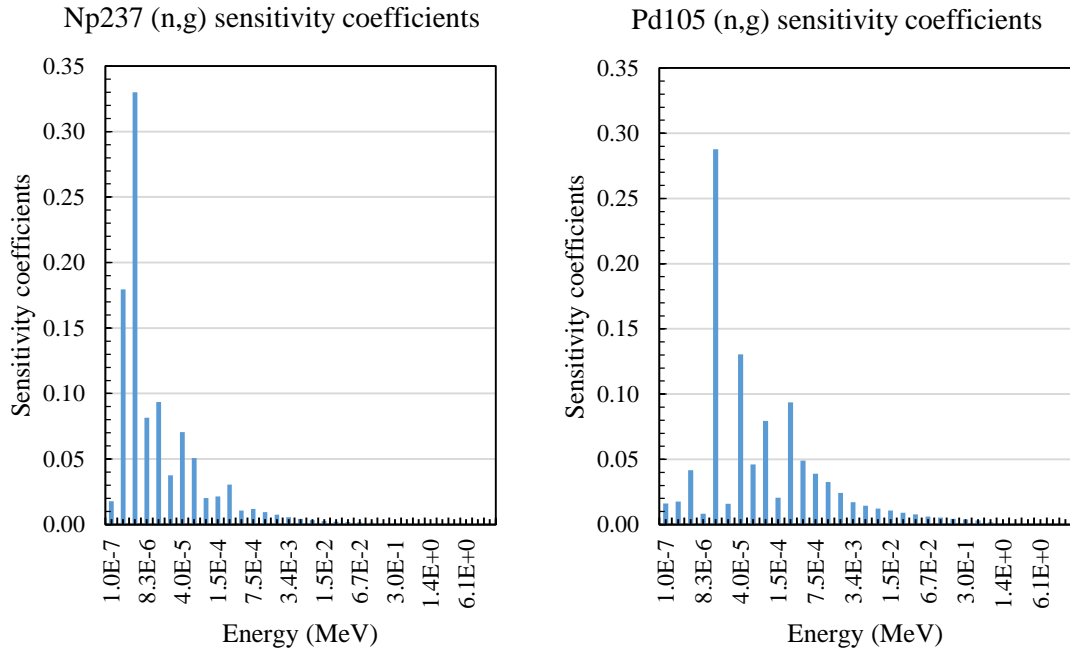


Figure C.13 Sensitivity coefficients of Np237 (left) and Pd105 (right)  $\sigma_g$  cross-sections

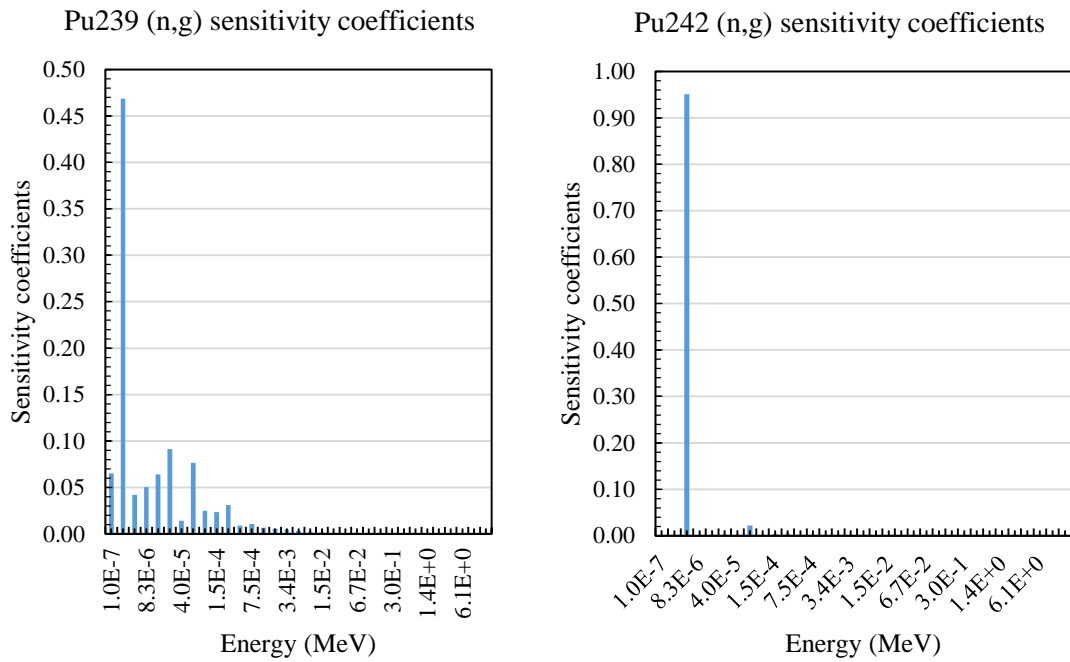


Figure C.14 Sensitivity coefficients of Pu239 (left) and Pu242 (right)  $\sigma_g$  cross-sections

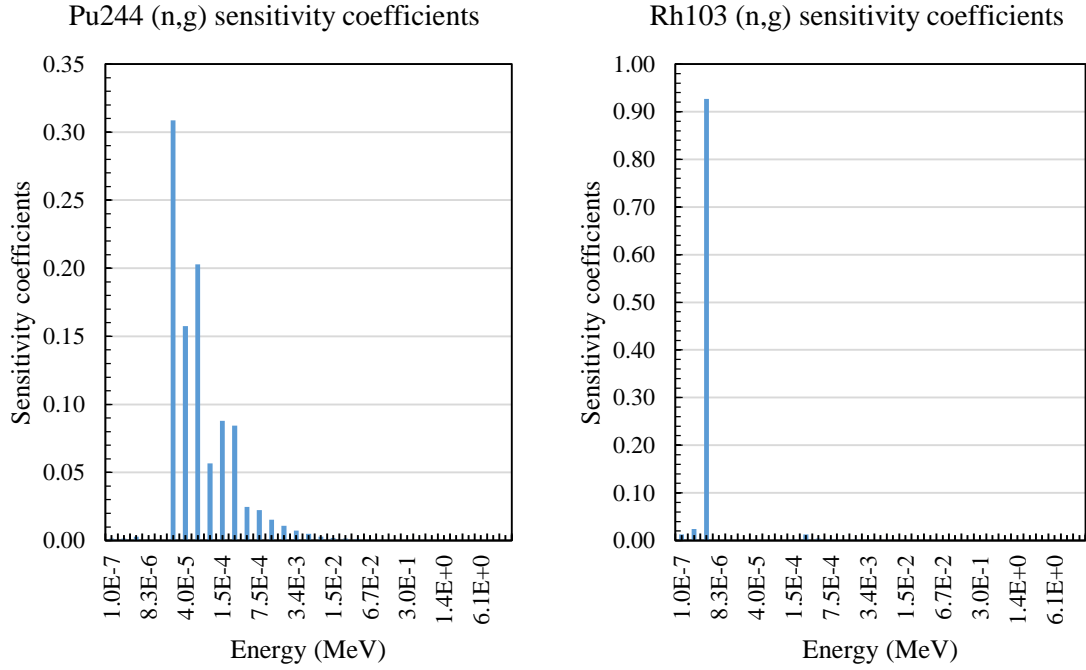


Figure C.15 Sensitivity coefficients of Pu244 (left) and Rh103 (right)  $\sigma_g$  cross-sections

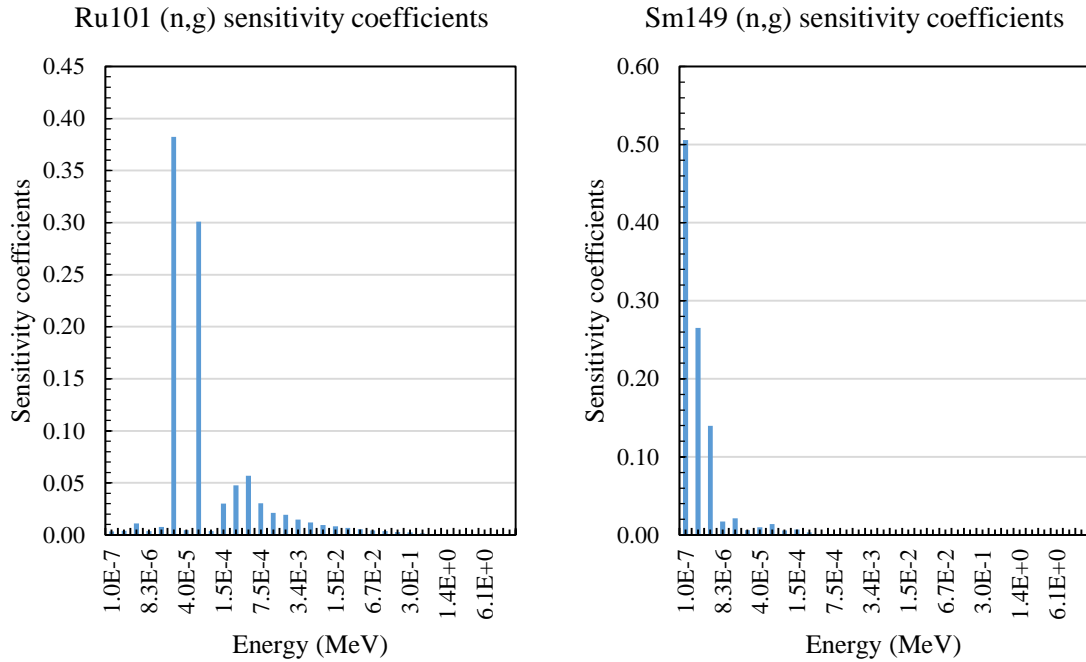


Figure C.16 Sensitivity coefficients of Ru101 (left) and Sm149 (right)  $\sigma_g$  cross-sections

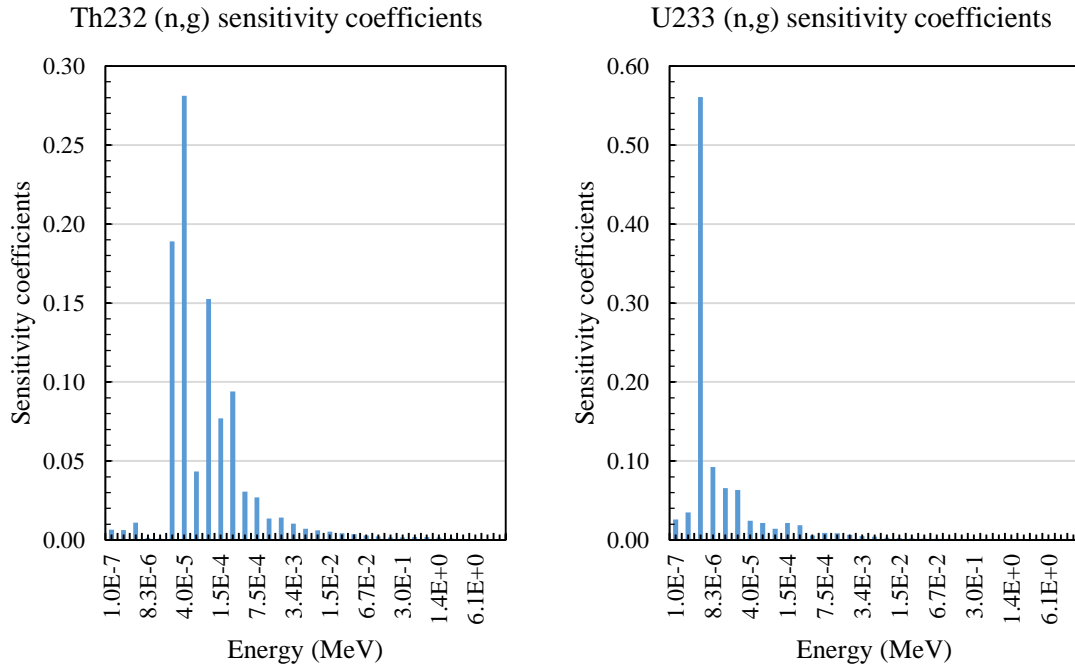


Figure C.17 Sensitivity coefficients of Th232 (left) and U233 (right)  $\sigma_g$  cross-sections

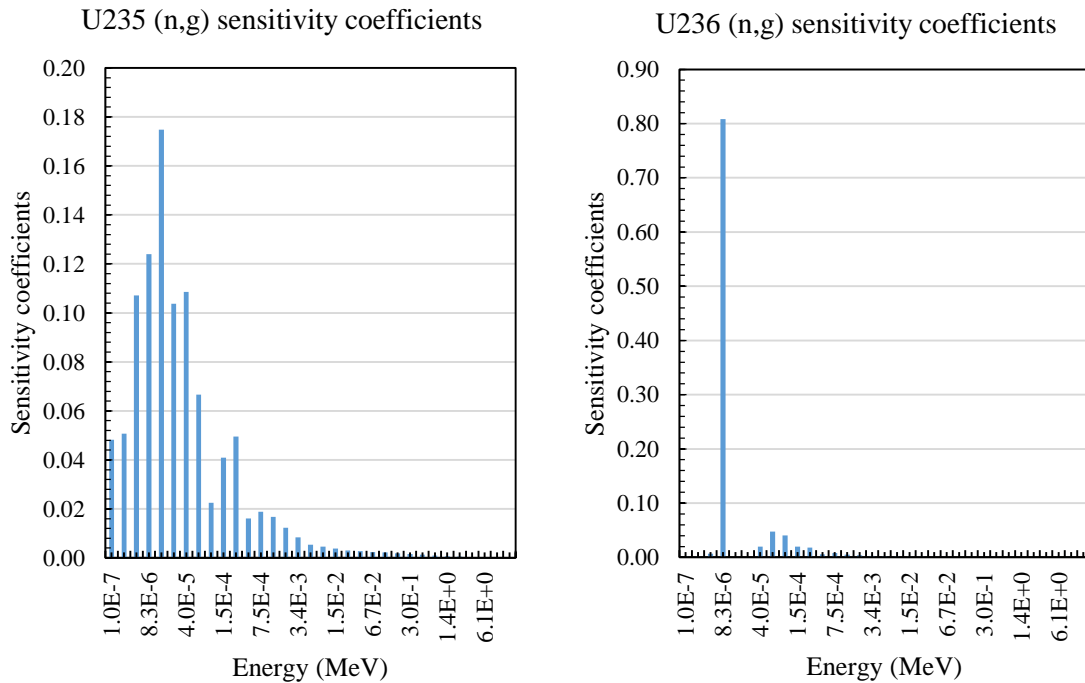


Figure C.18 Sensitivity coefficients of U235 (left) and U236 (right)  $\sigma_g$  cross-sections

## APPENDIX D

The capture cross-section plots of all the samples for both the experiments were included here. The actual masses (pre-irradiated masses) of the samples were used to plot these cross-sections. The cross-section plots in the boron experiment can be seen below.

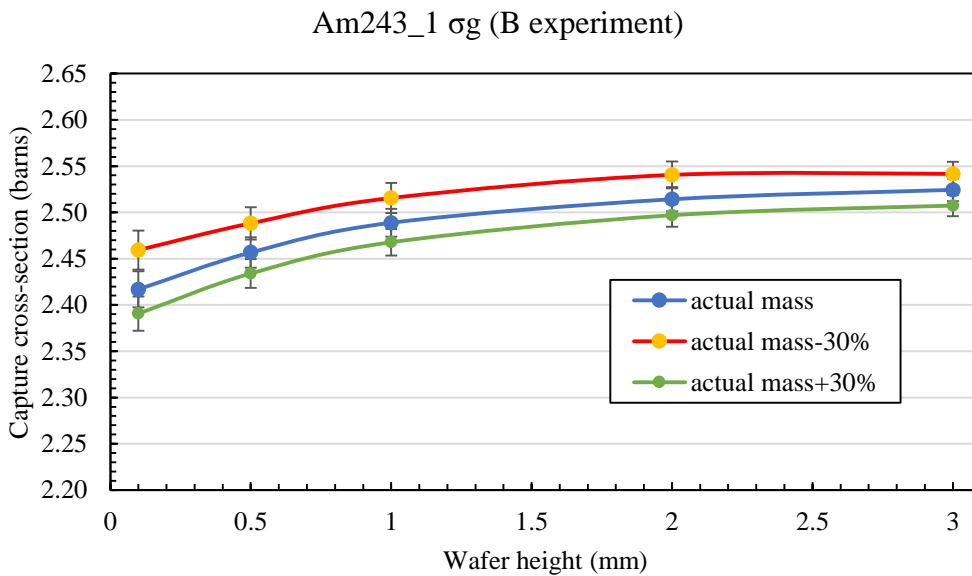
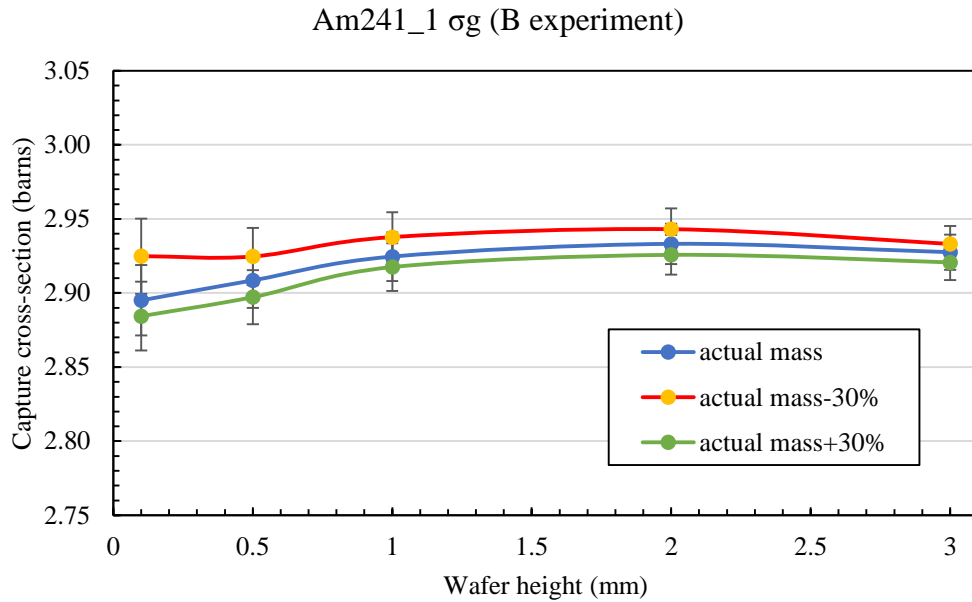
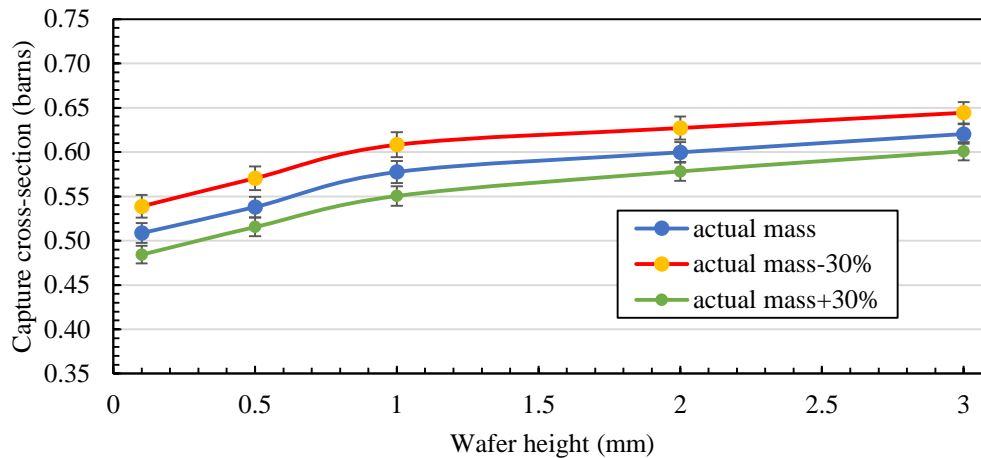
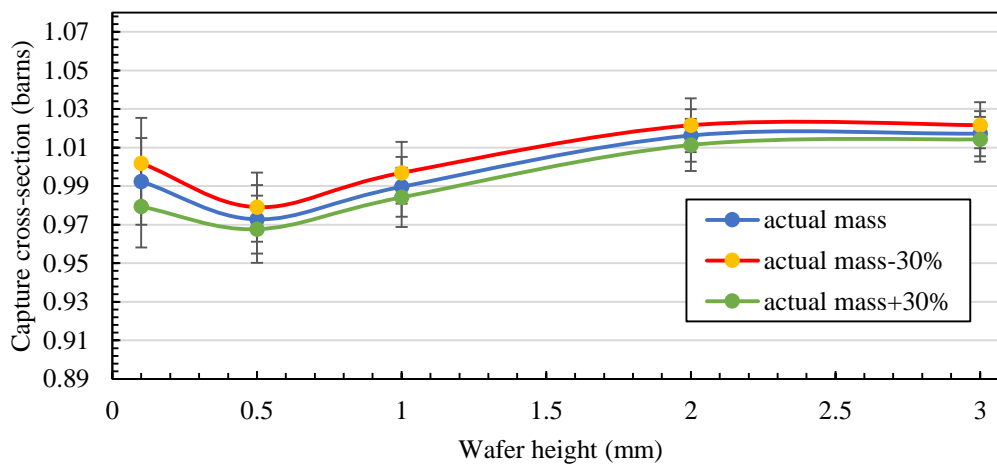


Figure D.1 Capture cross-sections of Am241 (top) and Am243 (bottom)

Cm248\_1  $\sigma_g$  (B experiment)



Cs133  $\sigma_g$  (B experiment)



Eu153  $\sigma_g$  (B experiment)

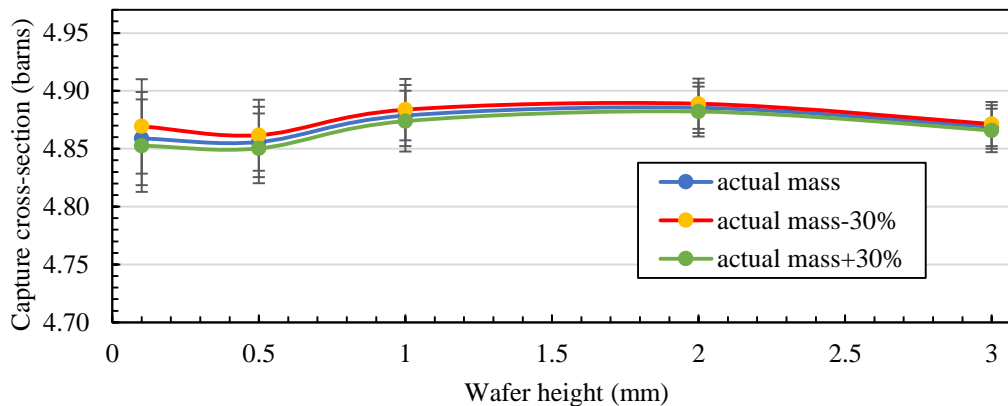


Figure D.2 Capture cross-sections of Cm248 (top), Cs133 (middle) and Eu153 (bottom)

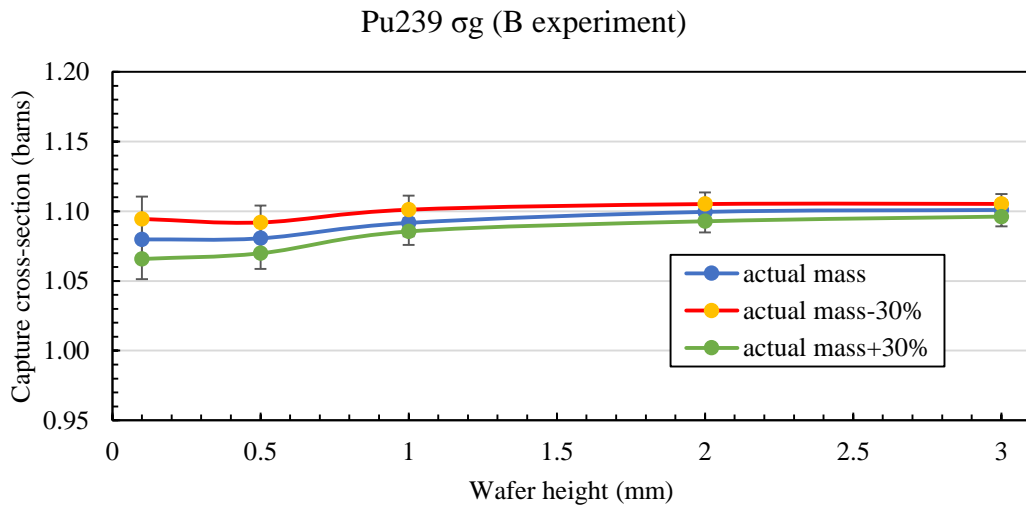
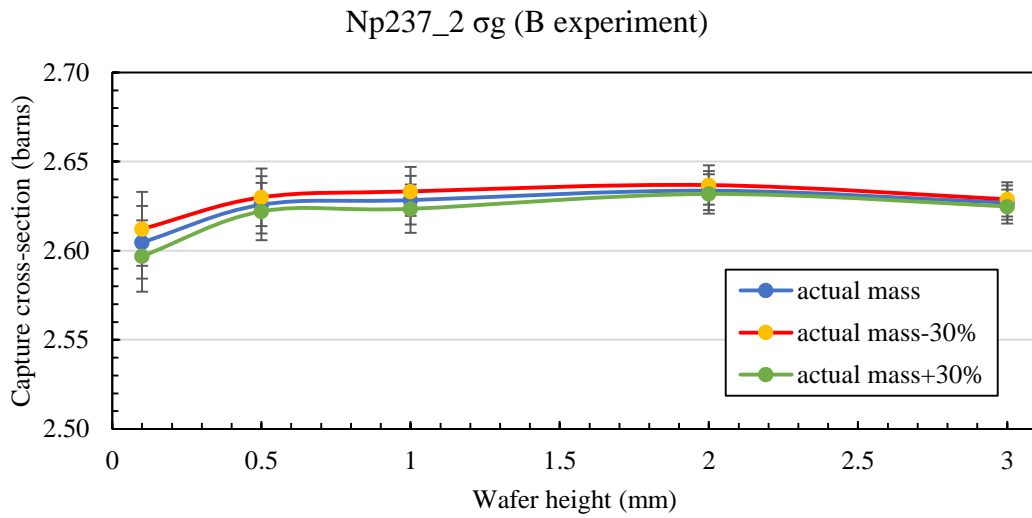
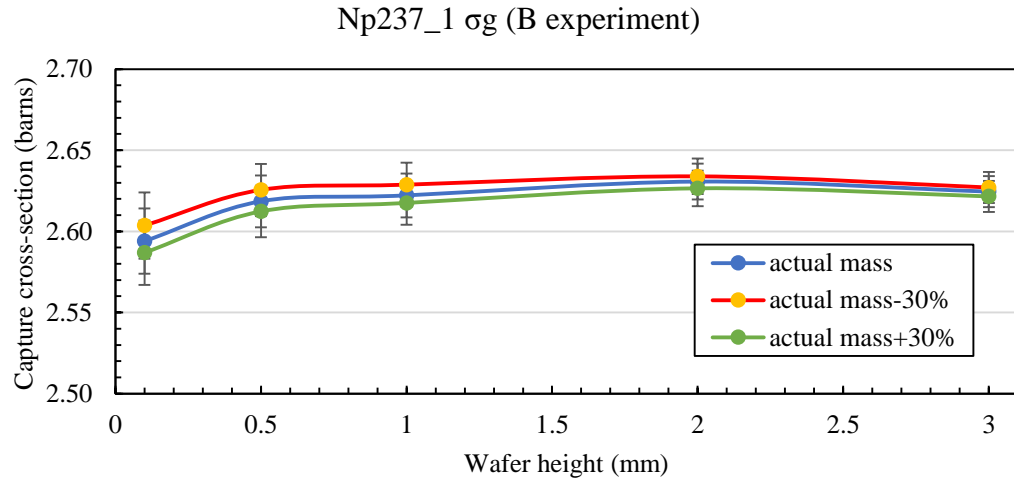


Figure D.3 Capture cross-sections of Np237\_1 (top), Np237\_2 (middle) and Pu239 (bottom)

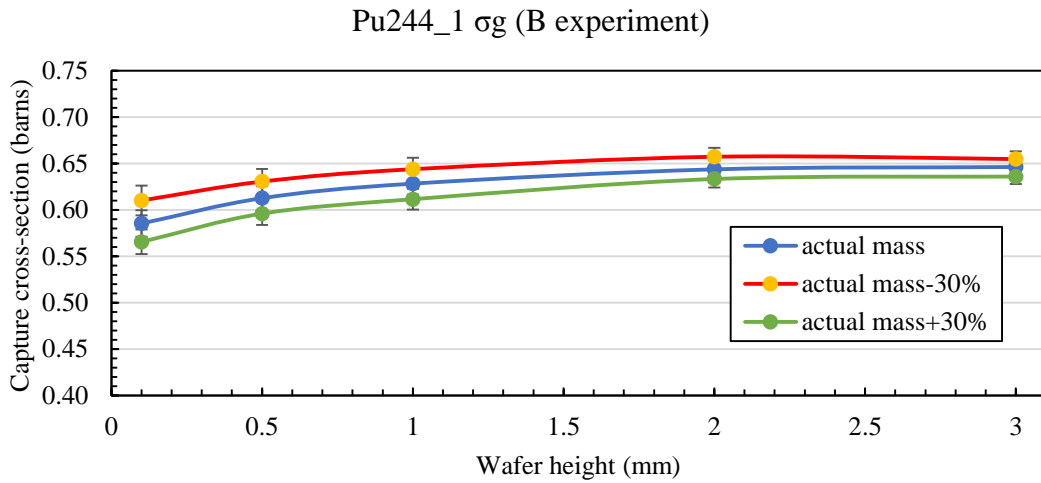
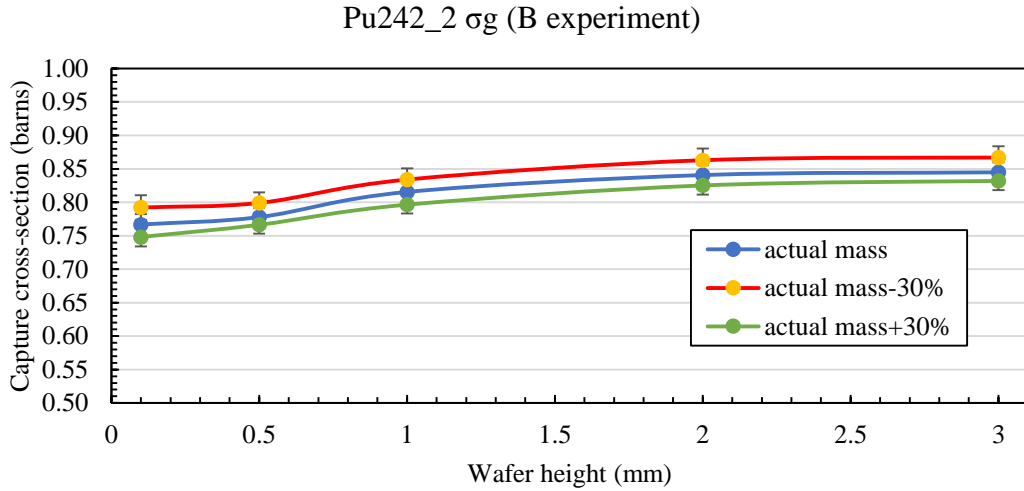
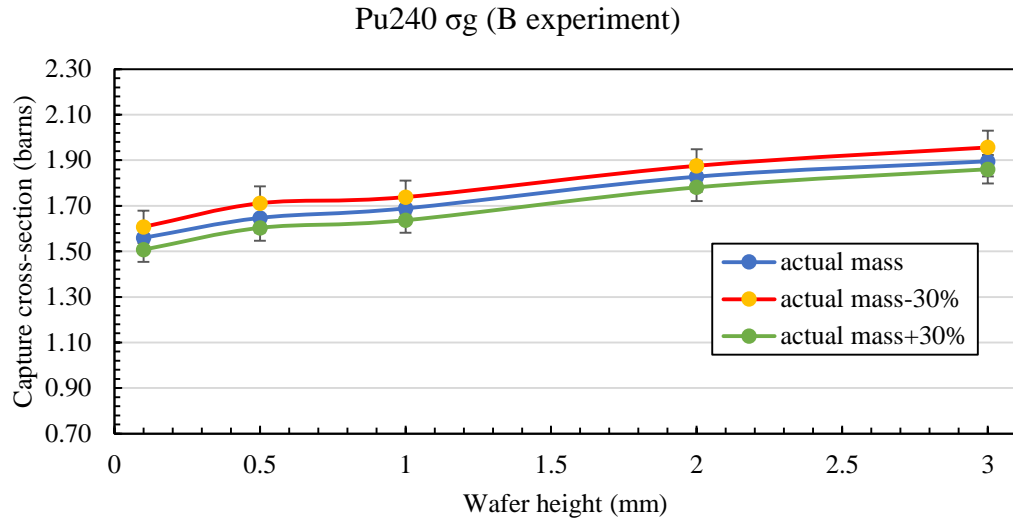
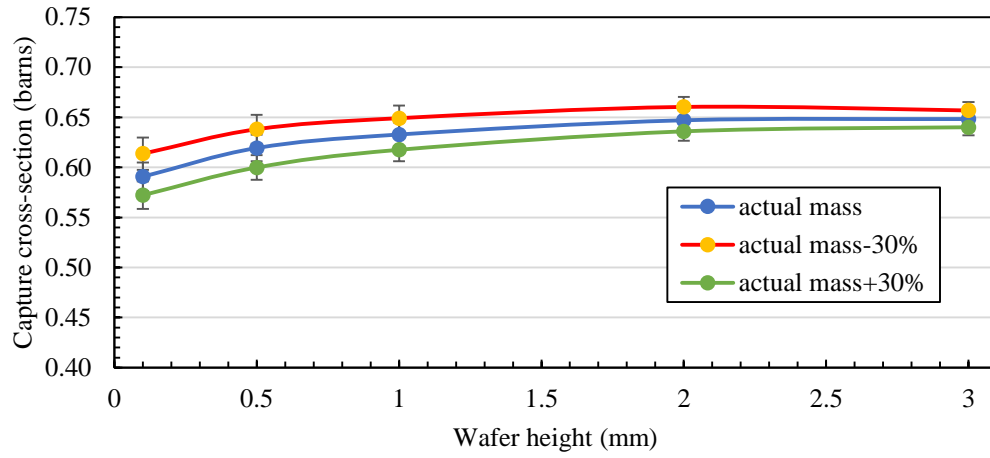
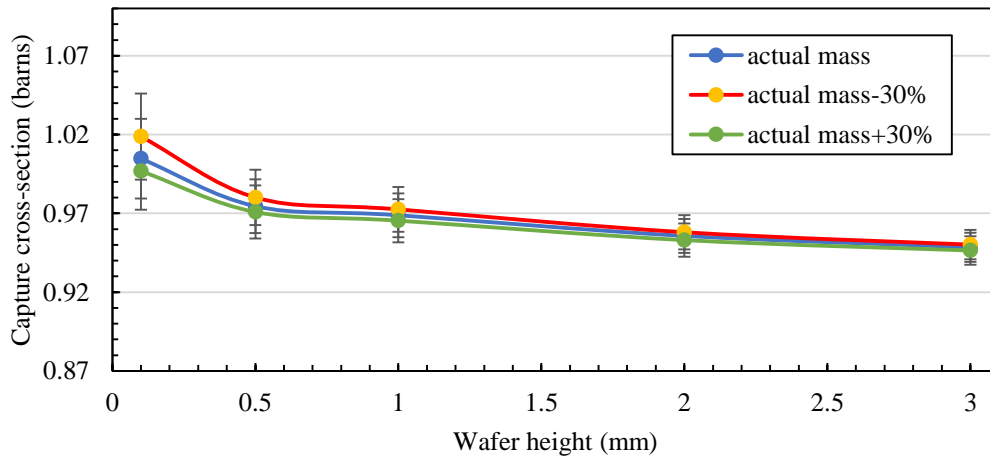


Figure D.4 Capture cross-sections of Pu240 (top), Pu242\_2 (middle) and Pu244\_1 (bottom)

Pu244\_1  $\sigma_g$  (B experiment)



Rh103  $\sigma_g$  (B experiment)



Sm149  $\sigma_g$  (B experiment)

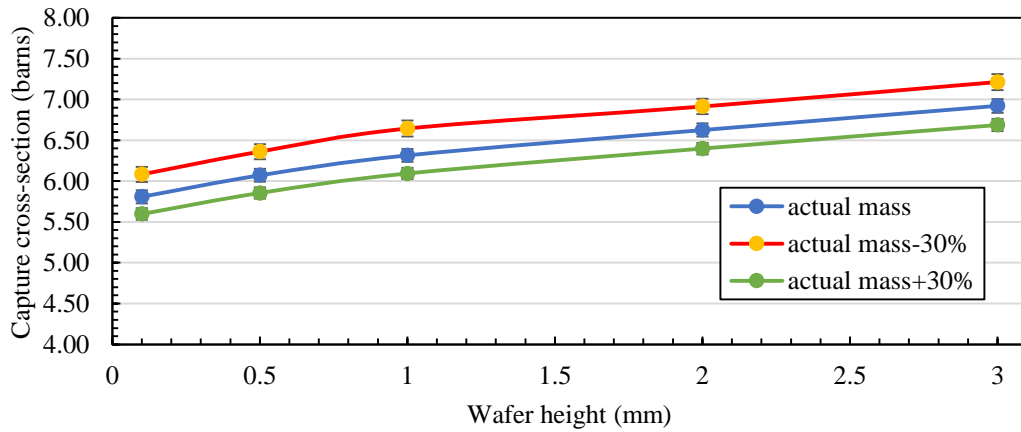
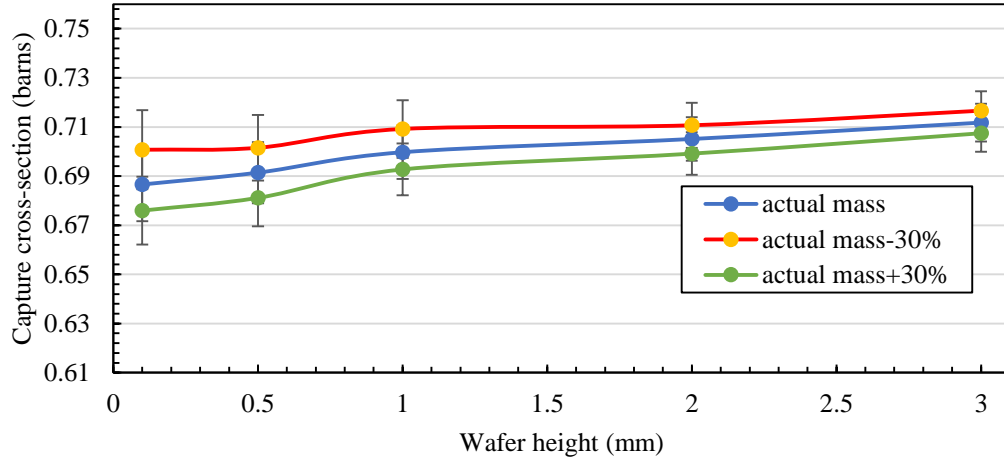
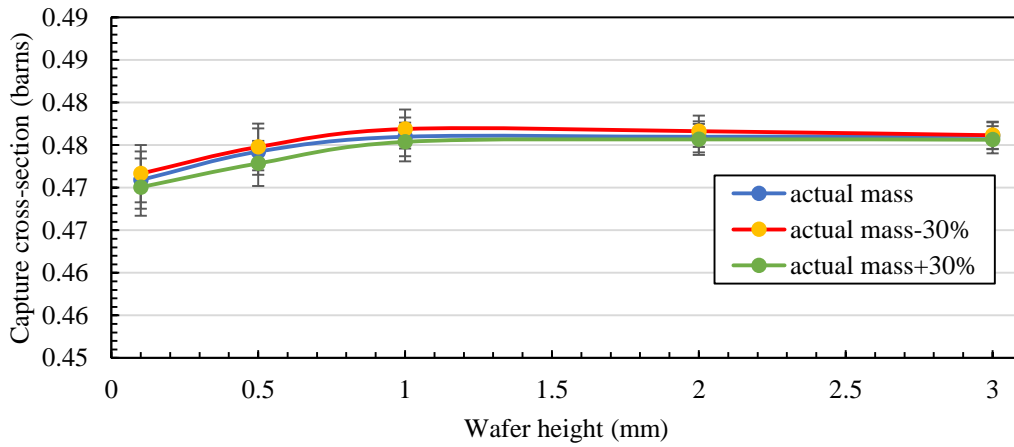


Figure D.5 Capture cross-sections of Pu244\_1 (top), Rh103 (middle) and Sm149 (bottom)

Th232  $\sigma_g$  (B experiment)



U233  $\sigma_g$  (B experiment)



U235  $\sigma_g$  (B experiment)

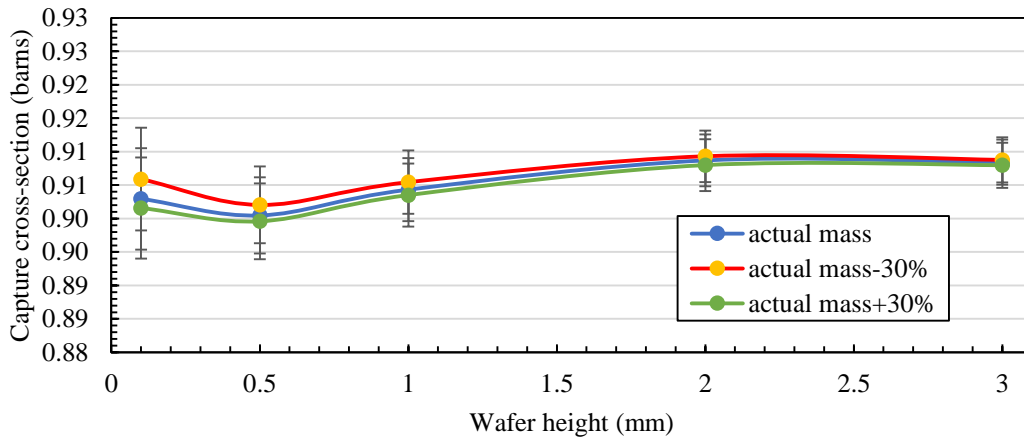
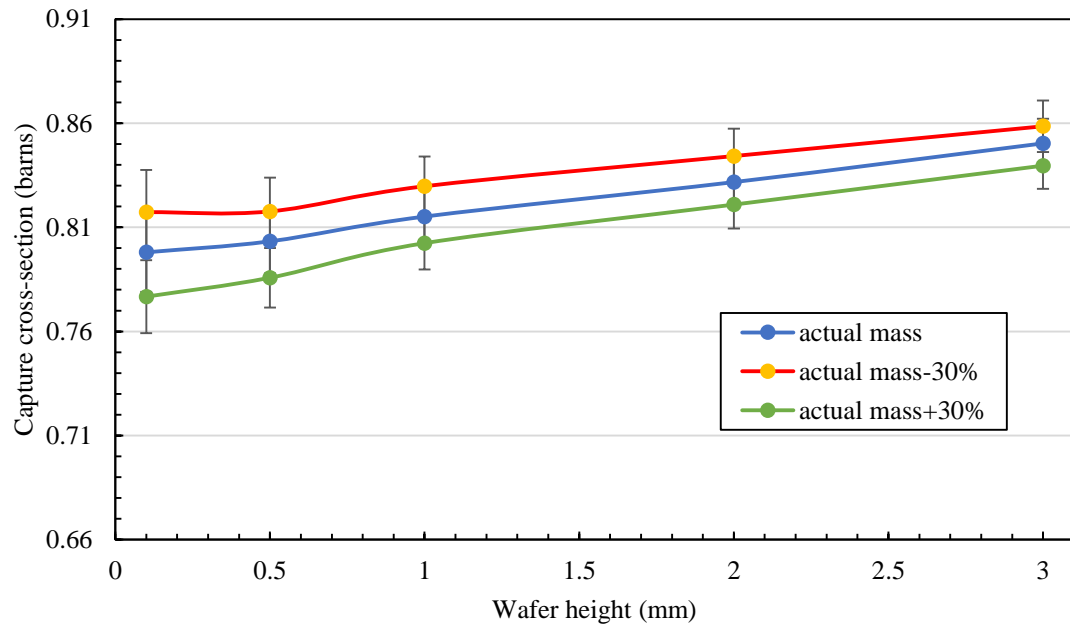


Figure D.6 Capture cross-sections of Th232 (top), U233 (middle) and U235 (bottom)

U236  $\sigma_g$  (B experiment)



U238  $\sigma_g$  (B experiment)

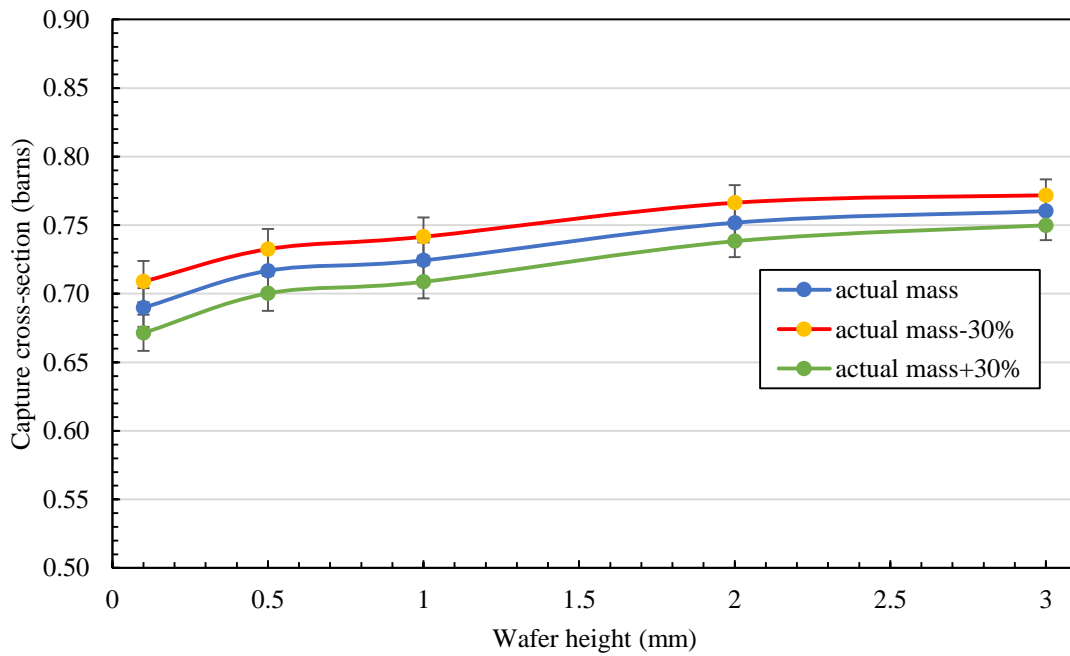


Figure D.7 Capture cross-sections of U236 (top) and U238 (bottom)

The capture cross-section plots of all samples in cadmium experiment can be seen below.

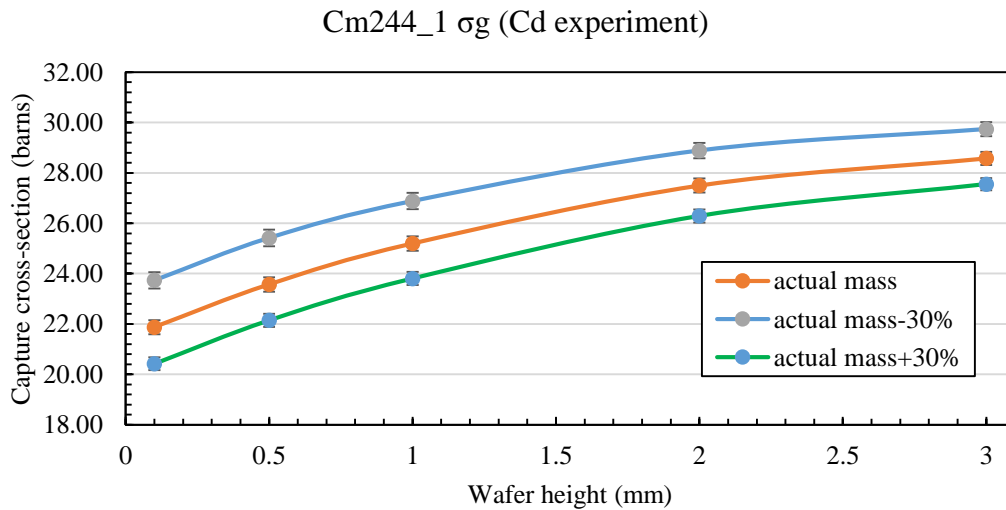
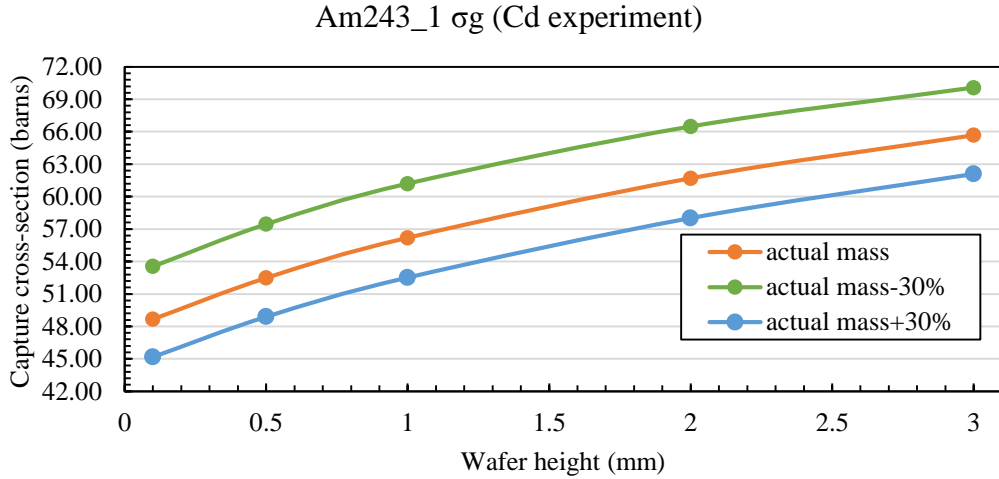
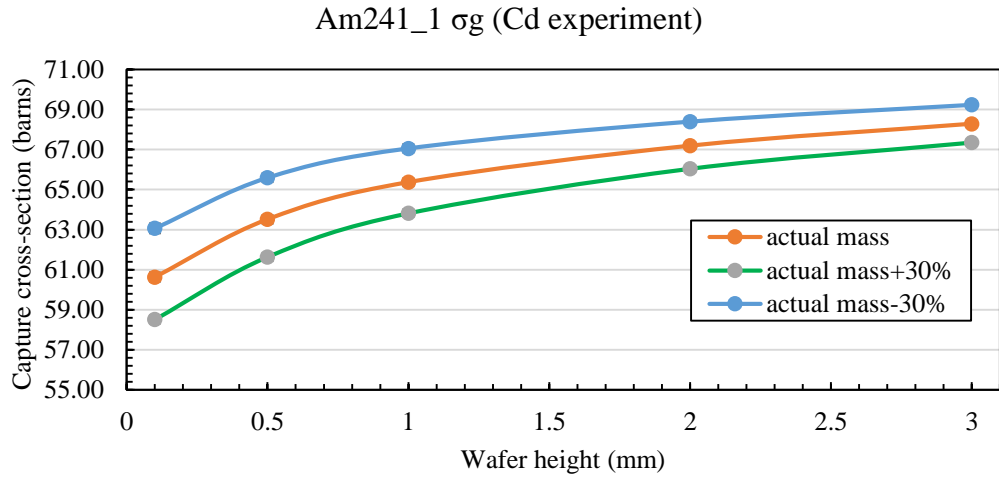
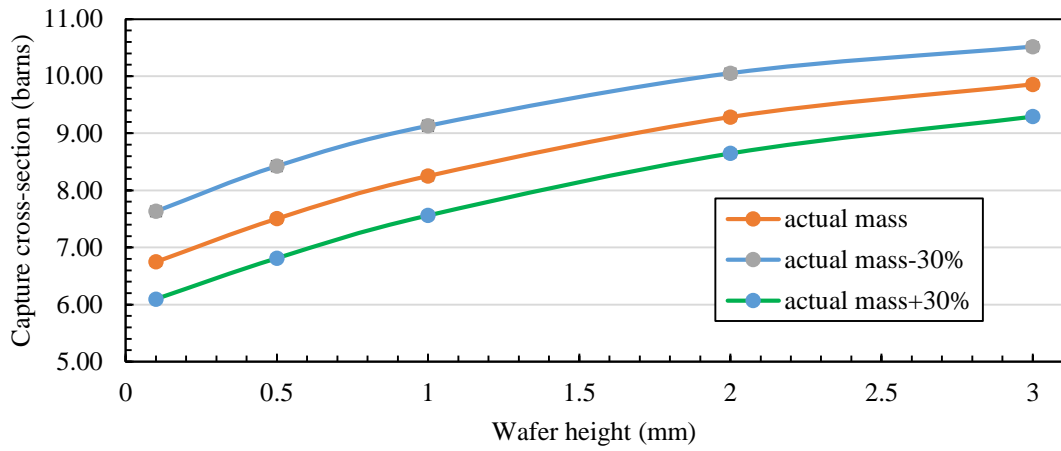
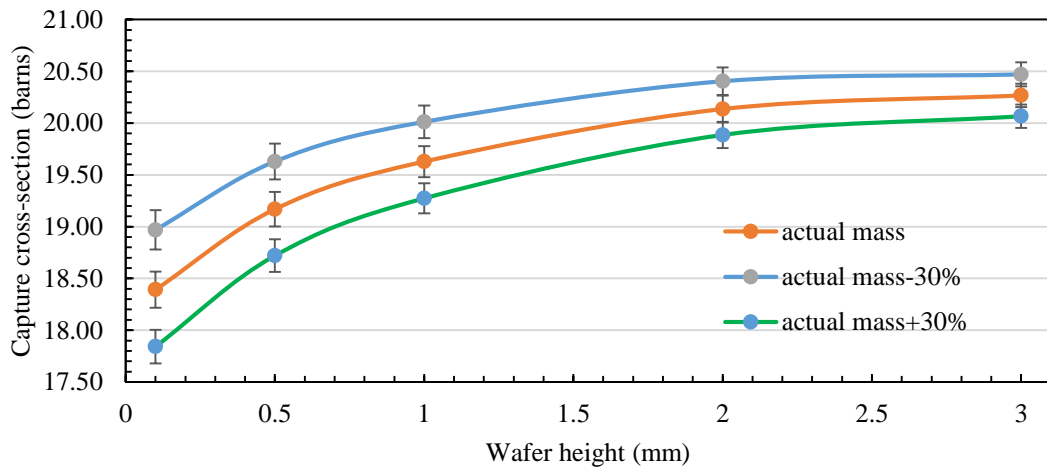


Figure D.8 Capture cross-sections of Am241\_1 (top), Am243\_1 (middle) and Cm244\_1 (bottom)

Cm248\_1  $\sigma$ g (Cd experiment)



Cs133  $\sigma$ g (Cd experiment)



Eu153  $\sigma$ g (Cd experiment)

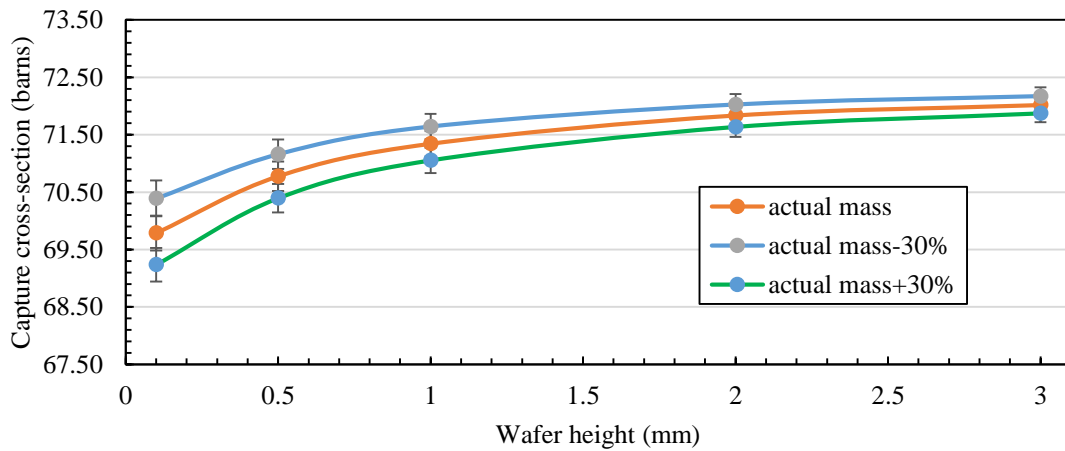


Figure D.9 Capture cross-sections of Cm248\_1 (top), Cs133 (middle) and Eu153 (bottom)

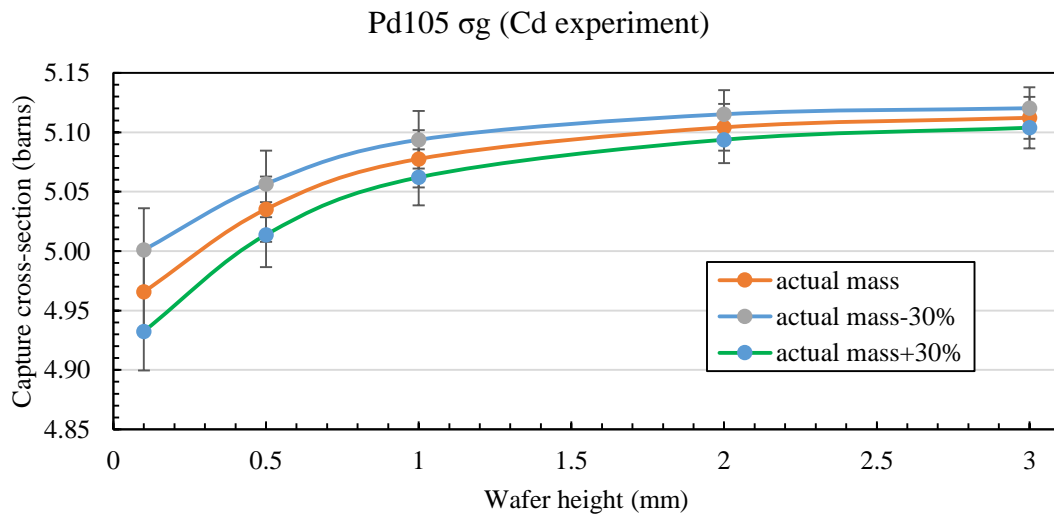
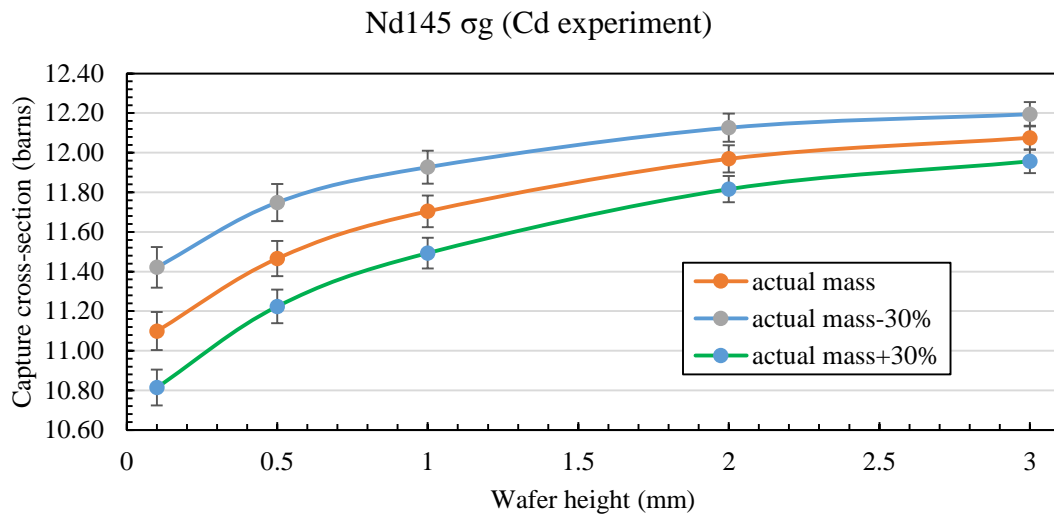
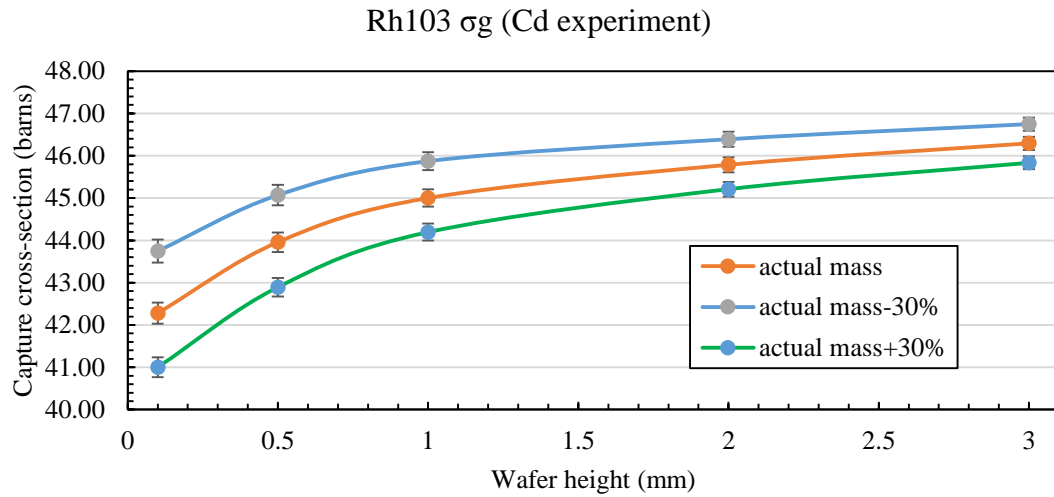


Figure D.10 Capture cross-sections of Rh103 (top), Nd145 (middle) and Pd105 (bottom)

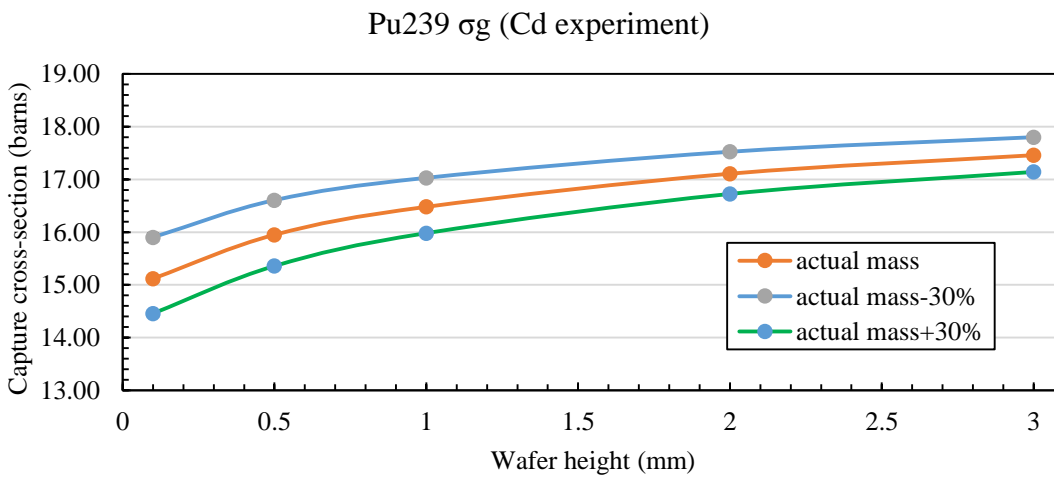
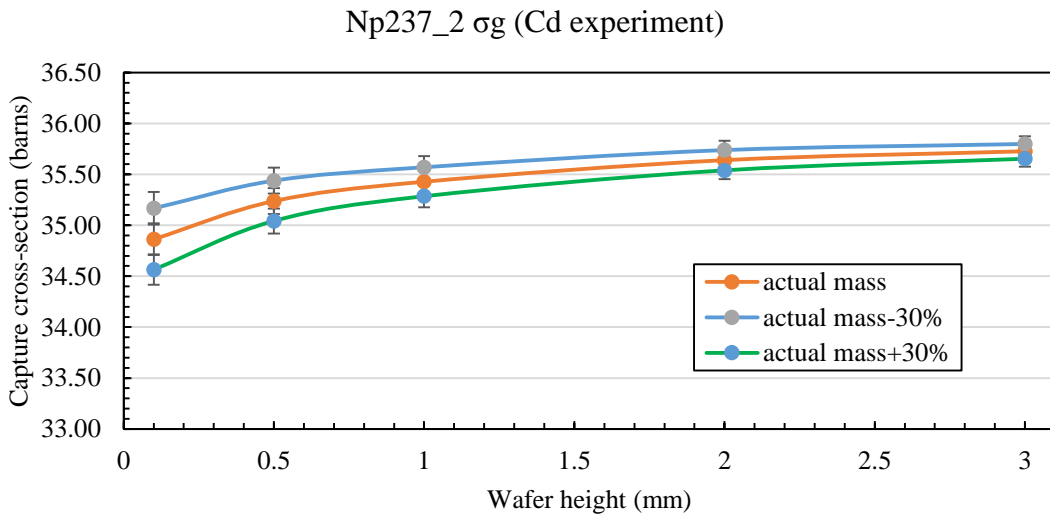
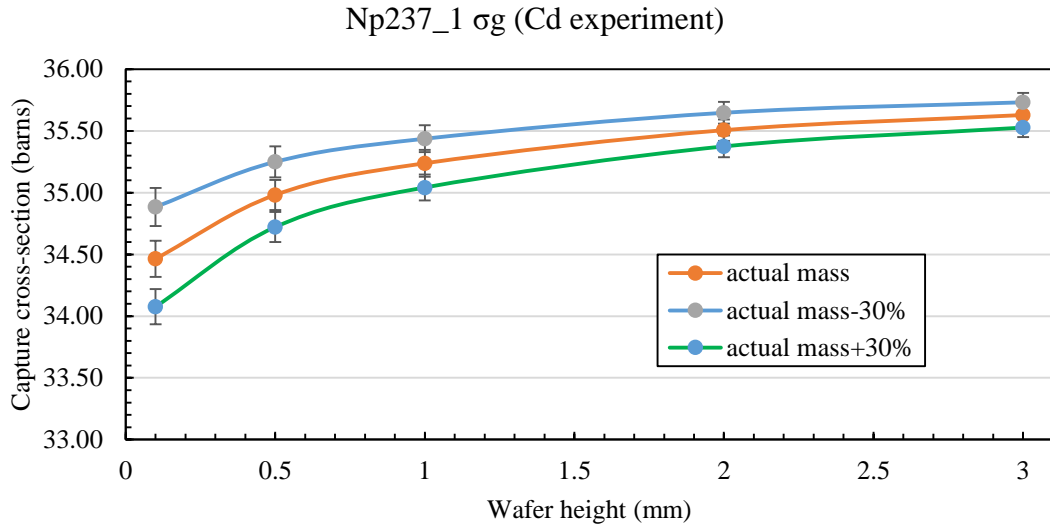


Figure D.11 Capture cross-sections of Np237\_1 (top), Np237\_2 (middle) and Pu239 (bottom)

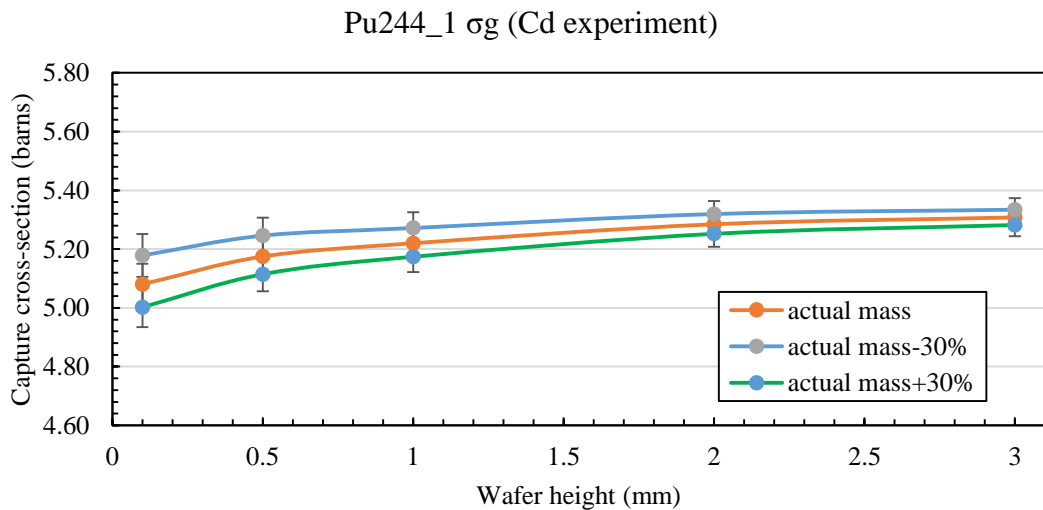
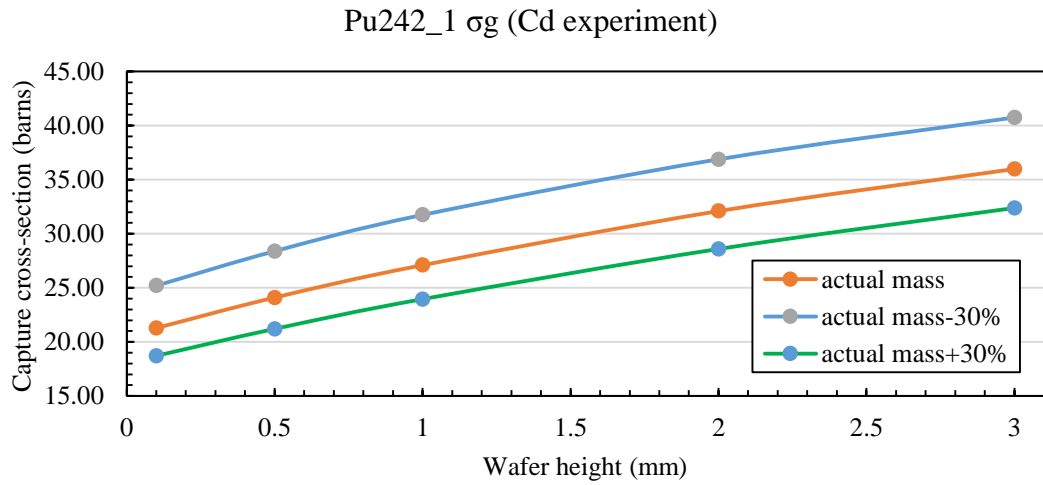
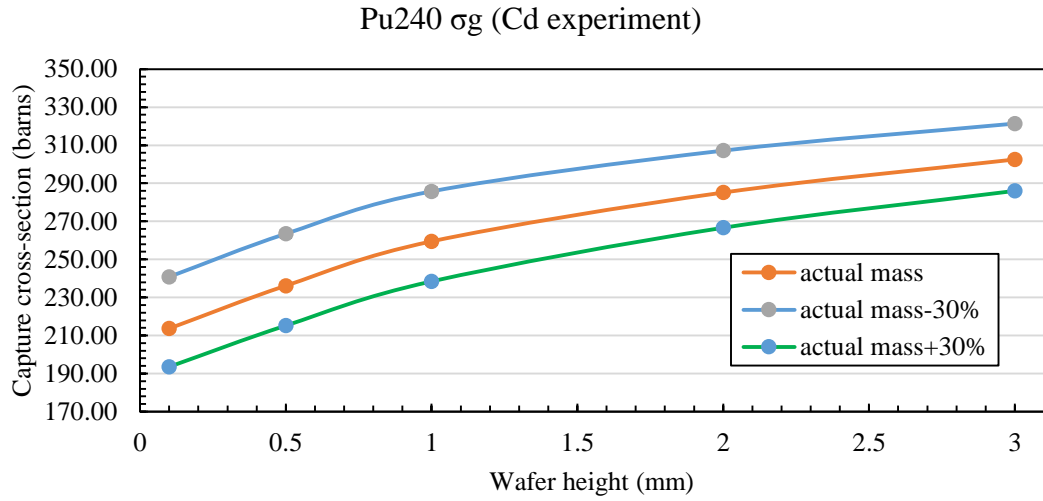
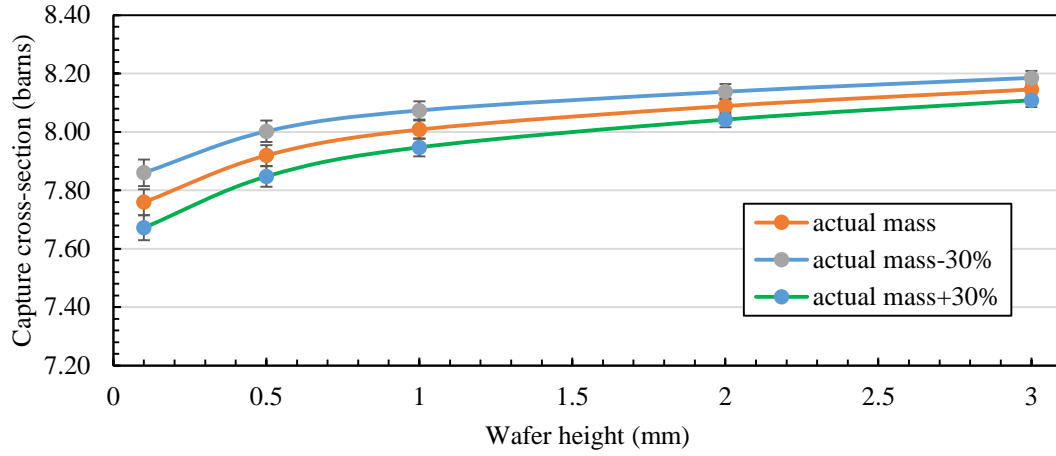
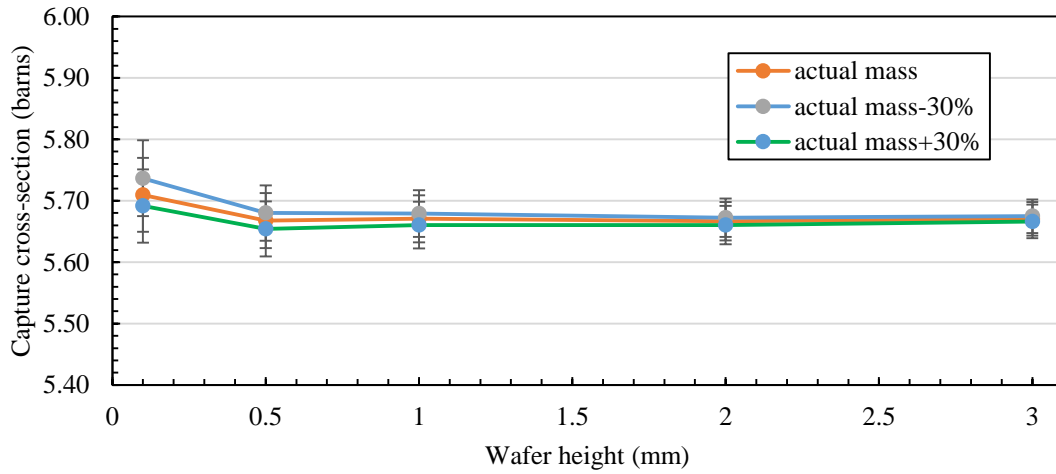


Figure D.12 Capture cross-sections of Pu240 (top), Pu242\_1 (middle) and Pu244\_1 (bottom)

Nd143  $\sigma_g$  (Cd experiment)



Ru101  $\sigma_g$  (Cd experiment)



Sm149  $\sigma_g$  (Cd experiment)

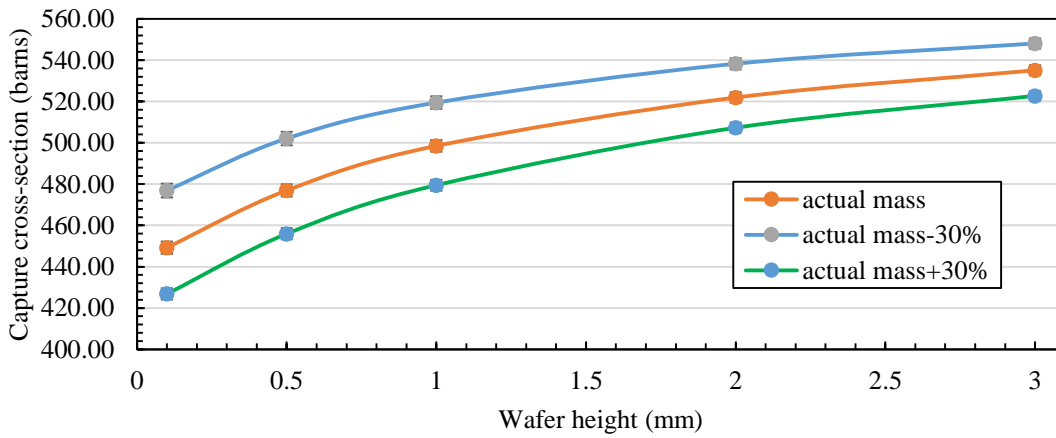


Figure D.13 Capture cross-sections of Nd143 (top), Ru101 (middle) and Sm149 (bottom)

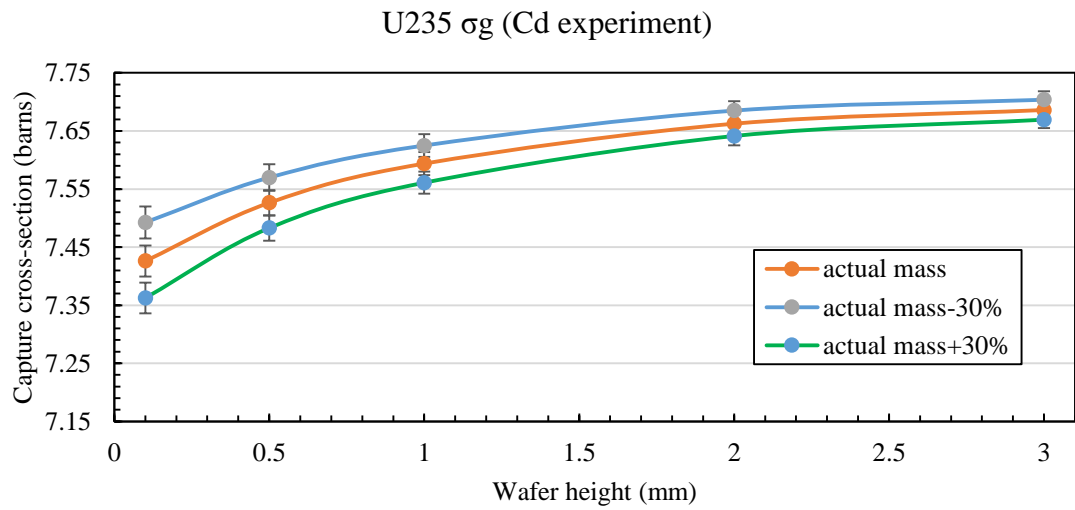
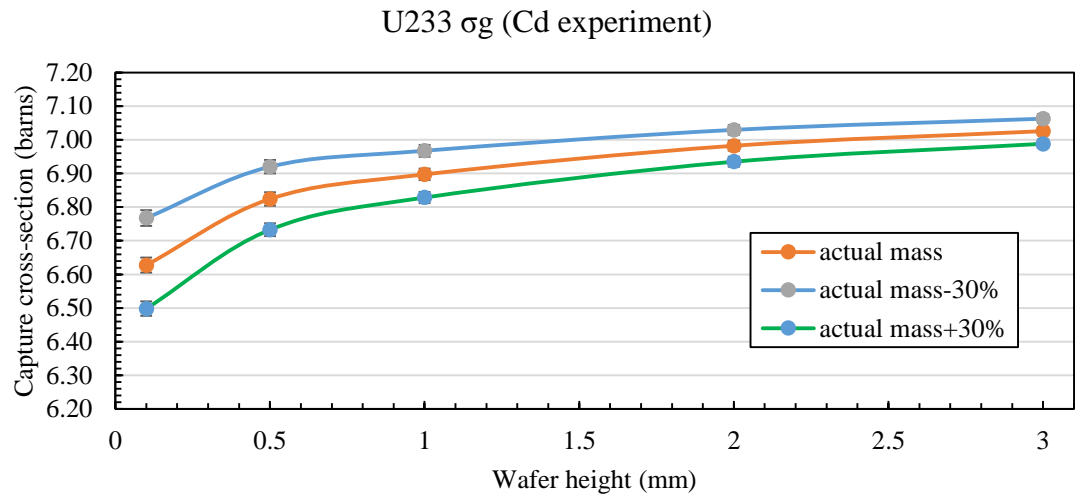
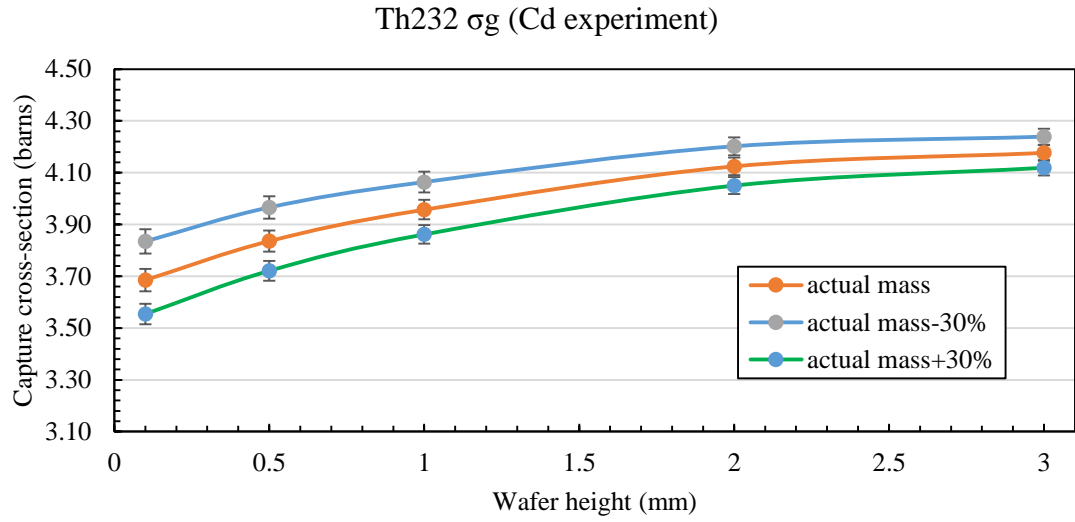
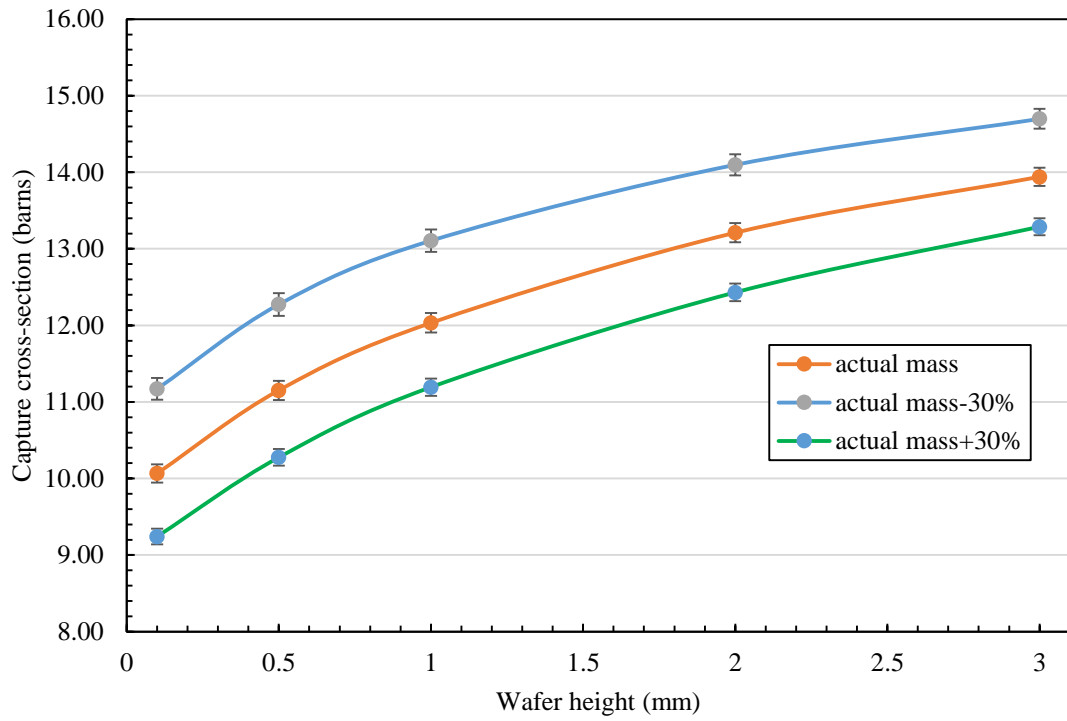


Figure D.14 Capture cross-sections of Th232 (top), U233 (middle) and U235 (bottom)

U236  $\sigma_g$  (Cd experiment)



U238  $\sigma_g$  (Cd experiment)

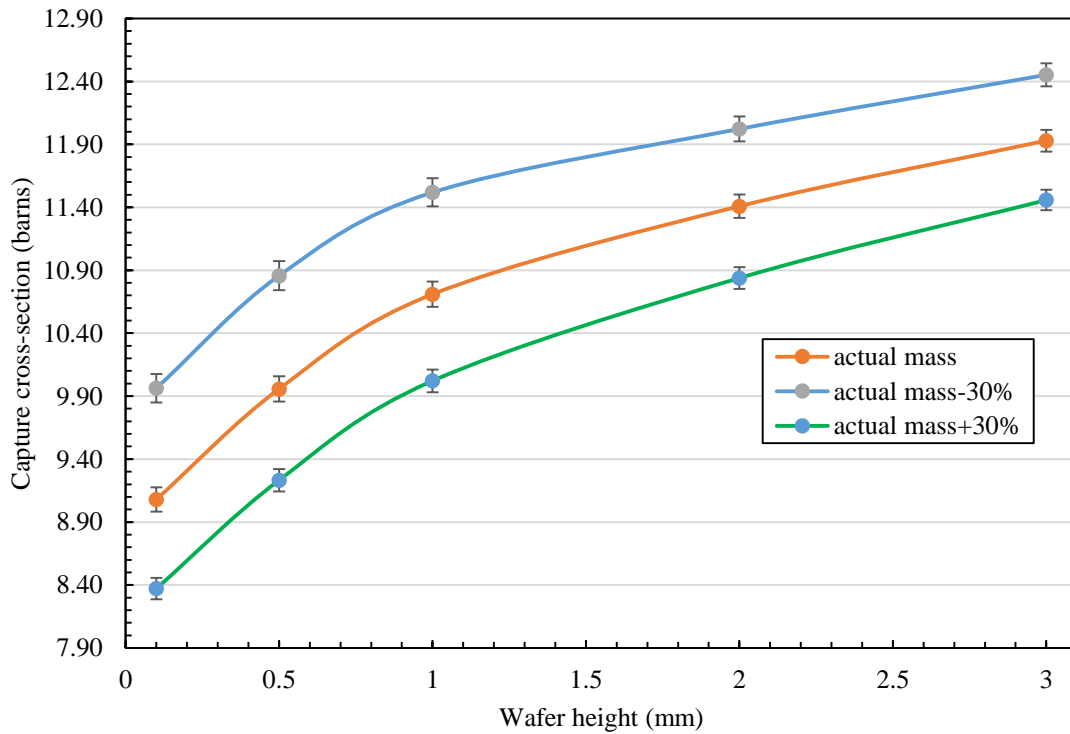


Figure D.15 Capture cross-sections of U236 (top) and U238 (bottom)

## APPENDIX E

Derivation of the final equation used to decay correct the measured activities in boron experiment.

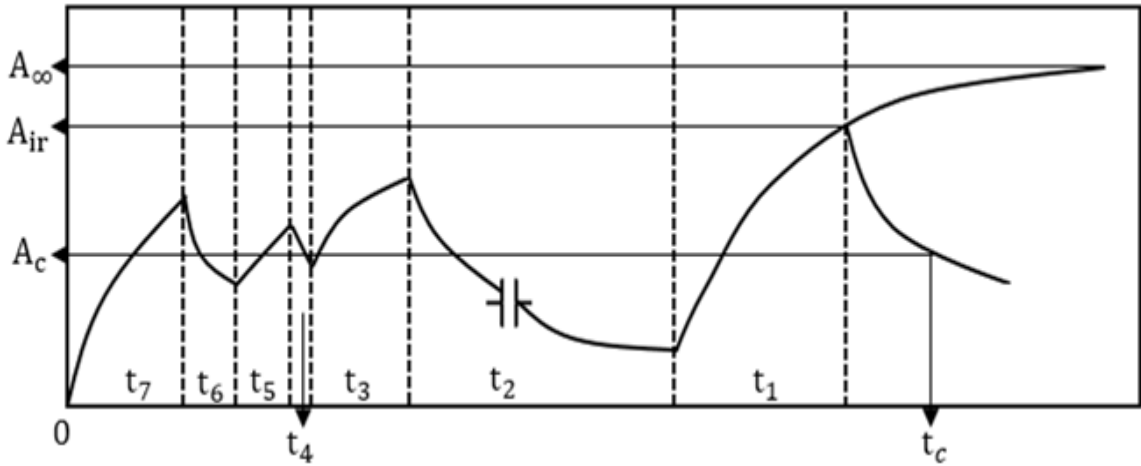


Figure E.1 Example of the activity profile of a flux wire in the boron experiment

In case of decay with production, the rate of change of the number of daughter nuclides is given by

$$\frac{dN_d(t)}{dt} = \text{rate of production} - \text{rate of decay} \quad [\text{E.1}]$$

$$\frac{dN_d(t)}{dt} = \phi\sigma N_p(t) - \lambda N_d(t) \quad [\text{E.2}]$$

Where,  $N_p$  = number of parent nuclides

$N_d$  = number of daughter nuclides

$\phi\sigma$  = activation rate (Bq)

Solving Equation E.2

$$\text{Let, } N_d(t) = a + be^{-\lambda t}$$

$$\Rightarrow \frac{dN_d(t)}{dt} = -\lambda be^{-\lambda t}$$

$$\Rightarrow a = \frac{\phi\sigma N_p(t)}{\lambda}$$

At  $t = 0$ ,  $N_d(0) = 0$

$$\Rightarrow b = \frac{-\phi\sigma N_p(t)}{\lambda}$$

$$\Rightarrow N_d(t) = \frac{\phi\sigma N_p(t)}{\lambda} (1 - e^{-\lambda t})$$

This is true in the case of the cadmium experiment. But in the case of the boron experiment,

Let  $N_{d1}(0) = N_1$  during the start of irradiation period  $t_1$  and assuming constant production

rate ( $N_p(t) = N_p$ )

$$\Rightarrow N_{d1}(t_1) = \frac{\phi\sigma N_p}{\lambda} (1 - e^{-\lambda t_1}) + N_1 e^{-\lambda t_1}$$

Let  $N_{d3}(0) = N_3$  during the start of irradiation period  $t_3$

$$\Rightarrow N_{d3}(t_3) = \frac{\phi\sigma N_p}{\lambda} (1 - e^{-\lambda t_3}) + N_3 e^{-\lambda t_3}$$

Let  $N_{d5}(0) = N_5$  during the start of irradiation period  $t_5$

$$\Rightarrow N_{d5}(t_5) = \frac{\phi\sigma N_p}{\lambda} (1 - e^{-\lambda t_5}) + N_5 e^{-\lambda t_5}$$

At  $N_{d7}(0) = 0$  during the start of irradiation period  $t_7$

$$\Rightarrow N_{d7}(t_7) = \frac{\phi\sigma N_p}{\lambda} (1 - e^{-\lambda t_7})$$

$$\text{Also, } N_1 = N_{d2}(t_2) e^{-\lambda t_2}$$

$$N_2 = N_{d3}(t_3) e^{-\lambda t_4}$$

$$N_3 = N_{d4}(t_4) e^{-\lambda t_6}$$

A total of seven equations and seven unknowns, solving for  $\phi\sigma$  gives the activation rate per atom (Bq/atom).

Since activity  $A = \lambda N$ , here  $A_{ir} = \lambda N_{d1}(t_1)$  (activity at the end of irradiation)

$$\frac{A_{ir}/N_p}{(1 - e^{-\lambda t_1}) + (1 - e^{-\lambda t_3})e^{-\lambda(t_1+t_2)} + (1 - e^{-\lambda t_5})e^{-\lambda(t_1+t_2+t_3+t_4)} + (1 - e^{-\lambda t_7})e^{-\lambda(t_1+t_2+t_3+t_4+t_5+t_6)}}$$

[E.3]

## APPENDIX F

More detailed explanation of the least squares method equations.

$$\begin{bmatrix}
 \mathbf{a}_{11} & \mathbf{a}_{12} & \mathbf{a}_{13} & \cdots & \cdots & \mathbf{a}_{1,NG} \\
 \mathbf{a}_{21} & \mathbf{a}_{22} & \mathbf{a}_{23} & \cdots & \cdots & \mathbf{a}_{2,NG} \\
 \vdots & \vdots & \vdots & & & \vdots \\
 \mathbf{a}_{NF,1} & \mathbf{a}_{NF,2} & \mathbf{a}_{NF,3} & \cdots & \cdots & \mathbf{a}_{NF,NG} \\
 1 & 0 & 0 & \cdots & \cdots & 0 \\
 0 & 1 & 0 & \cdots & \cdots & 0 \\
 0 & 0 & 1 & \cdots & \cdots & 0 \\
 \vdots & \vdots & \vdots & & & \vdots \\
 \vdots & \vdots & \vdots & & & \vdots \\
 0 & 0 & 0 & \cdots & \cdots & 1
 \end{bmatrix}
 \bullet
 \begin{bmatrix}
 \varphi_1 \\
 \varphi_2 \\
 \varphi_3 \\
 \vdots \\
 \vdots \\
 \vdots \\
 \varphi_{NG}
 \end{bmatrix}
 =
 \begin{bmatrix}
 \mathbf{R}_1 \\
 \mathbf{R}_2 \\
 \vdots \\
 \mathbf{R}_{NF} \\
 \varphi_{01} \\
 \varphi_{02} \\
 \varphi_{03} \\
 \vdots \\
 \vdots \\
 \varphi_{0NG}
 \end{bmatrix}
 = [\mathbf{A}][\Phi] = [\mathbf{C}]
 \tag{F.1}$$

Where,  $\varphi_{01} \dots \varphi_{0NG} = a \text{ priori}$  spectrum

$[\mathbf{C}] =$  augmented matrix

$$[\text{Cov}(\mathbf{C})] = \begin{bmatrix} [\text{Cov}(\mathbf{R})] & [0] \\ [0] & [\text{Cov}(\Phi_0)] \end{bmatrix}$$

Where,  $\text{Cov}(\Phi_0) =$  covariance matrix of *a priori* spectrum

$\text{Cov}(\mathbf{R}) =$  covariance matrix of measured responses

$\text{Cov}(\mathbf{C}) =$  covariance matrix which includes both measured responses portion and *a priori* portion

To calculate the solution spectrum ( $\Phi$ ), multiply both sides of the Equation F.1 with  $\mathbf{A}^T$  and  $[\text{Cov}(\mathbf{C})]^{-1}$  to obtain

$$\mathbf{A}^T [\text{Cov}(\mathbf{C})]^{-1} \mathbf{A} \Phi = \mathbf{A}^T [\text{Cov}(\mathbf{C})]^{-1} \mathbf{C}$$

$$\Phi = [\mathbf{A}^T [\text{Cov}(\mathbf{C})]^{-1} \mathbf{A}]^{-1} \mathbf{A}^T [\text{Cov}(\mathbf{C})]^{-1} \mathbf{C} \tag{F.2}$$

The covariance matrix of the solution spectrum can then be calculated using the basic uncertainty propagation formula in matrix algebra (24).

$$\text{Cov}(\Phi) = [\mathbf{A}^T [\text{Cov}(\mathbf{C})]^{-1} \mathbf{A}]^{-1} \mathbf{A}^T [\text{Cov}(\mathbf{C})]^{-1} \text{Cov}(\mathbf{C}) [\mathbf{A}^T [\text{Cov}(\mathbf{C})]^{-1} \mathbf{A}]^{-1} \mathbf{A}^T [\text{Cov}(\mathbf{C})]^{-1} \tag{F.3}$$

By application of the matrix inversion lemma described by (43) or by use of an equivalent independent derivation by (42), the same final equations can be derived.

$$\Phi = \Phi_0 + \text{Cov}(\Phi_0)A_0^T[\text{Cov}(\mathbf{R}) + A_0\text{Cov}(\Phi_0)A_0^T]^{-1}[\mathbf{R} - A_0\Phi_0] \quad [\text{F.4}]$$

$$\text{Cov}(\Phi) = \text{Cov}(\Phi_0) - \text{Cov}(\Phi_0)A_0^T[\text{Cov}(\mathbf{R}) + A_0\text{Cov}(\Phi_0)A_0^T]^{-1}A_0\text{Cov}(\Phi_0) \quad [\text{F.5}]$$

Where,  $\Phi$  = solution spectrum matrix

$\Phi_0$  = *a priori* spectrum matrix

$A_0$  = response matrix

$\mathbf{R}$  = reaction rate matrix

$\text{T}$  = matrix transpose

$-1$  = matrix inverse

$\text{Cov}$  = covariance matrix

The covariance of *a priori* spectrum can be calculated by applying the generally accepted formulation described in (46) and (47).

$$\text{Cov}(\Phi_0)_{i,j} = P^2\varphi_i\varphi_j + R^2\varphi_i\varphi_j\rho_{i,j} \quad [\text{F.6}]$$

Where,  $P$  = fractional normalization uncertainty for the *a priori* flux

$R$  = fractional random uncertainty for the *a priori* flux

$\varphi_i$  = *a priori* neutron flux in group  $i$

$\rho_{i,j}$  = correlation coefficient between groups  $i$  and  $j$

$$\rho_{i,j} = (1-\Theta)\delta_{i,j} + \Theta\exp(-(i-j)^2/2\Gamma^2) \quad [\text{F.7}]$$

Where,  $\delta_{i,j}$  = delta function ( $\delta_{i,j}=1$  if  $i=j$  and  $\delta_{i,j}=0$  otherwise)

$\Theta$  = correlation strength parameter typically has a value between 0.5 and 1.0

$\Gamma$  = correlation range parameter ( $0 \leq \Gamma \leq (NG-1)$ )

$NG$  = number of desired energy groups

A  $\Theta$  value of 0.8 and a  $\Gamma$  value of 4 were used in the current work.

## APPENDIX G

To calculate the uncertainties in the solution spectra from MAXED, an uncertainty code IQU can be used. This code is also part of the unfolding package UMG3.3. This code uses standard methods to do the sensitivity analysis and uncertainty propagation. However, MAXED does not use the *a priori* uncertainties in the unfolding process. The uncertainties of the solution spectra from MAXED were not calculated.

Table G.1 Average neutron fluxes (top to bottom) in 32 energy groups (Cd experiment)

Energy (MeV)	<i>A priori</i>	% Total error	MAXED	% Change	LSQ	% Total error	% Change
1.00E-07	7.393E+11	22.36	1.052E+12	42.32	7.542E+11	16.54	2.02
1.85E-07	5.613E+11	22.36	6.753E+11	20.31	5.730E+11	15.73	2.09
3.42E-07	8.909E+11	22.36	1.053E+12	18.14	9.125E+11	14.45	2.42
6.33E-07	2.584E+12	22.36	2.779E+12	7.53	2.657E+12	13.28	2.84
1.17E-06	4.873E+12	22.36	5.138E+12	5.43	5.046E+12	12.24	3.56
2.16E-06	5.529E+12	22.36	5.575E+12	0.83	5.766E+12	12.39	4.29
4.00E-06	5.774E+12	22.36	5.839E+12	1.12	6.087E+12	12.17	5.42
7.40E-06	5.803E+12	22.36	5.863E+12	1.03	6.175E+12	12.16	6.40
1.37E-05	6.034E+12	22.36	6.442E+12	6.76	6.476E+12	11.52	7.33
2.53E-05	6.104E+12	22.36	6.357E+12	4.15	6.538E+12	11.70	7.11
4.68E-05	6.011E+12	22.36	6.224E+12	3.55	6.375E+12	11.66	6.06
8.66E-05	6.037E+12	22.36	6.223E+12	3.08	6.287E+12	11.52	4.14
1.60E-04	6.035E+12	22.36	5.700E+12	-5.55	6.360E+12	4.03	5.38
2.96E-04	6.358E+12	22.36	6.450E+12	1.44	6.188E+12	11.16	-2.67
5.48E-04	6.050E+12	22.36	6.108E+12	0.96	5.505E+12	7.67	-9.02
1.01E-03	6.464E+12	22.36	6.512E+12	0.74	6.049E+12	13.77	-6.43
1.87E-03	6.520E+12	22.36	6.546E+12	0.40	6.026E+12	15.35	-7.57
3.47E-03	6.632E+12	22.36	6.634E+12	0.03	6.123E+12	16.94	-7.66
6.41E-03	6.716E+12	22.36	6.721E+12	0.08	6.252E+12	18.19	-6.90
1.19E-02	6.789E+12	22.36	6.778E+12	-0.17	6.418E+12	18.99	-5.46
2.19E-02	6.984E+12	22.36	6.973E+12	-0.15	6.779E+12	19.48	-2.94

Table G.1 cont.

Energy (MeV)	<i>A priori</i>	% Total error	MAXED	% Change	LSQ	% Total error	% Change
4.06E-02	6.989E+12	22.36	6.975E+12	-0.19	6.953E+12	19.39	-0.51
7.50E-02	8.104E+12	22.36	8.081E+12	-0.28	8.253E+12	18.89	1.84
1.39E-01	8.816E+12	22.36	8.791E+12	-0.28	9.162E+12	18.02	3.93
2.57E-01	9.651E+12	22.36	9.625E+12	-0.27	1.018E+13	16.81	5.45
4.75E-01	1.225E+13	22.36	1.221E+13	-0.31	1.301E+13	15.32	6.21
8.78E-01	1.187E+13	22.36	1.188E+13	0.10	1.261E+13	13.63	6.23
1.62E+00	1.306E+13	22.36	1.368E+13	4.79	1.394E+13	11.56	6.74
3.00E+00	9.148E+12	22.36	1.124E+13	22.87	1.063E+13	7.16	16.15
5.55E+00	3.484E+12	22.36	3.216E+12	-7.70	2.974E+12	5.05	-14.64
1.03E+01	8.059E+11	22.36	6.129E+11	-23.95	8.524E+11	3.43	5.76
1.90E+01	2.337E+10	22.36	4.976E+10	112.89	2.464E+10	11.14	5.40

Table G.2 Neutron fluxes in 32 energy groups at position 3 (B experiment)

Energy (MeV)	<i>A priori</i>	% Total error	MAXED	% Change	LSQ	% Total error	% Change
1.00E-07	2.232E+09	22.36	7.376E+09	230.53	2.050E+09	23.17	-8.15
1.85E-07	1.719E+09	22.36	2.058E+09	19.71	1.592E+09	22.94	-7.39
3.42E-07	2.598E+09	22.36	3.261E+09	25.51	2.438E+09	22.58	-6.19
6.33E-07	3.707E+09	22.36	2.976E+09	-19.74	3.530E+09	22.13	-4.78
1.17E-06	5.672E+09	22.36	4.262E+09	-24.86	5.495E+09	21.56	-3.12
2.16E-06	8.690E+09	22.36	5.119E+09	-41.09	8.552E+09	20.87	-1.59
4.00E-06	1.351E+10	22.36	8.526E+09	-36.90	1.345E+10	20.07	-0.48
7.40E-06	2.114E+10	22.36	1.381E+10	-34.66	2.103E+10	19.18	-0.50
1.37E-05	3.307E+10	22.36	2.952E+10	-10.74	3.244E+10	18.16	-1.90
2.53E-05	5.558E+10	22.36	4.747E+10	-14.60	5.236E+10	17.21	-5.78
4.68E-05	9.767E+10	22.36	8.080E+10	-17.26	8.610E+10	16.41	-11.84
8.66E-05	1.887E+11	22.36	1.500E+11	-20.50	1.520E+11	15.96	-19.44
1.60E-04	3.383E+11	22.36	2.359E+11	-30.27	2.656E+11	5.47	-21.48
2.96E-04	6.104E+11	22.36	3.002E+11	-50.83	3.580E+11	19.07	-41.35

Table G.2 cont.

Energy (MeV)	<i>A priori</i>	% Total error	MAXED	% Change	LSQ	% Total error	% Change
5.48E-04	8.390E+11	22.36	1.636E+11	-80.50	2.696E+11	27.13	-67.87
1.01E-03	1.343E+12	22.36	9.215E+11	-31.36	7.069E+11	23.04	-47.35
1.87E-03	1.750E+12	22.36	1.183E+12	-32.37	8.944E+11	24.21	-48.89
3.47E-03	2.237E+12	22.36	1.491E+12	-33.37	1.170E+12	23.92	-47.72
6.41E-03	2.788E+12	22.36	1.739E+12	-37.63	1.461E+12	23.53	-47.58
1.19E-02	3.154E+12	22.36	1.821E+12	-42.26	1.633E+12	23.49	-48.21
2.19E-02	3.679E+12	22.36	2.386E+12	-35.16	2.444E+12	20.22	-33.58
4.06E-02	4.178E+12	22.36	2.692E+12	-35.57	3.010E+12	19.47	-27.95
7.50E-02	5.019E+12	22.36	3.198E+12	-36.27	3.820E+12	19.08	-23.88
1.39E-01	6.059E+12	22.36	3.892E+12	-35.75	4.877E+12	18.43	-19.49
2.57E-01	7.107E+12	22.36	4.614E+12	-35.08	5.933E+12	17.65	-16.52
4.75E-01	8.436E+12	22.36	5.489E+12	-34.94	7.036E+12	16.98	-16.60
8.78E-01	8.643E+12	22.36	5.618E+12	-35.00	6.990E+12	16.32	-19.13
1.62E+00	9.454E+12	22.36	6.124E+12	-35.23	7.384E+12	15.00	-21.90
3.00E+00	6.365E+12	22.36	4.070E+12	-36.06	5.291E+12	10.36	-16.88
5.55E+00	2.306E+12	22.36	1.548E+12	-32.89	8.895E+11	12.58	-61.43
1.03E+01	5.888E+11	22.36	7.436E+11	26.29	5.062E+11	4.66	-14.03
1.90E+01	1.106E+10	22.36	3.600E+10	225.62	8.677E+09	15.35	-21.52

Table G.3 Neutron fluxes in 32 energy groups at position 10 (B experiment)

Energy (MeV)	<i>A priori</i>	% Total error	MAXED	% Change	LSQ	% Total error	% Change
1.00E-07	2.412E+09	22.36	1.224E+11	4977.27	2.638E+09	19.52	9.41
1.85E-07	1.875E+09	22.36	9.870E+09	426.27	2.072E+09	19.31	10.46
3.42E-07	2.860E+09	22.36	1.209E+10	322.69	3.209E+09	18.97	12.19
6.33E-07	4.260E+09	22.36	8.295E+09	94.74	4.879E+09	18.50	14.54
1.17E-06	6.395E+09	22.36	9.840E+09	53.87	7.528E+09	17.87	17.72
2.16E-06	9.915E+09	22.36	1.000E+10	0.88	1.206E+10	17.05	21.65
4.00E-06	1.524E+10	22.36	1.548E+10	1.56	1.924E+10	16.03	26.25

Table G.3 cont.

Energy (MeV)	<i>A priori</i>	% Total error	MAXED	% Change	LSQ	% Total error	% Change
7.40E-06	2.371E+10	22.36	2.372E+10	0.05	3.106E+10	14.85	30.97
1.37E-05	3.758E+10	22.36	5.372E+10	42.97	5.093E+10	13.52	35.53
2.53E-05	6.218E+10	22.36	8.123E+10	30.63	8.618E+10	12.17	38.58
4.68E-05	1.101E+11	22.36	1.351E+11	22.66	1.541E+11	10.90	39.94
8.66E-05	2.089E+11	22.36	2.393E+11	14.54	2.913E+11	9.85	39.45
1.60E-04	3.834E+11	22.36	3.983E+11	3.87	5.629E+11	5.17	46.82
2.96E-04	6.771E+11	22.36	6.808E+11	0.55	8.780E+11	9.26	29.69
5.48E-04	9.475E+11	22.36	8.947E+11	-5.57	1.051E+12	9.33	10.94
1.01E-03	1.488E+12	22.36	1.363E+12	-8.42	1.847E+12	10.30	24.08
1.87E-03	2.027E+12	22.36	1.814E+12	-10.50	2.448E+12	10.89	20.75
3.47E-03	2.511E+12	22.36	2.207E+12	-12.09	2.974E+12	11.42	18.44
6.41E-03	3.090E+12	22.36	2.687E+12	-13.03	3.565E+12	11.83	15.37
1.19E-02	3.548E+12	22.36	3.055E+12	-13.90	3.943E+12	12.33	11.15
2.19E-02	4.120E+12	22.36	3.533E+12	-14.25	4.846E+12	12.83	17.62
4.06E-02	4.684E+12	22.36	4.001E+12	-14.58	5.498E+12	13.38	17.39
7.50E-02	5.674E+12	22.36	4.832E+12	-14.84	6.549E+12	13.96	15.42
1.39E-01	6.785E+12	22.36	5.768E+12	-14.99	7.662E+12	14.43	12.92
2.57E-01	7.943E+12	22.36	6.742E+12	-15.12	8.621E+12	14.76	8.54
4.75E-01	9.579E+12	22.36	8.119E+12	-15.25	9.732E+12	14.94	1.59
8.78E-01	9.731E+12	22.36	8.235E+12	-15.38	9.039E+12	14.97	-7.11
1.62E+00	1.066E+13	22.36	8.968E+12	-15.89	9.058E+12	14.29	-15.04
3.00E+00	7.167E+12	22.36	5.699E+12	-20.49	6.139E+12	10.21	-14.34
5.55E+00	2.753E+12	22.36	1.666E+12	-39.48	1.037E+12	12.28	-62.32
1.03E+01	6.256E+11	22.36	3.768E+11	-39.78	5.162E+11	5.16	-17.49
1.90E+01	2.910E+10	22.36	1.456E+10	-49.96	2.480E+10	13.50	-14.79

Table G.4 Neutron fluxes in 32 energy groups at position 17 (B experiment)

Energy (MeV)	<i>A priori</i>	% Total error	MAXED	% Change	LSQ	% Total error	% Change
1.00E-07	2.419E+09	22.36	8.973E+10	3609.81	2.428E+09	21.24	0.38
1.85E-07	1.983E+09	22.36	8.864E+09	346.90	2.006E+09	21.06	1.12
3.42E-07	2.795E+09	22.36	9.969E+09	256.74	2.858E+09	20.77	2.27
6.33E-07	4.302E+09	22.36	7.561E+09	75.76	4.457E+09	20.41	3.61
1.17E-06	6.439E+09	22.36	9.025E+09	40.16	6.773E+09	19.93	5.18
2.16E-06	9.863E+09	22.36	9.398E+09	-4.71	1.052E+10	19.35	6.67
4.00E-06	1.517E+10	22.36	1.440E+10	-5.07	1.637E+10	18.62	7.90
7.40E-06	2.374E+10	22.36	2.208E+10	-6.98	2.572E+10	17.75	8.32
1.37E-05	3.744E+10	22.36	4.747E+10	26.78	4.040E+10	16.66	7.90
2.53E-05	6.238E+10	22.36	7.271E+10	16.56	6.592E+10	15.52	5.67
4.68E-05	1.099E+11	22.36	1.208E+11	9.96	1.122E+11	14.35	2.10
8.66E-05	2.104E+11	22.36	2.171E+11	3.18	2.056E+11	13.36	-2.27
1.60E-04	3.817E+11	22.36	3.333E+11	-12.69	3.669E+11	5.38	-3.88
2.96E-04	6.753E+11	22.36	6.640E+11	-1.68	5.726E+11	13.49	-15.22
5.48E-04	9.271E+11	22.36	1.007E+12	8.60	6.073E+11	14.73	-34.50
1.01E-03	1.499E+12	22.36	1.266E+12	-15.49	1.277E+12	14.57	-14.77
1.87E-03	2.039E+12	22.36	1.688E+12	-17.22	1.760E+12	14.76	-13.70
3.47E-03	2.513E+12	22.36	2.048E+12	-18.52	2.230E+12	14.64	-11.28
6.41E-03	3.078E+12	22.36	2.508E+12	-18.52	2.763E+12	14.44	-10.25
1.19E-02	3.541E+12	22.36	2.896E+12	-18.22	3.154E+12	14.43	-10.93
2.19E-02	4.176E+12	22.36	3.333E+12	-20.18	4.193E+12	14.21	0.41
4.06E-02	4.751E+12	22.36	3.781E+12	-20.40	4.905E+12	14.44	3.25
7.50E-02	5.708E+12	22.36	4.537E+12	-20.51	5.930E+12	14.81	3.89
1.39E-01	6.964E+12	22.36	5.519E+12	-20.76	7.240E+12	15.08	3.97
2.57E-01	7.965E+12	22.36	6.291E+12	-21.01	8.131E+12	15.20	2.09
4.75E-01	9.553E+12	22.36	7.531E+12	-21.17	9.304E+12	15.21	-2.61
8.78E-01	9.877E+12	22.36	7.764E+12	-21.40	8.955E+12	15.06	-9.33
1.62E+00	1.054E+13	22.36	8.094E+12	-23.24	8.873E+12	14.26	-15.86
3.00E+00	7.107E+12	22.36	4.861E+12	-31.60	6.052E+12	10.21	-14.84

Table G.4 cont.

Energy (MeV)	<i>A priori</i>	% Total error	MAXED	% Change	LSQ	% Total error	% Change
5.55E+00	2.667E+12	22.36	1.292E+12	-51.56	1.030E+12	12.18	-61.40
1.03E+01	6.055E+11	22.36	3.987E+11	-34.15	5.373E+11	4.79	-11.27
1.90E+01	1.587E+10	22.36	2.368E+10	49.23	1.310E+10	14.46	-17.47

Table G.5 Neutron fluxes in 32 energy groups at position 23 (B experiment)

Energy (MeV)	<i>A priori</i>	% Total error	MAXED	% Change	LSQ	% Total error	% Change
1.00E-07	2.223E+09	22.36	1.137E+10	411.38	2.053E+09	23.04	-7.63
1.85E-07	1.737E+09	22.36	2.726E+09	56.95	1.619E+09	22.80	-6.80
3.42E-07	2.544E+09	22.36	3.697E+09	45.30	2.404E+09	22.42	-5.49
6.33E-07	3.858E+09	22.36	3.650E+09	-5.39	3.706E+09	21.95	-3.94
1.17E-06	5.725E+09	22.36	4.834E+09	-15.57	5.602E+09	21.35	-2.15
2.16E-06	8.945E+09	22.36	5.979E+09	-33.16	8.900E+09	20.66	-0.50
4.00E-06	1.383E+10	22.36	9.431E+09	-31.82	1.393E+10	19.85	0.67
7.40E-06	2.140E+10	22.36	1.463E+10	-31.64	2.153E+10	18.97	0.62
1.37E-05	3.399E+10	22.36	2.907E+10	-14.48	3.368E+10	17.98	-0.91
2.53E-05	5.644E+10	22.36	4.599E+10	-18.51	5.354E+10	17.10	-5.14
4.68E-05	9.958E+10	22.36	7.846E+10	-21.21	8.798E+10	16.37	-11.64
8.66E-05	1.885E+11	22.36	1.430E+11	-24.12	1.512E+11	16.03	-19.79
1.60E-04	3.473E+11	22.36	2.450E+11	-29.47	2.703E+11	5.47	-22.18
2.96E-04	6.086E+11	22.36	3.884E+11	-36.17	3.464E+11	19.67	-43.09
5.48E-04	8.372E+11	22.36	4.134E+11	-50.62	2.381E+11	30.87	-71.57
1.01E-03	1.341E+12	22.36	8.951E+11	-33.27	6.852E+11	23.78	-48.92
1.87E-03	1.808E+12	22.36	1.191E+12	-34.13	9.014E+11	24.85	-50.15
3.47E-03	2.297E+12	22.36	1.496E+12	-34.86	1.180E+12	24.37	-48.64
6.41E-03	2.792E+12	22.36	1.781E+12	-36.21	1.442E+12	23.88	-48.35
1.19E-02	3.206E+12	22.36	1.998E+12	-37.67	1.639E+12	23.74	-48.86
2.19E-02	3.746E+12	22.36	2.399E+12	-35.95	2.522E+12	19.99	-32.68
4.06E-02	4.195E+12	22.36	2.678E+12	-36.15	3.089E+12	19.11	-26.37

Table G.5 cont.

Energy (MeV)	<i>A priori</i>	% Total error	MAXED	% Change	LSQ	% Total error	% Change
7.50E-02	5.130E+12	22.36	3.262E+12	-36.43	4.011E+12	18.62	-21.81
1.39E-01	6.272E+12	22.36	3.994E+12	-36.33	5.215E+12	17.90	-16.84
2.57E-01	7.317E+12	22.36	4.668E+12	-36.20	6.323E+12	17.12	-13.58
4.75E-01	8.666E+12	22.36	5.528E+12	-36.21	7.472E+12	16.48	-13.78
8.78E-01	8.871E+12	22.36	5.655E+12	-36.25	7.378E+12	15.92	-16.82
1.62E+00	9.587E+12	22.36	6.119E+12	-36.18	7.658E+12	14.72	-20.12
3.00E+00	6.554E+12	22.36	4.184E+12	-36.16	5.531E+12	10.27	-15.61
5.55E+00	2.487E+12	22.36	1.616E+12	-35.05	9.351E+11	12.44	-62.41
1.03E+01	6.063E+11	22.36	5.180E+11	-14.56	4.999E+11	4.89	-17.55
1.90E+01	1.973E+10	22.36	3.005E+10	52.28	1.570E+10	14.79	-20.44

## REFERENCES

1. **George Imel, et al.** *Measurement of Actinide Neutronic Transmutation Rates with Accelerator Mass.* Idaho Falls : INL, August, 2009.
2. **Plompen, Arjan.** Why do we still need nuclear data? s.l. : European commission, Joint Research Centre.
3. **Manson Benedict, Thomas H.Pigford, Hans Wolfgang Levi.** *Nuclear Chemical Engineering Second Edition.* New York : McGraw-Hill, 1981. 0-07-004531-3.
4. **G. Youinou, et al.** *MANTRA: An integral Reactor Physics Experiment to Infer the Neutron Capture Cross Sections of Actinides and Fission Products in Fast and Epithermal Spectra.* Nuclear Data Sheets, s.l. : ELSEVIER, May, 2014, Vols. 119, 169-172.
5. **The ATLAS Facility. Argonne National Laboratory.** [Online] [Cited: 09 13, 2011.] <http://www.phy.anl.gov/atlas/facility/index.html>.
6. **M. Ragheb.** *Lecture Notes on Neutron cross sections.* s.l. : University of Illionis, November 15, 2014.
7. **Klaus H. Guber, P. E. Koehler, D. Wiarda, J. A. Harvey, et al.** *New neutron-induced cross-section measurements for improved nuclear data.* s.l. : International Conference on the Physics of Reactors, September 14, 2008.
8. **Nuclear Energy Agency.** *Review of Integral Experiments for Minor Actinide Management.* s.l. : ORGANISATION FOR ECONOMIC CO-OPERATION AND DEVELOPMENT, February 6, 2015. NEA No. 7222.
9. **Giuseppe Palmiotti, et al.** *A global approach to the physics validation of simulation codes for future nuclear systems.* s.l. : Annals of Nuclear Energy, January 3, 2009, Vols. 36, 355-361.
10. **L. Mercatali, G. Palmiotti, M. Salvatores, J. Tommasi.** *Irradiation Experiment Analysis for Cross Section Validation.* The Physics of Fuel Cycles and Advanced Nuclear Systems, Lagrange Park, IL : American Nuclear Society, April 25, 2004.
11. **Allen Todd.** *Advanced Test Reactor National Scientific User Facility User's Guide.* Idaho Falls : INL, 2009.
12. **The Advanced Test Reactor at The INL. doe.** [Online] [Cited: 10 30, 2011.] [http://www.id.doe.gov/news/PDF/06-GA50553-02b\\_Web.pdf](http://www.id.doe.gov/news/PDF/06-GA50553-02b_Web.pdf).

- 13. Matzke, Manfred.** *Unfolding Methods*. Handbook on Neutron Spectrometry in Mixed Fields, Braunschweig, Germany : Radiation Protection Dosimetry, 2003, Vol. Chapter 9.
- 14. Donald Craig Stuart, Douglas Earl Ryan.** *Epithermal neutron activation analysis with a SLOWPOKE nuclear reactor*. s.l. : Canadian journal of chemistry, June 18, 1980, Vol. 59.
- 15. Patrick Griffin J, John Kelly G.** *An exact treatment of self-shielding and covers in neutron spectra determinations*. Albuquerque, NM : Sandia National Laboratories, July 17, 1995.
- 16. Reginatto, Marcel.** *The "few-channel" unfolding programs in the UMG package: MXD\_FC33, GRV\_FC33 and IQU\_FC33*. s.l. : Physikalisch-Technische Bundesanstalt, March 1, 2004.
- 17. X-5 Monte Carlo Team.** *MCNP-A General Monte Carlo N-Particle Transport Code, Version 5, Vol I Overview and Theory*. s.l. : Los Alamos National Laboratory, February 1, 2008.
- 18. John M. Ryskamp, James W. Sterbentz, et al.** *Mixed oxide fuels testing in the Advanced Test Reactor to support plutonium disposition*. s.l. : Idaho National Engineering Laboratory, September, 1995. INEL-95/0459.
- 19. Frances Marshall M.** *Advanced Test Reactor Capabilities and Future Operating Plans*. Idaho Falls, ID : Idaho National Laboratory, September, 2005. INL/CON-05-00549.
- 20. Nuclear Energy Agency.** ERANOS 2.0. *oecd-nea*. [Online] [Cited: 06 26, 2015.] <http://www.oecd-nea.org/tools/abstract/detail/nea-1683>.
- 21. G. Rimpault.** *Physics documentation of ERANOS the ECCO cell code*. s.l. : CEA, French Atomic Energy Commission, October, 1997. RT/SPRC/LEPh 97-001.
- 22. A. Trkov, G. Zerovnik, L. Snoj, M. Ravnik.** *On the self-shielding factors in neutron activation analysis*. Nuclear Instruments and Methods in Physics research A, s.l. : ELSEVIER, September 9, 2009, Vols. 610, 553-565.
- 23. E. Martinho, I.F. Goncalves, J. Salgado.** *Universal curve of epithermal neutron resonance self-shielding factors in foils, wires and spheres*. Applied Radiation and Isotopes, s.l. : ELSEVIER, October 16, 2002, Vols. 58, 371-375.
- 24. David W. Nigg, Kevin A. Steuhm.** *Advanced Test Reactor Core Modeling Update Project*. s.l. : Idaho National Laboratory, September, 2011. INL/EXT-11-23348.

- 25. Joshua Peterson, Germina Ilas.** *Calculation of heating values for the high flux isotope reactor.* s.l. : American Nuclear Society, April 15, 2012.
- 26. ASTM International.** Standard test method for measuring neutron fluence rates by radioactivation of cobalt and silver (E-481). *Section-12-Nuclear, Solar and Geothermal Energy.* s.l. : ASTM International, 2003.
- 27. Edward M. Baum, Harold D. Knox and Thomas R. Miller.** *Nuclides and Isotopes, Sixteenth Edition.* s.l. : Lockheed Martin Distribution Services, 2002. 227910.
- 28. ASTM International.** Standard test method for measuring fast-neutron reaction rates by radioactivation of copper (E-523). *Section 12-Nuclear, Solar and Geothermal Energy.* s.l. : ASTM international, 2002.
- 29. ASTM International.** Standard test method for measuring fast-neutron reaction rates by radioactivation of iron (E-263). *Section 12-Nuclear, Solar and Geothermal energy.* s.l. : ASTM International, 2000.
- 30. ASTM International.** Standard test method for measuring fast-neutron reaction rates by radioactivation of nickel (E-264). *Section 12-Nuclear, Solar and Geothermal energy.* s.l. : ASTM International, 2002.
- 31. ASTM International.** Standard test method for measuring fast-neutron reaction rates by radioactivation of titanium (E-526). *Section 12-Nuclear, Solar and Geothermal Energy.* s.l. : ASTM International, 2002.
- 32. Chenkovich, Robert Jeremy.** *Refinement and validation of existing computer models of the OSU research reactor using activation analysis and spectral unfolding codes.* Columbus : Ohio state university, 2008.
- 33. ASTM International.** Standard Practice for determining neutron fluence, fluence rate, and spectra by radioactivation techniques (E-261). *Section 12-Nuclear, Solar, and Geothermal Energy.* s.l. : ASTM International, 2003.
- 34. Glenn F. Knoll.** *Radiation Detection and Measurement Third Edition.* New York : John Wiley & Sons, Inc., 2000. 0-471-07338-5.
- 35. Shultis Kenneth J, Richard Faw E.** *Fundamentals of nuclear science and engineering.* s.l. : Marcel Dekker, Inc, 2002. 0-8247-0834-2.
- 36. Erik Andersson Sunden, et al.** *Evaluation of spectral unfolding techniques for neutron spectroscopy.* Abingdon, UK : JET-EFDA, Culham science center, September 24, 2007.

- 37. Jaynes E. T.** *Information Theory and Statistical Mechanics*. s.l. : The Physical Review, March 4, 1957, Vols. 106, 620-630.
- 38. Marcel Reginatto.** *Unfolding with MAXED and GRAVEL*. Oak Ridge : Radiation Safety Information Computational Center (RSICC), March 1, 2004.
- 39. Linden, von der W.** *Maximum-entropy data analysis*. Materials Science & Processing, Garching, Germany : Applied Physics A , September 14, 1994, Vols. 60, 155-165.
- 40. Marcel Reginatto, Paul Goldhagen, Sonja Neumann.** *Spectrum unfolding, sensitivity analysis and propagation of uncertainties with the maximum entropy deconvolution code MAXED*. Accelerators, Spectrometers, Detectors and Associated Equipment, s.l. : Nuclear Instruments and Methods in Physics Research Section A, January 1, 2002, Nuclear Instruments and Methods in Physics Research A 476 , Vols. 476, 242–246, pp. 242–246.
- 41. David Nigg W, et al.** *Improved computational neutronics methods and validation protocols for the advanced test reactor*. s.l. : American Nuclear Society, April 15, 2012.
- 42. F.G. Perey.** *Contributions to Few-Channel Spectrum Unfolding*. s.l. : Oak Ridge National Laboratory, 1978. ORNL/TM-6267.
- 43. Williams J. G.** *Least-Squares Data Adjustment with Rank-Deficient Data Covariance Matrices*. s.l. : American Society for Testing and Materials, July 1, 2011.
- 44. David W. Nigg, Kevin A. Steuhm.** *Advanced Test Reactor Core Modeling Update Project*. s.l. : Idaho National Laboratory, September, 2012. INL/EXT-12-27059.
- 45. Ronald F. Fleming.** *Neutron Self-shielding Factors for simple Geometries*. International Journal of Applied Radiation and Isotopes, s.l. : Pergamon Press Ltd, February 10, 1982, Vols. 33, 1263-1268.
- 46. ASTM International.** *Standard Guide for Application of Neutron Spectrum Adjustment Methods in Reactor Surveillance. Section-12 Nuclear, Solar and Geothermal Energy*. s.l. : ASTM International, 2008.
- 47. F. Schmittroth.** *FERRET Data Analysis Code*. s.l. : Handford Engineering Development Laboratory, August, 1979.